UNIVERSITY OF OXFORD
DEPARTMENT OF ENGINEERING SCIENCE

Liquid Crystal Diffractive Optical Elements for Beam Steering and Holographic Display Applications

---

Qihao Han
St Cross College



A thesis submitted for the degree of
Doctor of Philosophy

Department of Engineering Science
University of Oxford
Trinity Term 2026

Abstract

LC DIFFRACTIVE OPTICAL ELEMENTS FOR BEAM STEERING AND HOLOGRAPHIC DISPLAY APPLICATIONS

by QIHAO HAN

This thesis presents the design, modelling, and experimental realisation of liquid crystal (LC) diffractive optical elements for beam steering and holographic display applications, with a particular emphasis on flexoelectric coupling. Three distinct LC grating configurations are investigated to achieve dynamic optical beam steering. These include a flexoelectric nematic LC diffraction grating, a chiral nematic LC diffraction grating, and an optical system comprising static polarisation gratings interspersed with voltage-controlled nematic LC phase shifters. Together, these approaches demonstrate controllable and reconfigurable optical beam steering suitable for advanced photonic systems.

The flexoelectric LC diffraction grating is first analysed through comprehensive theoretical and numerical modelling, wherein a nonlinear model is established to describe director reorientation under the combined influence of elastic, dielectric, and flexoelectric effects, extending beyond the limitations of linear small-angle approximations. The model incorporates both dielectric and flexoelectric coupling within an LC coordinate framework and is solved numerically using a finite-difference relaxation algorithm implemented in MATLAB. The simulations produced spatial director profiles that revealed both in-plane and out-of-plane director tilts, enabling the calculation of the corresponding diffraction pattern characteristics. Experimentally, flexoelectric diffraction gratings are realised using the LC dimer CB7CB. Diffraction effects were initially observed at elevated temperatures under AC excitation, although electrohydrodynamic instabilities are also found to be present. To enable stable operation at room temperature, a new LC mixture is developed by combining wide-temperature-range nematogen mixtures such as BL006 and MLC-6882 with CB7CB. This mixture exhibits reliable grating formation under DC driving conditions. The experimental diffraction patterns confirm the predictions of the nonlinear model and demonstrate controllable beam steering through voltage modulation.

A second approach demonstrates a switchable and rotatable chiral nematic LC diffraction grating. By optimising the ratio of the cell gap to the helical pitch and employing homeotropic alignment layers, we obtained a uniformly lying helix configuration. The inclusion of a small quantity of the LC dimer CB7CB introduces asymmetry in the flexoelectro-optic tilt, generating torque along the helix axis and enabling full in-plane rotation of the diffraction grating. The corresponding far-field diffraction pattern is rotated by adjusting the amplitude and temporal parameters of the applied tailored voltage waveform. Analysis of the diffracted light intensity

reveals a systematic dependence on both the waveform characteristics and the polarisation state of the incident light. These results demonstrate the feasibility of voltage-controlled rotational beam steering using chiral nematic LCs.

The third and final technique presented in the thesis is based on a polarisation grating integrated with tunable nematic LC phase shifters, which is employed to achieve real-time holographic display enlargement and location control. The system modulates the polarisation state of light to steer the reconstructed holographic image among discrete spatial positions with high efficiency and rapid response. By synchronising the driving signals of the LC phase shifters with the refresh rate of the spatial light modulator, the reconstructed images are dynamically steered in real time. At lower modulation frequencies, individual holographic subframes are displayed sequentially at separate positions. At higher frequencies, switching occurs faster than the human visual threshold, resulting in the perception of an enlarged holographic display area. Experimental results demonstrate beam steering among four discrete positions, corresponding to a four-fold expansion of the effective display field.

In addition to device development, the last part of the thesis explores the use of third-harmonic generation microscopy to study the internal director profiles of nematic and chiral nematic LCs. This nonlinear optical diagnostic technique provides valuable insight into the director profile, thereby improving the understanding of the internal director behaviour under applied electric fields.

In summary, the research presented in this thesis establishes a versatile framework for LC diffraction gratings through integrated theoretical, numerical, and experimental studies. The combination of flexoelectric, chiral nematic, and polarisation grating technologies enables tunable and reconfigurable beam steering. These results provide a foundation for the future development of next generation optical communication systems and dynamic holographic displays that require efficient and scalable beam-steering solutions.

Acknowledgements

It feels almost unreal to have reached the stage of writing the acknowledgements that conclude my DPhil journey. Time has passed so quickly that words seem insufficient to convey my sincere gratitude to my supervisors, Professor Stephen M. Morris and Professor Steve J. Elston. Their wisdom, patience, and unwavering guidance have shaped not only my research but also the way I think as a scientist. I will always remember the many discussions that inspired new ideas in LC research and the constant encouragement that sustained and motivated me throughout my studies. I feel incredibly fortunate to have had both of them as my supervisors. I am also deeply grateful that in October 2022, I chose to join the Soft Matter Photonics Group at Oxford, even though I also had an offer from the University of Cambridge.

I would like to express my gratitude to Steve M for his continuous guidance from my very first interview to the final stages of my DPhil thesis. I still vividly remember that first meeting, during which you introduced me to the fascinating world of liquid crystals and inspired me to embark on this journey. I am deeply grateful for your help in facilitating the acquisition of essential equipment and resources that made my research possible. Your exceptional leadership and management of the group created an environment in which I could always seek advice and receive support from colleagues. I am especially grateful that you considered my undergraduate background and thoughtfully guided me towards the research direction of LC beam steering, a field that has proven to be both intellectually stimulating and perfectly suited to my strengths. Thank you also for helping me integrate smoothly into the group and for your patience and encouragement throughout the publication process. Although I often felt anxious during the preparation of the manuscript, your constructive feedback and reassuring words gave me the confidence to publish several research articles in reputable journals. It is truly remarkable how you manage such a large group while still caring for every member with genuine attention and kindness.

I also would like to express my heartfelt thanks to Steve E. I still remember our first interview when I was travelling in Serbia. I was deeply impressed by your humour, intelligence, and kindness. When my return flight from Serbia landed at London Heathrow, I received the conditional offer from Oxford, a moment I will never forget. Your in-person tutorials during my first year helped me develop a solid understanding of LC physics. I also remember the time when I was struggling to identify a suitable topic for my first research project. It was you who helped me find direction, generously using your own time to guide and encourage me, and reassuring me that I was not behind others. You were the first person ever to call me a natural scientist, recognising my attention to detail while using your well-known rabbit hole story to remind me not to lose focus on what truly matters. Our regular discussions, whether in the morning around ten or in the afternoon around half past two, have always inspired me and moved my research forward. You have treated me not only as a student but as a valued research partner, and those conversations have been among the most enjoyable and rewarding

moments of my PhD experience. Sometimes I even feel that you treat everyone in our group with the same care and patience that a mentor would offer to his own children.

A special acknowledgement goes to Dr Waqas Kamal, who played a crucial role in teaching me how to operate the equipment in our group and in introducing me to the fundamental principles of the flexoelectric effect in liquid crystals. He also taught me how to prepare LC mixtures, a skill that became central to my subsequent DPhil research. I still remember one occasion when you noticed that I was feeling low and kindly asked me, almost as one would ask a child, whether I would like some ice cream. You have been like an older brother to me, always offering guidance and encouragement.

I also would like to thank all members of the Soft Matter Photonics Group, especially Chao, Jinge, Waqas, Linpei, Runcheng, Ji, Tessar, Jingyu and Guanxiong, with whom I have had the pleasure of collaborating on several publications. Your support and cooperation have meant a lot to me. I am especially grateful to Dr Peng Xie, an experienced postdoctoral researcher who sat behind me when I first joined the group. Peng helped me settle into the SMP Group and into life at Oxford. To my friend Adi, thank you for the many conversations we had, especially about football. It still feels like a small miracle that, although I support Tottenham and you support Arsenal, we managed to sit together peacefully for so long. My sincere thanks also go to Yihan, Bohan, and Zimo, who patiently taught me the basics of LC research in my first year and showed me around when I first joined the office. I am deeply grateful to Mengmeng, who has consistently offered thoughtful advice in both my research and daily life and has cared for me like an older sibling. I also thank Urban. I truly enjoyed attending conferences together and greatly appreciated the mutual encouragement and support we shared throughout this journey. I would like to thank Nathan and Camron for their patience and guidance in the lab. They have helped me refine my experimental techniques, reminded me to follow proper procedures, and prevented me from making careless mistakes. Finally, I would like to thank Qianlin, Ruofu, Zeyi, Yuanzhe, and Yuanhao, the youngest members of our group. Although our time together was brief, your energy, curiosity, and companionship brought warmth and joy to my final days in the lab. I sincerely wish you all the very best in your research and in the journeys that lie ahead.

Outside the Soft Matter Photonics Group, I would like to express my heartfelt thanks to the Oxford Chinese Students and Scholars Association. I have met many close Chinese friends through this community, especially during my time serving as President from 2024 to 2025. Leading the association, whose mission is to share Chinese stories and promote Chinese culture, has taught me a lot about understanding and connecting with different cultures. I often think of it as a stew with ingredients from both East and West, each with its own flavour, yet together creating something truly special. Through this experience, I have come to appreciate how Eastern and Western cultures can blend in harmony. The association has made Oxford feel like home and, more importantly, it is where I met my beloved Yicheng Wang, who has accompanied me for almost four years in Oxford and made my life here more complete and meaningful.

I would also like to express my deepest gratitude to my parents, Ms Yanlin Ding and Mr Yezhong Han, who have always been my greatest supporters and my first and most loyal fans. Their constant encouragement gave me the courage to pursue a DPhil and to become

the first Doctor in my family, and perhaps one day the first postdoctoral researcher as well. I still remember that you were the first two people to mention the University of Oxford to me when I was only a six-year-old boy. Perhaps from that moment on, a connection with Oxford quietly began to form. I truly love you both.

The movie About Time once said: "The truth is that now I don't travel back at all. I just try to live every day as if I have deliberately come back to this one day, to enjoy it, as if it were the full last day of my extraordinary and ordinary life." During my time in Oxford, I came to truly understand these words. I am deeply grateful for every ordinary, yet extraordinary day that this city and its people have given me.

Publications

Thesis-related Publications

Han, Q., Wang, J., Wang, T., Guo, J., Elston, S. J., and Morris, S. M., 2026. Third Harmonic Generation Imaging of Nematic and Chiral Nematic Liquid Crystals. [In submission]

Han, Q., Wang, T., Zhang, G., Kamal, W., Guo, J., Zhao, Z., He, C., Elston, S. J., Morris, S. M. 2026. Holographic projection display enlargement via polarization-grating beam steering with fast-response liquid crystal Pi-cells. *ACS Photonics*, 13(10), p.2943-2953.

Han, Q., Elston, S. J., Kamal, W., Xue, L. and Morris, S. M., 2025. A switchable and rotatable chiral nematic liquid crystal diffraction grating for beam-steering technology. *Advanced Optical Materials*, 13(21), p.2500794.

Han, Q., Elston, S. J., Kamal, W., Xue, L. and Morris, S. M., 2025. A nonlinear model of flexoelectric liquid crystal diffraction gratings. *Optics & Laser Technology*, 180, p.111502.

Non-thesis-related Publications

Guo, J., Qiu, X., Zhang, R., **Han, Q.**, Zhao, Z., Kamal, W., Elston, S. J., Castejon-Pita, A. A., He, C. and Morris, S. M., 2025. Drop-on-demand printed negative dielectric anisotropy liquid crystal droplets for adaptive complex beam manipulation and assessment. *Advanced Functional Materials*. [In submission]

Zhang, R., Marozsak, T., Wang, A. A., Zhang, Y., Ma, Y., Gao, T., Geng, H., **Han, Q.**, Dai, B., Elston, S. J., Morris, S. M., He, C. 2025. Multiplexed vector beam conversion via complex structured matter. *arXiv*, arXiv:2512.22980.

Conference Presentations

SPIE Photonics West
San Francisco – January 2026 (Presentation)
"Tunable and rotatable liquid crystal diffraction grating for dynamic beam steering technology"

University of Oxford Photonics Day
Oxford – January 2026 (Poster)
"Liquid crystal gratings for holography and dynamic beam-steering applications"

21st Optics of Liquid Crystals Conference
Taiwan – September 2025 (Presentation)
"Simulation and experimental characterization of liquid crystal gratings for dynamic beam-steering applications"

SPIE Digital Optical Technologies
Munich – June 2025 (Presentation)
"Switchable liquid crystal gratings for holography and dynamic beam steering application"

17th European Conference on Liquid Crystals
Prague – June 2025 (Poster)
"Liquid crystal diffraction gratings for optical beam steering"

University of Oxford Photonics Day
Oxford – April 2025 (Poster)
"Liquid crystal diffraction gratings for optical beam steering"

2025 British Liquid Crystal Society Annual Meeting
Birmingham – April 2025 (Presentation)
"Liquid crystal diffraction gratings for beam steering technology"

2024 British Liquid Crystal Society Annual Meeting
Oxford – April 2024 (Poster)
"Liquid crystal diffraction gratings for beam steering technology"

Awards

Best Oral Presentation Award at OLC 2025

Contents

Abstract **i**

Acknowledgements **iii**

Publications **vi**

Conference Presentations, Awards **vii**

List of Figures **xi**

List of Tables **xiv**

List of Abbreviations **xv**

1 Introduction **1**
1.1 Motivation . . . 1
1.2 Thesis Outline . . . 3

2 Background **7**
2.1 Introduction to LCs . . . 7
2.2 Nematic LC Phase . . . 8
2.3 Chiral Nematic LC Phase . . . 9
2.4 Optical Properties of LCs . . . 11
2.4.1 Birefringence . . . 11
2.4.2 Propagation of Light Wave in Birefringent Material . . . 13
2.4.3 Jones Matrices . . . 15
2.5 Elastic Energy and Continuum Theory . . . 19
2.6 Alignment and Cell Structure . . . 21
2.7 Electrical Properties of LCs . . . 22
2.7.1 Dielectric Coupling . . . 22
2.7.2 Fréedericksz Threshold . . . 24
2.8 Flexoelectricity . . . 24
2.8.1 Flexoelectric Effect . . . 24
2.8.2 Flexoelectro-optic Effect . . . 27
2.9 Uniform Lying Helix Structure . . . 29
2.10 Diffraction . . . 31
2.10.1 Raman-Nath and Bragg Diffraction . . . 31
2.10.2 Diffraction Grating . . . 32
2.10.3 LC Diffraction Gratings . . . 33
2.10.4 Modelling of LC Diffraction Grating . . . 34
2.11 Holographic Displays . . . 35
2.11.1 LC Spatial Light Modulators (LC-SLMs) . . . 35
2.11.2 LC Beam Steering for Holographic Displays . . . 36

2.12 Summary . . . 37

3 Experimental Techniques 38
3.1 LC Mixture Development . . . 38
3.2 LC Cell Preparation . . . 40
3.3 Polarised Optical Microscopy . . . 42
3.4 Flexoelectro-optic Tilt Angle Measurement . . . 44
3.5 Capacitance Measurements . . . 47
3.6 Summary . . . 50

4 Theoretical Modelling and Simulation of Flexoelectric Diffraction Gratings 52
4.1 Introduction . . . 52
4.2 Linear Model . . . 54
4.2.1 Unconstrained Model . . . 55
4.2.2 Constrained Model (Conical Model) . . . 59
4.3 Non-Linear Model . . . 61
4.4 Simulations . . . 63
4.4.1 Director Profiles . . . 65
4.4.2 Polarised Optical Microscope Imaging . . . 69
4.4.3 Far-field Diffraction . . . 71
4.5 Summary . . . 72

5 Flexoelectric Liquid Crystal Diffraction Gratings 75
5.1 Introduction . . . 75
5.2 Pitch Definition and Concept of Splay-Bend Structure . . . 77
5.3 Materials and Methods . . . 78
5.4 LC Diffraction Grating Formation . . . 80
5.4.1 High Temperature Formation . . . 80
5.4.2 Room Temperature Formation . . . 82
5.5 Diffraction Pattern . . . 85
5.6 Comparison with Simulations . . . 88
5.7 Limitations . . . 91
5.7.1 Imperfect Uniformity . . . 91
5.7.2 Crystal Formation . . . 94
5.8 Summary . . . 95

6 Chiral Nematic Liquid Crystal Diffraction Gratings 97
6.1 Introduction . . . 97
6.2 Chiral Nematic LC Director Profile Simulations . . . 102
6.3 Materials and Methods . . . 105
6.4 Experimental Results and Discussion . . . 107
6.4.1 A Switchable Grating . . . 108
6.4.2 An Electrically Rotatable Grating . . . 108
6.5 Summary . . . 123

7 Holographic Projection Displays Using Liquid Crystal Diffraction Gratings 125
7.1 Introduction . . . 125
7.2 Experimental Methods . . . 130
7.2.1 Materials . . . 130
7.2.2 Holographic Projection System . . . 131
7.2.3 Synchronisation . . . 132
7.3 Switching Speed Characteristics and Transmittance Analysis . . . 136
7.4 Holographic Projection Display Enlargement . . . 142
7.5 Simulation of the Scalability of the System . . . 147
7.6 Flexoelectric Grating for Electrically Controllable Wide Viewing Angles . . . 150
7.7 Summary . . . 153

8 Third Harmonic Generation Imaging of Liquid Crystals 156
8.1 Introduction . . . 156
8.2 Experimental Methods . . . 160
8.2.1 Materials . . . 160
8.2.2 Cell Preparation . . . 161
8.2.3 THG Imaging System . . . 162
8.3 Third Harmonic Generation . . . 165
8.4 Simulations . . . 170
8.4.1 Simulations of LC Director Profile . . . 170
8.4.2 Simulations of THG Signal . . . 171
8.5 THG Results . . . 172
8.5.1 Nematic LC . . . 174
8.5.2 Chiral Nematic LC (Grandjean state) . . . 175
8.5.3 Chiral Nematic LC (ULH state) . . . 177
8.5.4 Flexoelectric Nematic LC . . . 184
8.6 Summary . . . 189

9 Conclusions and Future Work 191
9.1 Thesis Conclusions . . . 191
9.2 Future Work . . . 197
9.2.1 UV Photo-polymerisation . . . 197
9.2.2 Pixelation in LC Devices . . . 199
9.2.3 Suppression of Unwanted Diffraction Orders . . . 200
9.2.4 High-Speed LC Devices . . . 202
9.2.5 THG Imaging in Other LC Phases and Devices . . . 203

References 205

List of Figures

2.1 Temperature dependence of nematic LC order parameter 8
2.2 Structure of a chiral nematic LC 10
2.3 Ordinary and extraordinary refractive indices in LCs 12
2.4 Schematic illustration of a birefringent material 14
2.5 Optical configuration including polariser, analyser, and LC sample 18
2.6 Fundamental LC distortion modes 20
2.7 Schematic illustrations of homogeneous and homeotropic alignment 21
2.8 Schematic illustrations of Fréedericksz cell and pi-cell 21
2.9 Flexoelectric polarisation induced by molecular deformation 25
2.10 Schematic illustration of the flexoelectric nematic LC director configuration in the voltage-on state. 27
2.11 The flexoelectro-optic effect in chiral nematic liquid crystals 29
2.12 Grandjean and ULH states under applied electric field 30
2.13 Schematic representation of light passing through a Raman-Nath diffraction grating 33

3.1 Preparation procedure for chiral dopant LC mixtures 39
3.2 Fabrication process of LC cell 42
3.3 Cross-sectional structure and layered configuration of LC cell 42
3.4 Experimental optical microscopy setup 43
3.5 Input and transmission signals under AC modulation 45
3.6 Transmission waveforms measured at different positions 47
3.7 C-V characteristics and Fréedericksz transition fitting of the homeotropic LC cell 49

4.1 Voltage-induced flexoelectric instability in LCs 55
4.2 Splay-bend liquid crystal grid configuration 65
4.3 Simulated voltage-dependent director profile and splay-bend structures 67
4.4 Simulated angular distributions of LC directors at different voltages 68
4.5 Simulated LC director configurations and conical angle evolution under applied voltages 70
4.6 Voltage-dependent far-field diffraction intensity distributions of the flexoelectric liquid crystal diffraction grating 73

5.1 Transition from the initial state to the splay-bend LC structure 77
5.2 Chemical structure of CB7CB 78
5.3 Optical setup for observing diffraction from the flexoelectric nematic LC diffraction grating 80
5.4 Microscope images of LC diffraction gratings under different AC field at high temperature 81
5.5 Comparison of experimental and simulated LC grating structures under different DC voltages 84
5.6 Voltage-dependent far-field diffraction patterns of the flexoelectric nematic LC diffraction grating 86

5.7 Voltage-dependent zero-order light intensity for different incident polarisation angles . . . 87
5.8 Experimental, simulated and analytical grating periods versus applied voltage . 90
5.9 Frequency-dependent EHD instability in the LC grating . . . 92
5.10 Dislocations formation in LC diffraction gratings induced by different mechanisms 93
5.11 Crystallisation observed in the LC mixture . . . 95

6.1 Optic axis rotation and device configuration of the chiral liquid crystal grating . 101
6.2 Simulated chiral nematic LC director profiles for planar and homeotropic alignments in Grandjean and ULH states . . . 103
6.3 Voltage-driven switching between different states of the chiral nematic LC diffraction grating . . . 109
6.4 Dynamic flexoelectro-optic tilt responses of different chiral nematic LC mixtures 111
6.5 Voltage waveform sequence for rotational control of the chiral nematic LC diffraction grating . . . 112
6.6 polarised optical microscopy images and diffraction patterns of different chiral nematic LC mixtures . . . 114
6.7 Helix-axis rotation controlled by the tailored waveform duration in different chiral nematic LC mixtures . . . 118
6.8 Waveform-controlled diffraction patterns and helix-axis orientations . . . 119
6.9 Diffraction angles and polarisation-dependent light intensity in chiral nematic LC gratings . . . 121

7.1 Configuration of the holographic projection display with LC beam-steering modules 132
7.2 Example of the temporal synchronisation schematic of the holographic display system . . . 135
7.3 Comparison of director reorientation and switching dynamics in Fréedericksz and nematic pi-cells . . . 138
7.4 Beam steering and holographic reconstruction using parallel polarisation gratings 143
7.5 Experimental holographic reconstructions using the polarisation-grating beam-steering system . . . 146
7.6 Demonstration of generating sixteen beam-steering positions using polarisation gratings with different periodicities (Λ) . . . 149
7.7 Diffraction behaviour of the holographic display incorporating a flexoelectric grating under different applied DC voltages . . . 151

8.1 Schematic of the THG microscopy setup used to characterise LC samples . . . 163
8.2 Mechanism of third-harmonic generation in chiral nematic LCs . . . 166
8.3 Helical-pitch-dependent THG generation in chiral nematic LCs . . . 169
8.4 Simulated long-pitch chiral nematic LC director profiles of the Grandjean and ULH state . . . 171
8.5 Simulated THG intensity maps of a chiral nematic LC in the Grandjean state . 172
8.6 THG signal distribution and intensity profile of neat E7 in the x-z plane . . . 174
8.7 THG signal distribution and intensity profile of the chiral nematic LC in the x-z plane . . . 176
8.8 THG signals of the chiral nematic LC in the ULH state at different depths within the LC layer . . . 178
8.9 THG signals in the ULH state with and without adaptive optics correction . . . 181
8.10 Convergence of adaptive optics correction and THG intensity improvement . . . 182

8.11 Director profiles in different planes under flexoelectric coupling 185
8.12 Voltage-dependent effective refractive index distributions in the y-z plane 186
8.13 THG imaging of the flexoelectric nematic LC device in the x-y and y-z planes . 187

9.1 The chemical structure of RM257 and the typical photoinitiator IR819. 198
9.2 Pixelated flexoelectric splay-bend structures with variable voltage application . . 199
9.3 Beam steering using an ideal blazed grating with a 2π phase ramp 200
9.4 Photopolymerisation methods in LC devices 201

List of Tables

4.1 Coupling regimes of flexoelectric nematic LC gratings under different dielectric anisotropies 59

5.1 Experimental and simulated diffraction-order separations under different applied voltages 90
5.2 Threshold voltages for flexoelectric and EHD onset under different AC frequencies 92

6.1 Composition and clearing temperatures of the investigated chiral nematic LC mixtures 106
6.2 Normalised rotation angle under different tailored waveform initial voltages . . . 115
6.3 Normalised rotation angle under different tailored waveform step sizes 115
6.4 Waveform timing conditions for different diffraction-pattern states 119
6.5 First- and second-order diffraction efficiencies for different chiral nematic LC mixtures 122

7.1 Voltage states for one-dimensional beam steering using LC phase shifters 144
7.2 Voltage states for two-dimensional beam steering using LC phase shifters 145
7.3 Diffraction angles under different applied DC voltages 152

8.1 Composition of the mixtures considered with varying concentrations of R811 . . 161

9.1 Comparison of beam-steering performance for different LC grating technologies . 196

List of Abbreviations

AC . . . . . **A**lternating **C**urrent.
AO . . . . . **A**daptive **O**ptics.
AR . . . . . **A**ugmented **R**eality.
ARC . . . . . **A**nti-**R**eflective **C**oating.
CBG . . . . . **C**ompound **B**lazed **G**rating.
CCD . . . . . **C**harge-**C**oupled **D**evice.
CGH . . . . . **C**omputer-**G**enerated **H**olograms.
DC . . . . . **D**irect **C**urrent.
DM . . . . . **D**eformable **M**irror.
EHD . . . . . **E**lectro**h**ydro**d**ynamic.
EHDI . . . . . **E**lectro**h**ydro**d**ynamic **I**nstability.
FDTD . . . . . **F**inite **D**ifference **T**ime **D**omain.
FM . . . . . **F**lip **M**irror.
FWHM . . . . **F**ull **W**idth at **H**alf **M**aximum.
GS . . . . . **G**erchberg–**S**axton.
He–Ne . . . . . **H**elium–**N**eon.
HGM . . . . . **H**armonic **G**eneration **M**icroscopy.
HOE . . . . . **H**olographic **O**ptical **E**lement.
HTP . . . . . **H**elical **T**wisting **P**ower.
HWP . . . . . **H**alf-**W**ave **P**late.
ITO . . . . . **I**ndium **T**in **O**xide.
LC . . . . . **L**iquid **C**rystal.
LCoS . . . . . **L**iquid-**C**rystal-**o**n-**S**ilicon.
LC-SLM . . . **L**iquid-**C**rystal **S**patial **L**ight **M**odulator.
LCP . . . . . **L**eft-**C**ircularly **P**olarised.
LiDAR . . . . **Li**ght **D**etection **a**nd **R**anging.
NA . . . . . **N**umerical **A**perture.
ND . . . . . **N**eutral **D**ensity.
NLC . . . . . **N**ematic **L**iquid **C**rystal.
NTB . . . . . **N**ematic **T**wist-**B**end.
OPA . . . . . **O**ptical **P**hased **A**rray.
PBS . . . . . **P**olarising **B**eam **S**plitter.

PDE . . . . . **P**artial **D**ifferential **E**quation.
PG . . . . . **P**olarisation **G**rating.
PI . . . . . **P**oly**i**mide.
POM . . . . . **P**olarised **O**ptical **M**icroscopy.
PSF . . . . . **P**oint **S**pread **F**unction.
PVA . . . . . **P**oly**v**inyl **A**lcohol.
PZ . . . . . **P**iezo **S**tage.
RCP . . . . . **R**ight-**C**ircularly **P**olarised.
SHG . . . . . **S**econd-**H**armonic **G**eneration.
SLM . . . . . **S**patial **L**ight **M**odulator.
THG . . . . . **T**hird-**H**armonic **G**eneration.
TPP-DLW . . **T**wo-**P**hoton **P**olymerisation **D**irect **L**aser **W**riting.
ULH . . . . . **U**niform **L**ying **H**elix.
UV . . . . . **U**ltra**v**iolet.
VBPM . . . . **V**ector **B**eam **P**ropagation **M**ethod.
VLC . . . . . **V**isible **L**ight **C**ommunication.
VR . . . . . **V**irtual **R**eality.

1 Introduction

1.1 Motivation

Beam steering is a fundamental technique in photonics that enables controlled manipulation of the direction of light propagation. It is central to numerous emerging technologies, including visible light communication (VLC), holographic displays, virtual- and augmented reality (VR/AR) imaging, and light detection and ranging (LiDAR) systems. The ability to dynamically direct light beams with high precision and low power consumption has therefore become an essential requirement for next-generation optical communication and display systems.

In the field of optical communications, particularly visible light communication, beam steering provides a pathway to improve link stability, mobility, and data transmission efficiency. VLC has attracted increasing interest as a potential solution to the increasing demand for high-speed wireless communication [1–3].

Its advantages include immunity to electromagnetic interference and the potential for exceptionally high data rates [1]. However, this technology's communication link is easily disrupted by movements and has a limited communication range due to the propagation of the light beam in a straight line. Beam steering can improve power efficiency and increase the system's mobility by allowing multiple beams to be steered in various directions to circumvent this issue. In addition, it is advantageous for a LiDAR system to direct its laser pulses quickly and accurately in multiple directions, allowing it to generate a three-dimensional map of the surrounding environment [4–6]. Moreover, in holography and display systems, beam steering plays a crucial role in accurately aligning and projecting images within VR/AR applications [7]. Beam steering is a significant area of research and development because the ability to control the direction of light beams improves the precision, efficiency, and functionality of various systems and devices.

Beam steering methods can generally be categorised into mechanical and non-mechanical approaches. Mechanical methods, such as rotating prisms and gimbal mechanisms, are fast and reliable, but have limited lifetimes and high energy consumption [8]. In contrast to mechanical methods, non-mechanical approaches include technologies such as variable focus lenses [9–12], acousto-optic deflectors [13–16], and LC-based technologies. Among these, LC-based technologies are the primary focus, as they overcome challenges of mechanical methods with benefits like compact size, low power consumption, and lightweight design.

Among LC-based methods, optical phased array (OPA) systems are popular, enabling a rapid response through phase modifications. However, they require precise control, which makes fabrication more difficult. Other methods, such as compound blazed gratings (CBGs), face inefficiency issues due to the flyback effect [17]. While methods that utilise resistive electrodes to establish a voltage gradient

across the surface can influence the behaviour of LCs, they may introduce defects, leading to non-uniform optical performance [17].

The motivation for the research in this thesis stems from the growing demand for high-performance, energy-efficient, and scalable optical beam steering technologies for both holography and optical communication. By developing and characterising tunable LC-based gratings that combine flexoelectric, chiral, and polarisation effects, this work aims to establish a unified framework for dynamic light control. The investigation presented in this thesis, therefore, focuses on the modelling, fabrication, and application of LC diffraction gratings as a versatile and effective solution for beam steering, holographic display enhancement, and adaptive optical communication systems.

1.2 Thesis Outline

The introductory Chapter 1 presents the background and motivation for this research. It outlines the importance of beam steering in photonics and discusses its applications in areas such as visible light communication, LiDAR, and holographic display technologies. The chapter also highlights the advantages of LC–based systems compared to alternative mechanical beam steering methods, emphasising their potential for compact, low-power, and tunable optical control.

The next chapter, Chapter 2, provides the background necessary for understanding the research presented in subsequent chapters. The chapter begins with an overview of the LC materials and their optical and electrical properties, followed by an introduction to alignment techniques and cell structures. The chapter then explains the fundamental principles of the flexoelectric effect, the flexoelectro-optic effect, and the uniform lying helix (ULH) configuration. Further sections introduce

diffraction theory, including Raman–Nath and Bragg regimes, and the modelling of LC diffraction gratings. The chapter concludes with a discussion on holographic displays, which is relevant to the work in Chapter 7.

Chapter 3 describes the experimental methods and characterisation techniques employed throughout this research. It outlines the preparation of LC mixtures and the fabrication of LC cells, including surface alignment procedures and cell-gap measurements. Polarised optical microscopy is introduced as a method for examining LC textures and alignment. The chapter also describes the measurement of flexoelectro-optic tilt angles in chiral nematic LCs and the use of capacitance–voltage measurements to determine dielectric properties and elastic constants. These methods establish the experimental framework for the investigations presented in the subsequent chapters.

Chapter 4 presents the theoretical modelling and simulation of the flexoelectric effect for optical diffraction. The chapter introduces both linear and nonlinear analytical models, describing unconstrained and conical configurations of the LC director. The nonlinear model, which incorporates dielectric and flexoelectric coupling, provides a more accurate description of molecular behaviour under applied electric fields. Simulations of director profiles, polarised optical microscope images, and far-field diffraction patterns are discussed in detail. The work presented in this chapter has been published in Optics & Laser Technology, 180, p.111502 [18].

Following this, Chapter 5 focuses on the experimental realisation of nematic flexoelectric LC diffraction gratings. It describes the formulation of new LC mixtures based on CB7CB, BL006, and MLC-6882 to enable room-temperature operation, as well as the characterisation of diffraction efficiency and beam steering behaviour. Comparisons between experimental observations and theoretical simulations are presented, confirming the validity of the nonlinear model developed

earlier. The work presented in this chapter has also been published in Optics & Laser Technology, 180 [18].

Chapter 6 investigates the development of a switchable and rotatable chiral nematic LC diffraction grating for beam-steering applications. The chapter describes simulations of chiral nematic director profiles, mixture preparation, and experimental verification of switchable and continuously rotatable diffraction gratings. It demonstrates that by employing tailored voltage waveforms, full 360° in-plane rotation of the diffraction pattern can be achieved. The work presented in this chapter has been published in Advanced Optical Materials, 13(21) [19].

Chapter 7 presents a polarisation-grating-based LC device designed for advanced holographic display applications. This chapter introduces a system architecture that integrates polarisation gratings with voltage-controlled pi-cell phase shifters to achieve high-speed beam steering. Experimental results demonstrate both fast-response and wide-angle holographic displays, effectively enlarging the visual display area and achieving wide-angle beam steering through the synchronised operation of the LC device and the incorporation of flexoelectric gratings. The work presented in this chapter has also been published in ACS Photonics, 13(10) [20].

Chapter 8 introduces the application of third-harmonic generation (THG) microscopy to investigate the internal molecular structure of complex LC systems. This nonlinear imaging technique is employed to analyse nematic and chiral nematic diffraction gratings with different pitches, as well as flexoelectric diffraction gratings, providing insights into their molecular alignment, pitch uniformity, and structural stability. The mechanisms governing THG intensity are further systematically explored and discussed. The manuscript describing this work is currently under submission.

Finally, Chapter 9 summarises the key findings of this research and discusses

directions for future work. It provides concluding remarks on the development and modelling of LC gratings for holography and optical communications, emphasising their potential for next-generation photonic systems. Prospective research avenues include the optimisation of LC mixture compositions, the integration of photopolymerisable materials to enhance device stability, and the development of high-speed devices for advanced optical communication applications.

2

Background

2.1 Introduction to LCs

Liquid crystals (LCs) are remarkable materials that represent a unique state of matter that sits between crystalline solids and isotropic fluid phases, which was first discovered by the Austrian botanist Friedrich Reinitzer in 1888 [5, 21]. Similar to liquids, LC molecules do not retain rigid positional order and have flowability. However, unlike an isotropic fluid, LC molecules exhibit orientational and positional ordering. Thus, they represent a composite state exhibiting both solid and liquid properties [22, 23]. Meanwhile, LCs can be classified into various mesophases based on molecular arrangement, including nematic, smectic, and cholesteric mesophases [23]. LCs can be categorised as thermotropic and lyotropic. The phase transitions of thermotropic materials are reliant on temperature, while lyotropics depend both on temperature and the concentration of the molecules in a solvent [24].

Consequently, temperature will affect the phase transitions of the LC. For instance, a thermotropic nematic LC undergoes several phase transitions as temperature rises (shown in **Figure 2.1**). Initially, below the melting point, it presents as a crystalline solid with an ordered molecular arrangement. As the temperature increases, it shifts to the liquid nematic phase, with most molecules pointing in the same direction. At a certain temperature, known as the 'clearing point', it transforms into an isotropic liquid phase with randomly positioned and oriented molecules.

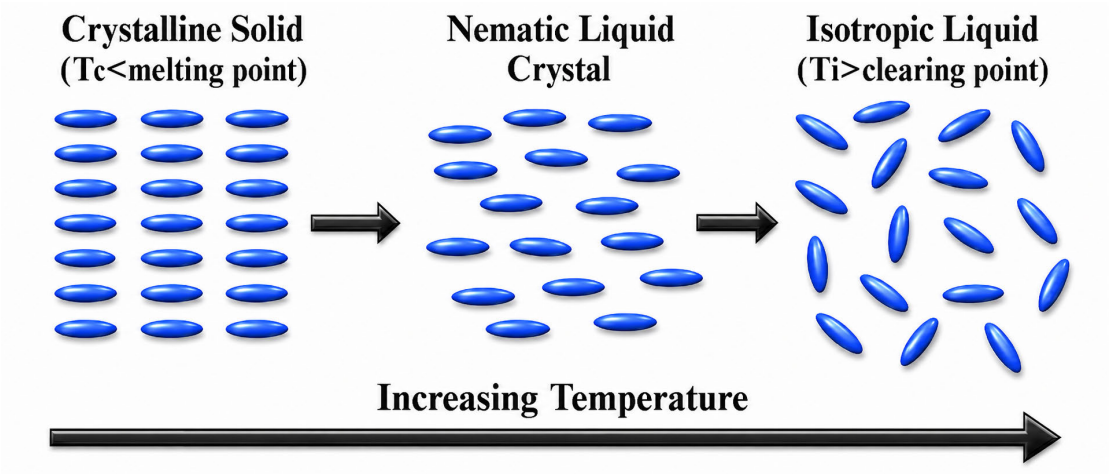


Figure 2.1: The impact of temperature on the order in thermotropic nematic LC. This author-created illustration was enhanced using AI tools for visual clarity.

LCs have been extensively studied due to their unusual electrical and optical properties and capacity to react to external stimuli such as electric fields and temperature.

2.2 Nematic LC Phase

Nematic LCs are one of the most utilised LC phases. These LCs are distinguished by the presence of permanent dipoles at a molecular level. This inherent characteristic has led to numerous benefits, including electro-optic modulation and enhanced

sensitivity. Meanwhile, the rod-shaped nematic molecules tend to align along a preferred direction, resulting in long-range orientation order. The preferred direction is characterised by the nematic director $\vec{n}$, which represents the average orientation of the molecules. It refers to a unit vector aligned with the time-averaged axis of an individual molecule or the average axis of a local group of molecules [25].

The scalar order parameter S can be used to describe the orientational order of the molecules with respect to the director, which is an average of the second Legendre polynomial [19]:

$$S = \langle P_2(\cos\theta)\rangle = \left\langle \frac{1}{2}\left(3\cos^2\theta - 1\right)\right\rangle \tag{2.1}$$

where θ is the angle between the long axis of the molecule and the local director, the brackets represent that the average is taken over many molecules.

Nematic LCs occur if $0 < S < 1$, whereby $S = 0$ in the isotropic phase. Meanwhile, if $\theta = 0$, $S = 1$, all the molecules are precisely aligned with no departure from the local director [26]. A negative value of S indicates that the molecular long axes preferentially lie in the plane perpendicular to the chosen reference direction rather than aligning along it. The limiting value $S = -1/2$ corresponds to all molecular long axes being perpendicular to that direction.

2.3 Chiral Nematic LC Phase

The chiral nematic LC phase is a periodical helical structure where the orientation of the local director follows a twisted profile in a particular direction. It can be generated by doping the nematic LC with a chiral dopant, which breaks the mirror symmetry inherent in the nematic LC. The chiral nematic LC phase also displays long-range orientational order but no long-range position order [23, 25].

The director rotates continuously along the helix axis, as illustrated in **Figure 2.2**,

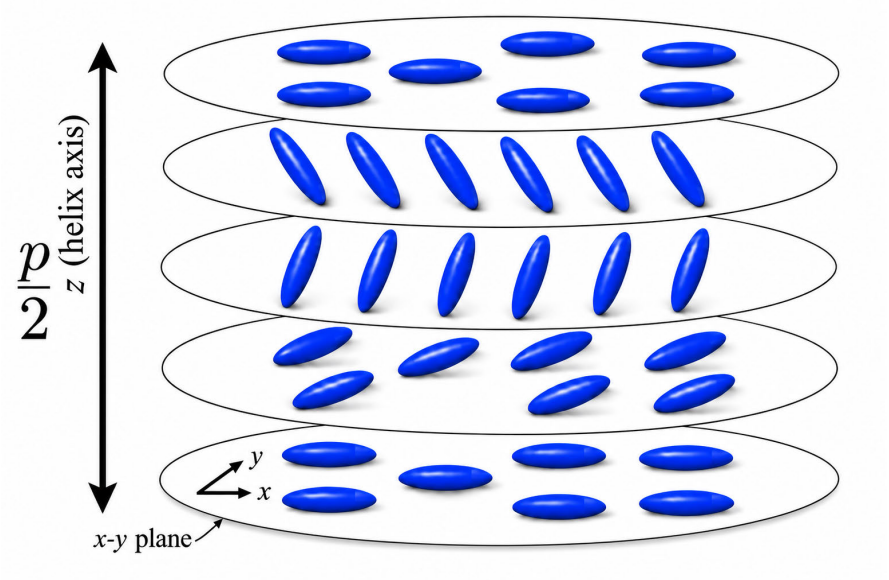


Figure 2.2: Schematic of the chiral nematic LC structure. The helix axis is along z, while the director remains in the x–y plane and rotates within that plane as z increases. The distance $\frac{p}{2}$ corresponds to a 180° director rotation. This author-created illustration was enhanced using AI tools for visual clarity.

the pitch of the helix determining the distance over which the local director rotates 2π around the helical axis. The pitch can be determined by the helical twisting power (HTP), which regulates the amount of chiral additive necessary to achieve the desired pitch (p):

$$p = \frac{1}{\text{HTP} \times \text{concentration}} \tag{2.2}$$

The HTP value is positive for right-handed chirality, whereas it is negative for left-handed chirality. The equation above demonstrates that the pitch can be altered by raising or reducing the chiral dopant concentration. Meanwhile, the pitch will also vary with the temperature and electric field. The periodic helical structure creates a photonic band gap within which circularly polarised light matching the handedness of the helix is selectively reflected, with the reflected

wavelength determined by the helical pitch. A nematic LC can be considered the infinite-pitch limit of a chiral nematic LC [22].

The chiral structure is crucial to the research in this thesis as it provides one method for generating a diffraction grating, as discussed in Chapter 6. This is achieved by applying an electric field at an appropriate strength. However, if the electric field is too strong, the chiral structure will unwind and be destroyed. When such a sample is observed under a cross-polarised microscope, it appears completely dark.

2.4 Optical Properties of LCs

LCs can selectively modulate light through mechanisms such as birefringence, anisotropic refractive indices, and controllable polarisation effects. These dynamic optical behaviours make LCs essential in modern display technologies and valuable in various photonic, sensing, and adaptive optics applications where precise and reversible control of light is required.

2.4.1 Birefringence

The behaviour of light as it travels through a non-magnetic material can be characterised by refractive index n, and it is related to the optical relative dielectric permittivity ε_r, following the equation:

$$n = \sqrt{\varepsilon_r} \tag{2.3}$$

The refractive index affects the speed and wavelength of light, expressed in the relationships:

$$v = \frac{c}{n} \tag{2.4}$$

$$\lambda = \frac{\lambda_0}{n} \tag{2.5}$$

where λ_0 is the wavelength of light in a vacuum.

LCs possess anisotropic properties, including the birefringence property, which is characterised by the difference between the extraordinary refractive index n_e and the ordinary refractive index n_o, where n_e, n_o represent the refractive indices parallel and perpendicular to the LC director, respectively (shown in **Figure 2.3**). Consequently, the birefringence can be expressed as

$$\Delta n = n_e - n_o = n_{\parallel} - n_{\perp} \tag{2.6}$$

The anisotropy of the refractive index can induce optical phase difference. Consider

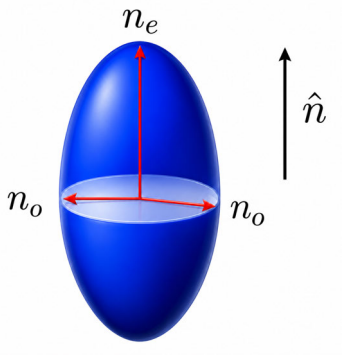


Figure 2.3: The extraordinary and ordinary refractive indices of an LC material. This author-created illustration was enhanced using AI tools for visual clarity.

a scenario where light passes through two media with refractive indices n_1 and n_2, respectively. The phase difference, denoted by $\Delta\varphi$, can be calculated by calculating the wavelength (λ_1, λ_2) and phase (φ_1, φ_2) for each medium, $\lambda_1 = \frac{\lambda_0}{n_1}$, $\lambda_2 = \frac{\lambda_0}{n_2}$, $\varphi_1 = \frac{2\pi d}{\lambda_1}$, $\varphi_2 = \frac{2\pi d}{\lambda_2}$.

$$\Delta\varphi = \varphi_1 - \varphi_2 = \frac{2\pi\,\Delta n\,d}{\lambda_0} \tag{2.7}$$

where λ_0 is the wavelength in free space, d is the distance travelled by the light through the LC layer. In LCs, light travels at various velocities when polarised parallel and perpendicular to the long axis of the LC molecules. This velocity difference results in a phase difference, which modifies the light's overall polarisation state. This phenomenon, known as optical retardation, is the primary cause of colour variations observed when examining birefringent samples under a microscope between crossed polarisers.

2.4.2 Propagation of Light Wave in Birefringent Material

Optical waves, a subset of electromagnetic waves, have perpendicular oscillating electric and magnetic fields. The Maxwell equations characterise the interaction between electric and magnetic fields, with the electric field typically representing light properties. The wave equation for an optical light wave is

$$\vec{E} = \vec{E}_0 \exp[j(\omega t - \vec{k}\cdot\vec{r})] \tag{2.8}$$

$\vec{E}_0$ is the amplitude of the electric field, $\vec{k}$ is the wavevector, which represents the propagation direction and has a magnitude equal to $\frac{2\pi}{\lambda}$, $\vec{r}$ is the position vector.

Polarised light refers to the vibrations of light that occur in a single plane. The electric field can oscillate in one direction (linear polarisation) or rotate while propagating (circular or elliptical polarisation). Circular polarisation has two perpendicular linear components with equal amplitude and a $\frac{\pi}{2}$ phase difference. Elliptical polarisation varies in phase and amplitude.

A waveplate is an excellent option for modifying the polarisation state of light

with minimal energy loss. It operates on the basis of the principle of birefringence. As depicted in **Figure 2.4**, a phase difference is introduced when light enters a birefringent material due to the differing refractive indices in the x and y directions, resulting in the light travelling at different velocities in each direction. The refractive indices along the principal axes, n_x and n_y, determine the corresponding phase velocities V_x and V_y. When $n_x < n_y$, the phase velocity along the x-axis exceeds that along the y-axis, $V_x > V_y$. Conversely, when $n_x > n_y$, the relation reverses, $V_x < V_y$. This anisotropy forms the basis of birefringent behaviour.

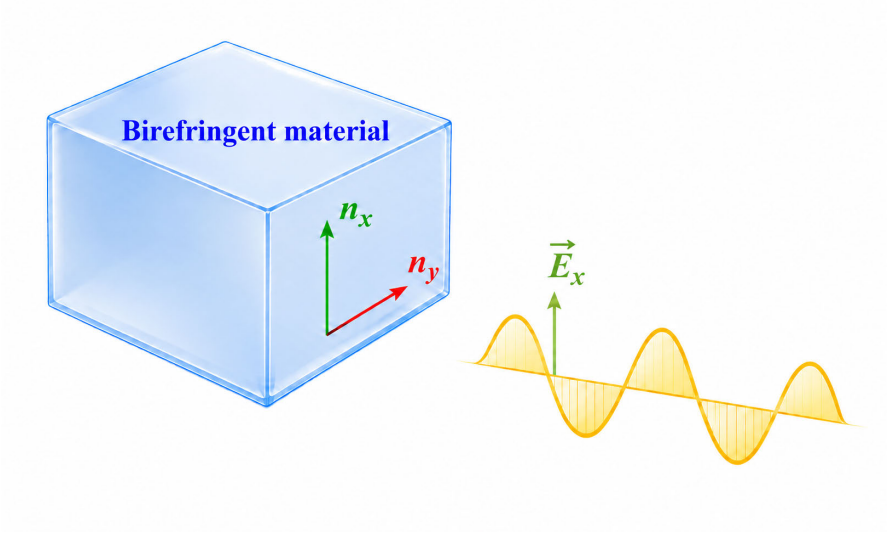


Figure 2.4: Schematic illustration of a birefringent material with refractive indices n_x and n_y along its principal axes. The yellow waveform represents the x-directed electric-field component $\vec{E}_x$, which experiences n_x. The y-component is not shown.

A half-waveplate can induce a phase shift equal to half the wavelength, thereby rotating the polarisation of linearly polarised light. The quarter-wave plate, on the other hand, can induce a quarter-wavelength phase shift, which converts linearly polarised light into circularly polarised light.

LCs, as birefringent materials, introduce a polarisation-dependent phase delay. This results in an optical path difference for light propagating through the medium. When the orientation of the LC is spatially modulated, the induced phase variation

can give rise to a periodic optical path difference, thereby providing the fundamental condition for the formation of a diffraction grating.

2.4.3 Jones Matrices

The finite-difference relaxation method is widely used in LC simulations as it provides an efficient and stable way to compute the equilibrium director distribution by minimising the total free energy under applied voltages and boundary conditions. Since the LC director varies continuously through the cell, it is helpful to discretise the LC layer into many small segments and then iteratively relax the molecular orientation until a physically accurate director profile is achieved. Each discretised LC layer can be modelled as a small element with its own retardation and optical axis. Jones calculus allows these many layers, as well as components like polarisers and waveplates, to be combined into an overall optical response modelled purely through matrix multiplication [27–29].

The electric field of a monochromatic plane wave propagating along the z-axis can be decomposed into two orthogonal components. The x-component is

$$\vec{E}_x = \vec{E}_{0x} e^{j(\omega t - kz)}, \tag{2.9}$$

and the y-component is

$$\vec{E}_y = \vec{E}_{0y} e^{j(\omega t - kz)}. \tag{2.10}$$

Here, k is the wave number, while $\vec{E}_{0x}$ and $\vec{E}_{0y}$ are complex amplitude vectors directed along the x- and y-axes, respectively. The total electric field is

$$\vec{E}_{\text{tot}} = \vec{E}_x + \vec{E}_y = \left(\vec{E}_{0x} + \vec{E}_{0y}\right) e^{j(\omega t - kz)}. \tag{2.11}$$

Because the exponential factor is common to both components, the polarisation state can be described by the complex amplitude vector

$$\vec{E}_{0,\text{tot}} = \vec{E}_{0x} + \vec{E}_{0y}. \tag{2.12}$$

In the x–y basis, let E_{0x} and E_{0y} denote the corresponding scalar complex amplitudes. The Jones vector is then

$$\vec{E}_{\text{Jones}} = \begin{bmatrix} E_{0x} \\ E_{0y} \end{bmatrix} \tag{2.13}$$

If we had an electric field pointing in the x-direction and y-direction, the normalised Jones vector would be

$$\vec{J}_x = \begin{pmatrix} 1 \\ 0 \end{pmatrix}, \qquad \vec{J}_y = \begin{pmatrix} 0 \\ 1 \end{pmatrix} \tag{2.14}$$

If the electric field points equally in the x-direction and y-direction (i.e., 45° to each axis), the Jones vector would be

$$\vec{J}_{45^\circ} = \frac{1}{\sqrt{2}} \begin{pmatrix} 1 \\ 1 \end{pmatrix} \tag{2.15}$$

For circularly polarised electric fields, one component is delayed with respect to the other by $\frac{\lambda}{4}$. Hence, the Jones vectors for circular polarisation states are given by:

$$\vec{J}_{\text{circular}} = \frac{1}{\sqrt{2}} \begin{pmatrix} 1 \\ \pm j \end{pmatrix} \tag{2.16}$$

where $+j$ and $-j$ represent left and right circular polarisation, respectively.

When a waveplate or LC layer has an arbitrary optical-axis orientation, a

rotation matrix is used to transform the Jones vector into the coordinate system aligned with that axis. The rotation matrix is defined as:

$$R(\theta) = \begin{pmatrix} \cos\theta & -\sin\theta \\ \sin\theta & \cos\theta \end{pmatrix}. \tag{2.17}$$

When polarised light traverses an optical element characterised by a Jones matrix M, the output Jones vector is expressed as $\vec{J}_{\text{out}} = M\vec{J}_{\text{in}}$. Common optical elements such as polarisers and waveplates are typically described by 2×2 matrices. For a birefringent waveplate, as discussed in the previous section (Eq. 2.7), the retardance $\Gamma = \Delta\varphi = \frac{2\pi\Delta n_{\text{eff}}\, d}{\lambda_0}$. When the optic axis is aligned at 45° relative to the x-axis, the corresponding Jones matrix is given by:

$$J\left(\frac{\pi}{4}\right) = R\left(-\frac{\pi}{4}\right) \begin{pmatrix} e^{i\Gamma/2} & 0 \\ 0 & e^{-i\Gamma/2} \end{pmatrix} R\left(\frac{\pi}{4}\right). \tag{2.18}$$

This expression arises from representing the optical element in its principal axis system, where the Jones matrix is diagonal. This multiplication yields:

$$\begin{pmatrix} \cos\frac{\Gamma}{2} & -i\sin\frac{\Gamma}{2} \\ -i\sin\frac{\Gamma}{2} & \cos\frac{\Gamma}{2} \end{pmatrix}. \tag{2.19}$$

where $R\left(\pm\frac{\pi}{4}\right)$ represents the rotation matrix that rotates coordinate axes by ±45°.

In our experimental setup, we routinely employ cross-polarised optical microscopy to characterise the LC director configuration. This arrangement can be conveniently described using the Jones matrix formalism. When the LC optic axis is oriented at 45° with respect to the transmission axis of the polariser, as illustrated in **Figure 2.5**, the resulting optical response can be analysed straightforwardly. The

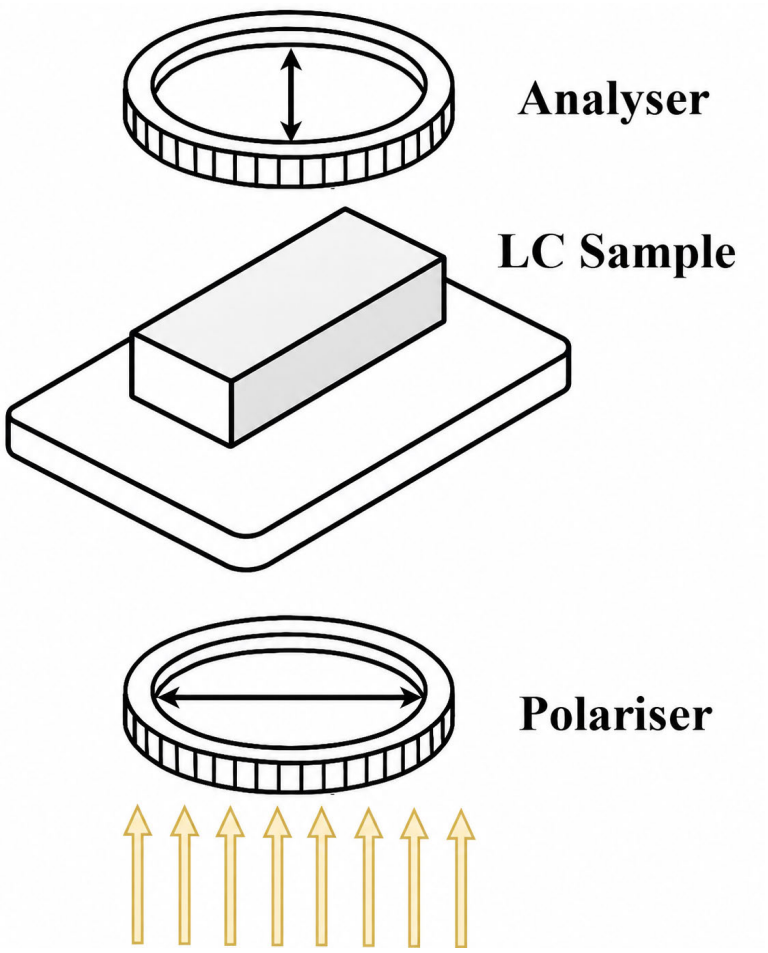


Figure 2.5: Stack of optical components including a polariser, an analyser, and an LC sample. The black arrows represent the transmission axis of the polariser and analyser.

complete Jones matrix representation of this optical system is expressed as follows:

$$J_{\text{out}} = \begin{pmatrix} 1 & 0 \\ 0 & 0 \end{pmatrix} \begin{pmatrix} \cos\frac{\Gamma}{2} & -i\sin\frac{\Gamma}{2} \\ -i\sin\frac{\Gamma}{2} & \cos\frac{\Gamma}{2} \end{pmatrix} \begin{pmatrix} 0 \\ 1 \end{pmatrix} = \begin{pmatrix} -i\sin\frac{\Gamma}{2} \\ 0 \end{pmatrix} \tag{2.20}$$

The leading matrix corresponds to the analyser (second polariser) encountered by the transmitted light, the middle matrix describes the LC cell, and the final column vector represents the incident polarisation state. The intensity transmission can subsequently be determined by computing the product of the output Jones vector with its complex conjugate:

$$T = \sin^2\left(\frac{\pi \Delta n_{\text{eff}}\, d}{\lambda}\right) \tag{2.21}$$

When the optic axis of the LC device is at an arbitrary angle χ to the first polariser's axis, the transmission becomes:

$$T = \sin^2(2\chi)\sin^2\left(\frac{\pi \Delta n_{\text{eff}}\, d}{\lambda}\right) \tag{2.22}$$

where Δn_{eff} is the effective birefringence, which is related to the applied voltage and the orientation of the LC alignment. This concept is useful for modelling microscope images, as will be discussed in Chapter 4.

Note that the Jones vector approach is suitable only for describing fully polarised optical fields. It cannot represent partially polarised or unpolarised light, and reflected components are not accounted for in the model.

2.5 Elastic Energy and Continuum Theory

Sir Charles Frank, a physicist, created the continuum theory in the 1950s [30], expanding on the work of Zocher [31], to characterise the behaviour of LCs. The LC director undergoes continuous reaction in response to external factors such as electric or magnetic fields, resulting in elastic deformation that deviates from its lowest-energy state. This deformation can be classified into three fundamental distortions: splay (divergence of the director), twist (curl of the director dotted with the director), and bend (cross-product of the director with the curl of the director field), which are depicted in **Figure 2.6**. These distortion types are characterised by their corresponding Frank elastic constants, denoted as K_{11}, K_{22}, and K_{33}, in units of N [32].

The elastic free-energy associated with these three types of director distortion

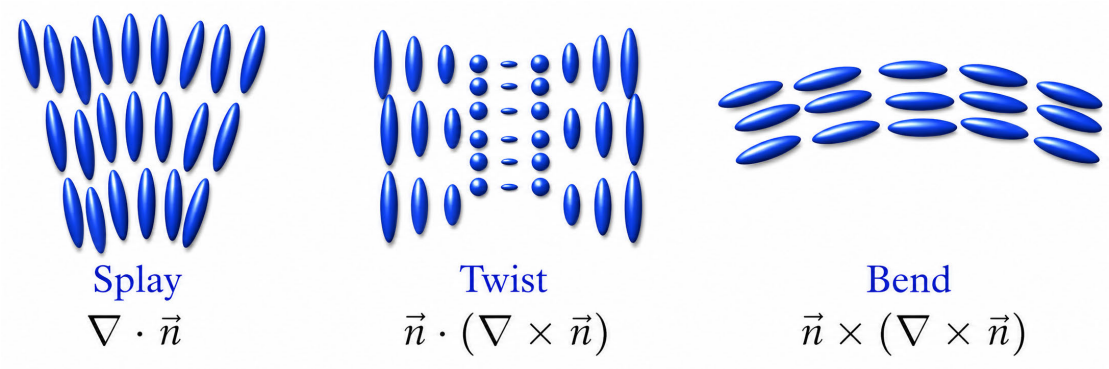


Figure 2.6: Fundamental LC distortions along with their respective mathematical representations. This author-created illustration was enhanced using AI tools for visual clarity.

is described by the Frank–Oseen free-energy density [30]:

$$f_{\text{elastic}}(\vec{n}) = f_{\text{splay}}(\vec{n}) + f_{\text{twist}}(\vec{n}) + f_{\text{bend}}(\vec{n}) \tag{2.23}$$

$$= \frac{1}{2}\left\{K_{11}[\nabla \cdot \vec{n}]^2 + K_{22}[\vec{n} \cdot (\nabla \times \vec{n})]^2 + K_{33}[\vec{n} \times (\nabla \times \vec{n})]^2\right\} \tag{2.24}$$

Where $\vec{n} = (n_x, n_y, n_z)$. In general, $K_{33} > K_{11} > K_{22}$ means that the impact of bend distortions on LCs is greater than that of splay and twist distortions. As a practical measure to simplify the analysis, a one-constant elastic free energy density expression is commonly used, with the assumption that $K = K_{33} = K_{22} = K_{11}$:

$$f_{\text{elastic}}(\vec{n}) = \frac{1}{2}K\left\{[\nabla \cdot \vec{n}]^2 + [\nabla \times \vec{n}]^2\right\} \tag{2.25}$$

Physical systems seek to maintain a minimum amount of free energy. As distortions or deformations occur, the molecules in these systems strive to return to their original, undistorted arrangement. This indicates that an electric field can be employed to reorient the LC director.

2.6 Alignment and Cell Structure

To analyse the electro-optical properties of LCs, we filled glass cells with LCs. The LC alignment layer defines the initial orientation of the surface LC molecules without applying an electric field, thus significantly influencing the optical properties and performance of the device. **Figure 2.7** illustrates the two primary alignment types: homogeneous (planar) and homeotropic. Homogeneous alignment further divides into two categories: the Fréedericksz cell, with substrates rubbed in opposite directions, and the pi-cell, with substrates rubbed the same way (shown in **Figure 2.8**). This research primarily utilises the Fréedericksz cell.

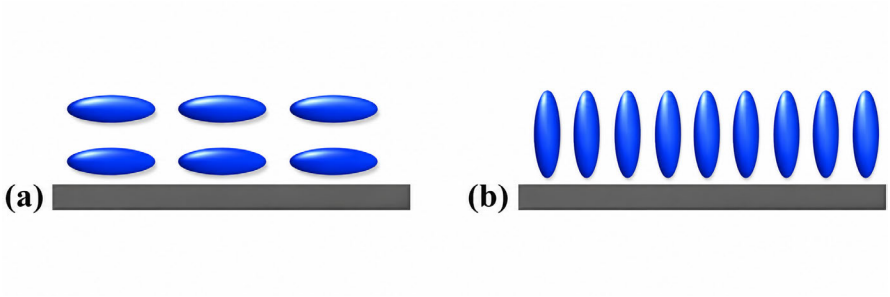


Figure 2.7: Schematic illustrations of (a) homogeneous alignment (LC directors parallel to the substrate). (b) homeotropic alignment (LC directors perpendicular to the substrate). This author-created illustration was enhanced using AI tools for visual clarity.

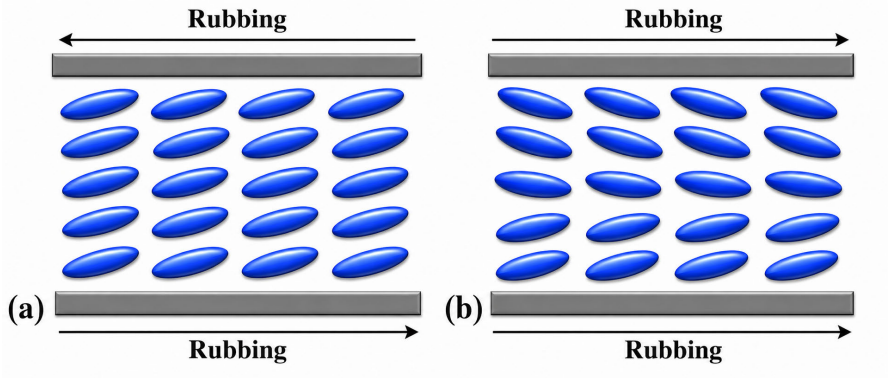


Figure 2.8: Schematic illustrations of (a) Fréedericksz cell (b) pi-cell. This author-created illustration was enhanced using AI tools for visual clarity.

2.7 Electrical Properties of LCs

LCs are highly sensitive to external stimuli, particularly electric fields. When a sufficient electric field is applied, the torque exerted on the anisotropic molecules can reorient the director. This section will discuss these electric field effects in detail.

2.7.1 Dielectric Coupling

As dielectric materials, LCs possess dipole moments because of the positive and negative charges at each end of the molecule structure. The dipole moments in the molecules will be oriented when the electric field is applied to the LC, leading to net bulk polarisations. The relationship between induced polarisation and applied electric field is given by the formula:

$$\vec{P} = \varepsilon_0 \chi_e \vec{E} \tag{2.26}$$

where ε_0 represents the free space permittivity, and χ_e represents the electric susceptibility.

For a uniaxial material, the electric displacement is defined as [32]:

$$\vec{D} = \varepsilon_0 \vec{E} + \vec{P} = \varepsilon_0 (\vec{I} + \vec{\chi}_e)\vec{E} = \varepsilon_0 \vec{\varepsilon}_r \vec{E} \tag{2.27}$$

In this expression, $\vec{\varepsilon}_r$ represents the relative dielectric permittivity. In the case of anisotropic materials, $\vec{\varepsilon}_r$ is a tensor, represented as follows:

$$\vec{\varepsilon}_r = \begin{pmatrix} \varepsilon_\perp & 0 & 0 \\ 0 & \varepsilon_\perp & 0 \\ 0 & 0 & \varepsilon_\parallel \end{pmatrix} \tag{2.28}$$

where the $\varepsilon_\perp$ and $\varepsilon_\parallel$ are the permittivities perpendicular and parallel to the director, respectively. The dielectric anisotropy is denoted as $\Delta\varepsilon = \varepsilon_\parallel - \varepsilon_\perp$. Thus, the electric displacement can be written as:

$$\vec{D} = \varepsilon_0 \varepsilon_\perp \vec{E} + \varepsilon_0 \Delta\varepsilon \, (\vec{n} \cdot \vec{E}) \, \vec{n} \tag{2.29}$$

where the director is given by $\vec{n} = \begin{pmatrix} 0 \\ 0 \\ 1 \end{pmatrix}$. Therefore, the free energy due to the dielectric coupling can be written as:

$$f_{\text{dielectric}} = -\frac{1}{2} \vec{D} \cdot \vec{E} \;\; = -\frac{1}{2} \varepsilon_0 \varepsilon_\perp E^2 \; - \; \frac{1}{2} \varepsilon_0 \Delta\varepsilon \, (\vec{n} \cdot \vec{E})^2. \tag{2.30}$$

However, we are primarily considering the second term, as it depends on the orientation of the LC director. Hence, the free energy equation due to the dielectric coupling simplifies to:

$$f_{\text{dielectric}} = -\frac{1}{2} \varepsilon_0 \Delta\varepsilon \, (\vec{n} \cdot \vec{E})^2 \tag{2.31}$$

The above equation demonstrates that for a material with positive $\Delta\varepsilon$, the free energy due to dielectric coupling is minimised when the director is aligned parallel to the electric field. In contrast, for negative $\Delta\varepsilon$ materials, the minimum free energy state occurs when the director is perpendicular to the electric field. Physical systems inherently tend to minimise their free energy [26]. Consequently, manipulation of the strength of the applied electric field can effectively regulate the degree of molecular reorientation.

2.7.2 Fréedericksz Threshold

As discussed in the previous section, the electric field will cause reorientation of the LC molecules. However, when the electric field is relatively small, the molecules tend to resist aligning with the electric field as a result of their elastic energy, maintaining their original orientation. Once the electric field exceeds the critical threshold value, known as the Fréedericksz threshold ($V_{(\text{th_frkz})}$), the electric field compels the molecules to overcome the elastic force of the LC, causing them to align with the electric field. The Fréedericksz threshold can be described using the following equation [26]:

$$V_{(\text{th_frkz})} = \pi \sqrt{\frac{K}{\Delta\varepsilon\,\varepsilon_0}} \tag{2.32}$$

In this equation, K represents an elastic constant, assuming a uniform electric field is applied.

2.8 Flexoelectricity

The flexoelectric effect is a direct coupling between the mechanical deformation (bend, splay) and the electrical polarisation of anisotropic materials such as LCs [33].

2.8.1 Flexoelectric Effect

A uniformly aligned conventional nematic LC is non-polar because the director orientations $\vec{n}$ and $-\vec{n}$ are physically equivalent. Even if its molecules possess permanent electric dipoles, there is no net macroscopic polarisation in this state. However, the elastic distortion can potentially generate net electric polarisation, which can be induced by the mechanical deformation of the director field. Specifically, as shown

in **Figure 2.9**, splay and bend distortions of the liquid-crystal director can give rise to a net flexoelectric polarisation [34]. Pear-shaped and banana-shaped molecules are used to illustrate these two mechanisms, respectively. An applied electric field can, conversely, induce a director distortion through flexoelectric coupling.

The molecular configuration is influenced by the flexoelectric coefficients of the LC material. The flexoelectric coefficients of splay (e_1) and bend (e_3) represent the proportionality constants associated with these deformations. Twist deformation, on the other hand, does not induce electric polarisation. This is because the twist deformation involves rotating the LC molecules around the director. Due to the centrosymmetry of the LCs, their electrical dipole moments remain unchanged during twist deformation, resulting in no net polarisation. Therefore, only bend or splay deformations, or a combination of the two, can produce a net flexoelectric polarisation.

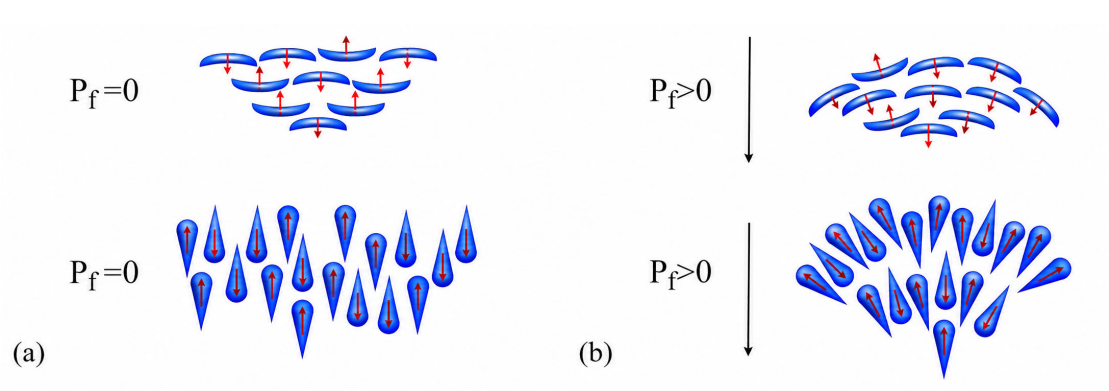


Figure 2.9: The flexoelectric polarisation. A schematic showing shaped molecules (a) with no net polarisation and (b) constrained to splay and bend geometries, respectively, which result in the generation of a net flexoelectric polarisation. This author-created illustration was enhanced using AI tools for visual clarity.

In general, the molecular shape of nematic LCs is not solely pear- or banana-shaped but rather has a geometrical arrangement that permits polarisation to arise for both splay and bend distortions. By applying an electric field across the LC, it is also feasible to achieve the inverse flexoelectric effect, which induces the

alignment of the dipole moments and generates local deformation of the director field [34]. The flexoelectric polarisation can be expressed as:

$$\vec{P} = e_1\vec{n}(\nabla \cdot \vec{n}) + e_3(\nabla \times \vec{n}) \times \vec{n} \tag{2.33}$$

where $\vec{n}$ represents the director, $\nabla \cdot \vec{n}$ and $\nabla \times \vec{n}$ represent the splay and bend deformation gradients, respectively. The free energy equation characterises the coupling between the flexoelectric polarisation and an applied field. It can be expressed as follows.

$$f_{\text{flexo}}(\vec{n}) = -\vec{P}_{\text{flexo}} \cdot \vec{E} = -\Big(e_1\,\vec{n}\,(\nabla\cdot\vec{n}) + e_3\,(\nabla \times \vec{n}) \times \vec{n}\Big) \cdot \vec{E} \tag{2.34}$$

In a bent-core nematic cell, flexoelectric coupling can also produce collective deformation of the director field over distances much larger than the molecular scale. Above an appropriate applied-field threshold, a spatially periodic combination of splay and bend may develop across the cell, forming stripes known as flexodomains. Under suitable conditions, flexodomains form stationary periodic director patterns. They are distinct from flow-driven electrohydrodynamic convection, which is discussed in Chapter 5. Their stability depends on driving conditions and material properties, and stationary stripes alone do not establish hydrodynamic stability. **Figure 2.10** schematically illustrates this director pattern in the voltage-on state, with the rubbing direction along the x-axis. The periodic modulation of the director produces a spatially varying optical response, allowing the cell to act as a diffraction grating.

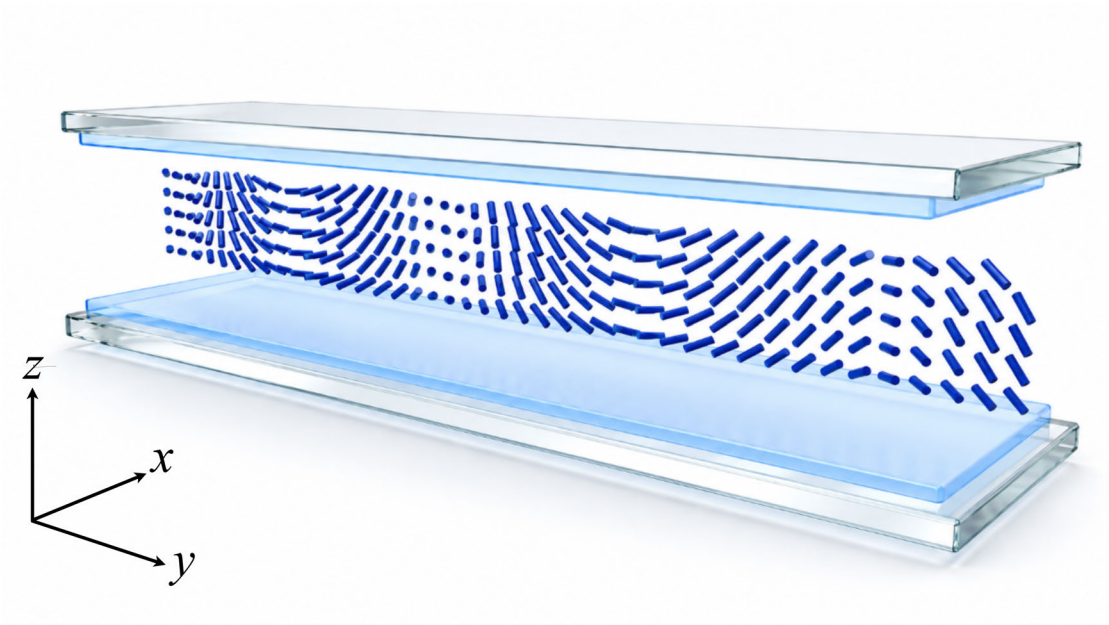


Figure 2.10: Schematic illustration of the flexoelectric nematic LC director configuration in the voltage-on state, showing a periodic splay–bend distortion. The rubbing direction is along the x-axis.

2.8.2 Flexoelectro-optic Effect

The chiral nematic system inherently exhibits a natural twist distortion, forming a periodic helicoidal structure when no electric field is applied. The flexoelectricity refers to the coupling between director deformation and electric polarisation, whereas the flexoelectro-optic effect refers to the optical-axis response arising from this coupling in a chiral nematic liquid crystal. The flexoelectro-optic response depends on the orientation of the helix axis relative to the applied field. In the uniform lying helix geometry, the helical axis lies parallel to the substrates, so an electric field applied across the cell is perpendicular to the helix and can induce an in-plane rotation of the effective optical axis by an angle ($\varnothing$). The tilt angle is the equilibrium between the elastic energy and the flexoelectric free energy of the LC. The coupling between the electric field and the chiral nematic LC results in a fast switching of the optical axis. The switching speed is around 100 µs

for chiral nematic LCs with short pitch (< 300 nm) [35–37]. This phenomenon is known as the flexoelectro-optic effect and is observed when the electric field is applied perpendicular to the helical axis. The behaviour of the optical-axis rotation is shown in **Figure 2.11**.

In the absence of an applied electric field, as shown in Figure 2.11(a), the helix axis is perpendicular to the substrate. The Bouligand cut-through plane (a cross-sectional plane that reveals the internal helical architecture) shows no splay or bend deformation, and consequently no polarisation is induced. When an electric field is applied at a voltage below the threshold required to unwind the LC molecules, as shown in Figure 2.11(b), the helix axis remains perpendicular to the substrate. However, the LC molecules undergo a tilt from their initial alignment. In the Bouligand cut-through plane, this tilt manifests as molecular bending and splaying, which creates a flexoelectric polarisation that responds to the applied electric field. The measurement of the tilt angle will be described in Chapter 3 [34].

The flexoelectric tilt angle ($\varnothing$) can be derived as a function of the electric field based on the minimisation of the free energy equation. It can be expressed as

$$\varnothing(E) = \frac{e_1 - e_3}{K_1 + K_3}\frac{E}{q} \tag{2.35}$$

where E is the electric field and q is the helical pitch wave number, $\frac{e_1 - e_3}{K_1 + K_3}$ represents the flexo-elastic ratio, which refers to the coupling between elastic and flexoelectric effects in LCs [38]. Thus, it becomes evident that the tilt angle is influenced by both the applied electric field and the flexo-elastic ratio.

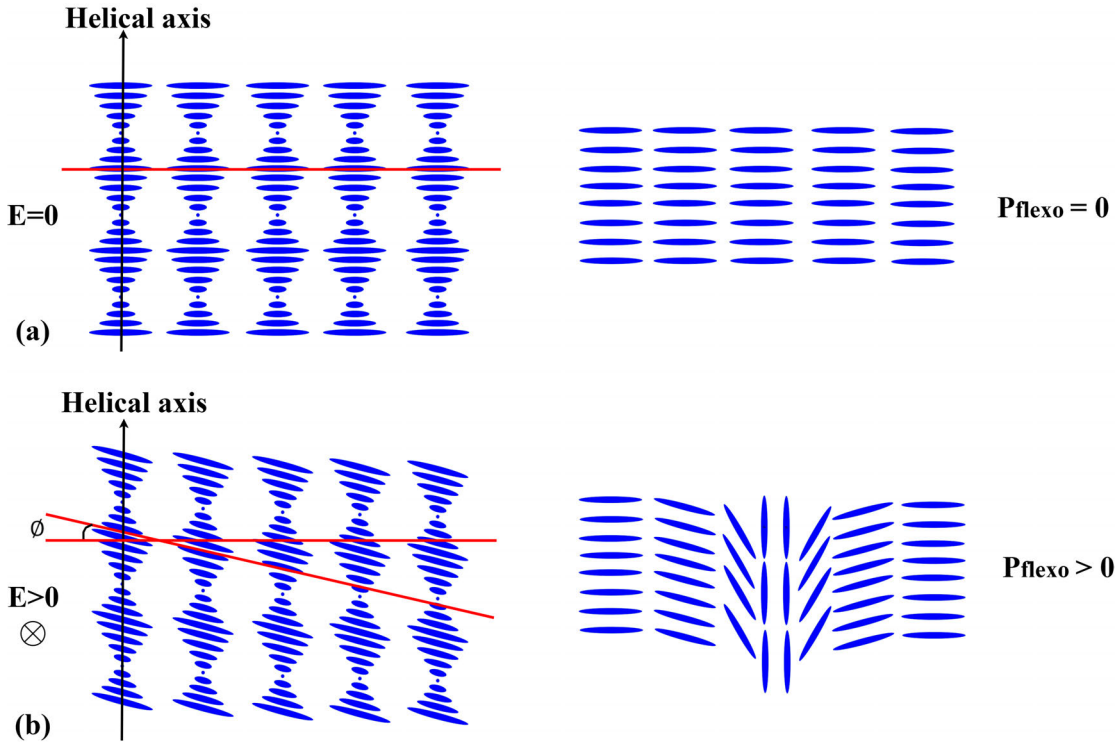


Figure 2.11: The flexoelectro-optic effect in chiral nematic LCs. (a) Left: The helical structure without the applied electric field. Right: The Bouligand cut-through plane without showing splay or bend deformation. (b) Left: The tilted helical structure with applied electric field. Right: The Bouligand cut-through plane shows splay-bend distortion. The cut (red lines) is always along the director planes.

2.9 Uniform Lying Helix Structure

In the case of LCs with positive dielectric anisotropy, the formation of the ULH requires a specific set of conditions. As mentioned previously, the natural state of such an LC at room temperature is known as the Grandjean state, in which the axis of the helix is orientated perpendicular to the device surfaces. It is difficult to transfer the helical structure from the Grandjean state to the ULH state directly. Initially, the LC must be heated to the isotropic phase, which is characterised by orientation-independent properties, and then the device must be cooled while an electric field should be applied concurrently. In the helical configuration, the dielectric constant along the helical axis is $\varepsilon_{\perp}$. However, the

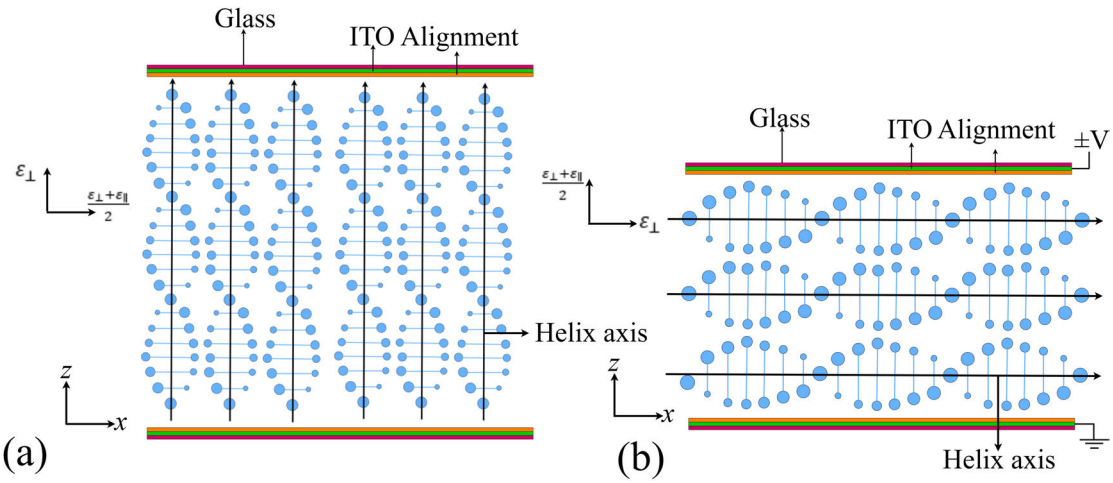


Figure 2.12: The geometry of a chiral nematic LC in the (a) Grandjean state (b) ULH alignment with applied electric field.

dielectric constant orthogonal to the helical axis exhibits variability depending on the spatial coordinates. Consequently, it can be represented as the average of $\varepsilon_\perp$ and $\varepsilon_\parallel$, calculated as $\frac{\varepsilon_\perp + \varepsilon_\parallel}{2}$. For most chiral materials, $\varepsilon_\parallel$ is much larger than $\varepsilon_\perp$, which consequently means that the dielectric constant orthogonal to the axis in a helical structure is typically quite substantial. The electric field tends to align the LC director along the direction with the larger dielectric constant. Consequently, this proclivity propels the helical structure lying down and aligns with the direction perpendicular to the helical axis, as shown in **Figure 2.12**.

A lying helix can give rise to periodic fingerprint stripes when viewed across the substrate plane. The uniform lying helix is the more regularly aligned configuration in which the helical axes are approximately parallel over an extended region. These stripes originate from the long-range helical order of the chiral nematic phase and should therefore be distinguished from the field-induced flexodomains described in Section 2.8.1. Whether a uniform ULH texture persists depends on the cell geometry, surface anchoring, and preparation conditions. It should not be assumed to be unconditionally stable, the structure may revert to a Grandjean state when

we remove the electric field, techniques including photo-polymerisation and direct laser writing can be employed to stabilise the structure [37].

2.10 Diffraction

Diffraction is the spreading of light into different directions when a wavefront encounters an aperture, obstacle, or spatially varying optical structure. According to Huygens' principle, when a plane wave meets a narrow aperture, it creates wavelets that follow unique paths, leading to relative phase changes. These differences cause constructive or destructive interference. Constructive interference occurs when the phase difference between interacting wavelets is an integer multiple of 2π. In contrast, destructive interference occurs and cancels out the wavelets when the phase difference is an odd multiple of π.

2.10.1 Raman-Nath and Bragg Diffraction

Diffraction typically manifests itself in one of two ways: Raman-Nath diffraction, characterised by multiple diffraction orders, and Bragg diffraction, which presents only a single order. Raman–Nath diffraction arises when the thickness (d) of the device meets the following condition:

$$d \ll \frac{\Lambda^2 n_0}{2\pi\lambda_0} \tag{2.36}$$

where Λ is the gap between each grating, n_0 is the refractive index of the medium, and λ_0 is the wavelength of free-space. In this case, the incident light will diffract in multiple orders.

Conversely, if the thickness of the device satisfies the following:

$$d \gg \frac{\Lambda^2 n_0}{2\pi\lambda_0} \tag{2.37}$$

when the Bragg condition is met (incident angle $\theta_i = \sin^{-1}\left(\frac{\lambda_0}{2n_0\Lambda}\right)$), the Bragg diffraction will occur. As a result, only a single diffraction order is observed [39].

2.10.2 Diffraction Grating

As light traverses a grating, it undergoes diffraction, as illustrated in **Figure 2.13**. This operation is based on the principles of diffraction and interference, and the grating itself consists of a periodic structure that can modulate the amplitude or phase of incident light. A diffraction grating is an optical component designed to diffract light into discrete diffraction orders [40]. The difference in path lengths between two waves results in constructive interference if the following condition is satisfied:

$$m\lambda = \Lambda \sin\theta_d \tag{2.38}$$

where Λ is the spacing between the slits, m is the order of diffraction, and θ_d is the diffraction angle measured from the normal grating to the m-th diffracted beam.

The diffraction angle is related to the wavelength of light and the spacing of the grating. In the case of an LC diffraction grating, we can also manipulate the diffraction angle by modulating the grating's spacing.

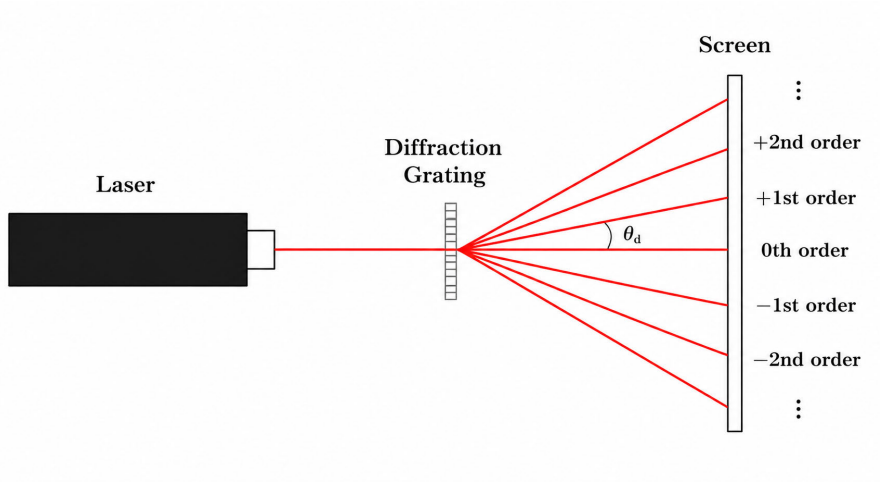


Figure 2.13: Schematic representation of light passing through a Raman-Nath diffraction grating.

2.10.3 LC Diffraction Gratings

Due to their unique properties, LCs can be employed to create effective diffraction gratings. By modulating the applied electric field, LC gratings offer real-time control over the diffraction pattern [41]. In addition, LC materials can be incorporated into thin films, enabling the development of controllable and lightweight diffraction gratings. The development of future electro-optical devices is heavily dependent on LC-based tunable diffraction gratings [42–46]. As indispensable components in optical routing, data storage, and three-dimensional display, they promise to advance these technologies [47].

The majority of tunable gratings based on nematic LCs [48–53] are sensitive to the polarisation of incident light because the reorientation of the director in response to the electric field causes a change in the effective refractive index of incident light for one polarisation. Meanwhile, patterning of electrodes is required, which involves structuring the electrodes in a particular manner (e.g., periodic stripes) to generate a spatial distribution of the electric field across the LC device. Recently, potential applications of the flexoelectric effect in designing tunable diffraction

gratings have attracted significant interest [54]. The use of the flexoelectric effect in bent-core nematic LCs presents a promising approach for fabricating adjustable diffraction gratings. As mentioned in a previous section, the flexoelectric effect causes net electric polarisation in splay and bend deformations in response to the applied electric field. LC naturally forms a periodic 1-dimensional structure due to the flexoelectric effect when an electric field is applied to the device, and can subsequently diffract incident light to achieve beam steering [41].

2.10.4 Modelling of LC Diffraction Grating

To investigate LC diffraction gratings, a model can be used to simulate the behaviour of LC molecules under varying electric field magnitudes [38, 55, 56]. First, a coordinate system for the LC device is established, often with the z-axis normal to the cell surface. The director field is then represented as matrices. The total free energy, including the elastic, dielectric, and flexoelectric contributions, is considered. By incorporating the director field and the applied electric field into the formulation and applying the Euler–Lagrange equation, the free energy can be minimised, yielding functions that correspond to minimal energy solutions (this will be discussed in Chapter 4). Once the partial differential equation solutions are obtained, we can determine the light properties in the near field using Jones calculus. To obtain the intensity distribution of diffraction spots on a distant screen (far field), we must then utilise the Fourier transform.

Alternative approaches, such as the Vector Beam Propagation Method (VBPM), are based on numerical analysis and are well suited for analysing light propagation through LC systems. VBPM can capture wavefront variations induced by the LC layer and simulate light diffraction as it travels through the material [57]. The Finite Difference Time Domain (FDTD) method is another numerical technique that simulates the interaction between electromagnetic fields and physical structures,

enabling the modelling of complex propagation behaviours. These numerical methods offer the advantage of accommodating devices operating beyond the Raman-Nath regime.

2.11 Holographic Displays

Holographic display technology relies on the precise manipulation of light wavefronts to reconstruct three-dimensional images. LC devices can play a key role in this process by providing dynamic control over the wavefront. With electrically tunable phase modulation, an LC device can steer not only the incident light itself but also the holographic image generated by the spatial light modulator. This capability enables flexible beam steering, improved viewing zones, and improved scalability in holographic display systems.

2.11.1 LC Spatial Light Modulators (LC-SLMs)

LC-SLMs are fundamental components in modern optical systems that require dynamic control of light. Using the electrically tunable refractive index of LC materials, LC-SLMs can modulate the phase, amplitude, or polarisation of incident light with high spatial resolution. This capability makes them indispensable in applications such as digital holographic displays [6, 58–60]. A typical LC-SLM comprises a pixelated electrode array, frequently realised through LC-on-silicon (LCoS) architecture, where individual pixels control molecular alignment through the response of LC molecules to an external electric field. This reorientation mechanism produces a precise optical path difference in the outgoing or reflected wavefront, allowing the device to manipulate beam profiles with exceptional spatial precision [58]. Based on their phase control capabilities, spatial light modulator

technologies LC fall into two primary classes: those offering digital, binary, or quantised phase control (typically between 0 and π) and those providing continuous, analogue phase control (commonly spanning 0 to 2π). Binary modulators can achieve response times well below 1 millisecond. In contrast, analogue modulation technology exhibits considerably longer transition periods, typically ranging from several milliseconds to more than 1 millisecond even in premium, high-cost systems [61]. In Chapter 7, LC-SLMs are employed to generate holographic patterns in the far field.

2.11.2 LC Beam Steering for Holographic Displays

A major drawback of SLM-based holographic displays is their limited viewing angle, which is inherently determined by pixel pitch [62]. Another limitation is the relatively small holographic display area, constrained by the active aperture of the SLM. For instance, a 10-megapixel Holoeye SLM with a 1.6 cm $\times$ 0.94 cm panel yields only a 8.2° full viewing angle [63], and larger devices, while beneficial, are often prohibitively expensive. Consequently, expanding the effective display area and redirecting the holographic image to different spatial positions remain key challenges in the development of practical holographic display systems [64].

To address this issue, we can potentially utilise a tunable LC device to steer the light, enabling dynamic redirection of the reconstructed holographic wavefront without relying on mechanical components. By generating controllable phase gradients using different levels of electric field, the LC device can deflect the beam to different angular positions, effectively enlarging the viewing zone and allowing the holographic image to be observed from multiple directions. When placed downstream of the SLM, this additional LC element operates independently of the hologram generation process, providing an extra degree of freedom for manipulating

the far-field distribution. The detailed demonstration of this technology will be presented in Chapter 7.

2.12 Summary

In this chapter, the fundamental properties of LC materials relevant to this research have been introduced. The discussion begins with an overview of the nematic and chiral nematic LC phases, describing their molecular structures, alignment configurations, and electro-optic behaviour. The optical and electrical properties of these materials, including refractive index anisotropy and dielectric response, are then discussed to establish the basis for their light-modulating capabilities. The elastic theory governing molecular deformations such as splay, twist, and bend is presented, followed by an explanation of the flexoelectric and flexoelectro-optic effects, which enable electric-field-induced polarisation and form the foundation for flexoelectric diffraction gratings. The uniform lying helix structure of chiral nematic LCs is introduced for its potential in dynamic beam steering applications. The chapter also reviews the principles of optical diffraction, including Raman–Nath and Bragg regimes. Meanwhile, electrohydrodynamic instabilities are discussed as factors that influence device performance and stability. Finally, LC spatial light modulators are presented as the primary devices for generating computer-controlled holographic wavefronts, with emphasis on how the pixel pitch and phase modulation range constrain the viewing angle and display size. To overcome these inherent limitations, LC-based steering devices are discussed as a potential way to steer the holographic display to different locations. In general, this chapter provides the theoretical foundation for the modelling and experimental investigations presented in the following chapters.

3

Experimental Techniques

3.1 LC Mixture Development

The LC mixtures used in the following chapters were prepared in a wet laboratory dedicated to material preparation and device fabrication. As an example, we refer to the chiral mixture used in Chapters 6 and 8, consisting of 5 wt.% R811 and 95 wt.% E7.

As illustrated in **Figure 3.1**, the preparation process begins by placing an empty vial on a precision balance, allowing the reading to stabilise, and then resetting the balance to zero. To fill an LC cell, whether it is a custom-made cell or a commercial one, approximately 10–20 μL of LC mixture is typically required. For this reason, the LC mixtures were usually prepared in batches of approximately 100 mg to provide enough material for multiple fillings. The components were added in order of increasing weight percentage and in most cases, any powder chemical was

added to the vial first. As shown in Figure 3.1, 5 mg of R811 was carefully weighed and transferred to the vial. After the reading stabilised, the balance was reset to zero. The same procedure was followed for the addition of 95 mg of E7, and the total mass was verified. Once all components were included, the vial was sealed and placed in an oven set to 80 °C. The heating temperature was chosen according to the clearing temperatures of the individual LC materials. The mixture was heated for at least four hours to ensure complete mixing in the isotropic phase. The same general procedure was applied for the preparation of other LC mixtures.

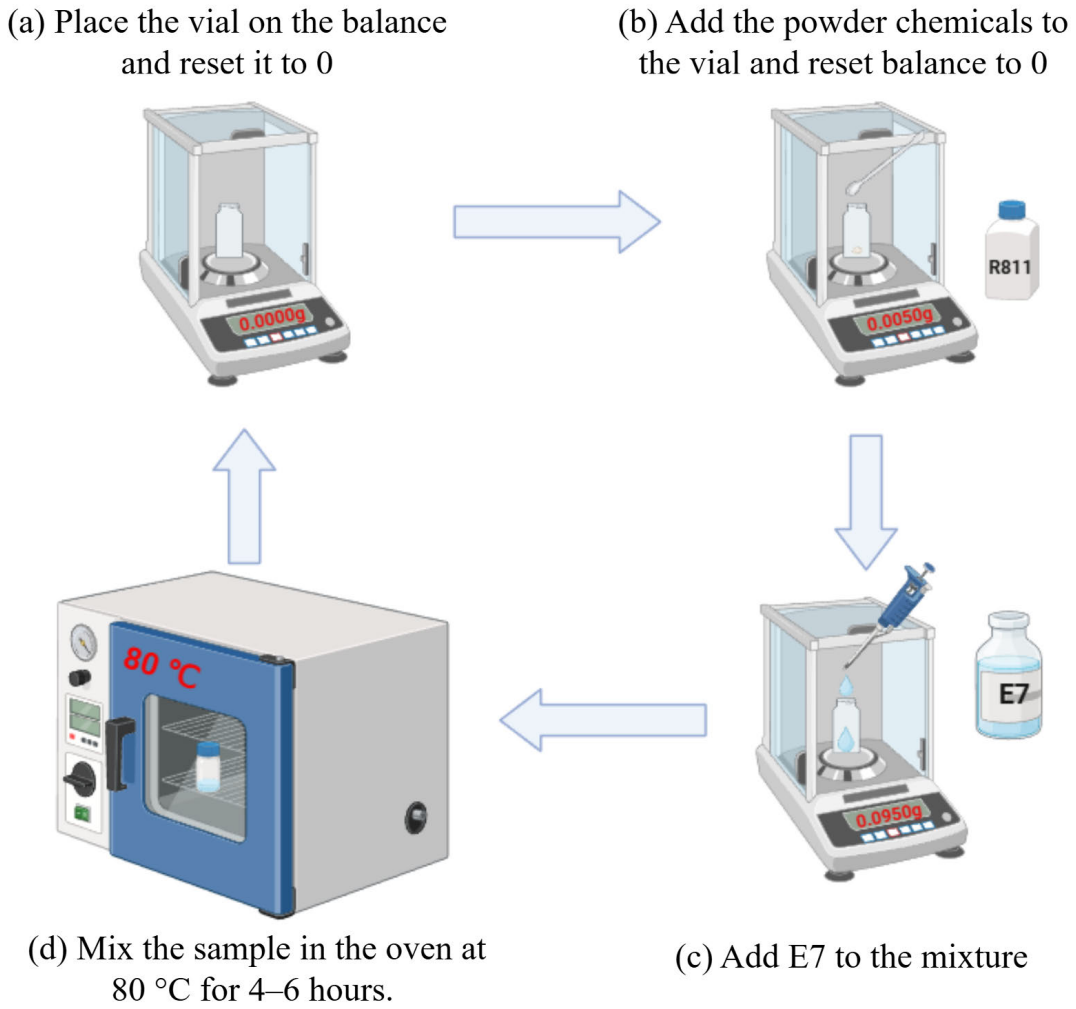


Figure 3.1: The typical preparation procedures of chiral dopant LC mixtures.

3.2 LC Cell Preparation

In this thesis, the fabrication of LC devices was primarily performed in a cleanroom environment. Under certain conditions, commercially available cells could be used directly. For example, LC cells supplied by Instec or Synthon were used in several experiments, where LC materials were filled into the cells via the capillary filling method. This approach was used for the flexoelectric grating and chiral-dopant LC grating experiments discussed in Chapters 4 to 6. In other cases, prefabricated LC cells that did not require additional filling were purchased and used directly. An example is the polarisation grating cell utilised in Chapter 7 for the holographic display experiments. These ready-to-use cells offered convenience and high uniformity when the standard specifications met the experimental requirements.

The gap of the empty LC cell was measured before filling using interference fringes in its UV–Vis spectrum. The absorbance data were exported as a CSV file and analysed in MATLAB. The data were converted to a transmission spectrum from which the interference peaks were identified. A range of consecutive peaks was selected and the cell gap was calculated from a linear fit to their inverse wavelengths.

However, certain specialised experiments required the manual fabrication of custom LC cells to meet unique experimental requirements. In such cases, ITO-coated glass substrates, or coverslips, were used, with spacers applied to control the cell gap and define the device thickness. This approach was essential when specific parameters, such as nonstandard cell thicknesses, custom alignment conditions, or particular optical path constraints, could not be achieved using commercial cells. For example, when the working distance of the objective lens in the experimental setup was limited, self-fabricated cells with a thinner substrate were designed to ensure compatibility with the optical system. The LC devices described in Chapter

8 exemplify such custom-fabricated cells, specifically engineered to accommodate these experimental constraints.

The self-made cell fabrication procedure is illustrated in **Figure 3.2**. It typically begins with a pair of glass substrates (or coverslips) featuring patterned transparent electrodes, commonly comprising an indium tin oxide (ITO) layer. Initially, an acetone-soaked wipe is used to remove any residual dust particles. Following this cleaning procedure, the substrates are positioned on a spin-coater platform [**44**].

Next, an alignment layer is deposited onto each substrate to control the orientation of the LC director. Polyvinyl alcohol (PVA) can be rubbed. For planar alignment, a 1 wt.% PVA solution prepared in distilled water is typically deposited onto the glass substrate. After deposition, the substrates are spun at 1000 rpm for 30 seconds and then baked at 90 °C for 2 minutes to remove residual moisture.

Subsequently, the substrates were mounted on the translation stage of a rubbing apparatus. This stage is connected to a vacuum pump that secures the substrates during rubbing. The rubbing mechanism consists of a drum wrapped with a clean velvet cloth that processes the PVA-coated surface. The drum can rotate clockwise or counter-clockwise at adjustable speeds, depending on experimental requirements. During rubbing, the stage advances in a single direction, typically with the drum rotating counter-clockwise at 2000 rpm. To achieve strong alignment and high uniformity in the PVA layer, the surface is usually rubbed 2–3 times.

After rubbing, thin-film spacers are placed between the ITO-coated substrates to define the cell gap. Spacer thicknesses of 1 µm, 5 µm, 6 µm, 8 µm, 12 µm, 16 µm, 20 µm, 23 µm, and 25 µm are selected as required. The substrates are then pressed together and the adhesive is applied around the cell edges using a glue dispenser (Nordson Performus V, 0–100 psi) equipped with a syringe fitted with a 30 GA lavender Nordson Precision Tip. The adhesive is subsequently photopolymerised

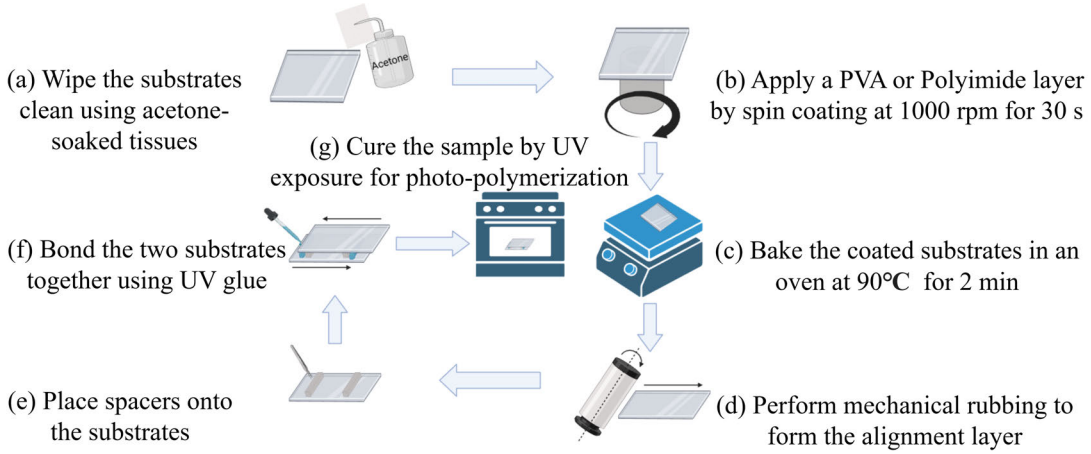


Figure 3.2: Illustration of the procedure used to fabricate the LC cell. The black arrow indicates the rubbing direction of the corresponding substrate.

under an ultraviolet crosslinker (Analytik Jena CL-1000L) at 100 µJ/cm^2 for 20 minutes. An illustration of the completed cell structure that includes the substrate, ITO, and alignment layers is shown in **Figure 3.3**(a). Indium shot is used to connect electrical leads to the ITO as shown in Figure 3.3(b).

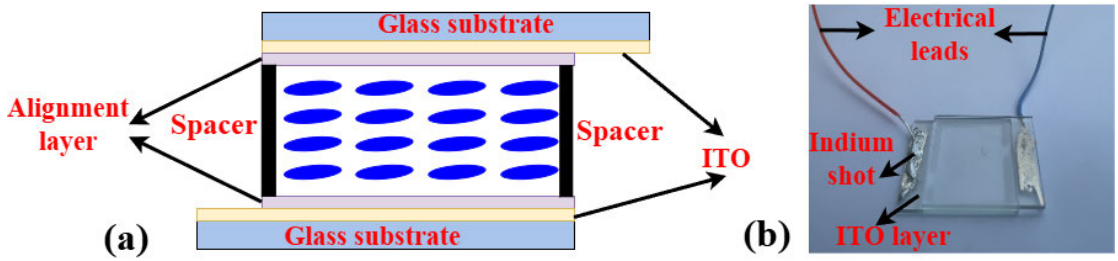


Figure 3.3: (a) Cross-sectional schematic of the LC cell, illustrating the substrates, ITO layers, and alignment layers. (b) Photograph of the fabricated Instec cell, illustrating the indium connection between the electrical leads and the ITO electrodes.

3.3 Polarised Optical Microscopy

Observing the texture and colour of an LC cell under polarised optical microscopy (POM) is essential to understand both the internal structure and the optical properties of the device. In this thesis, all microscope images were acquired using

the polarised optical microscope shown in **Figure 3.4**. The instrument is an Olympus BX51 equipped with an R6 QImaging camera.

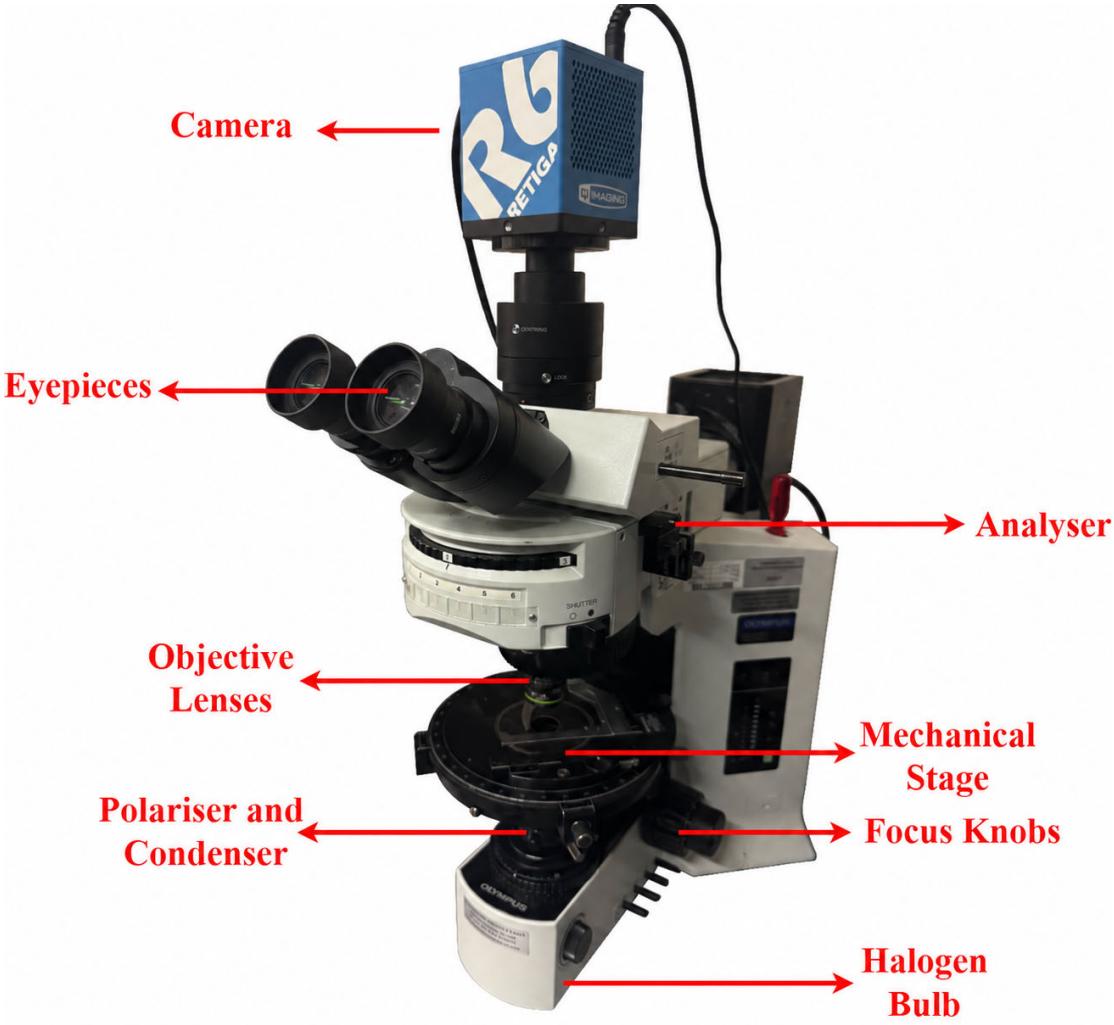


Figure 3.4: Photograph showing the Olympus BX51 microscope along with the QImaging camera used in this study.

Light emitted from the halogen bulb first passes through a polariser and is then focused onto the sample by the condenser. When required, an optical bandpass or long-pass filter can be placed after the condenser (this component is not shown in Figure 3.4), particularly when the LC material is sensitive to specific wavelengths. For example, a long-pass filter is used during observation of LC mixtures containing reactive mesogens and photoinitiators in order to prevent

unintended curing caused by ultraviolet light.

After passing through these optical elements, the incident light illuminates the LC device. Directly above the sample is the set of objective lenses, which provides a range of magnifications including 4×, 10×, 20×, 40×, and 50×. The next component is the second linear polariser, known as the analyser. The analyser is typically orientated perpendicular to the first polariser so that the optical response of anisotropic materials can be distinguished from that of isotropic materials.

The sample image can be captured by the R6 QImaging camera mounted on top of the microscope, which connects to a computer for image analysis.

The sample is placed on a mechanical stage that allows horizontal movement in two dimensions as well as vertical adjustment through coarse and fine focus knobs. Temperature control is available when required through the use of a hot stage, specifically the Linkam LTS420 system operated with a LinkPad controller. This setup is used for temperature-sensitive samples such as flexoelectric gratings. When investigating the influence of an electric field on the behaviour of the LC director, a dual-channel waveform generator (Multicomp Pro MP750510) together with a dual-channel amplifier with a tenfold gain (FLC Electronics F10AD) is connected to the sample during polarised optical microscopy.

3.4 Flexoelectro-optic Tilt Angle Measurement

The in-plane flexoelectric tilt angle plays a crucial role in the study of switchable and rotatable chiral nematic LCs discussed in Chapter 6 (see Section 6.4.2 for details). The asymmetry of the tilt angle is a key mechanism that enables the rotational behaviour of chiral nematic LCs. Therefore, it is essential to understand how to accurately measure the in-plane tilt angle induced by the flexoelectro-optic

effect under an applied electric field. The rotation method is used to measure the tilt angle, which is caused by the flexoelectric effect under the external electric field. The chiral nematic LC device is positioned on the mechanical stage of a polarised optical microscope. An external electric field is applied via a function generator, while a photodiode is used to detect the transmitted signal. Within the framework of the rotation method, the transmission through the chiral nematic LCs is presented as a function of the rotation angle with respect to the polariser axis (χ)

$$T = T_{\max} \sin^2\left(\frac{\pi \Delta n_{\text{eff}} d}{\lambda}\right) \sin^2(2\chi) \tag{3.1}$$

This equation implies that transmission will attain its maximum ($T_{\max}$) when the rotation angle χ equals $\frac{\pi}{4}$ (45°), and its minimum ($T_{\min}$) when the rotation angle equals zero. Once the LC device is positioned on the microscope stage, as

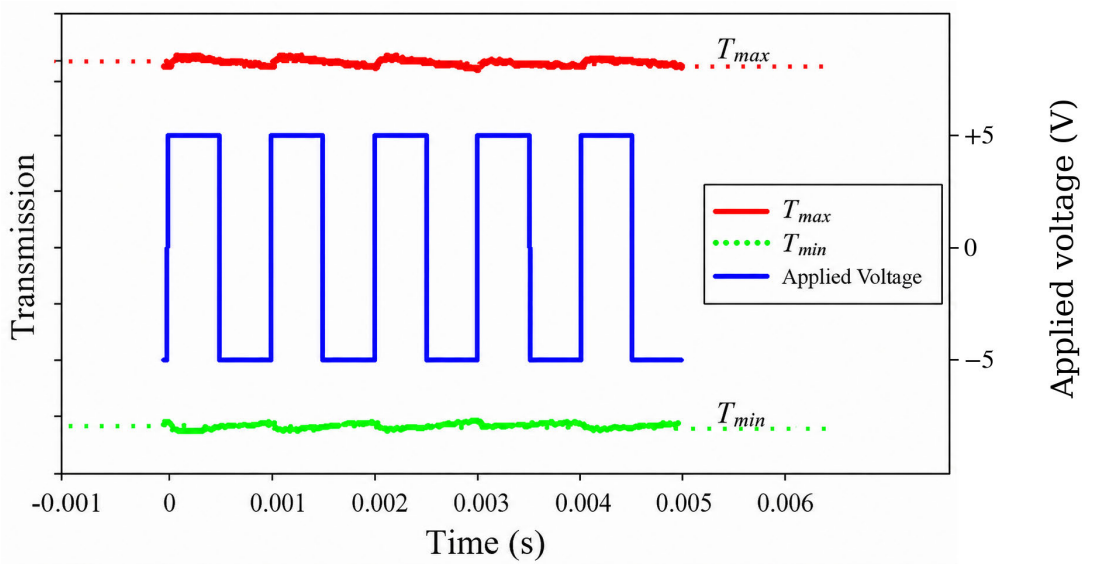


Figure 3.5: The input signal and the signal when the transmission achieves maximum and minimum. The blue curve shows the applied AC voltage (1 kHz, 5 V_{rms}), with its scale indicated on the right-hand axis.

shown in **Figure 3.5**, rotation begins to identify maximum ($T_{\max}$) and minimum ($T_{\min}$) light levels. The mean position of the transmission curve ($\langle T \rangle$, $\chi = 22.5°$)

can be deduced using the oscilloscope's cursor with the equation:

$$\langle T \rangle = T_{\max} - \frac{(T_{\max} - T_{\min})}{2} \tag{3.2}$$

As shown in **Figure 3.6**, to obtain the tilt angle ($\varnothing$), we first rotate the stage through an angle of χ_1 in one direction until the intensity, due to the positive electric field, aligns with $\langle T \rangle$. Similarly, we rotate the device through an angle of χ_2 in the opposite direction until the intensity resulting from the negative electric field aligns with $\langle T \rangle$. The full switching angle ($2\varnothing$) is then given by:

$$2\varnothing = |\chi_1 - \chi_2| \tag{3.3}$$

The applied 1 kHz square wave reverses the polarity every 0.5 ms. As shown in Figure 3.6, the transmitted intensity changes after each reversal and reaches different levels for the two voltage polarities. This is consistent with a flexoelectro-optic rotation of the optical axis that follows the applied field within each half-cycle. In comparison, the dielectric torque depends on the square of the electric field and is unchanged when the voltage switches between equal positive and negative values. Dielectric coupling may affect the overall director configuration and mean transmission, but alone cannot explain the polarity-dependent signal. These traces show the optical response to repeated field reversals. They do not independently determine the flexoelectric and dielectric response times.

This method has a limitation in accuracy due to the manual rotation of the stage, which can introduce an error of approximately 1°.

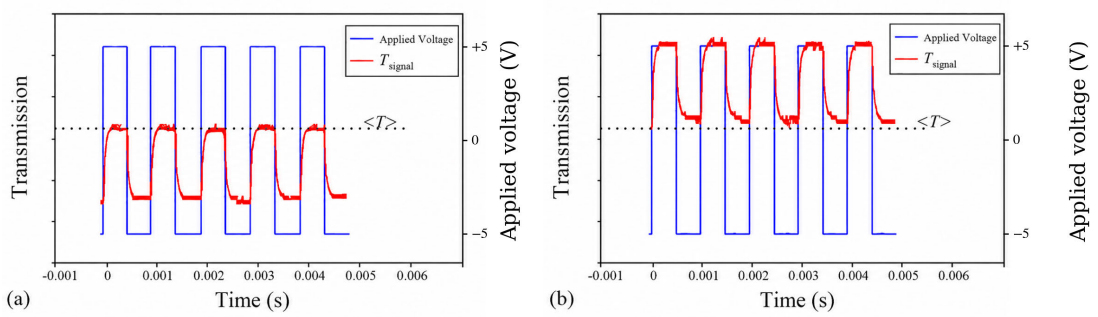


Figure 3.6: (a) The input and transmission waveform observed when $\chi = \chi_1$. (b) The input and transmission waveform observed when $\chi = \chi_2$. The blue curve shows the applied AC voltage (1 kHz, 5 V_{rms}), with its scale indicated on the right-hand axis, whereas the red curve shows the corresponding signal detected by the photodiode.

3.5 Capacitance Measurements

Capacitance measurement of LCs is essential because it allows researchers to extract key material properties such as the elastic constants and dielectric anisotropy. These electrical responses are directly linked to the molecular orientation and structure of the LC, making capacitance an effective way to evaluate how the material behaves under different applied electric fields.

We selected the key material MLC-6882 (Merck), which has a negative dielectric anisotropy, for the flexoelectric grating studies presented in Chapters 4 and 5. LC materials with low dielectric anisotropy are known to enhance the formation of flexoelectric domains, making MLC-6882 a useful material in mixture development. This material exhibits a nematic phase at room temperature and can be used to adjust the overall dielectric anisotropy of the mixtures to approximately zero. However, the exact dielectric anisotropy value of MLC-6882 is not available in the literature, so we must measure it ourselves.

To understand its potential benefits in this field better, we measured its key material parameters, namely the elastic constants K_{11} (splay), K_{33} (bend), as well as the dielectric permittivities $\varepsilon_\perp$ (perpendicular), $\varepsilon_\parallel$ (parallel). These

measurements were performed using a homeotropic cell in which the LC directors are aligned perpendicular to the substrates. The capacitance–voltage measurement was performed using an inductance–capacitance–resistance (LCR) meter. A sinusoidal AC voltage at 1 kHz was applied across the ITO electrodes and its amplitude was varied incrementally. At each voltage, the LCR meter determined the capacitance from the measured magnitude and phase of the complex impedance. As a first step, we measured the capacitance of the empty cell (i.e., without LC), denoted C_{empty}. The capacitance in such a cell is determined by the formula:

$$C_{\text{empty}} = \frac{\varepsilon_0 A}{d} \tag{3.4}$$

where ε_0 is the permittivity of free space, A is the electrode area, and d is the cell gap. The measured empty-cell capacitance was 176 pF.

Subsequently, the homeotropic cell was filled with MLC-6882 and an electric field was applied perpendicularly to the surface. The applied AC ranged from 0 to 20 V_{rms} in increments of 0.1 V_{rms}, with the resulting capacitance measured at each step. Based on the measured data, the resulting C–V curve is shown in **Figure 3.7**(a).

When the applied voltage is below the threshold voltage ($0 < V_{\text{rms}} < V_{\text{th}}$), where V_{rms} denotes the AC voltage applied across the LC cell, the elastic restoration force dominates over the dielectric torque. In this regime, the director remains essentially perpendicular to the substrates, with only a small pre-tilt angle. The capacitance in this state, denoted C_{low}, is given by:

$$C_{\text{low}} = \frac{\varepsilon_0 \varepsilon_{\parallel} A}{d} \tag{3.5}$$

As the applied voltage exceeds the threshold voltage ($V_{\text{rms}} > V_{\text{th}}$), the director starts to transition towards a parallel alignment to the surface to minimise the

system's free energy. With the applied voltage significantly surpassing the threshold voltage ($V_{\text{rms}} \gg V_{\text{th}}$), the dielectric coupling is dominating, and the director assumes a completely parallel orientation to the substrate. In this saturated state, the capacitance reaches C_{high}, which is expressed as:

$$C_{\text{high}} = \frac{\varepsilon_0 \, \varepsilon_\perp \, A}{d} \tag{3.6}$$

From the capacitance of the empty-cell C_{empty}, the permittivity can be extracted using:

$$\varepsilon_\parallel = \frac{C_{\text{low}}}{C_{\text{empty}}}, \qquad \varepsilon_\perp = \frac{C_{\text{high}}}{C_{\text{empty}}} \tag{3.7}$$

Consequently, the dielectric anisotropy is calculated as $\Delta\varepsilon = \varepsilon_\parallel - \varepsilon_\perp$. K_{33} can be calculated using the Fréedericksz threshold equation, given by:

$$K_{33} = \left(\frac{V_{\text{th}}}{\pi}\right)^2 |\Delta\varepsilon| \varepsilon_0 \tag{3.8}$$

Analysis of the C–V curve yielded C_{high} as 1112 pF, C_{low} is 615.43 pF, so $\Delta\varepsilon = -2.82$, and $K_{33} = 9.12$ pN.

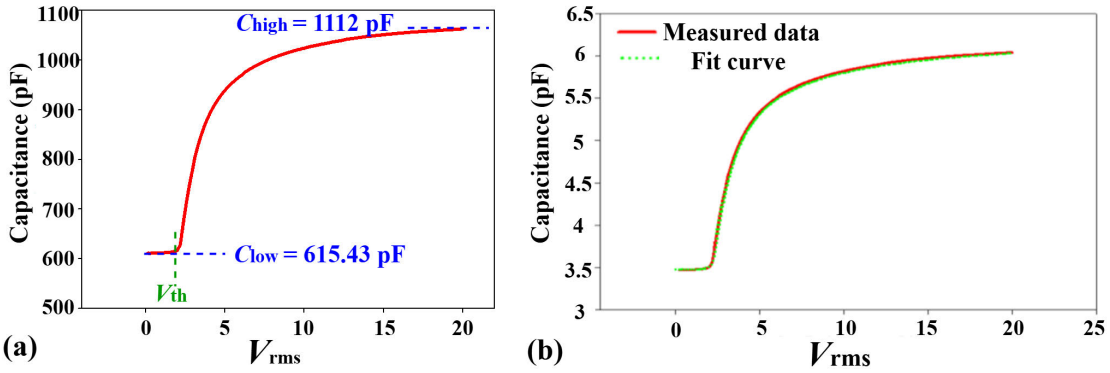


Figure 3.7: (a): The measured C-V curve of the homeotropic LC device filled with MLC-6882. (b): Measurement and the fit curve of the Fréedericksz transition.

The determination of K_{11} was obtained using the finite difference relaxation method in MATLAB, designed specifically to predict the dielectric switching curve. The inputs required for the code were the known values of K_{11}, K_{33}, and $\Delta\varepsilon$. K_{11} was the value subject to adjustment while K_{33} and $\Delta\varepsilon$ remained fixed. The green curve in Figure 3.7(b) is for $K_{11} = 13$ pN, $K_{33} = 9.12$ pN, $\Delta\varepsilon = -2.82$, pre-tilt angle = 2.3°. This simulated curve closely matches the measured C–V response, following the conversion of capacitance to permittivity by normalising with the empty-cell value.

3.6 Summary

This chapter presents the experimental methodologies that underpin the research described in the subsequent chapters. First, the mixture development and device fabrication process are outlined, detailing how LC devices are formed through precise control of the weight percentage of each LC constituent and through an appropriate fabrication procedure to produce diffraction gratings. Understanding the role of each component in the mixture is essential, as even minor variations in composition can significantly influence the optical and structural properties of the resulting device. The primary structural characterisation technique, POM, is then introduced as the principal tool for investigating LC structures. POM enables direct visual examination of the LC alignment and grating morphology, providing critical insights into the quality and uniformity of the fabricated devices. In addition, a methodology for measuring the flexoelectro-optic tilt angle under applied electric fields is presented. This parameter is of particular importance as it governs the helix rotation in chiral nematic LCs, a phenomenon that is discussed in greater detail in Chapter 6. Finally, capacitance measurement is introduced as a valuable technique

for characterising the dielectric properties and elastic constants of the LC materials.

4

Theoretical Modelling and Simulation of Flexoelectric Diffraction Gratings

4.1 Introduction

Recent studies have demonstrated the possibility of forming tunable diffraction gratings using the flexoelectric effect in bent-core LCs [54, 65, 66], as described in Section 2.8. However, these studies have not examined in detail the role of dielectric coupling, as discussed in Section 2.7.1, and how it suppresses the desired periodic structure, thus degrading the performance of the diffraction grating.

As described in Section 2.8 and illustrated in Figure 2.10, an applied field can favour spatially periodic splay–bend deformation when the flexoelectric coupling overcomes the elastic cost of distorting the director. This pattern forms flexodomains: stripes in which the director orientation, and therefore the optical

response, varies periodically across the cell. Under suitable conditions, the resulting refractive-index modulation acts as a diffraction grating. Whether the pattern forms and persists also depends on dielectric coupling and the material and driving conditions, which are examined in this chapter.

The modelling of flexoelectric nematic LC diffraction gratings plays a crucial role in predicting, analysing, and visualising the behaviour of the LC director. As introduced in Section 2.10.4, LC diffraction grating modelling involves determining the equilibrium director configuration by minimising free-energy and calculating the resulting optical response. Building on this theoretical framework, Bobylev and Pikin proposed a theoretical model that employs the small angle approximation to linearise the LC director distortion and used an Euler-Lagrange approach to minimise the total free energy equation [67]. This model accurately clarified the threshold conditions required to trigger the flexoelectric effect. However, their analysis did not extend to the role of dielectric anisotropy ($\Delta\varepsilon$) on the overall profile of the director. Additionally, the equations presented are only applicable under certain threshold conditions and do not necessarily hold in more general situations. Separately, Shin proposed a conical model that assumes that the alignment of the LC director is arranged within a cone [41]. Through the computation of the average free energy density, aimed at the optimal minimisation of the total free energy, this methodology can be used to precisely calculate the periodicity of the flexoelectric undulations. Nevertheless, the conical model that was proposed does not sufficiently consider the impact of dielectric coupling and is thus unable to provide an accurate simulation of the LC director profile when both flexoelectric and dielectric coupling needs to be accounted for.

This chapter presents a nonlinear model for flexoelectric nematic LC diffraction gratings and compares the results from simulations with those obtained from

experiments, providing a more accurate description of the behaviour of the flexoelectric nematic LC grating than that offered by the linear models that have been considered previously. The constructed nonlinear model considers both dielectric and flexoelectric coupling and, with the aid of numerical simulations, enables the visualisation of the behaviour of the LC director in response to flexoelectric, dielectric, and elastic effects. From the numerical simulations, both in-plane and out-of-plane tilt angles are obtained, which are then used to simulate the optical wave propagation and diffraction characteristics for light passing through the LC flexoelectric grating. The simulation results presented in this chapter have been published in Optics & Laser Technology, 180, 111502 (2025) [18].

4.2 Linear Model

LC molecules with certain shape asymmetry can result in the formation of splay-bend deformations in the LC director when subjected to an applied electric field. A three-dimensional coordinate system is employed to model the splay-bend distortion (as shown in **Figure 4.1**), whereby the z-axis is defined as the direction perpendicular to the plane of the glass substrates, effectively representing the thickness of the LC layer (d). The y-axis aligns with the initial alignment orientation, as shown in Figure 4.1(a), whereas the x-axis is the direction of the periodic flexoelectric splay-bend distortion. Two analytic models are used here. Firstly, an unconstrained approach is adopted to allow for the independent variation of the out-of-plane and in-plane tilt of the director, as demonstrated in Figure 4.1(b). In addition, a constrained approach is employed that forces the alignment of the LC director to be within a conical structure, as shown in Figure 4.1(c). Here, we define the pitch (p) as the spatial period of the flexoelectric director modulation

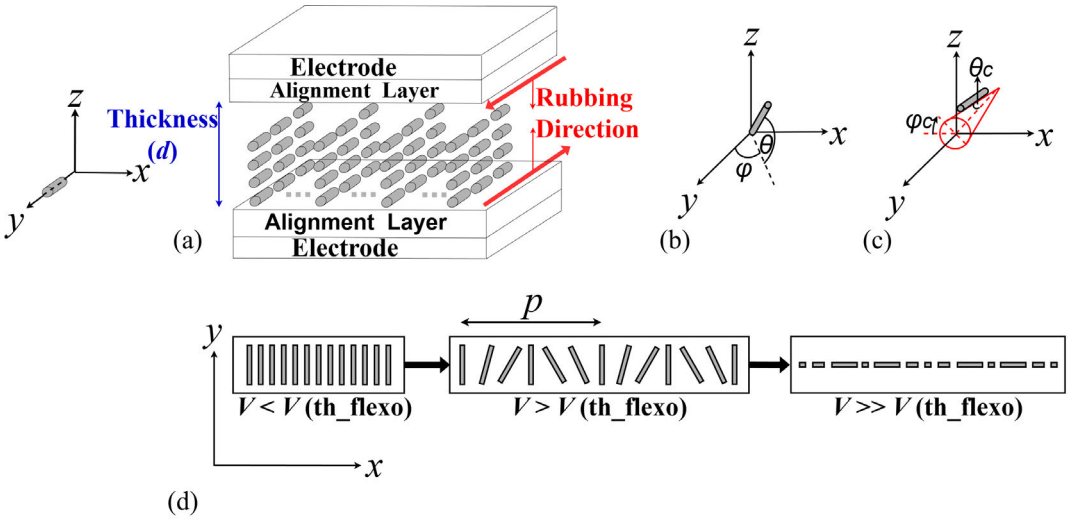


Figure 4.1: (a) Initial alignment in an anti-parallel rubbed homogeneous LC cell without an applied voltage. (b) Unconstrained perturbation of the LC director in the coordinate system (c) Constrained perturbation of the LC director in a conical configuration, with one end anchored at the base circumference and the opposite end directed towards the vertex. (d) Approximate top-view representation of the evolution of the LC director in the presence of flexoelectric coupling for different applied voltages, $V_{(\text{th_flexo})}$ represents the threshold voltage to trigger the flexoelectric effect. Reproduced from Ref. [18] with permission from Elsevier.

along the x-axis. It is the distance over which the splay–bend pattern repeats.

4.2.1 Unconstrained Model

Bobylev and Pikin employed a model analogous to the unconstrained version, as referenced in [67]. The situation of small undulations was considered, where the magnitudes of $|\theta|$ and $|\varphi|$ are much lower than 1. This condition significantly simplifies the computational process. For completeness, we now summarise the key findings from Ref. [67] and identify the conditions when the Fréedericksz threshold voltage and the threshold voltage for flexoelectric instability are the same. This enables us to distinguish when either dielectric coupling or flexoelectric coupling dominates.

In the small undulation scenario, where $|\theta|, |\varphi| \ll 1$, the LC director for

unconstrained perturbations can be defined as follows:

$$\vec{n} = \begin{pmatrix} \cos\theta \sin\varphi \\ \cos\theta \cos\varphi \\ \sin\theta \end{pmatrix} \approx \begin{pmatrix} \varphi \\ 1 \\ \theta \end{pmatrix} \tag{4.1}$$

The interaction between the dielectric energy, flexoelectric energy, and elastic energies described in Chapter 2 determines the orientation of the LC director. Assuming the Frank elastic constants are approximately equal, and $\vec{E} = \begin{pmatrix} 0 \\ 0 \\ E \end{pmatrix}$ is the electric field applied along the z-axis, the total free energy can then be recast as

$$f = f_{\text{elastic}} + f_{\text{flexoelectric}} + f_{\text{dielectric}} \tag{4.2}$$

$$\begin{aligned} f = {} & \tfrac{1}{2}K\Big\{[\nabla\cdot\vec{n}]^2 + [\nabla\times\vec{n}]^2\Big\} \\ & - \Big(e_1\,\vec{n}\,(\nabla\cdot\vec{n}) + e_3\,(\nabla\times\vec{n})\times\vec{n}\Big)\cdot\vec{E} - \tfrac{1}{2}\varepsilon_0\Delta\varepsilon\,(\vec{n}\cdot\vec{E})^2 \end{aligned} \tag{4.3}$$

$$\begin{aligned} f = {} & \tfrac{1}{2}K\left[\left(\frac{\partial\varphi}{\partial x} + \frac{\partial\theta}{\partial z}\right)^2 + \left(\frac{\partial\varphi}{\partial z} - \frac{\partial\theta}{\partial x}\right)^2\right] \\ & - e_1\,E\left(\frac{\partial\varphi}{\partial x} + \frac{\partial\theta}{\partial z}\right)\theta - e_3\,E\left(\frac{\partial\theta}{\partial x} - \frac{\partial\varphi}{\partial z}\right)\varphi - \tfrac{1}{2}\varepsilon_0\Delta\varepsilon\,E^2\theta^2 \end{aligned} \tag{4.4}$$

Minimising the free energy with respect to θ and φ necessitates the application of the Euler-Lagrange equations. We can get the equations that represent the stationary orientation structure of the LC, respectively:

For φ:

$$\frac{\partial}{\partial x}\left(\frac{\partial f}{\partial(\partial\varphi/\partial x)}\right) + \frac{\partial}{\partial z}\left(\frac{\partial f}{\partial(\partial\varphi/\partial z)}\right) - \frac{\partial f}{\partial\varphi} = 0 \tag{4.5}$$

$$f_1(\varphi,\theta) = \frac{\partial^2\varphi}{\partial x^2} + \frac{\partial^2\varphi}{\partial z^2} - \frac{(e_1 - e_3)E}{K}\frac{\partial\theta}{\partial x} = 0 \tag{4.6}$$

For θ:

$$\frac{\partial}{\partial x}\left(\frac{\partial f}{\partial(\partial\theta/\partial x)}\right) + \frac{\partial}{\partial z}\left(\frac{\partial f}{\partial(\partial\theta/\partial z)}\right) - \frac{\partial f}{\partial\theta} = 0 \tag{4.7}$$

$$g_1(\theta,\varphi) = \frac{\partial^2\theta}{\partial x^2} + \frac{\partial^2\theta}{\partial z^2} + \frac{(e_1 - e_3)E}{K}\frac{\partial\varphi}{\partial x} + \frac{\varepsilon_0\Delta\varepsilon E^2}{K}\,\theta = 0 \tag{4.8}$$

Taking into account the boundary conditions, $\theta = \varphi = 0$ at $z = 0$ and $z = d$ and using the Euler–Lagrange equations, we define the wavenumber $q = \frac{2\pi}{p}$, where p is the spatial period along the x-axis. Thus, solutions for these equations can be expressed as:

$$\theta = \theta_0\cos(qx)\sin\left(\frac{\pi z}{d}\right), \qquad \varphi = \varphi_0\sin(qx)\sin\left(\frac{\pi z}{d}\right) \tag{4.9}$$

Substituting these solutions into Eq. 4.6 and Eq. 4.8, and ensuring non-triviality of the quantities θ_0 and φ_0, we deduced the following equations:

$$-\varphi_0 q^2\sin(qx)\sin\left(\frac{\pi z}{d}\right) - \varphi_0\left(\frac{\pi}{d}\right)^2\sin(qx)\sin\left(\frac{\pi z}{d}\right) + \frac{(e_1 - e_3)E}{K}\,q\theta_0\sin(qx)\sin\left(\frac{\pi z}{d}\right) = 0 \tag{4.10}$$

$$-\theta_0 q^2\cos(qx)\sin\left(\frac{\pi z}{d}\right) - \theta_0\left(\frac{\pi}{d}\right)^2\cos(qx)\sin\left(\frac{\pi z}{d}\right) + \frac{(e_1 - e_3)E}{K}\,q\varphi_0\cos(qx)\sin\left(\frac{\pi z}{d}\right) + \frac{\varepsilon_0\Delta\varepsilon E^2}{K}\,\theta_0\cos(qx)\sin\left(\frac{\pi z}{d}\right) = 0 \tag{4.11}$$

We can then derive the expression of E as a function of the wavenumber (q):

$$E^2 = \left(\frac{K}{e_1 - e_3}\right)^2 \frac{\left[q^2 + \left(\frac{\pi}{d}\right)^2\right]^2}{q^2 + \mu\left[q^2 + \left(\frac{\pi}{d}\right)^2\right]} \tag{4.12}$$

where $\mu = \dfrac{\Delta\varepsilon\,\varepsilon_0 K}{(e_1 - e_3)^2}$. It should be noted, however, that Eq. 4.12 is only valid at the threshold voltage where the director starts to reorient to form the splay-bend structure. This is because the equation has been derived from the Euler–Lagrange equations using the small angle approximation and perturbation solution.

The threshold voltage for flexoelectric instability can be ascertained by examining the minimum electric field at $q = q_{\text{th}}$. By setting $\dfrac{d(E^2)}{dq} = 0$, we obtain

$$V_{(\text{th_flexo})} = \frac{2\pi K}{(e_1 - e_3)(1 + \mu)} \tag{4.13}$$

$$q_{\text{th}} = \frac{\pi}{d}\sqrt{\frac{1 - \mu}{1 + \mu}} \tag{4.14}$$

In our LC tunable grating device, we anticipate a predominant flexoelectric effect, which is expected to facilitate more precise control over the alignment of the LC director. Nevertheless, it is also essential to investigate the impact of dielectric anisotropy on the formation of the gratings. According to Eq. 4.14, the flexoelectric instability can only occur if $|\mu| < 1$, which suggests that for a periodic flexoelectric structure to form we require $|\Delta\varepsilon| < \frac{(e_1 - e_3)^2}{K\varepsilon_0}$.

The threshold voltage to cause the Fréedericksz transition is calculated as $V_{(\text{th_frkz})} = \pi\sqrt{\frac{K}{\Delta\varepsilon\,\varepsilon_0}}$, as discussed in Section 2.7.2. If $\mu = 1$, then $\Delta\varepsilon = \dfrac{(e_1 - e_3)^2}{K\varepsilon_0}$, and thus $V_{(\text{th_flexo})} = \dfrac{2\pi K}{(e_1 - e_3)(1 + \mu)} = \dfrac{2\pi K}{\sqrt{K\varepsilon_0\Delta\varepsilon}(1 + 1)} = \pi\sqrt{\dfrac{K}{\Delta\varepsilon\,\varepsilon_0}}$, which implies that $V_{(\text{th_flexo})} = V_{(\text{th_frkz})}$ when $\mu = 1$. **Table 4.1** considers the dominant form of coupling for various magnitudes of $|\Delta\varepsilon|$ relative to the flexoelectric coefficients. This analysis provides guidance for future mixture development.

Table 4.1: Coupling regimes for the flexoelectric nematic LC grating for different magnitudes of the dielectric anisotropy relative to the flexoelectric coefficients.

Relative Magnitudes	**Coupling Mechanism**
$\lvert\Delta\varepsilon\rvert \ll \frac{(e_1 - e_3)^2}{K\varepsilon_0}$	Flexoelectric coupling dominates
$\lvert\Delta\varepsilon\rvert \gg \frac{(e_1 - e_3)^2}{K\varepsilon_0}$	Dielectric coupling dominates
$\lvert\Delta\varepsilon\rvert \approx \frac{(e_1 - e_3)^2}{K\varepsilon_0}$	Flexoelectric coupling and dielectric coupling co-exist

To enhance the dominance of the flexoelectric effect in LC devices, the dielectric anisotropy should be minimised. This strategy is implemented and discussed in detail in Chapter 5.

4.2.2 Constrained Model (Conical Model)

For the conical model, as first proposed by Shin [41], θ_c represents the angle at which the LC director tilts out of the axis of the cone whereas φ_c represents the rotation angle around the cone. Using this notation, a constrained model was constructed as shown in Figure 4.1(c). The model assumes a smooth rotation of the LC director along the x-axis to form a flexoelectric periodic splay–bend structure within the cone. Consequently, we can define $\varphi_c = qx$, where q represents the wavenumber as previously discussed. The LC director can thus be expressed in the small-angle approximation as

$$\vec{n} = \begin{pmatrix} \sin\theta_c \cos\varphi_c \\ \cos\theta_c \\ \sin\theta_c \sin\varphi_c \end{pmatrix} \approx \begin{pmatrix} \theta_c \cos(qx) \\ 1 \\ \theta_c \sin(qx) \end{pmatrix}. \tag{4.15}$$

Linking the above with Eq. 4.1, we obtain the following

$$\varphi = \theta_c \cos(qx) \qquad \theta = \theta_c \sin(qx) \tag{4.16}$$

Considering the strong surface anchoring ($\theta = 0$ at $z = 0$ and $z = d$), θ can be treated as a z-dependent sine-like perturbation, similar to that when deriving the Fréedericksz threshold in a nematic LC. We thus propose the form $\theta_c = \theta_0 \sin\left(\frac{\pi z}{d}\right)$ where $\theta_0 \ll 1$. Inserting Eq. 4.16 into the free-energy equation (Eq. 4.3) and simplifying through integration over the cell thickness (the z-direction) and one spatial period in the x-direction, we obtain a reduced form of the free energy as

$$\langle f \rangle = \frac{K}{4}\theta_0^2\left(\frac{\pi^2}{d^2} + q^2\right) - \frac{q}{4}\theta_0^2(e_3 - e_1)E - \frac{1}{8}\varepsilon_0 \Delta\varepsilon\, E^2\theta_0^2 \tag{4.17}$$

The minimisation of $\langle f \rangle$ can be achieved by setting $\dfrac{\partial\langle f \rangle}{\partial q} = 0$. The last term containing $\Delta\varepsilon$ will not contribute to the derivation since it lacks dependence on q, thereby excluding dielectric components from the free energy equation. We can then obtain an expression for the pitch of the periodic splay–bend structure as a function of the material properties and the electric field, as well as the threshold voltage required to trigger the flexoelectric-induced distortion. Respectively, these equations take the form

$$p = \frac{4\pi K}{E(e_3 - e_1)} \tag{4.18}$$

$$V_{(\text{th_flexo})} = \frac{2\pi K}{(e_3 - e_1)} \tag{4.19}$$

Compared to Eq. 4.13 and Eq. 4.14, Eq. 4.18 and Eq. 4.19 present a more simplified form by omitting the dielectric coupling. This simplification reduces the complexity of the model while retaining the essential elastic contributions relevant

to the present analysis. Furthermore, Eq. 4.18 yields the same results as those obtained from a different model, described in Ref. [68], under the assumption that the elastic constants for splay and bend are equal.

4.3 Non-Linear Model

In the above linear analytic models, the small-angle approximation has been employed to simplify the mathematical analysis. However, the application of the small-angle approximation limits the validity of the resulting equations to scenarios with small undulations, thereby potentially compromising their accuracy in representing the LC director's actual behaviour in most nematic LC mixtures. Therefore, a nonlinear model that removes the need for the small-angle approximation would be desirable.

To accomplish this, we propose eliminating the simplifications and incorporating the completely unconstrained form of the LC director $\vec{n} = \begin{pmatrix} \cos\theta \, \sin\varphi \\ \cos\theta \, \cos\varphi \\ \sin\theta \end{pmatrix}$ directly into the total free energy equation. It can then be expressed as:

$$f = f_{\text{elastic}} + f_{\text{flexoelectric}} + f_{\text{dielectric}} \tag{4.20}$$

$$= \frac{1}{2}K\{[\nabla \cdot \vec{n}]^2 + [\nabla \times \vec{n}]^2\} - (e_1\vec{n}(\nabla \cdot \vec{n}) + e_3(\nabla \times \vec{n}) \times \vec{n}) \cdot \vec{E} - \frac{1}{2}\varepsilon_0\Delta\varepsilon(\vec{n} \cdot \vec{E})^2 \tag{4.21}$$

$$
\begin{aligned}
&= \tfrac{1}{2}K\Bigg[\left(\frac{\partial\theta}{\partial z}\right)^2 + \left(\frac{\partial\theta}{\partial x}\right)^2 + \cos^2\theta\left(\frac{\partial\varphi}{\partial z}\right)^2 + \cos^2\theta\left(\frac{\partial\varphi}{\partial x}\right)^2 \\
&\qquad + 2\cos^2\theta\cos\varphi\left(\frac{\partial\varphi}{\partial x}\frac{\partial\theta}{\partial z} - \frac{\partial\varphi}{\partial z}\frac{\partial\theta}{\partial x}\right)\Bigg] \\
&\quad - e_1E\left(\sin\theta\cos\theta\cos\varphi\frac{\partial\varphi}{\partial x} - \sin^2\theta\sin\varphi\frac{\partial\theta}{\partial x} + \sin\theta\cos\theta\frac{\partial\theta}{\partial z}\right) \\
&\quad - e_3E\left(\sin\theta\cos\theta\frac{\partial\theta}{\partial z} + \cos^2\theta\sin\varphi\frac{\partial\theta}{\partial x}\right) - \tfrac{1}{2}\varepsilon_0\Delta\varepsilon\,E^2\sin^2\theta.
\end{aligned}
\tag{4.22}
$$

Upon employing the Euler-Lagrange equations for minimising the free energy with respect to variables θ and φ, a set of equations is generated as follows:

For φ: $f_2(\varphi,\theta)$

$$
= \frac{\partial^2\varphi}{\partial x^2} + \frac{\partial^2\varphi}{\partial z^2} - \frac{(e_1-e_3)E\cos\varphi}{K}\frac{\partial\theta}{\partial x} - 2\tan(\theta)\left(\frac{\partial\theta}{\partial x}\frac{\partial\varphi}{\partial x} + \frac{\partial\varphi}{\partial z}\frac{\partial\theta}{\partial z}\right) = 0 \tag{4.23}
$$

For θ: $g_2(\theta,\varphi)$

$$
\begin{aligned}
&= \frac{\partial^2\theta}{\partial x^2} + \frac{\partial^2\theta}{\partial z^2} + \frac{(e_1-e_3)\cos\varphi\,(\cos\theta)^2}{K}E\frac{\partial\varphi}{\partial x} + \frac{\varepsilon_0\Delta\varepsilon\cos\theta\,\sin(\theta)\,E^2}{K} \\
&\qquad + \cos\theta\sin(\theta)\left[\left(\frac{\partial\varphi}{\partial x}\right)^2 + \left(\frac{\partial\varphi}{\partial z}\right)^2\right] = 0
\end{aligned}
\tag{4.24}
$$

The above two equations, which represent the stationary orientation of the LC director in the presence of flexoelectric coupling, contain additional terms that do not appear when the form of the LC director follows that of Eq. 4.1. It can be seen in Eq. 4.23 that $\dfrac{(e_1-e_3)\,E\cos\varphi}{K}\dfrac{\partial\theta}{\partial x}$ becomes the dominant factor when the LC is subjected to high voltages. Consequently, the contributions from the other terms

can be considered negligible. Therefore, for the condition of $\frac{(e_1 - e_3)E\cos\varphi}{K}\frac{\partial\theta}{\partial x} = 0$, $\cos(\varphi)$ should be equal to zero. This implies that φ must be $-\frac{\pi}{2}$ or $\frac{\pi}{2}$.

In the bulk of the LC, this suggests that, due to the combined influence of flexoelectric and dielectric coupling, the directors tend to orient in the x–z plane, with little tilting in the x–y plane when extremely high voltages are applied, as shown in Figure 4.1(d).

Understanding the voltage-dependent molecular behaviour under the flexoelectric effect, therefore, establishes a direct link between director reorientation mechanisms and macroscopic beam-steering performance, enabling predictive control of diffraction efficiency, steering angle, and switching stability.

4.4 Simulations

To solve the partial differential equations (PDEs) obtained from the model described in the previous section and to understand the variations in θ and φ with respect to spatial coordinates, it is necessary to implement a finite difference relaxation method, a numerical technique that is adept at converting PDEs into a series of algebraic equations [38]. For example, using the Taylor series expansion, some terms in Eq. 4.23 can be approximated as:

$$\begin{aligned} &\frac{\partial^2\varphi_i}{\partial x_i^2} \approx \frac{\varphi_{i+1} - 2\varphi_i + \varphi_{i-1}}{h^2}, \qquad \frac{\partial^2\varphi_j}{\partial z_j^2} \approx \frac{\varphi_{j+1} - 2\varphi_j + \varphi_{j-1}}{h^2}, \\ &\frac{\partial\varphi_i}{\partial x_i} \approx \frac{\varphi_{i+1} - \varphi_{i-1}}{2h}, \qquad \frac{\partial\varphi_j}{\partial z_j} \approx \frac{\varphi_{j+1} - \varphi_{j-1}}{2h} \end{aligned} \tag{4.25}$$

where i and j represent discrete points along the x-axis and z-axis respectively, and h represents the distance between discrete points. In the computational framework of our study, we designated N_x and N_z within a MATLAB code to

represent the number of grid points along the x-axis and the number of grid points across the thickness of the LC device, respectively. Furthermore, instead of setting $f_2(\varphi, \theta)$ and $g_2(\theta, \varphi)$ to zero, we could set them equal to $\gamma \dfrac{\varphi_{\text{new}} - \varphi_{\text{old}}}{\Delta t}$ and $\gamma \dfrac{\theta_{\text{new}} - \theta_{\text{old}}}{\Delta t}$, respectively. Therefore,

$$\varphi_{\text{new}} = \varphi_{\text{old}} + \frac{\Delta t}{\gamma} f_2(\varphi, \theta), \qquad \theta_{\text{new}} = \theta_{\text{old}} + \frac{\Delta t}{\gamma} g_2(\theta, \varphi) \tag{4.26}$$

The time step Δt does not represent a physical time scale but serves as a numerical stepping parameter that regulates the stability and smoothness of the iteration. The relaxation parameter γ functions as a control mechanism within the iterative process. It guarantees the stability and convergence of iterative solutions.

In the numerical implementation, the director field was discretised on a grid of $N_x = 800$ points along the x-direction and $N_z = 40$ points throughout the cell thickness. For the calculations shown in **Figure 4.4**, the cell thickness was $d = 5$ μm, with $K = 13$ pN, $e_3 - e_1 = 5.5$ pC/m, and $\Delta\varepsilon = 0.01$. The applied voltage ranged from 20 to 40 V. The initial tilt angle was set to $\theta = 0.05$ rad, with a small random perturbation added to ϕ. The director angles were fixed at the substrates, while the values at the lateral boundaries were obtained by linear extrapolation.

The director angles were updated for 20,000 iterations at each applied voltage. The dimensionless numerical relaxation factor was adjusted between 0.01 and 0.06 for different voltage conditions to maintain stable numerical updates. This factor multiplies the discretised right-hand sides of the director equations and controls the size of each update. The iterations seek a stationary director configuration at each applied voltage. Convergence was assessed by monitoring the maximum change in θ and ϕ between successive iterations. The calculation was regarded as converged when this change fell below 10^{-4} rad. The resulting in-plane and

out-of-plane director-angle profiles are shown in Figure 4.4.

4.4.1 Director Profiles

Jones matrix analysis is essential for understanding light propagation through the LC sample, as explained in detail in Section 2.4. As shown in **Figure 4.2**, we subdivide our LC into several grid units for computational purposes, as explained in the previous section. Each grid's corresponding Jones matrix can be represented as:

$$J_{\text{slice}} = \begin{pmatrix} \cos\varphi & \sin\varphi \\ -\sin\varphi & \cos\varphi \end{pmatrix}^{-1} \begin{pmatrix} e^{j\frac{2\pi}{\lambda}n_{\text{o}}d_{\text{slice}}} & 0 \\ 0 & e^{j\frac{2\pi}{\lambda}\left(\frac{n_{\text{e}}n_{\text{o}}}{\sqrt{n_{\text{o}}^2\cos^2\theta+n_{\text{e}}^2\sin^2\theta}}\right)d_{\text{slice}}} \end{pmatrix} \begin{pmatrix} \cos\varphi & \sin\varphi \\ -\sin\varphi & \cos\varphi \end{pmatrix} \tag{4.27}$$

where d_{slice} represents the thickness of a single grid, defined as $\left(\frac{d}{N_z}\right)$, where d is the cell thickness. To obtain the total Jones matrix (J_{total}), it is required to sequentially multiply the Jones matrices of each grid (J_{slice}) along the z-axis. Then, we can calculate the output electric field ($E_{\text{near_field}}$) at each grid point along the x-axis by multiplying J_{total} with the input electric field (E_{input}).

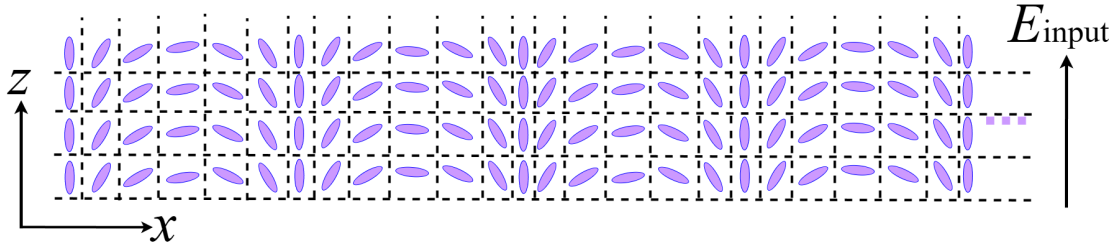


Figure 4.2: The grid configuration within the splay-bend LC structure.

For the simulations, values for macroscopic parameters such as the one elastic constant (K), splay flexoelectric coefficient (e_1), bend flexoelectric coefficient (e_3), dielectric anisotropy ($\Delta\varepsilon$), and refractive indices (n_{e}, n_{o}) of our LC mixture (to be discussed in detail later in Chapter 5) consisting of MLC6882 (Merck KGaA),

BL006 (Merck KGaA), and CB7CB were taken from the following references [33, 69–72] and the measurements described in Section 3.5. The relative concentration of each component was taken into account when determining the parameter values. Specifically, the elastic constant was assigned a value of $K = 13$ pN, the dielectric anisotropy ($\Delta\varepsilon$) was set to $\Delta\varepsilon = 0.01$, and the extraordinary refractive index (n_e) was set at 1.594. In contrast, the ordinary refractive index (n_o) was chosen to be 1.487, and the effective flexoelectric coefficient was $e^* = e_3 - e_1 = 5.5$ pC/m, which falls within the first regime of Table 4.1.

According to Eq. (4.19), the predicted threshold voltage for the onset of the periodic splay–bend director deformation is $V_{\mathrm{th,flexo}} = 14.85$ V, in reasonable agreement with the experimental and numerical results discussed in Chapter 5. All simulation results presented in this chapter are based on these estimated mixture parameters. However, the actual values of e^* and $\Delta\varepsilon$ might be higher than the estimates provided here because the application of the DC field can lead to the formation of ionic screening, which reduces the internal electric field and is not consistently controllable. Therefore, it is important to note that our simulations have not taken into account the influence of ions on the resultant behaviour. Examples of simulated LC director profiles for a range of applied voltages are shown in **Figure 4.3**.

As seen in Figure 4.3, when the applied voltage is below the threshold voltage, the LC director remains unchanged with uniform alignment along the y-axis, which is the direction of the initial alignment. Once the applied voltage significantly exceeds the threshold voltage, the LC director exhibits a splay–bend structure within the x–z plane. Meanwhile, as the voltage increases, the pitch decreases proportionally, which is consistent with Eq. 4.18.

Figure 4.4 demonstrates the variation of the in-plane tilt angle (φ) and out-

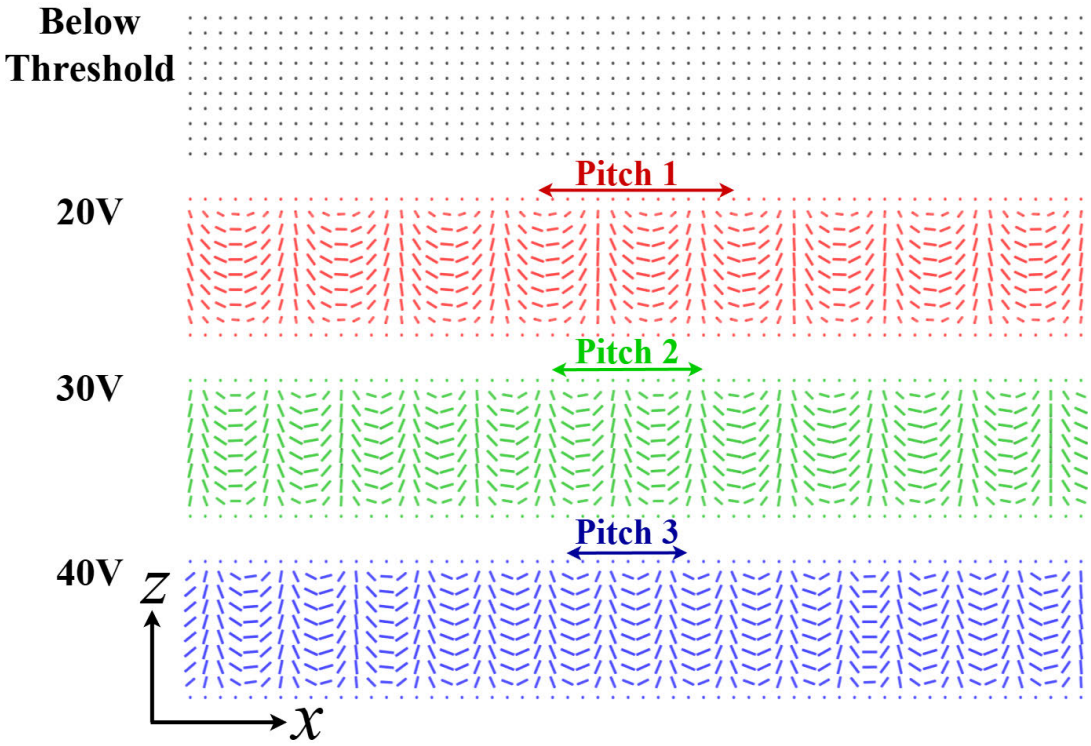


Figure 4.3: Simulated voltage-dependent director profile and splay-bend structures formed in a nematic LC when viewed in the x–z plane for the following parameters: pre-tilt angle, $T_s = 0.05$ rad, $K = 13$ pN, $e^* = 5.5$ pC/m, $d = 5\,\mu$m, and $\Delta\varepsilon = 0.01$. Reproduced from Ref. [18] with permission from Elsevier.

of-plane tilt angle (θ) along the x-axis under different applied voltages. It is evident that φ becomes a square waveform, while θ shows a triangular waveform at high voltages.

This behaviour arises at very high voltages due to the LC director's predominant tilt into the x–z plane, which creates a splay-bend state. This state is characterised by a continuous variation in tilt along the x-axis, with φ alternating between $-\frac{\pi}{2}$ and $\frac{\pi}{2}$, thus forming a square waveform. It also causes θ to exhibit a periodic oscillation with sharpened extrema. These observations are consistent with the predicted configurations of the LC director under different applied voltages, as shown in Figure 4.1(d).

To further study the behaviour of the LC director under the influence of

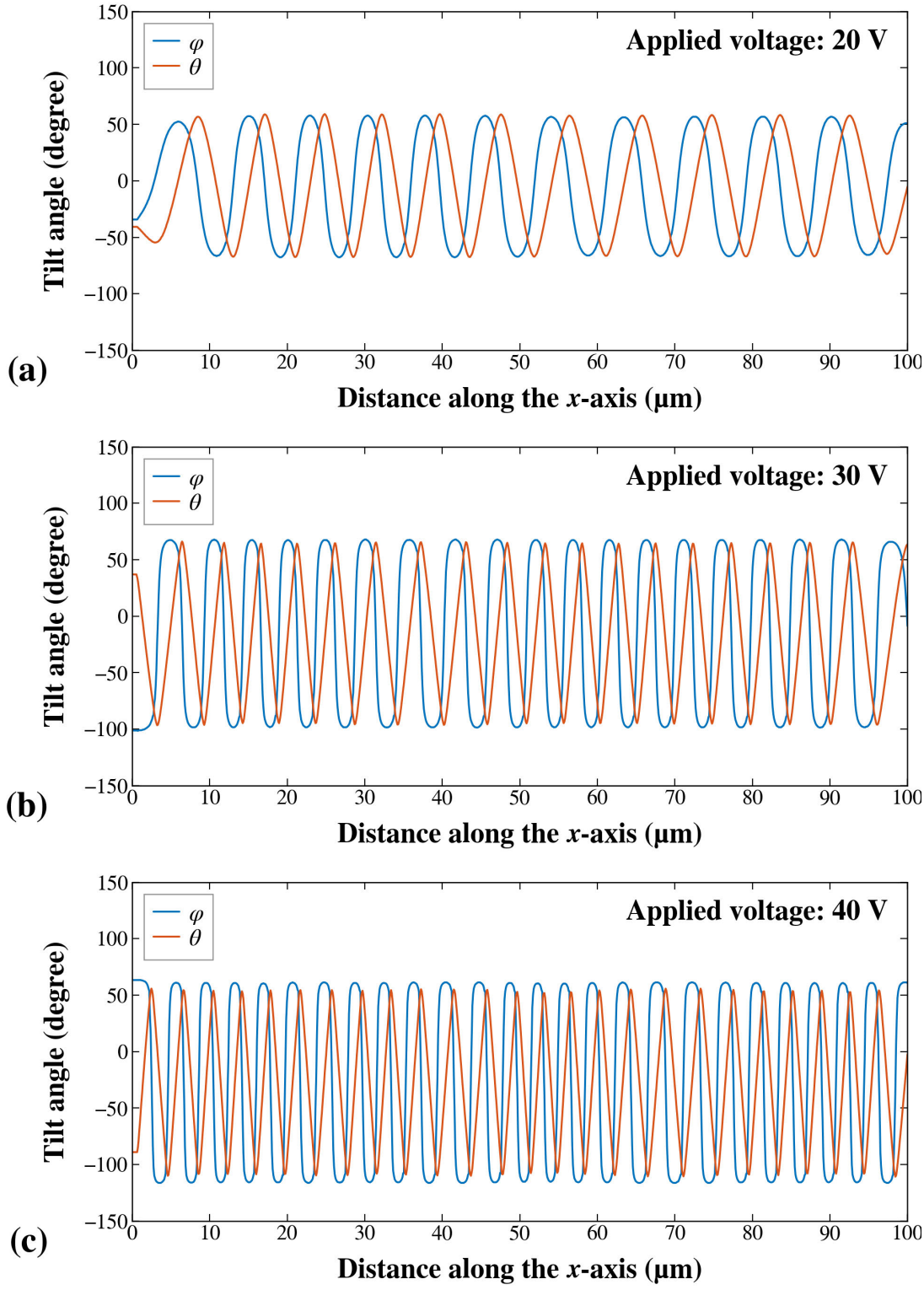


Figure 4.4: Comparison of the variations in θ and φ along the x-axis at the middle layer of the z-axis, under applied voltage of (a) 20 V (b) 30 V (c) 40 V, using the nonlinear numerical model. The simulations were conducted with the following parameters: $K = 13$ pN, $e^* = 5.5$ pC/m, $\Delta\varepsilon = 0.01$, $T_s = 0.05$ rad.

flexoelectric coupling, both side and top views of the director profile were simulated using our nonlinear model (see **Figure 4.5**). When the applied voltage is below the threshold, the LC director exhibits uniform alignment, parallel to the y-axis and predominantly lying within the x-y plane. However, once the applied voltage increases above the threshold voltage, it causes a gradual tilting of the director in both the x-y and x-z planes due to the combined influence of flexoelectric and dielectric effects. Under very strong electric field strengths, the LC director exhibits a predominant splay-bend structure in the x-z plane, with negligible tilt in the x-y plane. These simulation results align with the behaviour suggested in Figure 4.1(d).

The interplay of the flexoelectric and dielectric effects induces variability of the out-of-plane tilt angle, θ, along both the x-axis and z-axis, significantly influencing the variation in the effective refractive index experienced by light polarised along the x and y-directions. Additionally, the in-plane tilt angle (φ) within the x-y plane varies along the x-axis due to the flexoelectric effect.

Figure 4.5(c) shows the average cone angle, determined by $\theta_c = \arccos(n_y)$ where n_y is equal to $\cos(\theta)\cos(\varphi)$, as a metric to quantify the degree of tilt away from the y-direction. Here, D indicates the distance between the surface of the device and the depth within the LC layer. It indicates that as the voltage increases above the threshold, the cone angle becomes more pronounced towards the middle of the layer. This reflects a progressive reorientation of the LC director into a splay–bend configuration within the x–z plane, such that the y-component of the director, n_y, gradually decreases towards zero, consistent with the side-view profile.

4.4.2 Polarised Optical Microscope Imaging

To simulate crossed polarised optical microscope images to compare with those from experiments, the CIE 1931 colour space [73] is employed. Central to this

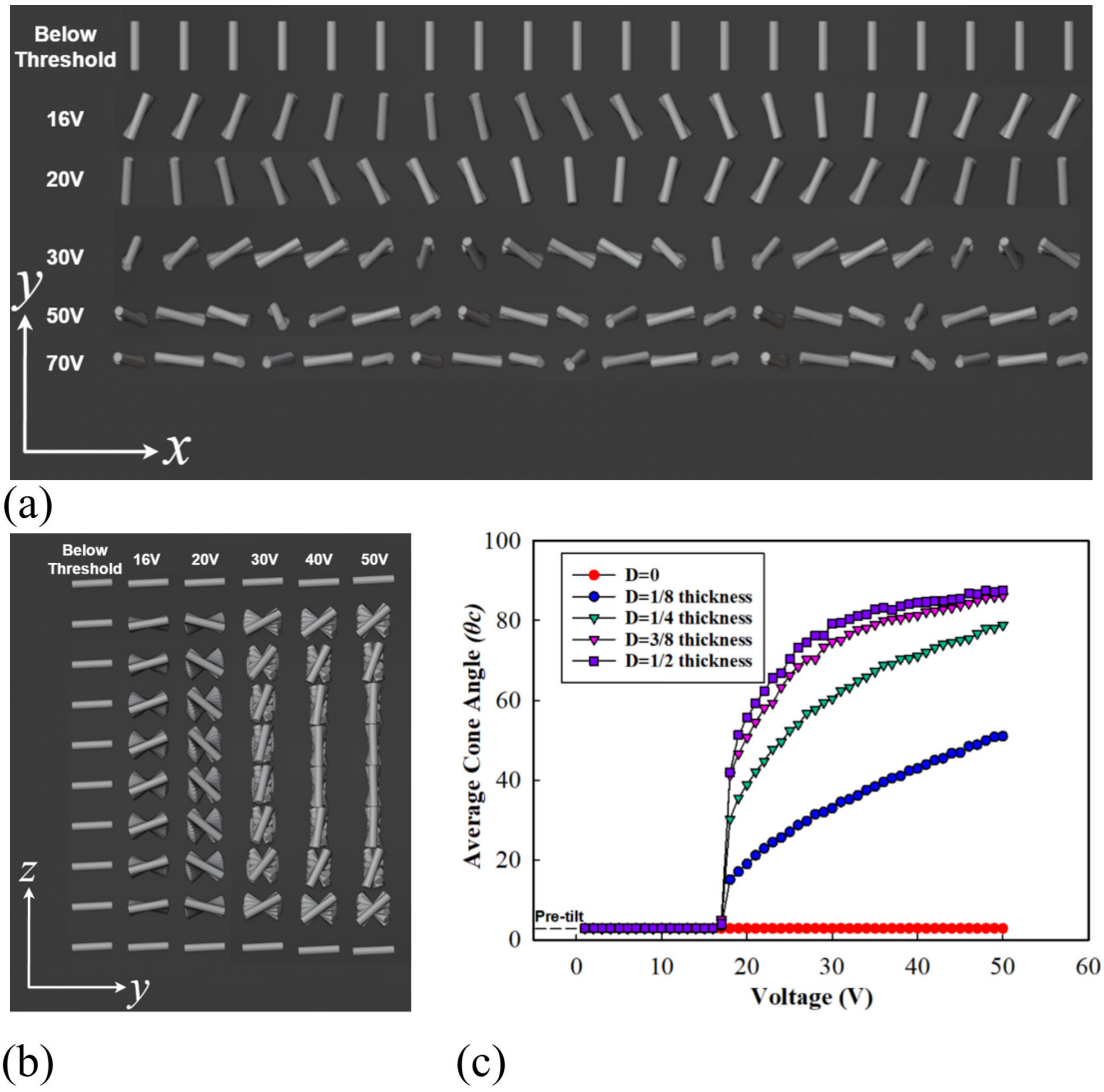


Figure 4.5: (a) Simulated top view of the LC director profile for different applied voltages, specifically within the LC layer depths ranging from $D = \frac{2}{9}d$ to $D = \frac{7}{9}d$ (i.e., excluding the strongly anchored surface regions). (b) Simulated side view of the LC director profile for different applied voltages, with the presence of a surface anchoring layer. (c) Simulations of the variation of the average conical angle ($\theta_c = \arccos(n_y)$) at different depths (D) within the LC layer. The simulations were conducted with the following parameters: $K = 13$ pN, $e^* = 5.5$ pC/m, $\Delta\varepsilon = 0.01$, $d = 5\,\mu$m, $T_s = 0.05$ rad. Reproduced from Ref. [18] with permission from Elsevier.

colour space are the colour-matching functions $\bar{x}(\lambda)$, $\bar{y}(\lambda)$, and $\bar{z}(\lambda)$, which span the wavelength range from 360 nm to 830 nm. These functions quantify the eye's response to different wavelengths of light, with $\bar{x}(\lambda)$ corresponding to the sensitivity to red light, $\bar{y}(\lambda)$ to green light, and $\bar{z}(\lambda)$ to blue light. As light interacts with the LC layer, a wavelength-dependent phase retardation is introduced between orthogonal polarisation components. Under crossed polarisers, this retardation alters the transmitted spectral intensity, which is subsequently converted into perceived colour using the CIE 1931 colour space.

The XYZ tristimulus values were calculated by integrating on the wavelength from 360 nm to 830 nm. This integration involves the multiplication of the colour-matching functions $\bar{x}(\lambda)$, $\bar{y}(\lambda)$ and $\bar{z}(\lambda)$, the transmittance properties of the LC material, and the spectral power distribution D65, which simulates standard daylight illuminance [73]. These XYZ tristimulus values were then transformed into RGB values through a matrix specific to the observing device's RGB colour space. Representative simulation results, along with the corresponding experimental observations, are presented in Chapter 5.

4.4.3 Far-field Diffraction

We simulate the normalised far-field light intensity, (η), defined as the ratio of the intensity of light after passing through the LC grating under an applied voltage to the intensity of light without the LC grating (I_0). MATLAB's Fourier transform functionality was employed to convert the near-field output light electric field ($E_{\text{near_field}}$) into the far-field intensity distribution ($E_{\text{far_field}}$). The intensity of the light in the far field is calculated using the formula $I_{\text{out}} = |E_{\text{far_field}}|^2$, and the initial light is calculated as $I_{\text{in}} = |E_0|^2$, where E_0 represents the incident electric field of light. Consequently, the normalised light intensities of the LC grating are derived

from the ratio of these two intensities, formulated as $\eta = I_{\text{out}}/I_{\text{in}}$. The spatial frequencies (f_x) of the diffraction orders obtained from the Fourier transform are then converted to the diffraction angles (δ) using the relation $\delta = \sin^{-1}(\lambda f_x)$. The physical distance along the screen can then be simulated using the expression $L\tan(\delta)$, where L is defined as the distance between the screen and the LC device. **Figure 4.6** shows the simulated intensity distributions and analytical diffraction patterns at different applied voltages using the nonlinear model. As the voltage increases, the spacing between diffraction orders increases (Figure 4.6(a)–(d)). X_1 represents the separation between the 0^{th} and 1^{st} order whereas X_2 denotes the separation between the 0^{th} and 2^{nd} order. However, the peaks in the distribution are not infinitely narrow and consequently do not exhibit δ-function characteristics because the numerically simulated splay-bend structure is not perfectly periodic. Additionally, we simulate the normalised light intensity as a function of the applied voltage amplitude. These effects are illustrated in Figure 4.6(e), where the increasing separation between diffraction orders is observed with increasing voltage.

4.5 Summary

In this chapter, we present the theoretical modelling and simulation of flexoelectric-based LC diffraction gratings, incorporating both flexoelectric and dielectric coupling effects. To capture the full complexity of the LC response, we employ linear analytic and nonlinear numerical models formulated in both unconstrained and constrained (conical) coordinate systems. We start by considering a linear analytic model in which the tilt of the LC director is assumed to be small in both the unconstrained and constrained (conical) coordinate systems and investigate the influence of dielectric anisotropy on the behaviour of the grating.

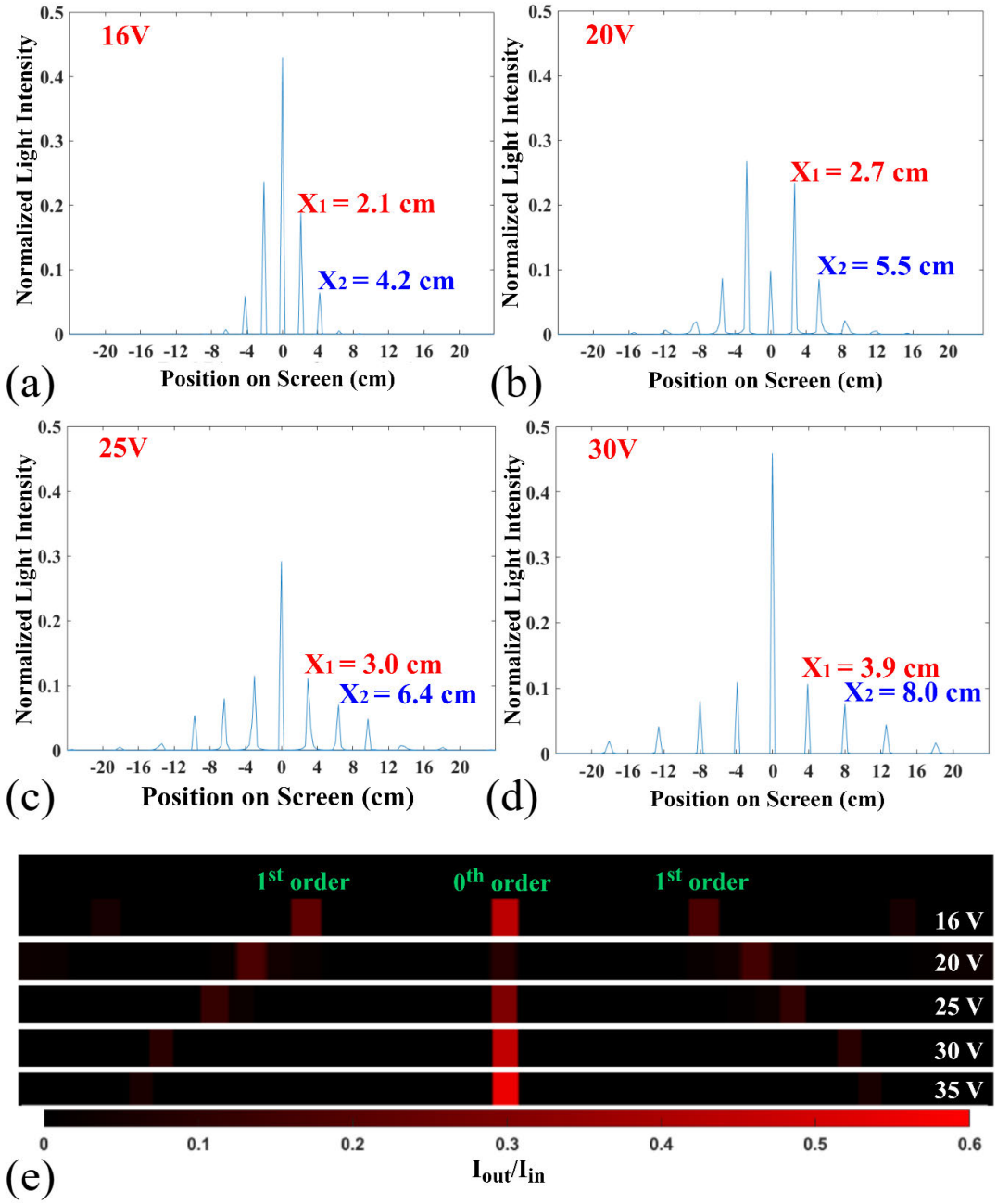


Figure 4.6: (a)–(d) Simulated light intensity distribution in the far-field diffraction pattern, showing the normalised light intensities (η) as a function of distance on the screen from the zero order. (e) Simulated far-field diffraction patterns (0^{th} order and 1^{st} order) of the flexoelectric nematic LC grating under various applied voltages, the colour bar is located at the bottom of the figure. The simulations were conducted with the following parameters: $K = 13$ pN, $e^* = 5.5$ pC/m, $n_e = 1.594$, $n_o = 1.487$, $\Delta\varepsilon = 0.01$, $T_s = 0.05$ rad. The incident linear polarisation angle is $\alpha = 30°$, and the distance between the screen and the LC device (L) is set at 30 cm. Reproduced from Ref. [18] with permission from Elsevier.

Subsequently, we present a nonlinear method that obviates the need for a small-angle approximation and includes dielectric coupling to provide a more sophisticated model of flexoelectric nematic LC gratings. Numerical simulations based on this model provide important insight into the behaviour of the LC director as the flexoelectric grating forms and varies, facilitating the simulation of the light intensity distribution in the far field and the resulting diffraction pattern, as well as the grating's dependence on incident polarisation using Jones matrices. These complementary modelling approaches reveal richer LC director behaviours and yield more accurate predictions that align closely with experimental behaviour.

Building on the theoretical framework, we perform detailed numerical simulations to compute the LC director field under a range of applied voltages and material parameters. In addition, we calculate the far-field light intensity distribution and diffraction patterns using Fourier-optics methods, illustrating how flexoelectric coupling modifies diffraction efficiency, diffraction angles, and intensity profiles. Together, these simulations provide comprehensive predictive capabilities that guide experimental design and validate the physical insights developed throughout the chapter.

5

Flexoelectric Liquid Crystal Diffraction Gratings

5.1 Introduction

Electrically switchable LC diffraction gratings are a key component for beam-steering applications, as they offer several key advantages, including cost-effectiveness, low weight, and low power consumption [45, 74]. Most importantly, they can facilitate real-time modification of the diffraction, aligning with the dynamic requirements of modern optical applications. In the fabrication of tunable LC gratings, nematic LCs, which are characterised by the absence of an inherent macroscopic periodic structure, have proven to be especially popular. A widely adopted technique used to induce a diffraction grating in a nematic LC is to apply a periodic electric field across the LC layer, which can be achieved with patterned

electrodes [75–77]. Alternatively, to avoid the need for patterned electrodes, the LC director can be spatially patterned using photoalignment layers in combination with ultraviolet light and photomasks [49, 78, 79]. However, the process of patterning the alignment layer can be complex, increasing the time and cost involved in manufacturing. Additionally, the morphology of the resulting diffraction grating can be inherently limited, confining its ability to diffract light to a limited range of angles. Chiral nematic LCs, characterised by their intrinsic macroscopic periodic helical structure, have also been explored for use as tunable diffraction gratings [80, 81]. In this case, the pitch of the chiral nematic LC grating can be tuned by adjusting both the concentration of the chiral dopant and the applied electric field [80, 81]. However, a significant constraint with such systems is the lack of control of diffraction efficiency and slow response time, which is typically of the order of several seconds [82]. The flexoelectric effect in nematic LCs offers a promising route to the realisation of tunable LC gratings, as discussed in Section 2.8. For certain molecules with shape asymmetry, splay and bend deformations can lead to a net electric polarisation within the material. In contrast, when an electric field is applied, it can generate a macroscopic splay–bend deformation, creating a periodic structure that will serve as an LC diffraction grating.

In this chapter, we present experimental results for CB7CB and an optimised LC mixture that is capable of forming diffraction gratings with the help of the flexoelectric effect at room temperature under a DC field. We then investigate whether the grating can dynamically tune the diffraction angle and efficiency when a laser beam passes through it. The comparison between our experimental findings and the results of our simulations shows the reliability and validity of our proposed nonlinear model discussed in the previous chapter. The experimental results presented in this chapter have also been published in Optics & Laser

Technology, 180, 111502 (2025) [18].

5.2 Pitch Definition and Concept of Splay-Bend Structure

Different authors offer varying definitions for the pitch of the splay–bend structure. In this thesis, we define it as the distance along the x-axis over which the director modulation repeats. After each cycle, a new period starts, replicating the exact molecular arrangement of the preceding one. Consequently, each period represents a 'reset' point. The equation for calculating the pitch is $p = \frac{2\pi}{q}$, where q is the spatial wavenumber of the modulation. Here, 2π refers to one cycle of spatial modulation, not a 2π rotation of the director.

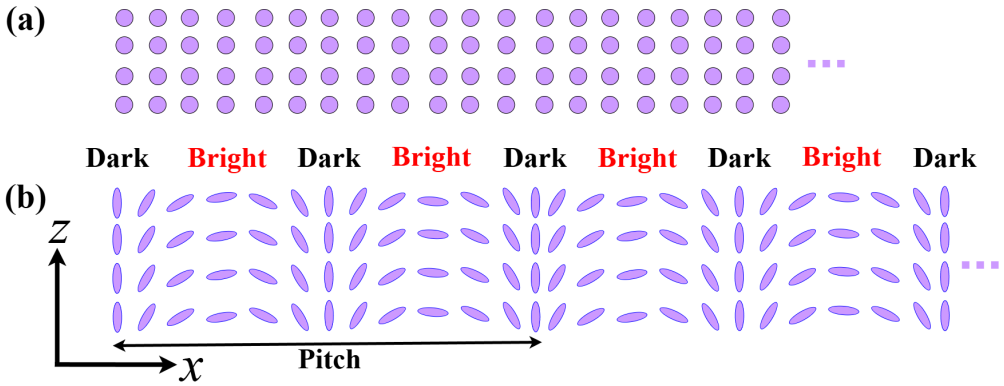


Figure 5.1: (a) The initial state with no applied electric field. (b) The splay-bend structure in the x–z plane under an electric field applied along the z-axis. The helical pitch is indicated along the x-axis.

Figure 5.1(a) shows the initial state without applied electric field. The long axes of the molecules are aligned along the y-axis in this state. Under the application of an electric field along the z-axis, as shown in Figure 5.1(b), a splay-bend structure begins to appear in the x–z plane. When this device is placed under a cross-polarised microscope, molecules in a vertical position appear black, while molecules in a

tilted position appear bright. The combination generates dark and bright stripes.

5.3 Materials and Methods

The formation of flexoelectric nematic LC gratings requires materials with significant flexoelectric coefficients. For the fabrication of a flexoelectric nematic LC diffraction grating, our primary material of choice was the Synthon-sourced LC dimer CB7CB (4',4"-(Heptane-1,7-diyl) dibiphenyl-4-carbonitrile). As depicted in **Figure 5.2**, CB7CB comprises two mesogenic biphenyl groups positioned at both sides and a flexible hydrocarbon chain in the middle. The permanent dipole is present in the cyano group of mesogenic groups because the cyano group has a strongly electron-withdrawing effect and tends to drag the electrons from the biphenyl group towards itself. Meanwhile, the hydrocarbon chain of CB7CB contains an odd number of carbon atoms, 7 in total, resulting in a distinctively curved structure [41].

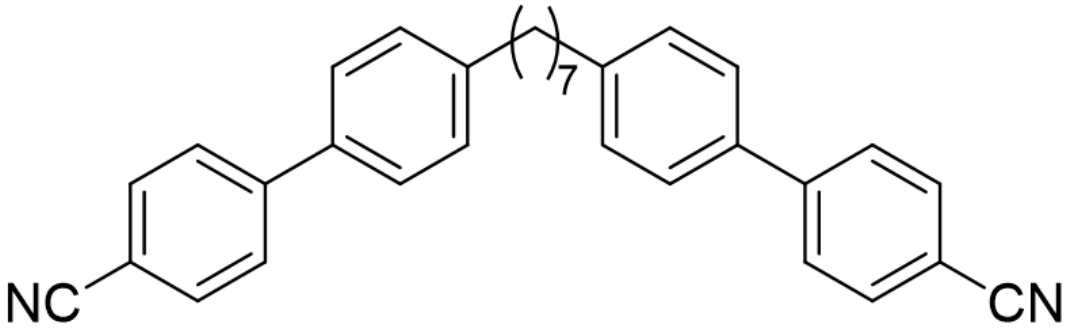


Figure 5.2: Chemical structure of CB7CB.

CB7CB is an exemplary candidate for flexoelectric applications as it exhibits a significant flexoelectric coefficient, reported to be approximately -31 pC/m [37]. Additionally, the dielectric anisotropy of CB7CB is quantified to be $\Delta\varepsilon = +2$ [70], which is low compared to more conventional nematic LCs. As discussed in Chapter

4, a low dielectric anisotropy is advantageous for promoting the dominance of the flexoelectric effect. However, CB7CB exhibits a nematic phase within the temperature range of 105 °C to 114 °C, while a twist-bend nematic or crystalline phase may occur at lower temperatures.

To obtain a nematic phase at room temperature, CB7CB needs to be mixed with other LC materials. For this purpose, we selected the wide temperature range mixture, BL006. The downside is that BL006 has a relatively high dielectric anisotropy of +17.3 [81], which is not conducive to the flexoelectric properties required for our device. To reduce the overall dielectric anisotropy close to zero, we also introduced a substantial proportion of MLC-6882 (Merck KGaA) into the mixture. The dielectric anisotropy of MLC-6882 was found to be $\Delta\varepsilon \approx -2.82$. Initially, a high weight percentage of MLC-6882 and a lower percentage of BL006 are combined to achieve an overall dielectric anisotropy close to zero or slightly positive. A small amount of CB7CB is then introduced to ensure that the overall dielectric anisotropy remains low. Through iterative optimisation, we have developed an LC mixture comprising 81 wt.% MLC-6882, 9 wt.% BL006, and 10 wt.% CB7CB. This mixture composition was filled into a 5 μm glass cell (INSTEC) by capillary action in the isotropic phase. The procedure follows the methodology described in Section 3.1.

As described in Section 3.3, a polarising optical microscope (BX51, Olympus) equipped with crossed polarisers and a CCD camera (R6, QImaging) mounted on the phototube was used to capture microphotographs of the gratings. A voltage was applied to the LC layer through a function generator that was connected to a voltage amplifier. To observe the diffraction pattern formed by the LC flexoelectric gratings, a PL202 laser diode ($\lambda = 635$ nm, Thorlabs) was used as a coherent light source and a neutral-density (ND) filter was used to attenuate the intensity to avoid saturation of the photodiode (PDA36A-EC, Thorlabs). A linear polariser

was placed before the LC grating to analyse the dependence of the flexoelectric grating on the incident polarisation. Diffraction patterns were displayed on a white screen and captured using a CCD camera, replacing the photodiode when required.

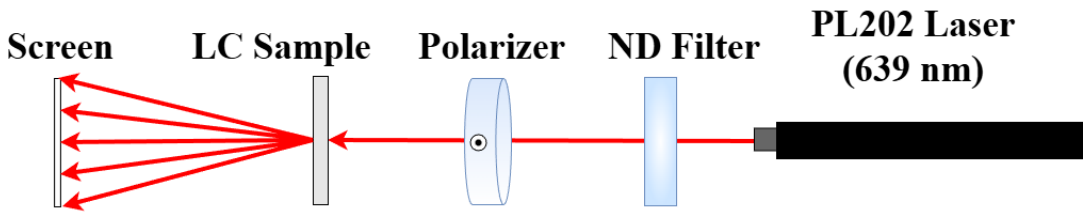


Figure 5.3: Schematic of the optical setup used to observe diffraction patterns from the flexoelectric nematic LC diffraction grating (top view).

The schematic of the optical setup for observing the diffraction is shown in **Figure 5.3**. The end screen functions as the viewing platform for our results, where we can observe the diffraction pattern if the light passes through our LC sample successfully.

5.4 LC Diffraction Grating Formation

Using the materials discussed above, a strong flexoelectric response is induced when the electric field is applied. In this section, the formation of the grating at elevated and room temperatures will be discussed using different LC materials.

5.4.1 High Temperature Formation

The LC devices used here were developed using CB7CB filled into a 5 µm INSTEC Fréedericksz cell by capillary action in the isotropic phase at a temperature above the clearing point. The electric field we chose to apply is a low-frequency, square-wave AC field. We did not select a DC field because the ionic mobility at this high temperature is very intense, and the ions tend to move towards the substrate. Some

of these ions adhere to the surfaces, creating a permanent electric field across them.

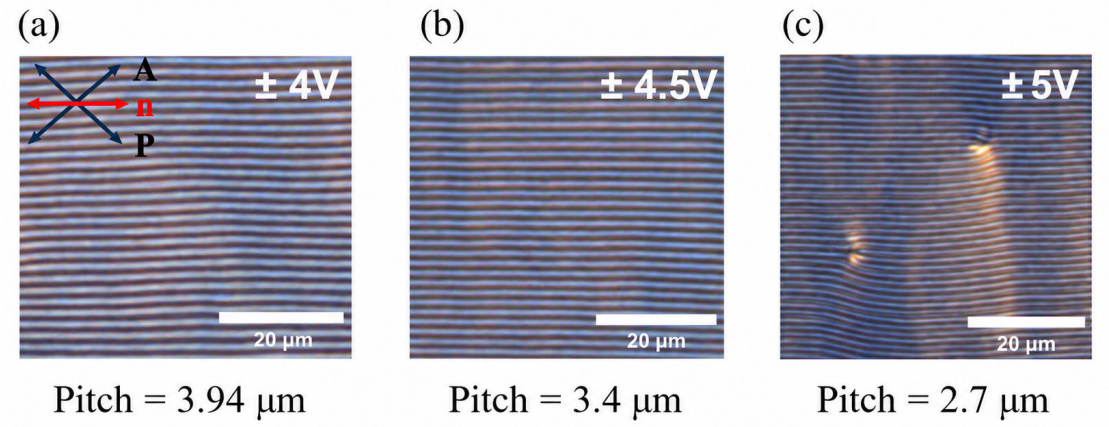


Figure 5.4: The microphotographs of the LC diffraction gratings at 114 °C under (a) 10 Hz, ±4 V (b) 10 Hz, ±4.5 V (c) 10 Hz, ±5 V AC field using a 5 µm INSTEC cell. Two black arrows perpendicular to each other represent the transmission axis of the polariser and analyser of the microscope, and the red arrow represents the direction of the LC director.

Under AC driving, the polarity of the applied electric field is periodically reversed, leading to alternating flexoelectric torques on the director field. When the driving frequency is sufficiently low, the LC director has adequate time to relax to its equilibrium configuration within each half-cycle. Provides sufficient time for the LC to reverse. However, low-frequency AC can easily trigger an electrohydrodynamic instability if the dielectric anisotropy is slightly positive, leading to unwanted patterns. Moreover, there are specific threshold voltages that play crucial roles. The first threshold voltage (indicated as $V_{(\text{th_flexo})}$) corresponds to the appearance of flexoelectric instability. At this voltage, a periodic splay–bend distortion develops, forming the flexoelectric grating. The second threshold voltage (indicated as $V_{(\text{th_EHD})}$) is the level above which EHD instability can occur, which disrupts the regular grating structure. The third threshold voltage (indicated as $V_{(\text{th_frdz})}$) is the Fréedericksz threshold, at which dielectric torque overcomes elastic restoring forces and induces bulk director reorientation (discussed in Section 2.7.2).

This threshold is not directly measured, since the operating regime is primarily governed by flexoelectric coupling. To analyse the CB7CB device in its nematic phase under a cross-polarised optical microscope, we heated it to 114 °C and tested its response to varying voltages at frequencies of 10 Hz. A low-frequency AC field effectively triggers the formation of a stripe pattern, allowing sufficient time for the LC to switch. The observed patterns are aligned parallel to the rubbing direction of the LC device. When $V_{\text{applied}} < V_{(\text{th_flexo})}$, the only phenomenon observed is dielectric coupling, without evidence of flexoelectric coupling.

Figure 5.4 presents the images captured by the optical polarising microscope when $V_{(\text{th_flexo})} < V_{\text{applied}} < V_{(\text{th_EHD})}$. At this point, the flexoelectric effect dominates, resulting in the visibility of bright–dark patterns. The dislocation appearing in Figure 5.4(c) is stress-generated and will be discussed further in Section 5.7. It was also observed that the grating period (or pitch) decreases with increasing applied voltage. The higher field effectively compresses the spatial period of the splay–bend structure, reducing the grating pitch. The observed field-dependent variation in pitch agrees well with the pitch equation derived from the conical model (Chapter 4, Eq. 4.18), further validating the theoretical framework.

5.4.2 Room Temperature Formation

As mentioned above, the optimised LC mixture comprising 81 wt.% MLC-6882, 9 wt.% BL006, and 10 wt.% CB7CB is used to form the LC diffraction grating at room temperature. This mixture composition was filled into a 5 μm glass cell (INSTEC) by capillary action in the isotropic phase.

For our experimental investigation, the diffraction grating exists only within a notably narrow frequency range, up to 1.5 Hz, when an AC field is applied, due to the relatively large viscosity of the LC at room temperature. Furthermore, a

high-frequency AC field was found to facilitate the onset of electrohydrodynamic instabilities, which will be discussed in Section 5.7, which arise predominantly due to the periodic motion of the ions. Consequently, all subsequent experiments were conducted using a DC field, which is considered more beneficial in ensuring the stability of the system at room temperature. The flexoelectric nematic LC grating was found to operate over the temperature range of 20 °C to 28 °C. When the temperature exceeds 28 °C, the flexoelectric effect is no longer observable. This may be attributed to a reduction in the flexoelectric coefficient.

Figure 5.5 presents observations of LC diffraction gratings on a cross-polarised optical microscope at a temperature of 23 °C. The microscope stage was rotated to align the rubbing direction at an angle 45° relative to the polariser and analyser. Below the threshold voltage, no grating was observed. The threshold voltage required to observe the formation of a grating throughout the electrode region was found to be 15.5 V, which is close to the value of $V_{(\text{th_flexo})}$ obtained from Eq. 4.19. As illustrated in Figure 5.5(a), exceeding the threshold voltage initiates a transformation into a striped appearance, whereby the pitch of the LC grating narrows with increasing voltage, leading to a variation in the colour of the stripe. This colour change arises from variations in the surface alignment tilt and the orientation of the LC director under different applied voltage amplitudes. Figure 5.5(a)(iv) shows the dislocations which emerge as the system transitions to a higher voltage regime. Meanwhile, as the temperature increases, the threshold voltage required to trigger the flexoelectric effect $V_{(\text{th_flexo})}$ decreases. A possible explanation is that higher temperatures lead to a change in the flexoelectric coefficients of the LC mixture. However, this hypothesis requires further validation.

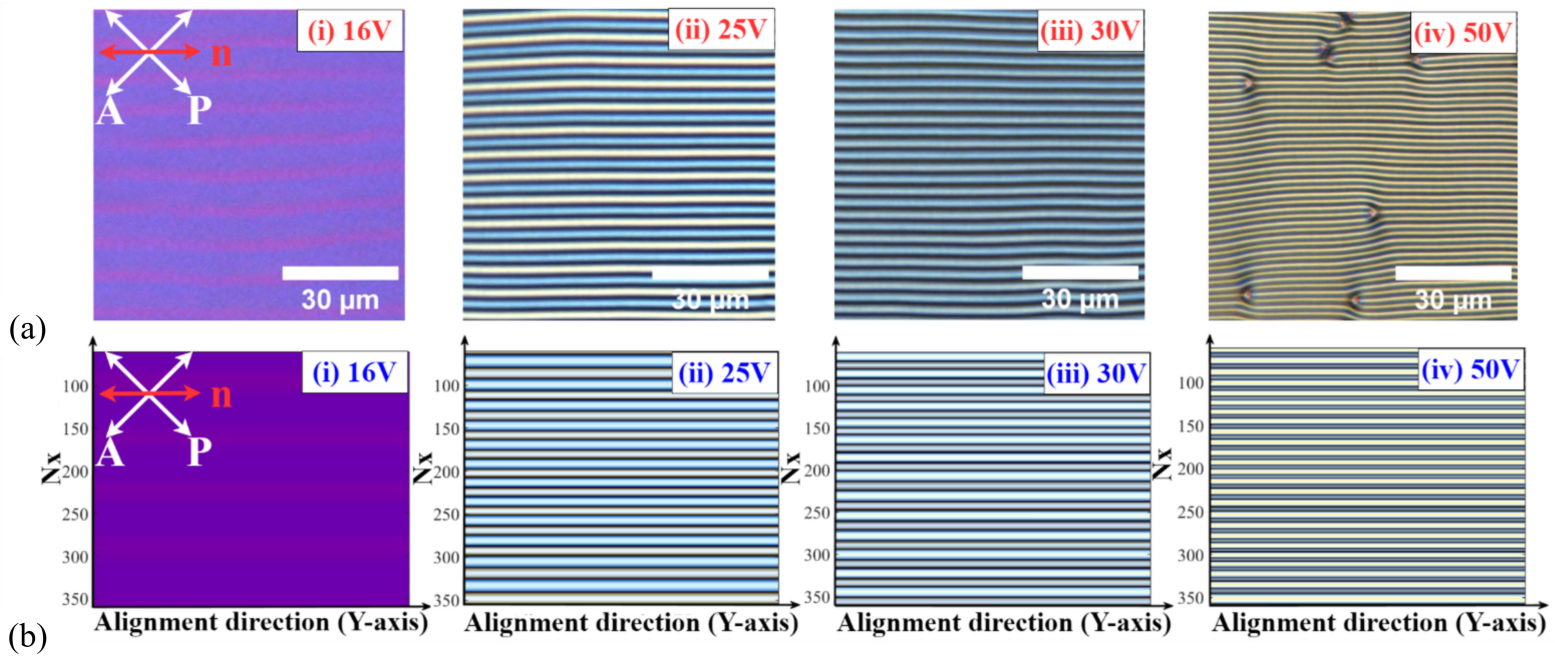


Figure 5.5: Comparative analysis of polarised optical microscope images for different applied DC voltages: (i) 16 V, (ii) 25 V, (iii) 30 V, and (iv) 50 V: experimental data (a) at a temperature of 23 °C and the corresponding simulations (b) for the parameters $K = 13\,\text{pN}$, $e^* = 5.5$ pC/m, $\Delta\varepsilon = 0.01$, $d = 5\,\mu\text{m}$, $n_e = 1.594$, $n_o = 1.487$, $N_x = 400$, and $N_z = 40$. N_x and N_z are employed in the numerical simulation to represent the number of grid points along the x-axis and the number of grid points across the thickness of the LC device, respectively. The white double-headed arrows represent the polariser (P) and analyser (A), while the red arrow represents the alignment direction (**n**) of the LC director. The experiments were carried out using an LC mixture composed of 81 wt.% MLC-6882, 9 wt.% BL006, and 10 wt.% CB7CB with an LC layer thickness of 5 µm. Images were taken at a temperature of 23 °C. Reproduced from Ref. [18] with permission from Elsevier.

5.5 Diffraction Pattern

In this thesis, we investigate the far-field diffraction characteristics using the optimised mixture at room temperature.

The incident polarisation angle, denoted α, defines the orientation of the polarisation with respect to the rubbing direction (y-axis) of the LC glass cell. **Figure 5.6** presents the results of experiments for the far-field diffraction patterns of light in our flexoelectric nematic LC gratings when $\alpha = 30°$. The results from the experiments show that the spacing between neighbouring diffraction orders increases as the voltage is increased, resulting from a decrease in the pitch as the voltage is increased. In addition, it is evident that when the applied voltage is close to the threshold value ($V_{(\text{th_flexo})}$, approximately 16 V in this case), the intensity of light in the 0^{th} order is high, indicating weak diffraction. As the voltage increases from 18 V to 24 V, there is a noticeable decrease in the 0^{th} order intensity, signifying a rise in diffraction. Beyond 24 V, the 0th order intensity starts to increase, implying a reduction in diffraction. The apparent change in colour of the 0^{th} order at low and high voltages is attributed to saturation of the CCD detector.

The replacement of the screen with a photodiode allows the measurement of the normalised light intensities to be obtained. In this case, we focus specifically on the zero-order diffraction peak. The data presented in **Figure 5.7** include results from simulations and experiments of the zero-order normalised light intensity as a function of the applied voltage for varying orientations of the incident linear polarisation angle (α) ranging from 0° to 90°. It is observed that there is a critical turning point observable in each curve, after which the zero-order normalised light intensity either begins to increase sharply or approaches zero. Before the turning point, there is a decrease in the zero-order normalised light intensity in each curve when the applied voltage exceeds the threshold ($V_{(\text{th_flexo})}$). The

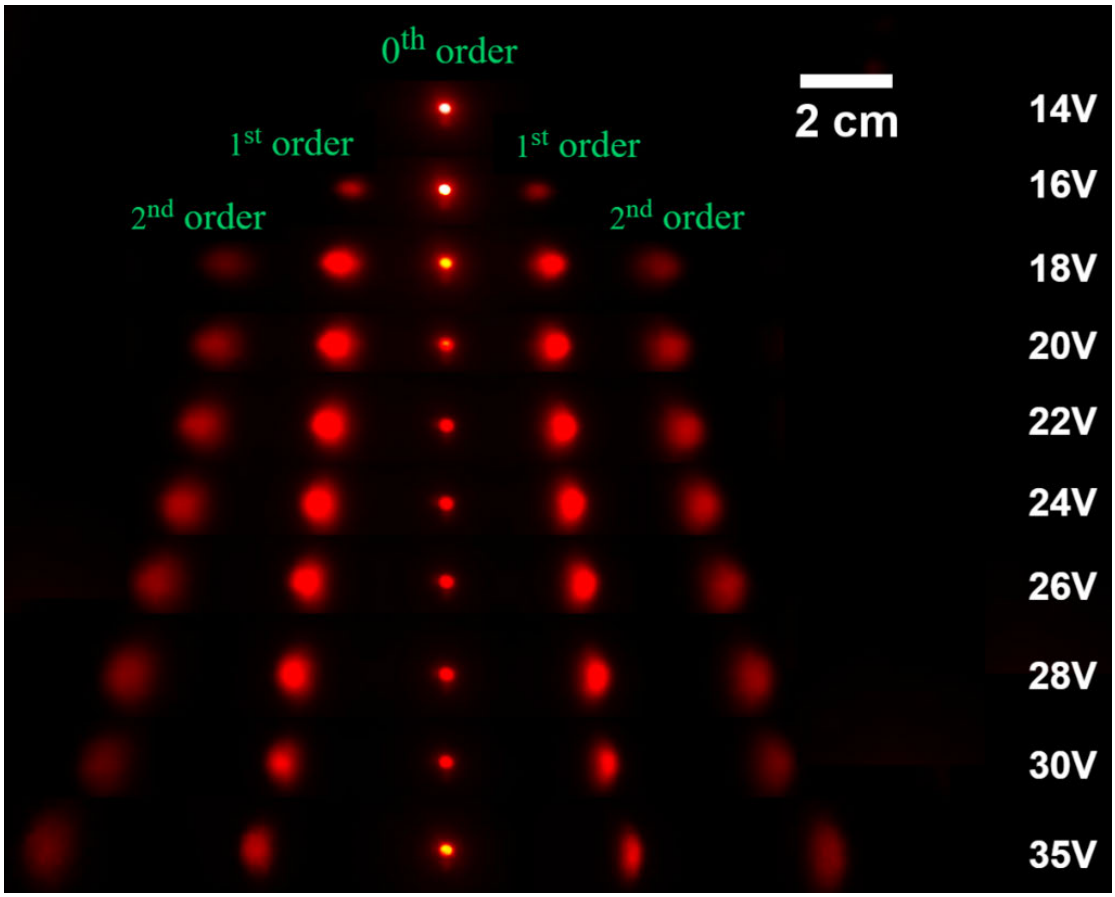


Figure 5.6: Far-field diffraction patterns for the flexoelectric nematic LC diffraction grating when illuminated with light from a laser diode and subjected to various applied voltages with the incident linear polarisation angle $\alpha = 30°$. The LC device operates under the same conditions as described in Figure 5.5. Reproduced from Ref. [18] with permission from Elsevier.

reduction in light intensity at the 0th order is caused by flexoelectric coupling, which leads to a tilt in both the x-y and the x-z planes, and a periodic splay–bend modulation develops. As a result, part of the incident light is redistributed from the 0^{th} diffraction order into higher diffraction orders, leading to a measurable reduction in the 0^{th} order intensity.

The results show that the zero-order normalised light intensity approached zero at high voltages for an incident polarisation angle of $\alpha = 90°$, indicating that the light is diffracted into other orders, decreasing the intensity of the 0^{th} order beam.

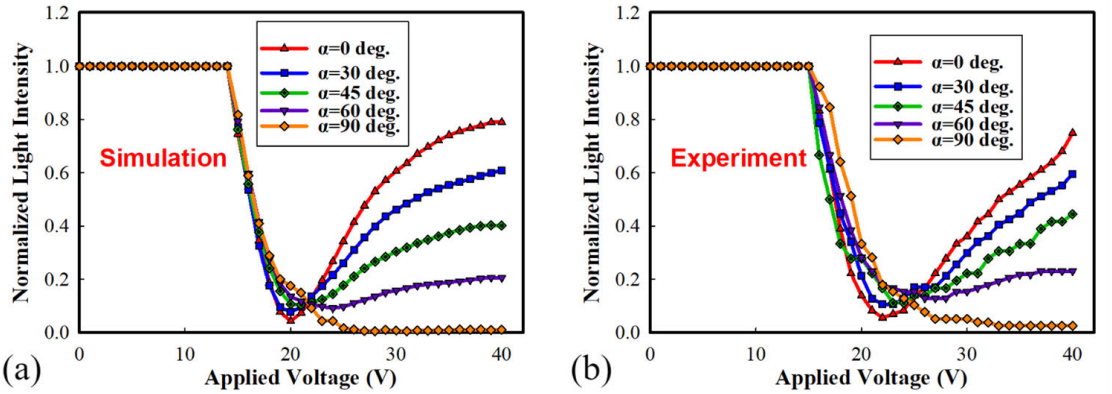


Figure 5.7: The zero-order normalised light intensity as a function of the voltage applied to the LC gratings. Results are presented for different orientations of the incident linear polarisation. (a) Simulation and (b) experimental results under the same conditions as described in Figure 5.5. Reproduced from Ref. [18] with permission from Elsevier.

Excluding the $\alpha = 90°$ case, the zero-order normalised light intensity increases with applied voltage after the turning point. Larger polarisation angles correlate with smaller increases in the zero-order normalised light intensity when the applied voltage is increased, which can be attributed to the behaviour of the LC director at high voltages as a result of flexoelectric coupling. As demonstrated in Chapter 4, at very high voltages, the LC director tends to orient predominantly within the x-z plane, exhibiting a purely splay-bend alignment along the x-axis. This reorientation modifies the effective refractive index experienced by the incident beam, thereby redistributing the optical power between the diffraction orders.

When the polarisation angle is set to 0°, aligning parallel to the y-axis (the rubbing direction of the LC glass cell), the incident polarised light only experiences the ordinary refractive index if the director is in the x-z plane. Under these conditions, at very high voltages, the light does not undergo significant diffraction, leading to a decrease in the intensity of light in the higher diffraction orders. Consequently, the intensity observed in the zero-order spot increases. In contrast, at a polarisation angle of 90°, where the polarisation direction is perpendicular

to the y-axis, the polarised light interacts with the pure splay-bend structure aligned within the x-z plane. This interaction results in a periodic variation of the refractive index along the x-axis, effectively forming a phase grating. Such a configuration facilitates maximal diffraction of light, thereby reducing the light intensity observed in the zero-order light. These results reinforce the simulated director behaviour shown in Figure 4.5.

Dielectric coupling may also contribute to the differences between the simulated and measured zero-order intensities at high voltages. Although the LC mixture was selected to have a small dielectric anisotropy, the dielectric contribution increases with the square of the electric field. It may therefore influence the director profile and the resulting optical response more strongly at higher voltages.

Meanwhile, the diffraction efficiency, defined as the ratio of the first- (or second-) order diffracted light intensity to the incident light intensity, was also investigated. As the applied DC voltage increased from 16 V to 35 V, the first-order diffraction efficiency decreased from approximately 60% to 40%, while the second-order diffraction efficiency decreased from around 25% to 18%.

5.6 Comparison with Simulations

The grating measurements presented in Section 5.4 and the diffraction results in Section 5.5 will be compared with the simulation results obtained using the nonlinear model described in Chapter 4.

Figure 5.5(b) displays the results of simulations employing our unconstrained nonlinear model. As described in Section 4.4.2, these simulations employ the CIE 1931 colour space and Jones matrix formalism to model light propagation through the grating when placed between crossed polarisers on an optical microscope.

The agreement between the predicted and observed grating patterns confirms the accuracy of our model and the computational techniques used.

Figure 5.8 shows a comparative analysis of the pitch of our optimised mixture at different voltages obtained using three different methods, including the predicted values, obtained from Eq. 4.18, the results from the numerical simulations of the nonlinear model, and the experimental observations. The experimental grating period was determined from calibrated microscope images by measuring the distance across several complete stripe periods and dividing by the number of periods. Measurements were made at different positions for each applied voltage. Figure 5.8 reports the resulting periods with a measurement uncertainty of $\pm$ 0.5 µm.

In both the pitch simulations and the analytical equations, the dielectric anisotropy is either set to a negligibly small value or omitted entirely. Consequently, the contribution of dielectric coupling is negligible in both cases. In the experimental setting, however, a non-zero dielectric anisotropy is present, which introduces a discrepancy between the simulated and measured values. As shown in Figure 5.8, both the experimental and simulated periods decrease with increasing voltage. Their differences range from 0.1 to 0.4 µm and lie within the experimental measurement uncertainty of $\pm$ 0.5 µm at all applied voltages.

A comparison of Figure 4.6(e) and Figure 5.6 shows that both simulations and experiments exhibit a consistent redistribution of optical power among the diffraction orders, as well as an increasing separation between diffraction spots with increasing applied electric field. Additionally, **Table 5.1** compares the separations of the diffraction orders in the far-field patterns for both experiments and simulations over the voltage range of 16–35 V. For both the 0^{th}–1^{st} and 0^{th}–2^{nd} order separations, the results closely match those shown in Figure 4.6(a)–(d). The strong agreement between the experimental measurements and the simulated

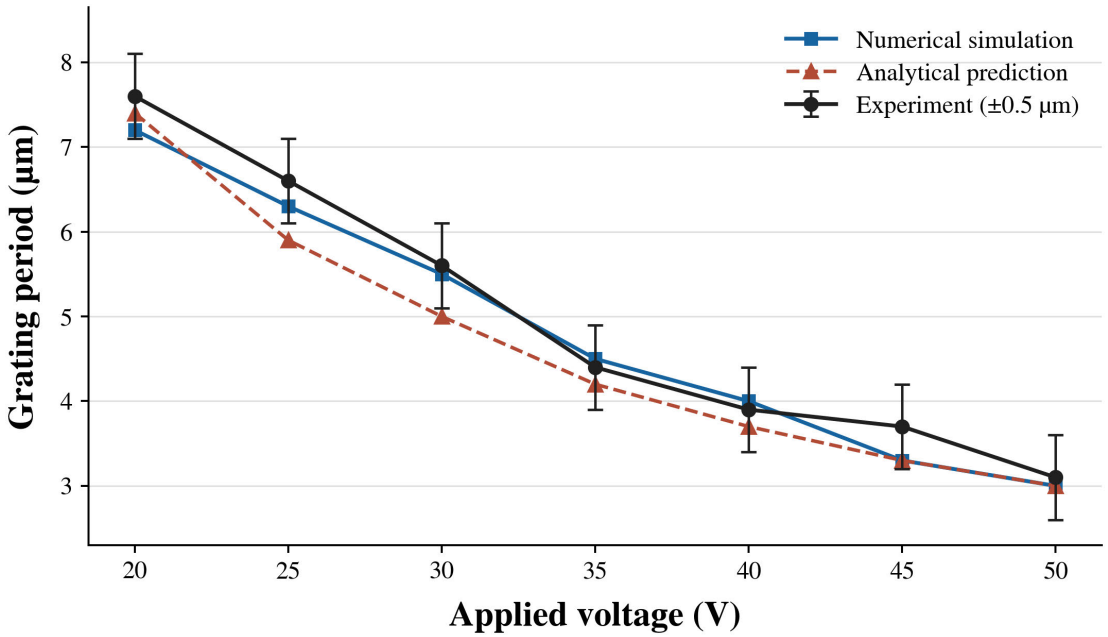


Figure 5.8: Experimental, simulated and analytical grating periods as functions of applied voltage for a 5 µm thick LC cell. The error bars represent the experimental measurement uncertainty of ± 0.5 µm. The numerical simulation used $K = 13\,\text{pN}$, $e_3 - e_1 = 5.5\,\text{pC/m}$ and $\Delta\varepsilon = 0.01$. The analytical values were calculated using Eq. (4.18).

Table 5.1: Comparison of the separation of the different diffraction orders obtained from both experiments and simulations for five different applied voltages. The incident linear polarisation angle is $\alpha = 30°$.

Applied Voltage (V)	**0th–1st order separation (cm)**		**0th–2nd order separation (cm)**	
	Experiment	**Simulation**	**Experiment**	**Simulation**
16	2.0	2.1	4.2	4.2
20	2.4	2.7	4.8	5.5
25	2.8	3.0	5.7	6.4
30	3.5	3.9	7.2	8.0
35	4.1	4.5	8.4	9.3

values further confirms the validity of the nonlinear model. It also provides an important practical advantage for future device optimisation. In particular, the consistency across all three approaches indicates that the grating behaviour can be reliably predicted prior to fabrication, enabling a predictive design strategy in which numerical simulations can be used to pre-select suitable material parameters and operating voltage ranges to achieve targeted pitch values or diffraction separations. Consequently, future experimental work can be guided by simulation-based parameter optimisation, significantly reducing trial-and-error efforts and improving overall development efficiency. Such a simulation-assisted design framework is especially valuable for engineering flexoelectric nematic LC gratings tailored to specific beam-steering or holographic projection applications.

5.7 Limitations

This flexoelectric grating, based on the optimised LC mixture, also exhibits limitations, including imperfect uniformity due to electrohydrodynamic instability and dislocations and a short operational lifetime caused by crystal formation.

5.7.1 Imperfect Uniformity

The instability of EHD will occur when we apply inappropriate AC fields or at high temperatures due to ionic motion [83, 84]. **Figure 5.9** shows that the device will exhibit EHD instability when $V_{\text{applied}} > V_{\text{th_EHD}}$.

The alignment of the EHD instability is usually perpendicular to the rubbing direction due to the periodic motion of the ions [84]. **Table 5.2** shows that the threshold that causes the EHD instability is proportional to the frequency, while the threshold voltage $V_{(\text{th_flexo})}$ that causes the stripe pattern remains consistent

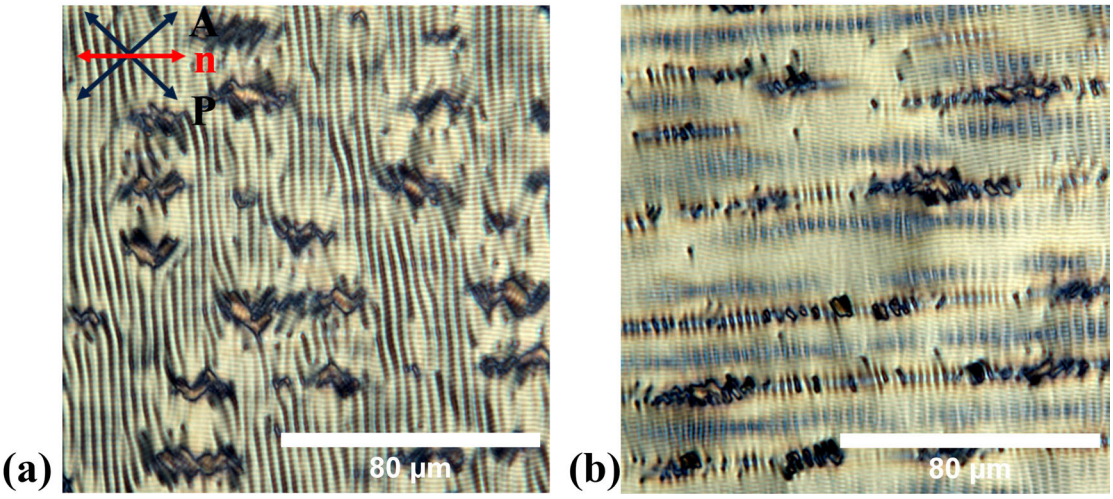


Figure 5.9: EHD instability when the $V_{\text{applied}} > V_{\text{th EHD}}$. (a) 10 Hz, ±8 V, AC; (b) 20 Hz, ±8 V, AC.

across varying frequencies. This aligns with the findings presented in Blinov's publication [85]. This shows that lower frequencies impose a limit on the stable electric field range, beyond which EHD instability occurs, disrupting the grating structure and degrading the diffraction performance.

Table 5.2: Threshold voltages for flexoelectric and EHD onset under different AC frequencies.

Threshold Type	**Frequency Group**		
	5 Hz	**10 Hz**	**20 Hz**
Start to see the flexoelectric domain $V_{(\text{th,flexo})}$	±3.75 V	±4 V	±4 V
Start to see the EHD instability $V_{(\text{th,EHD})}$	±4.25 V	±5.25 V	±6.25 V

In addition, our device may exhibit dislocations in some areas that negatively impact its overall performance. These dislocations are caused by three primary mechanisms. The first mechanism that causes dislocations occurs at the onset of AC field application, as shown in **Figure 5.10**(a). This is mainly because the spatial periodicity of the grating undergoes slight transient shifts during each

AC cycle, which can disrupt the long-range orientational order. However, the dislocations will diminish progressively over time. The second mechanism relates to the cell we are utilising, the INSTEC cell, which contains many beads that maintain cell thickness. These beads influence the alignment of LC molecules, causing dislocations (shown in Figure 5.10(b)). The third mechanism occurs during both the AC and the DC scenarios. When a voltage level changes, maintaining a regular pattern requires significant energy and molecular reorientations, causing stress within our system (shown in Figure 5.10(c)). To respond to this high-stress environment, the LC generates dislocations, thereby introducing an "extra" optical domain (shown in Figure 5.10). This allows the system to better adapt to new levels of electric field [86].

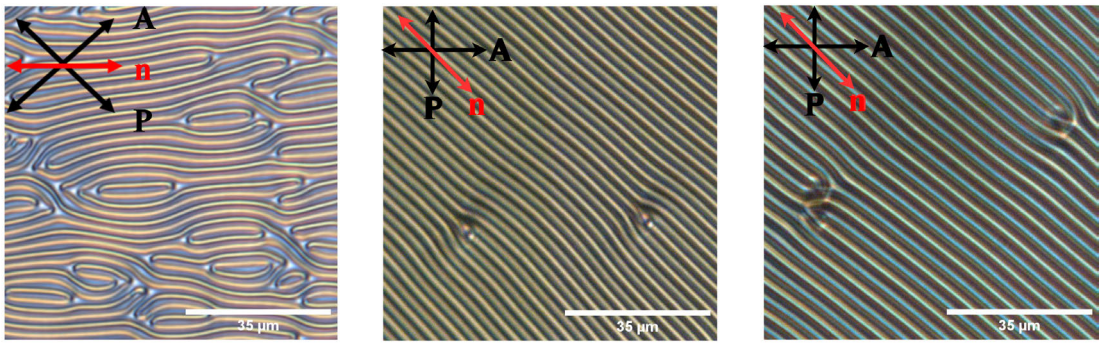


Figure 5.10: Dislocations arising from various mechanisms: (a) non-uniform alignment induced by an AC field at 20 Hz, ±3.75 V, 114 °C, using CB7CB grating. (b) Beads-caused dislocation in an MLC-6882Mix-based grating at 50 V DC and 25 °C. (c) Stress-generated dislocation in an MLC-6882Mix-based grating at 30 V DC and 25 °C.

Reducing the appearance of dislocation to improve the performance of our device would be a key part of our future work. To achieve this, it will be necessary to carefully optimise parameters such as the AC field frequency and the switching speed between different applied voltage levels. In addition, the investigation of various cell types with varying thicknesses and the testing of cells with fewer beads

may help reduce the occurrence of dislocations.

5.7.2 Crystal Formation

Although an LC diffraction grating was achieved at room temperature by incorporating BL006 and MLC-6882 into CB7CB, it was discovered that crystal formation occurs over time when the device is left at room temperature. After a few days, this crystal growth limits the device's performance, as shown in **Figure 5.11**. Efforts to remove crystals by heating diminish the flexoelectric effect upon cooling to room temperature. This issue can be ascribed to the mixture's non-eutectic nature. CB7CB exists in a crystal or twist-bend nematic phase at temperatures below 105 °C. The mixture maintains a nematic phase at room temperature for a few days, but then CB7CB begins to leave the solution.

To address the challenge of crystal formation, two potential solutions are proposed. The first method involves a prolonged initial heating period during the mixture preparation stage. By placing the mixture in a thermal oven for approximately 24 hours at the required temperature, thorough mixing can be ensured, and the time that the mixture remains in the nematic phase at room temperature can be extended. However, it should be noted that this approach may only delay crystal formation, rather than prevent it entirely. Alternatively, the mixture could be stored in an oven preheated to 40 °C. When measurements are needed at room temperature, the mixture can be removed from the oven. This approach ensures that the mixture is not affected by crystallisation for a period of 24 hours and could help prevent crystal formation, thereby preserving the optimal performance of the LC cell. Future commercial professional mixture development would aim to avoid this issue by developing a more optimised mixture that is eutectic and, therefore, would remain a stable solution over an extended time period.

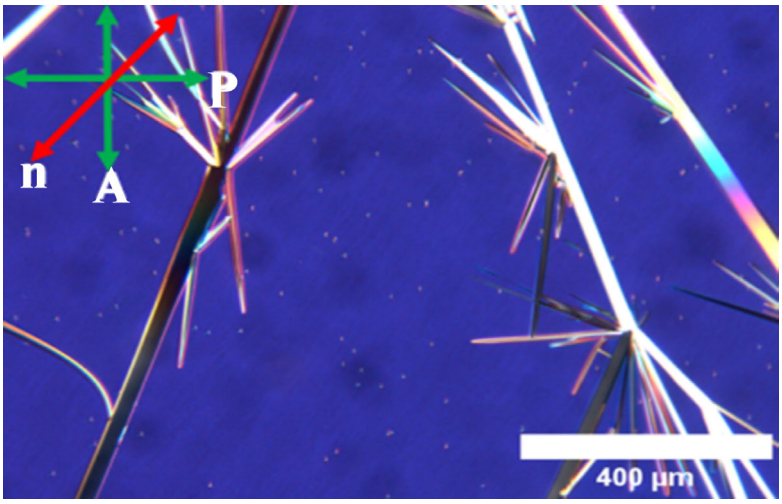


Figure 5.11: Crystal formation in MLC-6882Mix-Based mixture after several days of idle placement at room temperature.

5.8 Summary

Flexoelectric nematic LC diffraction gratings were successfully realised using both pure CB7CB and an optimised LC mixture. In the CB7CB-only device, operation required a low-frequency AC field, mainly due to the low viscosity and high ionic mobility of the material at elevated temperatures (> 110 °C). Under these conditions, DC driving was ineffective. Although diffraction gratings could be observed within a limited AC voltage range, the system was prone to electrohydrodynamic instabilities, and the need for high operating temperatures motivated further optimisation.

To overcome these limitations, we developed a room-temperature LC mixture capable of forming a stable flexoelectric diffraction grating. The optimised mixture, consisting of 9 wt.% BL006, 81 wt.% MLC-6882 and 10 wt.% CB7CB, exhibits low dielectric anisotropy and successfully produces a flexoelectric grating at 25 °C in a DC voltage range of 16–50 V. The pitch of the resulting grating ranges from approximately 3 µm to 8 µm, depending on the applied voltage.

Comparing the results of this chapter with the predictions in Chapter 4, we find

clear consistency. Increasing voltage progressively reorients the director from its initial rubbing-defined configuration towards a state featuring both in-plane (x–y) and out-of-plane (x–z) tilt. At very high voltages, a predominant splay-bend is observed in the x–z plane, with a negligible director component along the rubbing direction. The 0^{th} order light intensity confirms our predictions about the director profile, and there is a strong similarity between our modelling and experimental results of the pitch of the grating with applied voltage and the light intensity variation, further supporting the reliability of our model.

Finally, we discuss the limitations of the optimised flexoelectric nematic LC grating, particularly issues of imperfect uniformity and crystallisation-induced short lifetime. Potential strategies for mitigating these challenges were also discussed.

6

Chiral Nematic Liquid Crystal Diffraction Gratings

6.1 Introduction

Chiral nematic LCs, formed by combining nematic LCs with a chiral dopant, offer significant promise in beam steering technologies due to their intrinsic macroscopic helical structure [80, 81]. There are many different configurations that can be considered when using chiral nematic LCs. For example, these materials can be capillary filled into glass cells with homogeneous (planar) [87, 88], homeotropic [89, 90], or hybrid alignment layers [91] with a range of different values for the cell gap (d) and pitch of the helical structure (p). Depending on the combination of these parameters, this can result in the appearance of different optical textures when viewed in a polarising optical microscope, such as Grandjean, fingerprint,

and uniform lying helix (ULH) textures, in which the helix axis lies parallel to the device substrates, as discussed in Section 2.9 [87–89, 92]. Among these, the ULH state is particularly desirable for diffraction gratings as a result of its uniform periodic structure.

To achieve the optimal helical structure in the formation of a ULH state, two key conditions must be met. First, selecting an appropriate d/p ratio is essential for maintaining a uniform alignment of the helix, as a high d/p ratio can lead to less uniform alignment and the appearance of a focal-conic light-scattering texture [88]. Second, the pitch p, defined as the helical periodicity of the chiral nematic LC, must be smaller than the so-called threshold pitch (p_{th}) to ensure that the chiral torque, which maintains the helical structure, is sufficiently strong to induce it. The threshold pitch is given by

$$p_{\text{th}} = 2d\frac{K_{22}}{K_{33}}, \tag{6.1}$$

where K_{22} and K_{33} are the twist and bend elastic constants, respectively [89]. This relationship was obtained using the Noether theorem and a free energy analysis, resulting in equations that determine the critical pitch at which stable helical structures form [93].

The alignment configuration of the ULH is essential for inducing periodic changes in the effective refractive index (n_{eff}) along the helical structure, thereby allowing the formation of a diffraction grating [89, 94–96]. Efforts to achieve the ULH structure in glass cells with homogeneous alignment layers typically involve cooling the chiral nematic LC from the isotropic phase while simultaneously applying an electric field. However, the resulting ULH structure is often unstable and rapidly returns to the Grandjean state once the electric field is removed [92]. Research has explored the use of glass cells with homeotropic alignment

layers, treated with polyimide, to enhance the stability of the ULH structure [89, 96–98]. These homeotropic cells have been shown to be more appropriate than homogeneous (planar-aligned) cells for use in electrically controlled diffraction gratings because they offer a wider range of control [92]. In addition, ULH alignment in homeotropic cells demonstrates enhanced stability, requiring more time to return to the Grandjean state compared to comparable homogeneous cells [89, 90].

Depending on the magnitude of the flexoelectric coefficients of the chiral nematic LC mixture, the flexoelectro-optic effect observed with the application of an electric field applied perpendicular to the helix axis results in a rotation of the optic axis while leaving the helix axis unchanged, as illustrated in **Figure 6.1**(a). The orientation of the stripes on the chiral nematic LC grating has garnered significant interest among researchers [80, 87, 88, 90–92, 99], as it determines the orientation of the far-field diffraction pattern. Rotating the orientation of the chiral nematic LC grating requires a rotation of the orientation of the helix axis of the chiral nematic LC. An example of this rotation is illustrated in Figure 6.1(b). In this case, the helix axis and the optic axis share the same orientation, both being perpendicular to the orientation of the stripes of the grating.

The direction of the stripes on a chiral nematic LC grating can be adjusted by controlling the d/p ratio [88, 92, 99]. Figure 6.1(c) shows an example of a conventional chiral nematic LC grating with homeotropic alignment. Nevertheless, this approach offers little flexibility in modifying the orientation since achieving exact control of both the cell gap and pitch throughout the fabrication procedure can be challenging. Alternatively, researchers have explored electrical methods to control the stripe direction [80, 87, 91, 92]. Although altering the applied voltage can cause alterations in the stripe direction, these alterations are often insignificant and limited to a small region. Additionally, optical control methods have been

investigated, involving the incorporation of ultraviolet (UV)-sensitive materials into the chiral nematic LC. Through the photo-isomerisation effect, the helical twisting power (HTP) can be modulated by altering the UV exposure time or intensity [87, 90]. However, the potential for the photo-isomerisation process to be reversed may be restricted, posing difficulties in restoring the chiral nematic LC to its original state. Another approach involves incorporating a thermoresponsive chiral molecular switch into a chiral nematic LC host, where variations in temperature, in conjunction with a suitable electric field, can alter the stripe direction [100]. Nevertheless, temperature-induced changes typically occur more slowly than those induced by light or electric fields, resulting in slower response times.

It is common for chiral nematic LC diffraction gratings to exhibit slightly wavy patterns rather than perfectly straight lines. This waviness arises from the Helfrich-Hurault instability in chiral nematic LCs, a phenomenon in which variations in pitch induce undulations in the orientation of the helical axis [101]. To address such structural irregularities and achieve high-quality alignment, recent studies have demonstrated that photoalignment techniques significantly enhance the uniformity of chiral nematic LC alignment, allowing the fabrication of large-area, defect-free superstructures and dynamic textures [102, 103]. Although a detailed investigation of this instability and its mitigation strategies will not be discussed in this chapter, future work may address this issue by optimising material formulations to minimise the pitch variations under applied electric fields.

In this chapter, we present an electrically rotateable chiral nematic LC diffraction grating that would be of potential interest for optical beam steering applications. By employing a tailored waveform and adjusting the time duration of each segment in the waveform, we can obtain an in-plane reorientation of the chiral nematic LC helical structure with a high degree of uniformity, resulting in control of the

orientation of the far-field diffraction pattern. The work presented in this chapter has been published in Advanced Optical Materials, 13(21), 2500794 (2025) [19].

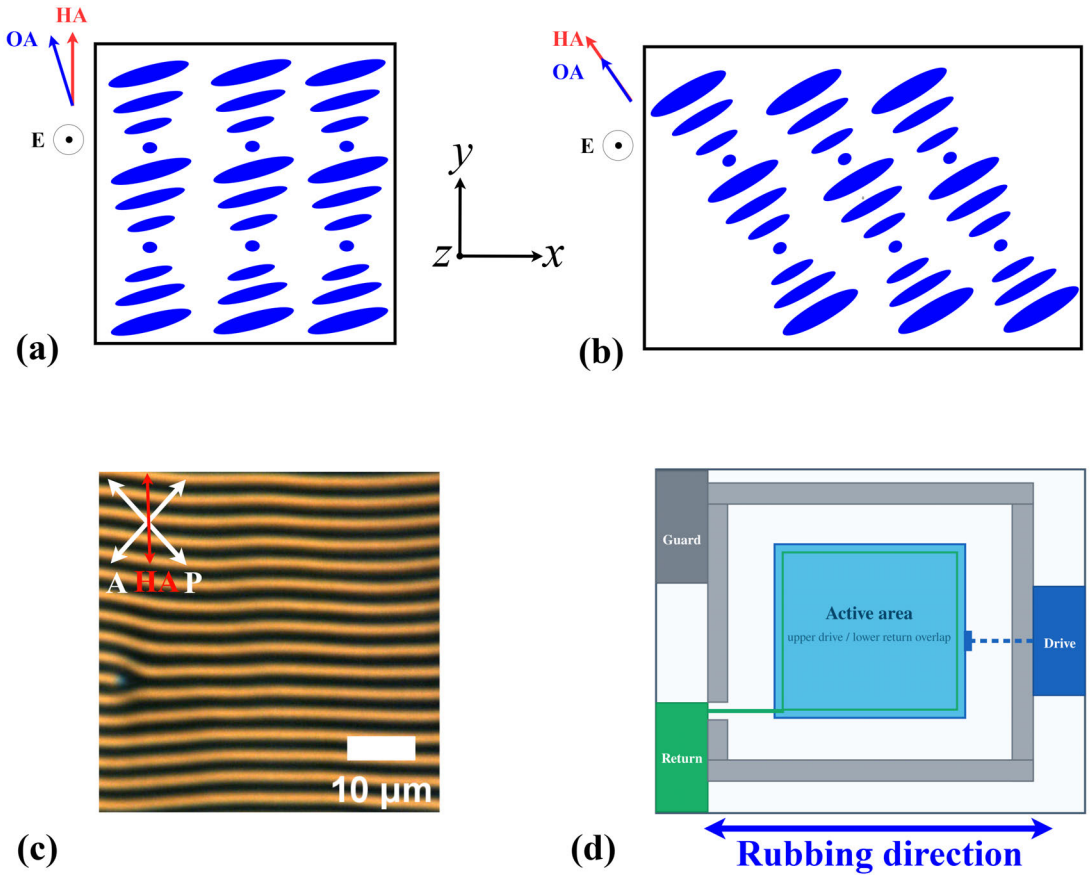


Figure 6.1: (a) Illustration of the optic axis (OA) rotation in a chiral nematic LC under an electric field applied perpendicular to the helix axis (HA). (b) An example of a rotation of the helix axis (HA)/optic axis (OA) in a chiral nematic LC. (c) A conventional cross-polarised microscope image of a chiral nematic LC diffraction grating with homeotropic alignment. The white double-headed arrows denote the orientations of the polariser (P) and analyser (A), while the red double-headed arrows indicate the orientation of the helix axis (HA). (d) Top-view schematic of the Instec SG-type LC cell, showing the Drive, Return, and Guard contacts. The overlap of the upper Drive and lower Return electrodes defines the active area. The separate Guard electrode surrounds this area, while the arrow indicates the rubbing direction. Reproduced from Ref. [19] under the terms of the CC BY licence.

6.2 Chiral Nematic LC Director Profile Simulations

For chiral nematic LCs, two distinct configurations can be observed depending on the orientation of the helical axis. In the absence of an electric field, the helix axis commonly orients perpendicular to the substrate surfaces, resulting in a stable configuration known as the Grandjean state. Upon the application of an electric field while at the same time cooling from the isotropic phase, combined with a material with positive dielectric anisotropy ($\Delta\varepsilon$), a chiral nematic LC can transition to the ULH alignment, characterised by a helical axis parallel to the substrate surfaces [34].

Surface treatment significantly influences these two configurations. In our work, we have used a computational model based on finite difference methods to simulate the director profile of the chiral nematic LC for both homeotropic and homogeneous alignment in a 2D x-z plane based on the theoretical framework previously presented [104]. In this model, the total free-energy of the chiral nematic LC is expressed as

$$f = \frac{1}{2}\left\{K_{11}(\nabla\cdot\vec{n})^2 + K_{22}\left(\vec{n}\cdot(\nabla\times\vec{n}) - q\right)^2 + K_{33}(\vec{n}\times(\nabla\times\vec{n}))^2\right\} - \frac{1}{2}\Delta\varepsilon\varepsilon_0(\vec{n}\cdot\vec{E})^2 \tag{6.2}$$

where $\vec{n} = (n_x, n_y, n_z)$ represents the LC director, K_{11}, K_{22}, and K_{33} are the elastic constants of Frank splay, twist and bend, respectively (measured in [N]), and $q = \frac{2\pi}{p}$, where p represents the pitch of the helical.

For homogeneous alignment, the boundary conditions were set as $n_x = 1$, $n_y = n_z = 0$ while for homeotropic alignment, the conditions were set as $n_x = n_y = 0$, $n_z = 1$. The distortion between the surface alignment and the bulk

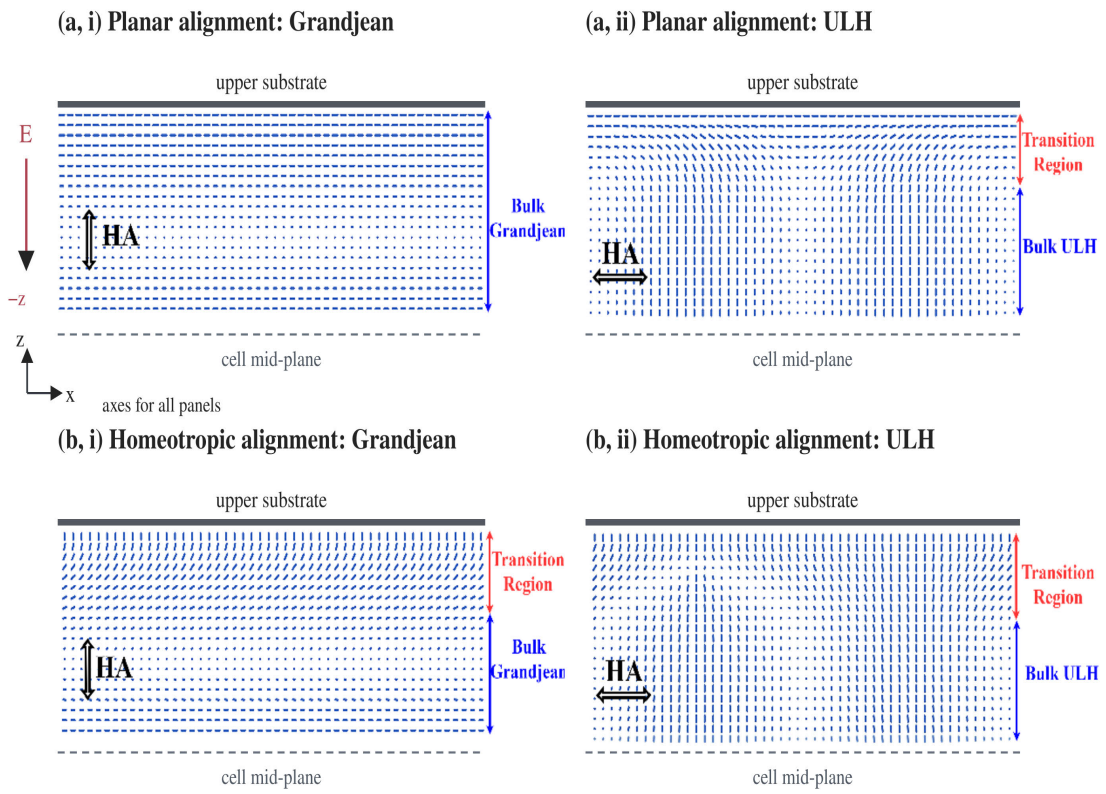


Figure 6.2: Two-dimensional simulated director profiles of the upper half of a chiral nematic LC cell in the x–z plane. (a) Planar and (b) homeotropic alignment, each shown in (i) the Grandjean state and (ii) the uniform lying helix state. The solid line above each profile indicates the upper substrate, while the dashed line below indicates the cell mid-plane. The electric field is normal to the substrates, with the arrow indicating a representative polarity along $-z$. Red double-headed arrows mark the transition regions, blue double-headed arrows mark the bulk Grandjean or ULH regions, and black double-headed arrows labelled HA indicate the helix-axis direction. Reproduced from Ref. [19] under the terms of the CC BY licence.

configuration was determined by minimising the total free-energy with appropriate relaxation parameters. **Figure 6.2** presents simulation results of the director profile of the Grandjean and ULH configurations in the x-z plane for both planar and homeotropic alignment layers.

Only the upper half of the cell is shown, from the upper substrate to the cell mid-plane. The director profile in the lower half is the mirror image of that shown here about the cell mid-plane, with a corresponding transition region

near the lower substrate.

As shown in Figure 6.2(a, i), the intrinsic director profile of chiral nematic LC in homogeneous (planar) glass cells demonstrates perfect compatibility with surface alignment in the Grandjean state, resulting in a smooth transition between surface and bulk regions. However, for the ULH state in homogeneous cells (planar), as illustrated in Figure 6.2(a, ii), it can be seen that there are significant structural distortions at the surface-bulk interface, consistent with the results reported in [104, 105]. Hence, the energy difference between the Grandjean state ($E_{\mathrm{g_pl}}$) and the ULH state ($E_{\mathrm{u_pl}}$) with homogeneous alignment ($\Delta E_{\mathrm{planar}} = E_{\mathrm{u,pl}} - E_{\mathrm{g_pl}}$) is substantial.

Figure 6.2(b,i) demonstrates that the Grandjean state in homeotropic cells creates distortions where the director conflicts with the orientation of the homeotropic substrate. Strong anchoring forces the director to gradually transition from perpendicular alignment near the surface to horizontal orientation in the bulk. In contrast, Figure 6.2(b, ii) illustrates that although the ULH state in homeotropic cells exhibits some distortion, it demonstrates better compatibility between the surface anchoring and the bulk helical structure compared to homogeneous cells, with less distortion. Consequently, the energy of the ULH state in homeotropic cells ($E_{\mathrm{u_ht}}$) is lower than that of planar cells ($E_{\mathrm{u_pl}}$). Therefore, the Grandjean state energy in homeotropic cells ($E_{\mathrm{g_ht}}$) exceeds that of homogeneous cells ($E_{\mathrm{g_pl}}$). The energy difference between Grandjean and ULH states in a homeotropic cell ($\Delta E_{\mathrm{homeotropic}}$) is consequently reduced compared to homogeneous cells, where $\Delta E_{\mathrm{homeotropic}} = E_{\mathrm{u_ht}} - E_{\mathrm{g_ht}} < \Delta E_{\mathrm{planar}}$. As a result, in the homeotropic glass cell, it is significantly more difficult for the chiral nematic LC grating to naturally revert to the Grandjean state when aligned in the ULH configuration, compared to that observed for a planar-aligned cell. This increases the stability of the device, enhancing its capability in terms of a non-mechanical rotation of the diffraction

grating, which will be discussed in detail later.

6.3 Materials and Methods

To fabricate chiral nematic LC diffraction gratings, the d/p ratio serves as a critical parameter. Experimental studies have shown that the optical transmittance of a chiral nematic liquid crystal cell increases with the d/p ratio [88]. Therefore, in our experiment, we adjusted the d/p ratio to $\approx$1.85, ensuring that the chiral nematic LC was capable of forming a diffraction grating. For this study, we used the E7 nematic LC mixture (Merck), which has been extensively characterised and is known to have a dielectric anisotropy of $\Delta\varepsilon = 13.8$. The host nematic LC was then doped with the chiral dopant R811 (Merck), which has an HTP of approximately $10\,\mu m^{-1}$ [106].

The resulting mixture consisted of 5 wt.% R811 and 95 wt.% E7 to obtain a chiral nematic LC with a pitch of 2 μm at 24 °C. The procedure follows the methodology described in Section 3.1. Incorporation of the LC dimer CB7CB (4',4"-(heptane-1,7-diyl) dibiphenyl-4-carbonitrile, sourced from Synthon) was essential to achieve a uniform rotatable grating at room temperature. CB7CB is known to be a good candidate for flexoelectric applications, exhibiting a significant flexoelectric coefficient of approximately -31 pC/m in its nematic phase [37]. The contribution of this dimer to the rotation of the diffraction grating will be elaborated in subsequent sections. Structurally, CB7CB consists of two cyanobiphenyl units linked by a seven-carbon spacer, forming a long molecular chain. Its extended molecular chain configuration contributes to enhanced viscosity. However, the concentration of CB7CB must be carefully controlled, as excessive amounts can induce crystallisation within the mixture at room temperature, potentially leading to phase separation due to the non-eutectic nature of the formulation. Although

neat CB7CB exhibits a twist-bend nematic (NTB) phase at room temperature, we limited its concentration to below 20 wt.% to suppress the formation of NTB phase, thereby ensuring optimal uniformity of the diffraction grating. To determine the optimal concentration of CB7CB, various mixtures with different percentages of CB7CB were tested, as detailed in **Table 6.1**. Each mixture was filled into the empty homeotropic cell via capillary action in the isotropic phase.

Table 6.1: Composition and clearing point (T_{iso}) of the mixtures considered in this study with varying concentrations of CB7CB.

Mixture ID	R811 (wt.%)	CB7CB (wt.%)	E7 (wt.%)	Clearing Temperature (°C)
Mixture 1	5	0	95	55.5
Mixture 2	5	5	90	57.5
Mixture 3	5	10	85	58.5
Mixture 4	5	15	80	59.0

The glass cells used in the experiment were sourced from Instec, and the inner surfaces of the glass substrates were coated with the homeotropic polyimide DL-6460T (Dalton). The cell gap was determined to be 3.7 μm from the interference fringes in the UV–Vis transmission spectrum of the empty cell, using the method described in Section 3.2. The Instec SG-type cell, shown in Figure 6.1(d), has three separate electrical contacts: Drive, Return, and Guard. Although all three contacts are accessible from the bottom-substrate side, the Drive contact connects to the upper electrode, and the Return contact connects to the lower electrode. The overlap of these electrodes defines the active area in which the applied voltage produces an electric field. The Guard electrode is electrically separate from the active electrodes and surrounds the active area. When connected to ground, it reduces edge-field effects and parasitic capacitance, improving the accuracy of electrical measurements compared to that of a standard two-electrode cell. The polyimide alignment layers of the homeotropic cell were rubbed in antiparallel

directions along the x-axis to achieve a 0° to 1° pretilt angle from the substrate normal. This weak pretilt breaks the in-plane symmetry and gives a weakly defined alignment direction in the LC device. Without sufficient rubbing, any switching to an ULH state would result in a random helix orientation due to the absence of a defined alignment direction. Consequently, an unrubbed cell would not achieve the desired switching and rotation of the diffraction grating.

A polarising optical microscope (BX51, Olympus) with crossed polarisers and a CCD camera (R6, QImaging) mounted on the phototube of the microscope was used to capture microphotographs of the chiral nematic LC diffraction gratings. To rotate the chiral nematic LC diffraction gratings, a specific voltage waveform, as shown in the following sections, was applied to each device using a function generator. To observe the diffraction pattern generated by the chiral nematic LC diffraction gratings, a PL202 laser diode (λ = 635 nm, Thorlabs) served as the coherent light source. The diffraction patterns were projected onto a white screen. For measurements of zero-order light intensity and 1st order and 2nd order diffraction efficiencies, the white screen was substituted with a photodiode (PDA36A-EC, Thorlabs), with a neutral-density (ND) filter added to prevent photodiode saturation during measurements. A linear polariser positioned before the LC device enabled systematic investigation of the relationship between the grating orientation and the incident light polarisation.

6.4 Experimental Results and Discussion

In this section, we demonstrate the formation of switchable and rotatable chiral nematic LC diffraction gratings.

6.4.1 A Switchable Grating

To investigate the switchable characteristics of the chiral nematic LC diffraction grating in a homeotropic cell, we employed Mixture 1 under the application of a 1 kHz symmetric square wave. As illustrated in **Figure 6.3**, the device exhibits different voltage-dependent states with a chiral nematic to homeotropic nematic transition threshold (V_{th}) of $2.9\,\mathrm{V_{rms}}$. Above this threshold voltage ($V_{\mathrm{a}} > V_{\mathrm{th}}$), the helical structure is unwound to form a homeotropic nematic alignment, where the director is orientated perpendicular to the plane of the substrate, effectively suppressing diffraction (the “off” state). Upon removal of the electric field, the chiral nematic LC grating begins a gradual transition from the homeotropic nematic state to the Grandjean state. During this transitional period, uniform pale-blue striations appear, indicating a transitional Grandjean state. These striations result from instabilities that generate periodic ripples within the bulk region. These ripples lead to the partial retention of a lying helix alignment in some areas, while other regions transition back to the Grandjean state. In this state, the device retains the capability to diffract light. When the applied voltage is in the range $1.7\,\mathrm{V_{rms}} < V_{\mathrm{b}} < 2.9\,\mathrm{V_{rms}}$, a stable ULH state is induced, resulting in the appearance of periodic stripes and visible diffraction patterns in the far-field. This corresponds to the "on" state. With the application and removal of the electric field, the device can switch reversibly between the "off" state with homeotropic alignment and suppressed diffraction, and the "on" state characterised by the ULH or transitional Grandjean state configuration accompanied by a diffraction pattern.

6.4.2 An Electrically Rotatable Grating

The initial test involved characterising the four mixtures (Mixtures 1–4) as discussed in the Materials and Methods section to measure the flexoelectro-optic tilt angles.

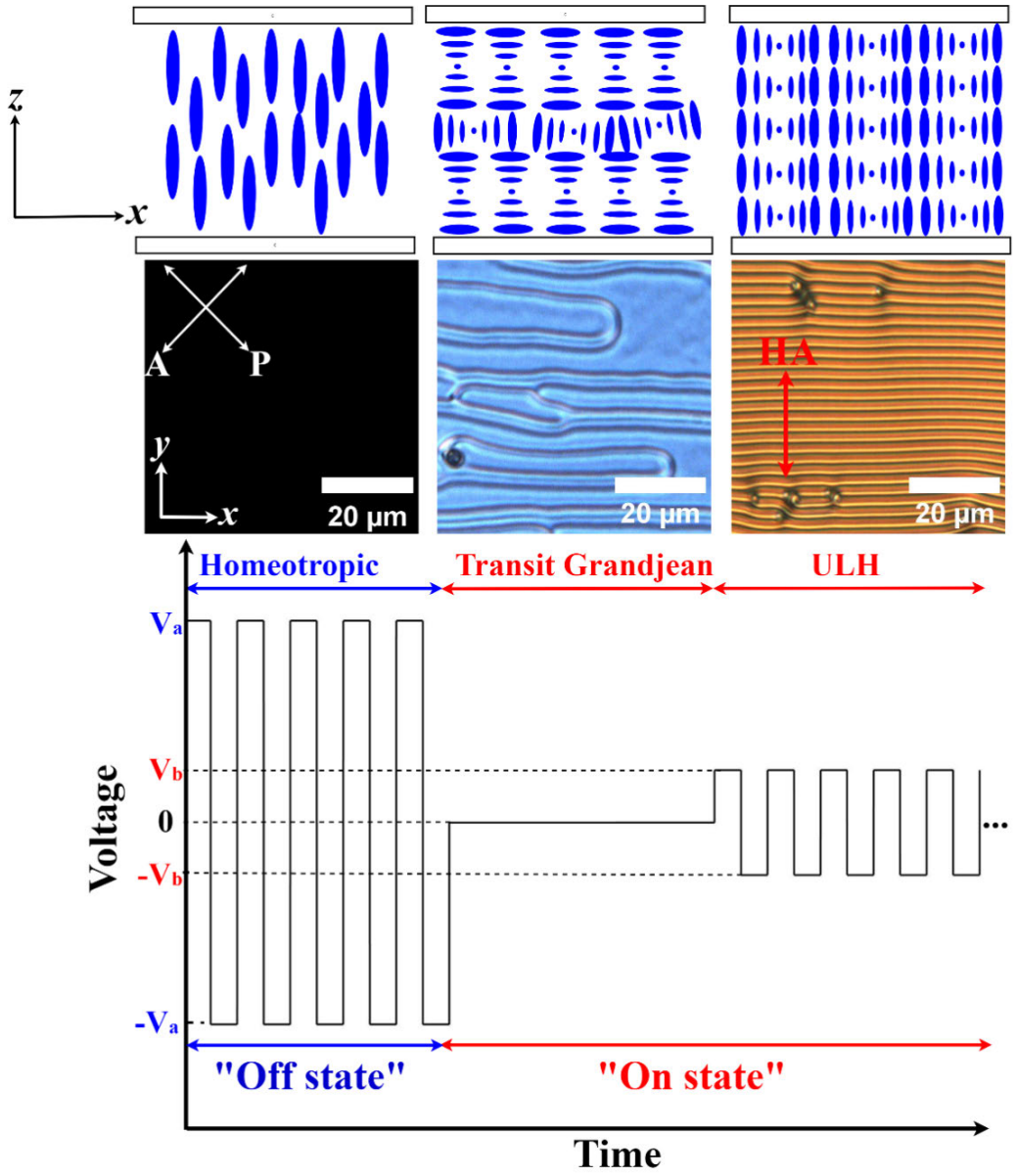


Figure 6.3: Voltage waveform sequence applied to the chiral nematic LC device illustrating the switchable states of the diffraction grating, showing transitions between the "homeotropic nematic," "transit Grandjean," and "ULH" alignments. The corresponding polarised optical microscope images are accompanied by schematic representations of the director profile in each state. The white double-headed arrows represent the orientations of the polariser (P) and analyser (A), while the red arrow (HA) indicates the helix axis of the ULH structure. Scale bars represent a length-scale of 20 µm. Experiments were conducted at a room temperature of 24 °C. Reproduced from Ref. [19] under the terms of the CC BY licence.

As illustrated in **Figure 6.4**(a), devices containing varying concentrations of CB7CB were subjected to an 80 Hz square wave with 2.6 V_{rms} to generate the ULH texture, while maintaining a fixed thickness-to-pitch ratio (d/p). The tilt angle was determined by analysing the optical transmission levels during the systematic rotation of the LC device on a rotation stage of the microscope, following the methodology described previously in Section 3.4. The experimental results reveal that the incorporation of CB7CB induces an asymmetric response in the tilt angle under an applied square wave voltage. Specifically, the tilt angle for the negative polarity electric field consistently exceeded that observed for the positive polarity electric field. Although the positive tilt angle remained constant at approximately 5° for all concentrations, the negative tilt angle increased from 5° to 11.5° as the CB7CB concentration increased from 5 wt.% to 15 wt.%. This indicates that the tilt angle becomes increasingly asymmetric with higher CB7CB concentrations.

It is important to note that increasing the CB7CB concentration simultaneously elevates the viscosity of the mixture, attributable to the long molecular structure of CB7CB. As a result, while higher CB7CB concentrations enhance the flexoelectro-optic effect, they also lead to slower response times. This slower response can introduce defects and cause non-uniform reorientation, ultimately degrading the quality of the diffraction grating. Therefore, precise control of the CB7CB concentration is crucial for optimising device performance, balancing enhanced asymmetric flexoelectro-optic effects with optimal viscosity to ensure high-quality diffraction gratings. Meanwhile, as shown in Figure 6.4(b) and Figure 6.4(c), when testing Mixture 2 under an 80 Hz square wave with varying voltage amplitudes, it is evident that higher voltage amplitudes result in larger tilt angles during both the positive and negative polarities of the applied electric field.

These results suggest that the asymmetric tilt angle switching induced by

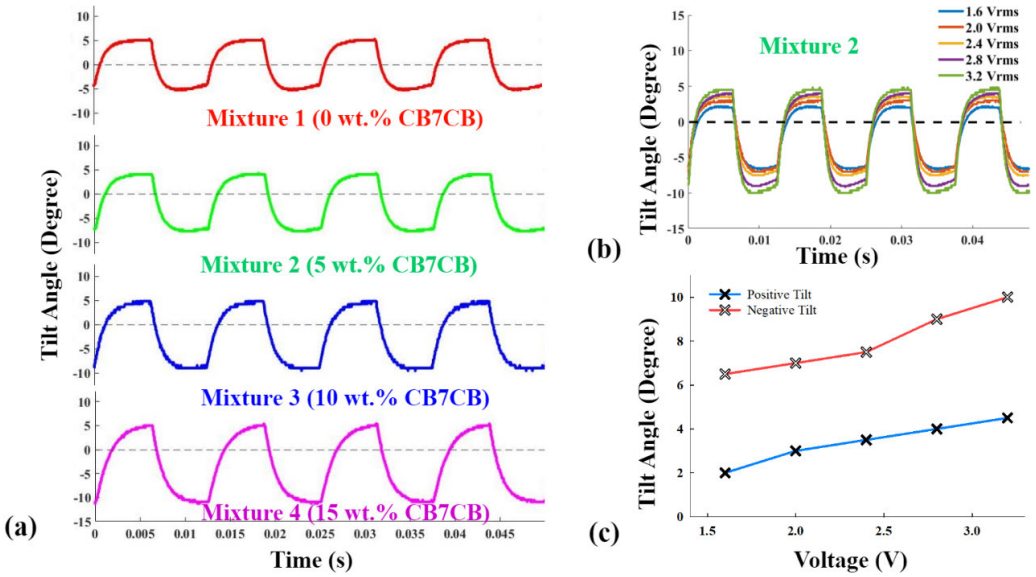


Figure 6.4: (a) Time-dependent flexoelectro-optic tilt angle responses of four different chiral nematic LC mixtures (discussed in the Materials and Methods section) under an identical square-wave voltage signal (±2.6 V, 80 Hz). (b) Dynamic tilt angle behaviour of Mixture 2 at various V_{rms} values ranging from 1.6 V to 3.2 V. (c) Voltage-dependent tilt angles for Mixture 2, showing asymmetric responses between positive and negative tilt directions with increasing voltage amplitude. All experiments were conducted at a room temperature of 24 °C. Reproduced from Ref. [19] under the terms of the CC BY licence.

CB7CB, combined with the asymmetry in tilt angle variations in the applied voltage over a specific and appropriate time period, can generate a non-zero time-averaged torque, potentially enabling the rotation of the helix axis.

To examine the rotational behaviour of chiral nematic LC diffraction gratings using varying concentrations of CB7CB, and based on previous experimental observations, a specialised waveform, as shown in **Figure 6.5**, was implemented to induce controlled rotation of the grating. The initial phase (Phase A) consists of a high-amplitude voltage oscillating between V_1 and $-V_1$ (with $V_1 > V_{\mathrm{th}}$), which is applied for a duration t_1, ensuring complete homeotropic alignment across all the mixtures discussed earlier, followed by a segment with a critical decrease in the staircase, during which the oscillation amplitude gradually decreases from

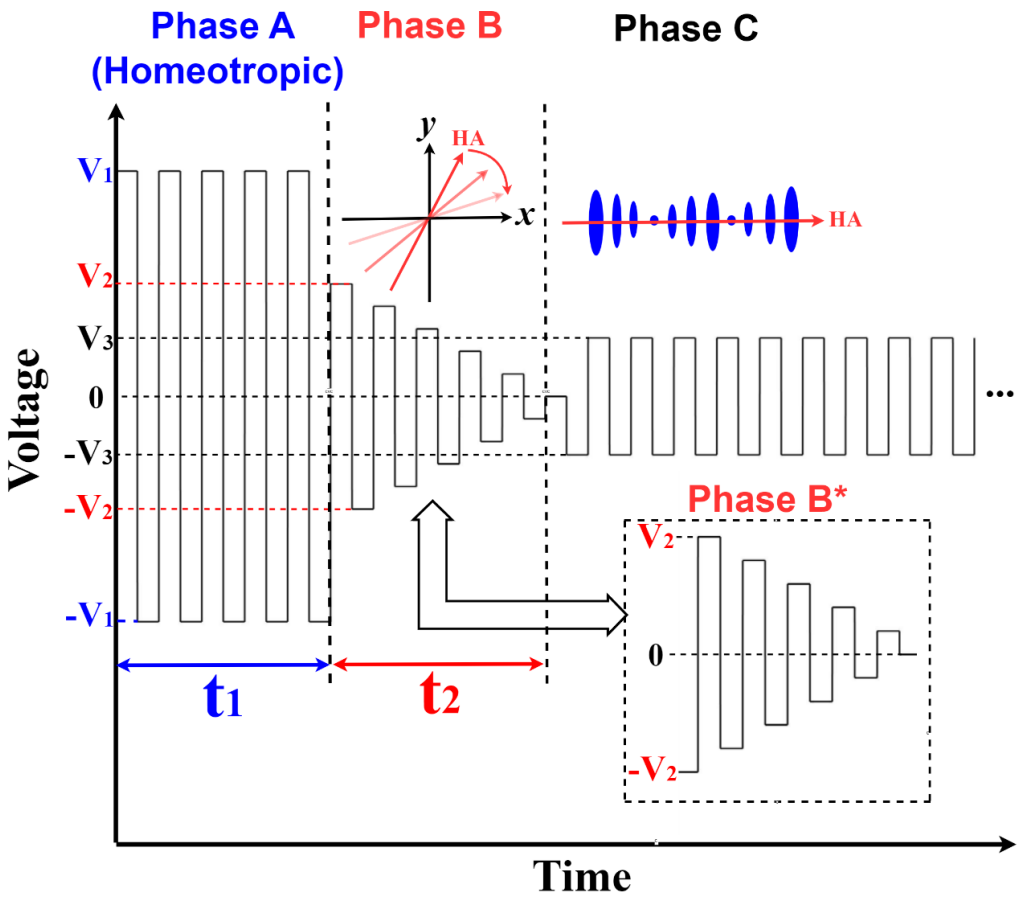


Figure 6.5: Applied voltage waveform sequence for controlling the rotational orientation of the chiral nematic LC diffraction grating. The sequence consists of three distinct phases. Phase A (homeotropic nematic alignment, duration t_1) with alternating $\pm V_1$ pulses; Phase B (HA reset, duration t_2), where voltage pulses gradually decrease in amplitude from V_2 towards 0. In Phase B*, the voltage waveform is symmetric to Phase B with respect to the zero-voltage line, and Phase C with sustained oscillations at $\pm V_3$. Reproduced from Ref. [19] under the terms of the CC BY licence.

$V_2 = 5$ V to 0 V over a duration of t_2. In the staircase segment (Phase B), each stage introduces a different tilt angle asymmetry rather than a simple return to equilibrium, inducing an accumulated torque on the helix axis. This cumulative torque over multiple steps acts as the driving force for the helix axis, allowing control over its rotational behaviour.

Reversing the polarity sequence of the staircase waveform reverses the direction of the torque on the helix axis. Thus, Phase B and its reversed polarity counterpart,

Phase B* (shown in Figure 6.5), allow the grating to rotate in opposite directions, as discussed later in this section. To return to the initial grating orientation, the helix can first be unwound into the homeotropic state using Phase A. The initial orientation is then re-established by applying the corresponding reference waveform during grating formation.

The rotation of the helix axis can be precisely controlled by adjusting the temporal duration t_2 of Phase B, while maintaining a constant step size of 1 V over five decreasing steps, allowing the wave frequency in Phase B to vary accordingly. After the voltage reaches 0 V at the end of Phase B, the system remained at 0 V for a short duration, the duration of this state was deliberately minimised and can be set within the range of $0 - 1$ ms. Experimental observations revealed that higher concentrations of CB7CB result in a faster reversion to the Grandjean state. If the system remains in the pure Grandjean state for a long period, the helix axis rotation induced during Phase B will vanish.

At lower concentrations of CB7CB, specifically when the weight percentage is below 10 *wt.*%, the mixture does not exhibit a more rapid reversion to the Grandjean alignment. For instance, with Mixture 2 (5 *wt.*% CB7CB), it took 50 seconds to fully revert to the pure Grandjean state after the voltage reached 0 V. By limiting the zero-voltage duration to less than 1 ms, the rotated helix axis was effectively preserved in all the mixtures considered in this study. Finally, as shown in Figure 6.5, when a continuous symmetric square wave oscillating between V_3 and $-V_3$ ($V_3 < V_{\text{th}}$), was applied, this phase supported the formation of the diffraction grating, ensuring stable grating performance.

To further investigate the influence of the waveform parameters on the rotation angle of the helix axis using Mixture 2, the results summarised in **Table 6.2** show that a higher initial voltage of Phase B, under the same step size, leads to a

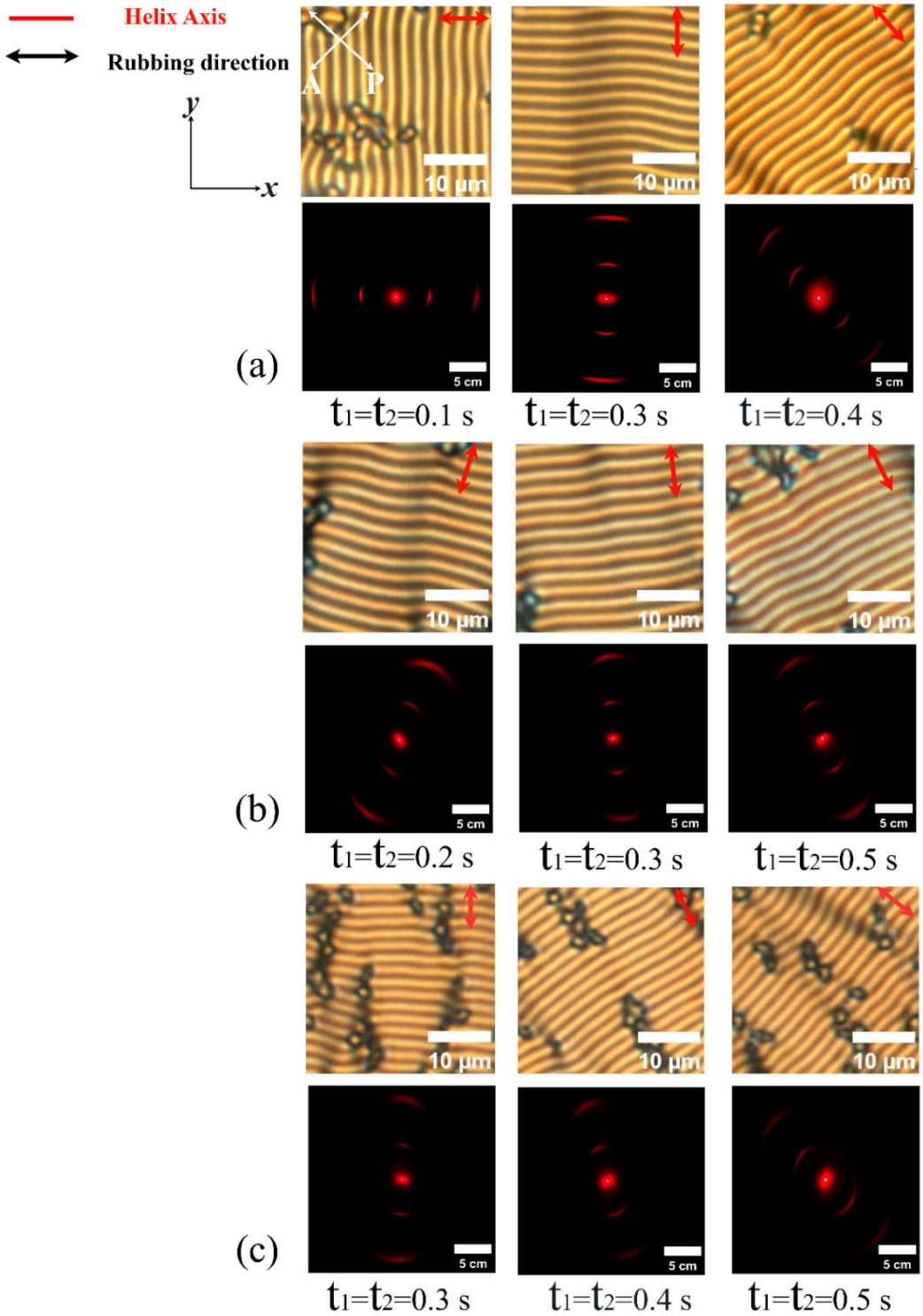


Figure 6.6: Polarised optical microscope images and corresponding diffraction patterns for the three different mixtures containing the LC dimer CB7CB: (a) Mixture 2, (b) Mixture 3, and (c) Mixture 4. The white double-headed arrows indicate the orientation of the polariser (P) and analyser (A), the red double-headed arrows indicate the orientation of the helix axis, and the black double-headed arrows indicate the rubbing direction of this homeotropic cell. Images were captured at 24 °C, and the distance between the screen and the chiral nematic LC device (L) is set at 15 cm. Reproduced from Ref. [19] under the terms of the CC BY licence.

greater change in the normalised rotation angle. As shown in Figure 6.4(b), this phenomenon can be attributed to the fact that higher applied voltages induce a greater asymmetry in the tilt angle switching of the LC director, thereby generating a larger net torque on the helix axis and enhancing its rotation.

Furthermore, as shown in **Table 6.3**, for a particular time duration, increasing the driving frequency in Phase B, which decreases the step size, degrades the rotation performance of the diffraction grating. This can be explained by the fact that a smaller step size corresponds to a higher frequency, which does not provide sufficient time for the LC to complete the switching. Under such conditions, the LC director exhibits only slight oscillations rather than reaching full reoriented states. As a result, the induced asymmetry in the tilt angle is minimal, which limits the effectiveness of the grating rotation.

Table 6.2: Normalised rotation angle under different Phase B initial voltage (V_2) with a constant step size of 1 V at a working temperature of 24 °C.

V_2 (V)	Normalised Rotation Angle ($\Delta\theta$)
5	45°
4	25°
3	10°
2	$< 5°$

Table 6.3: Normalised rotation angle under different Phase-B step size with a constant initial voltage ($V_2 = 4$ V) at a working temperature of 24 °C.

Phase-B Step Size (V)	Frequency of Phase-B ($t_2 = 0.1$ s)	Normalised Rotation Angle ($\Delta\theta$)
1.0	40 Hz	25°
0.8	50 Hz	18°
0.5	80 Hz	5°
0.1	400 Hz	0°

To trigger and control a rotation of the helix axis and consequently the far-field

diffraction pattern, the voltages were configured as follows: $V_1 = 10$ V, $V_2 = 5$ V and $V_3 = 2.6$ V, with t_1 consistently set equal to t_2. The experiment varied the duration of the step interval of the staircase (Phase B), t_2, ranging from 0.1 to 0.6 s. This range was selected based on two key considerations: shorter durations ($t_2 <$ 0.1 s) proved insufficient for complete grating formation, while extended durations ($t_2 > 0.6$ s) yielded no additional variation in the orientation of the grating.

The proposed waveform was applied to each mixture, successfully inducing rotation in all cases. The normalised rotation angle ($\Delta\theta$), defined as the helix axis angular displacement from the initial state ($t_2 = 0.1$ s) to the stable state ($t_2 = 0.6$ s), was measured. When applied to Mixture 1, which contained only the nematic host and the chiral dopant, the device demonstrated significantly limited rotation capability. This limitation can be attributed to the minimal inherent flexoelectro-optic switching of the chiral nematic LC mixture without CB7CB. The asymmetry in the tilt is also noticeably reduced (as shown in Figure 6.4(c)). As a result, no obvious rotational behaviour was observed, with only small, localised rotations occurring in confined regions, characterised by poor overall uniformity.

In contrast, as shown in **Figure 6.6**(a) and **Figure 6.7**, when applied to Mixture 2, containing 5 wt.% CB7CB, the device demonstrated optimal performance with the most extensive rotation angle range from 0° to 135°. Figure 6.6(b) and Figure 6.7 present the behaviour of Mixture 3 (10 wt.% CB7CB), which exhibited a rotation angle range from 0° to 60°. Meanwhile, Figure 6.6(c) and Figure 6.7 present the behaviour of Mixture 4 (15 wt.% CB7CB), with a controllable rotation range from 0° to 45°. These values are reproducible, with a margin of error of approximately ±5°, primarily due to inhomogeneities in the chiral structure of the LC. It indicates that mixtures containing higher concentrations of CB7CB exhibit progressively restricted rotation ranges, due to the increased viscosity of the mixture,

which effectively constrains the rotational freedom of the grating. Furthermore, Figure 6.6 illustrates that higher CB7CB concentrations were associated with increased grating defects, a phenomenon attributed to the elevated viscosity of the mixtures. In addition, for higher CB7CB concentrations, the mixture tends to become unstable, as CB7CB can precipitate out of the solution and form crystals, causing the overall performance to be deteriorated.

Based on these observations, Mixture 2 (5 wt.% CB7CB) was chosen as the optimal composition, demonstrating the most favourable combination of rotation capacity and uniformity. Consequently, it was selected for further experimental investigation. In particular, chiral nematic LC diffraction gratings demonstrate excellent spatial uniformity, with approximately 95 % of the active area maintaining consistent grating directionality, despite occasional defects appearing within localised regions. All measurements were conducted at 24 °C. It is important to note that variations in temperature and CB7CB concentration ratios significantly influence both the rotational direction of the gratings and the range of achievable rotation angles.

While the current implementation shows promising rotatable diffraction properties, further refinement to address the observed pattern inhomogeneities could be achieved through adjustments to the LC composition, combined with refined driving waveforms, which may provide more precise control over the electric field distribution during pattern formation. These improvements would enable more uniform ULH structures in larger areas, enhancing the potential for practical applications.

As mentioned previously and depicted in Figure 6.7, the rotation angle range was maximised when using Mixture 2, containing 5 wt.% CB7CB. To achieve a full 360° rotation in the plane, an alternative waveform (Phase B*) was applied, as highlighted by the dotted box in Figure 6.5. Phase B* features a decrease in

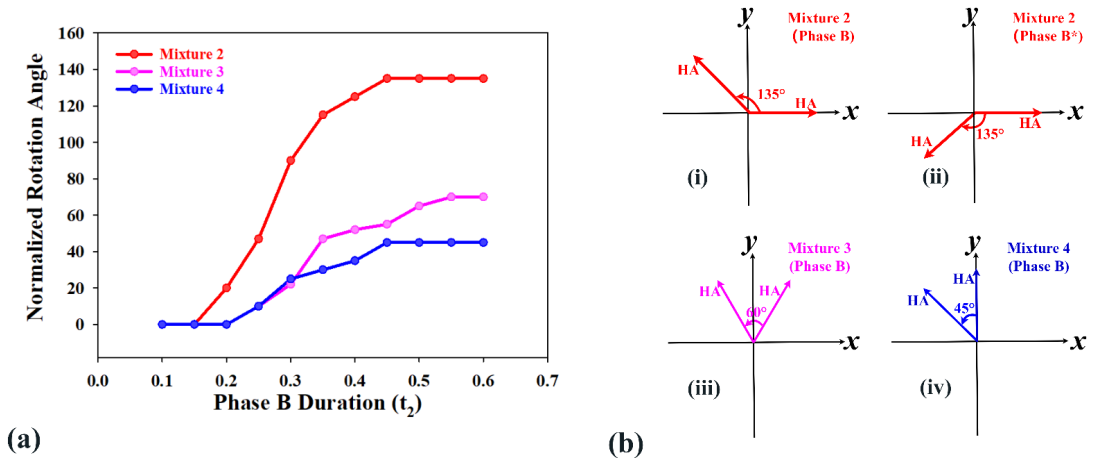


Figure 6.7: (a) Normalised rotation angle variation for different chiral nematic LC mixtures as a function of the duration of Phase B (see waveform in Figure 6.5). (b) Variation in helix axis rotation for the three different chiral nematic LC mixtures as the duration of Phase B or Phase B* (t_2) increased from 0.1 s to 0.6 s. All experiments were conducted at 24 °C. Reproduced from Ref. [19] under the terms of the CC BY licence.

the staircase with positive voltage levels just before reaching 0 V, in contrast to the previously used waveform (Phase B), which includes negative voltage levels before reaching 0 V. By replacing Phase B with Phase B* and adjusting the time intervals of the staircase within the range of 0.1 to 0.6 s, the rotation angle can be finely tuned. This behaviour arises from the opposite torque generated compared with that produced by Phase B, producing a range opposite to that achieved with the prior waveform (Phase B), as shown in **Figure 6.8** and **Table 6.4**. This complementary behaviour allows for precise and comprehensive control over the rotational orientation in the plane of the gratings, allowing complete 360° manipulation of the direction of the grating.

Figure 6.6 and Figure 6.8 illustrate the far-field diffraction patterns obtained. The patterns exhibit crescent-shaped formations with distinctive curvature. This observation may reflect non-uniformity in the LC grating. However, they may also be curvilinear distortion artefacts, such as pincushion or barrel distortion, caused by the optical system and screen positioning. These possible contributions

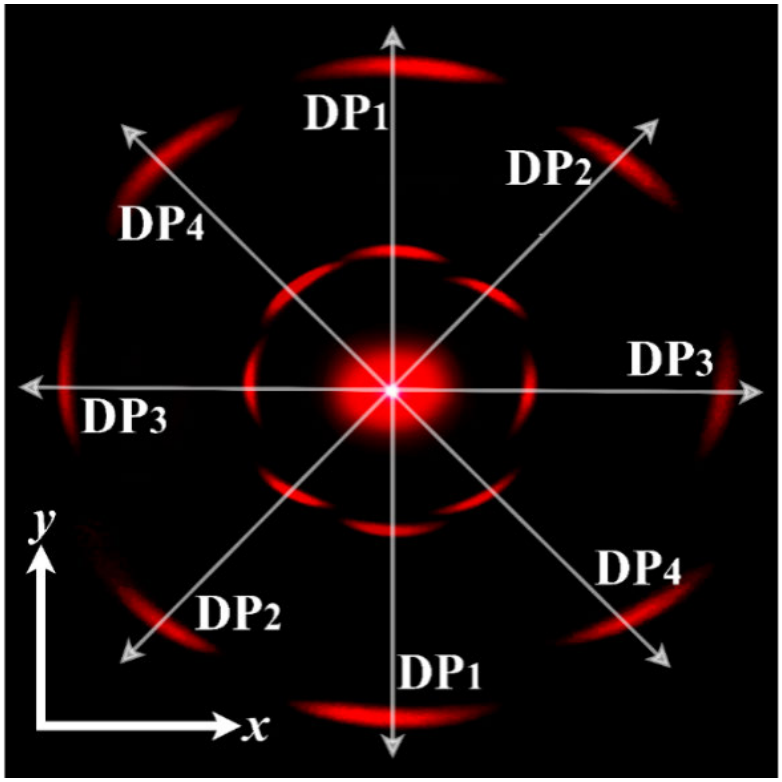


Figure 6.8: Diffraction patterns observed for four distinct electric field conditions with variations in the staircase waveform types and time durations (see Table 6.4). The white double-headed arrows indicate the directions of the helix axis corresponding to the diffraction grating in each far-field diffraction pattern. All experiments were conducted at 24 °C. Reproduced from Ref. [19] under the terms of the CC BY licence.

Table 6.4: Experimental conditions for the four diffraction patterns with varying time durations in Figure 6.8. All experiments were conducted at 24 °C.

Diffraction Pattern State	Phase B Duration (s)	Phase B* Duration (s)
DP_1	0.30	0.30
DP_2	0.25	0.45
DP_3	0.10	0.10
DP_4	0.45	0.25

were not independently quantified.

The chiral nematic LC mixture used in this study exhibits a chiral nematic phase at temperatures below 58 °C. The diffraction grating can be successfully generated using the waveform shown in Figure 6.3, provided that the material remains in the chiral nematic phase. The device demonstrates optimal performance at room temperature, where it achieves a wide and controllable range of rotation of the grating with good uniformity. However, when the temperature increases above 35 °C, it is necessary to decrease the duration of Phase B in the applied waveform to maintain effective rotation of the helix axis. Moreover, elevated temperatures lead to a degradation in the uniformity of the diffraction grating, likely due to decreased viscosity.

Figure 6.9(a) provides further information on the 1^{st} and 2^{nd} far-field diffraction orders for the various mixtures considered in this study. Prior to reaching the threshold voltage (V_{th}), we observed a slight decrease in the diffraction angle with increasing voltage. This occurs because the elevated electric field partially unwinds the natural helical arrangement of the chiral nematic LC, leading to an increase in the pitch of the diffraction grating. Our findings also demonstrate that higher concentrations of CB7CB correspond to higher threshold voltages and, notably, increased diffraction angles. A significant improvement in the diffraction angle was achieved with the addition of just 5 wt.% CB7CB. However, a further increase in the concentration of CB7CB to 10 wt.% did not produce substantial additional improvements in the diffraction angle, likely due to the introduction of additional defects and variations in the effective HTP of the chiral dopant.

As discussed above, to achieve optimal performance, we selected an LC device using Mixture 2 (containing 5 wt.% CB7CB) and operated it at 2.6 V_{rms}. Under these conditions, the device exhibited first- and second-order diffraction angles

of 15.6° and 33.5°, respectively. These diffraction angles remained stable during pattern rotation, showing negligible variation. Additionally, we assessed the zero-order normalised light intensity (η) in the far field, defined as the ratio of the intensity of light that has passed through the LC grating under an applied voltage to the intensity of light either without the LC grating or without the applied voltage. Figure 6.9(b) shows how variations in the time duration of the staircase segment of the waveform in Figure 6.5 influence the zero-order normalised light intensities.

Specifically, when $t_2 = 0.1$ s, with the orientation of the stripes perpendicular to the x-axis and the polarisation angle at 0° (aligned with the x-axis), the zero-order normalised light intensity peaks at 57%, as shown in Figure 6.9(b). In contrast, with a polarisation angle of 90° (aligned with the y-axis), the intensity dips to a minimum of 11.6%. At $t_2 = 0.3$ s, with the stripes aligned parallel to the x-axis, a polarisation angle of 0° (parallel to the stripes) results in a minimal intensity of 21%, whereas a 90° polarisation angle (perpendicular to the stripes) elevates the intensity to 52.1%.

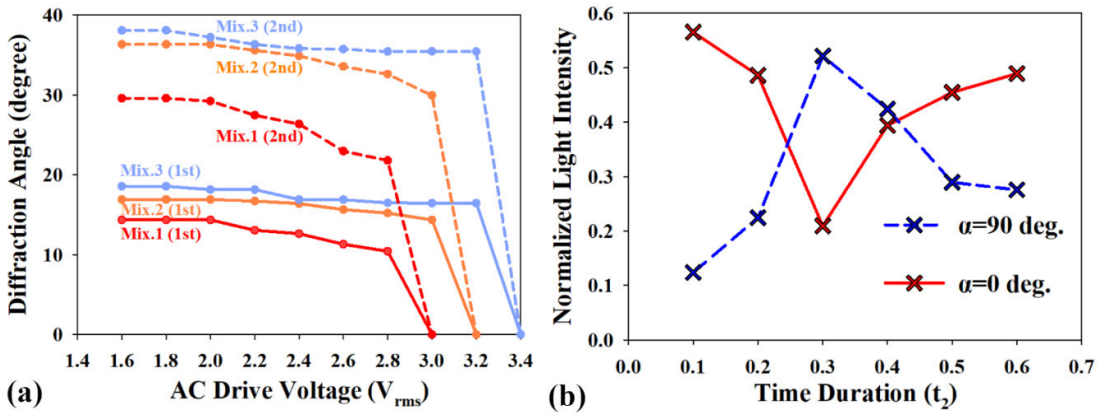


Figure 6.9: (a) The 1st- and 2nd-order diffraction angles as a function of the voltage applied to the chiral nematic LC diffraction grating for different mixtures. (b) Zero-order normalised light intensity as a function of the staircase waveform duration (t_2) for incident polarisation angles of 0° and 90° using Mixture 2. Experiments were conducted at 24 °C. Reproduced from Ref. [19] under the terms of the CC BY licence.

The dependence on polarisation arises from different optical interactions: when

incident polarised light is perpendicular to the orientation of the grating, it experiences only the ordinary refractive index (n_o), resulting in reduced higher-order diffraction and maximum zero-order intensity. Since the refractive index becomes constant (n_o), the polarised light theoretically does not experience any birefringence. However, imperfections in alignment and optical scattering result in some light loss. Conversely, when parallel to the grating orientation, light encounters periodic variations between the extraordinary (n_e) and ordinary (n_o) refractive indices, maximising diffraction efficiency and consequently reducing zero-order light intensity.

The first- and second-order diffraction efficiencies of the diffraction pattern were also investigated. The diffraction efficiency (η^*) is defined as the ratio of the first- (or second-) order light intensity to the incident light intensity, expressed as

$$\eta^* = \frac{I_1 \text{ (or } I_2)}{I_0}, \tag{6.3}$$

where I_1, I_2, and I_0 are the first-order, second-order, and incident light intensities, respectively. As demonstrated in **Table 6.5**, using the optimised mixture (Mixture 2), we achieved first- and second-order diffraction efficiencies of 25.4% and 14.8%, respectively. We observed that increasing the concentration of CB7CB resulted in a reduced diffraction efficiency, which can be attributed to imperfections in the LC alignment.

Table 6.5: Measured diffraction efficiencies of the 1st and 2nd order diffraction for different mixtures (discussed in the Materials and Methods section).

Mixture ID	1st Order Efficiency (%)	2nd Order Efficiency (%)
Mixture 2	25.4	14.8
Mixture 3	15.4	7.9
Mixture 4	9.6	6.3

6.5 Summary

In conclusion, we have demonstrated a novel chiral nematic LC diffraction grating device that can be switched 'on' and 'off' with an applied voltage and that enables uniform 360° rotational control of the orientation of the diffraction grating at room temperature. By setting the thickness-to-pitch ratio to be $d/p = 1.85$ and using homeotropic alignment layers, the chiral nematic LC is found to form a uniform lying helix configuration with the application of a suitable voltage waveform, resulting in the formation of a diffraction grating.

With the addition of a low concentration of LC dimer known to possess a large flexoelectric coefficient (CB7CB) and through a systematic adjustment of the waveform parameters, a complete in-plane rotation of the diffraction grating is observed that is triggered by a voltage-modulated torque acting on the helix axis, induced by asymmetric flexoelectro-optic tilt angles. The resulting devices show excellent stability. Under a continuous oscillating holding voltage with a fixed amplitude, they remained unchanged for more than an hour during continuous operation. Although we have not conducted long-term reliability tests, the observed short-term stability is promising. The energy consumption is expected to be low, as the system is dielectrically driven and is likely comparable to that of conventional LC technologies. However, a limitation remains in the response time. The formation of the grating structures typically occurs on the order of hundreds of milliseconds due to the time required for the reorganisation of the helical pitch.

The device exhibits diffraction angles of 15.6° and 33.5° for the first and second diffraction orders, respectively, and it is found that the diffracted intensity depends on the temporal characteristics of the applied voltage waveform and the polarisation of the incident light. These findings illustrate the proof-of-concept of this LC diffraction grating that could be of potential interest for advanced beam-steering

applications and dynamic optical display technologies.

7

Holographic Projection Displays Using Liquid Crystal Diffraction Gratings

7.1 Introduction

Holographic projection displays use controlled wavefront modulation to reconstruct images on a screen without requiring specialised glasses or headsets [107–109]. This technology is promising for applications in augmented reality (AR), virtual reality (VR) [110–113], and optical communications [114]. As described in Section 2.11, holographic projection systems based on SLMs are widely employed for dynamic wavefront reconstruction, in which phase or amplitude modulation is used to encode holographic information and project reconstructed optical fields into space [115, 116]. However, a key limitation of traditional holographic displays with SLMs is their narrow viewing angle (2φ), which restricts the observer's perspective and

reduces the usability of holographic content. The viewing angle is highly dependent on the pixel size of the SLM, as described by the equation

$$\varphi = \arcsin\left(\frac{\lambda}{2p_s}\right) \tag{7.1}$$

where λ is the optical wavelength and p_s is the SLM pixel pitch [62, 117]. Another significant limitation is the relatively small holographic display area (S), which is constrained by the limited active regions of common SLMs [118]. For single-SLM systems, the 10-megapixel SLM from Holoeye with a 1.6 cm $\times$ 0.94 cm screen size, for example, offers a full viewing angle of 8.2° [63]. Although larger screen sizes can increase the holographic display area under identical optical conditions, they typically involve significantly higher costs [75, 119]. Expanding both the holographic projection display area in the far-field and the viewing angle is particularly important, as these improvements enlarge the viewing zone, allowing comfortable and simultaneous viewing by multiple observers [64, 113].

To address these limitations, researchers have explored both spatial and temporal multiplexing methods. In spatial multiplexing, Holobricks uses spatial tiling of modules to achieve holographic screen enlargement with high space-bandwidth product [120, 121]. However, this method requires physically combining multiple SLM modules to form a larger aperture hologram, making it expensive and alignment-sensitive. Alternatively, temporal multiplexing approaches employ custom-made SLMs with precise control of the refresh rate and accurate synchronisation that can display different holograms sequentially at high refresh rates, thus expanding the display size and improving the viewing angle [122, 123]. However, brightness per view is reduced due to the temporal distribution of light energy across multiple frames. Another approach uses transparent holographic optical elements (HOEs) that function as diffractive or reflecting screens [124]. This

method simultaneously increases both display size and viewing angle while offering high flexibility and improved light use efficiency through digitally designed optical elements. Nevertheless, this approach is constrained by fabrication challenges associated with large-area, high-efficiency, multi-wavelength HOEs or metasurfaces, which remain difficult and costly to manufacture with sufficient precision. However, these limitations do not preclude the use of SLMs. Instead, they motivate the incorporation of additional optical modulation elements so that the inherent performance constraints of a single SLM can be alleviated and its capabilities more fully leveraged towards achieving large replay-field holographic projection.

Additional LC-based solutions have emerged as potential cost-effective optical elements that offer enhanced functionality of the optical modulation that, when used in combination with SLM technology, can overcome some of the intrinsic limitations as mentioned above. LCs exhibit unique electro-optical properties, characterised by their optical anisotropy and high sensitivity to external stimuli, such as electric fields and as exploited in SLM technology [125]. By applying voltage-controlled phase modulation, the beam steering of LC-based systems can also be achieved by forming LC diffraction gratings, allowing the steering of diffracted light over a wider angular range [18, 126]. Such diffraction gratings for beam steering can be realised using patterned electrodes that generate periodic electric fields [76, 77]. Previous research has used this method successfully to steer light for display applications, achieving enlargement of the display size [75]. However, the relatively slow response time of such a tunable LC grating represents a significant limitation that constrains the maximum achievable display size and affects system performance. Moreover, these approaches rely on temporal scanning accumulation across different diffraction orders rather than the simultaneous perception of multiple holographic replay-field spatial positions. As a result, the slow response

unavoidably reduces the quality of the holographic projection display [75].

Additionally, LC diffraction gratings can be formed through the flexoelectric effect in nematic LC, allowing real-time control of the diffraction angle by applying varying electric fields [18, 41]. Furthermore, beam steering can be accomplished using chiral nematic LCs due to their intrinsic macroscopic helical structure [19, 80]. These methods effectively steer light into different diffraction orders at various angles, offering the potential to significantly extend the viewing angle of holographic images. However, not all diffraction orders are desirable for practical applications, as higher-order diffraction often leads to energy dispersion and reduced efficiency. In many cases, it is advantageous to suppress unwanted orders and concentrate the optical power into a single diffraction order (e.g. the first order). Such single-order diffraction improves system efficiency by maximising the usable light intensity and minimising energy losses.

Polarisation gratings (PGs) represent a class of LC devices capable of optical beam-steering. These non-mechanical diffractive optical elements operate based on the Pancharatnam–Berry phase, enabling nearly 100% diffraction efficiency into a single order [127–130]. Previous studies have utilised combinations of two polarisation gratings for nonmechanical beam steering applications, including discrete laser beam steering and LC laser beam routing to four spatial locations [131, 132]. Meanwhile, the concept of combining PGs with LC optical elements has proven effective for realising actively tunable optical devices in AR/VR display systems [133, 134]. This property can be potentially exploited in holographic projection displays to expand the effective display area and viewing zone.

A pi-cell is a nematic LC cell whose two substrates have parallel rubbing directions, as described in Section 2.6. Under an applied voltage, the director can adopt a bend configuration, allowing faster electro-optic switching than in a

conventional planar Fréedericksz cell. For temporal multiplexing of holographic projections, faster switching reduces the time spent in intermediate polarisation states between successive projection positions, helping to suppress ghost images.

In this chapter, we present PGs combined with electrically controllable phase shifters using pi-cells to steer holographic images generated by an SLM to different locations. Fast switching is crucial for preserving synchronisation with the SLM, facilitating efficient time-multiplexing and robust hologram reconstruction. By attaining high switching speeds in the nematic pi-cell LC phase shifters and accurately synchronising the voltage drive signals with the SLM output, we achieve seamless temporal coordination of the holographic image-steering process. The concept of the proposed system is illustrated in **Figure 7.1**(a) and Figure 7.1(b). This method effectively enlarges the holographic projection display area by combining multiple sub-frames generated by separate holograms under high-frequency voltage driving conditions. Furthermore, this approach is fundamentally distinct from conventional tunable-LC-grating holographic enlargement methods, which depend on patterned electrodes to form periodic structures and are therefore limited by relatively slow switching speeds. Through the integration of fast-response pi-cells and high-transmittance PGs, our system enables simultaneous visual perception of multiple beam-steering positions with fast holographic projection display switching, thereby enhancing the overall display quality. The work presented in this chapter has also been published in ACS Photonics, 13(10), 2943–2953 (2026) [20].

7.2 Experimental Methods

In this section, we present the method developed in this work for achieving enlarged holographic projection displays using polarisation gratings and LC cells.

7.2.1 Materials

The nematic LC cells (N1 and N2) function as optical phase shifters. They were fabricated by capillary filling the nematic LC mixture E7 (Synthon Chemical Ltd.) into pi-cells that consisted of parallel-rubbed planar alignment layers coated onto transparent conductors in the form of indium tin oxide (ITO) that were, in turn, coated onto the inner surfaces of the glass substrates (glass cells were kindly provided by Samsung). The air gap in these cells was 5 µm. A function generator was used to apply a voltage across the LC layer to tune the optical retardance of the pi-cells, enabling them to operate as half-wave, quarter-wave, or full-wave plates, thereby controlling the polarisation state of the light as it passes through the nematic pi-cell. The PGs used in this study were commercially sourced from Edmund Optics, with a design wavelength of 550 nm. Each grating, comprising the LC layer and substrate, has a total thickness of 0.45 ± 0.04 mm, featuring a spatial frequency of 286 grooves mm^{-1}. According to the manufacturer's specifications, the first-order diffraction angle and efficiency are approximately 10° and 96%, respectively, indicating minimal leakage of the incident light into the zero-order, irrespective of its polarisation. The PGs were fabricated on D263 glass substrates with an anti-reflective coating (ARC) to minimise reflection losses.

7.2.2 Holographic Projection System

The experimental configuration for the display of the holographic projection is illustrated in Figure 7.1(c). A continuous-wave helium–neon (He–Ne) laser (05-LGP-193, Melles Griot) with an emission wavelength of $\lambda = 543.5$ nm was employed as a linearly polarised coherent light source. The laser provided an output power of 10 mW at this wavelength, ensuring sufficient brightness for the holographic display. To adjust the intensity as required, the beam first passed through a neutral density (ND) filter, after which it was reflected by a mirror. The beam was expanded by a $\times 4$ objective lens in combination with Lens 3 ($f_3 = 50$ mm). In certain versions of the experiment, a simpler beam expander consisting of a single lens with a longer focal length was employed. The incident light was then directed onto the spatial light modulator (SLM; Hamamatsu Photonics, X15213 series) after passing through a beam splitter. The SLM used in this work had a resolution of 1272×1024 pixels, enabling high-precision phase modulation for holographic pattern generation.

The polarisation state of the laser output was aligned with the operating polarisation of the spatial light modulator (SLM) to ensure optimal phase modulation performance. The SLM, driven by a computer, displayed the computer-generated holograms (CGH) calculated using the Gerchberg–Saxton (GS) iterative phase-retrieval algorithm. The reflected beam then passed through a polariser to ensure linear polarisation before being focused by the first lens (Lens1, $f_1 = 100$ mm). Light reflected from the SLM was then concentrated onto a set of LC optical elements consisting of two polarisation gratings (PG1, PG2) and two nematic LC pi-cells (N1, N2) acting as phase shifters, controlling whether the output light is left- or right-circularly polarised before it is directed onto the polarisation gratings. This combination of elements, positioned between Lens1 and Lens2, enabled dynamic beam steering.

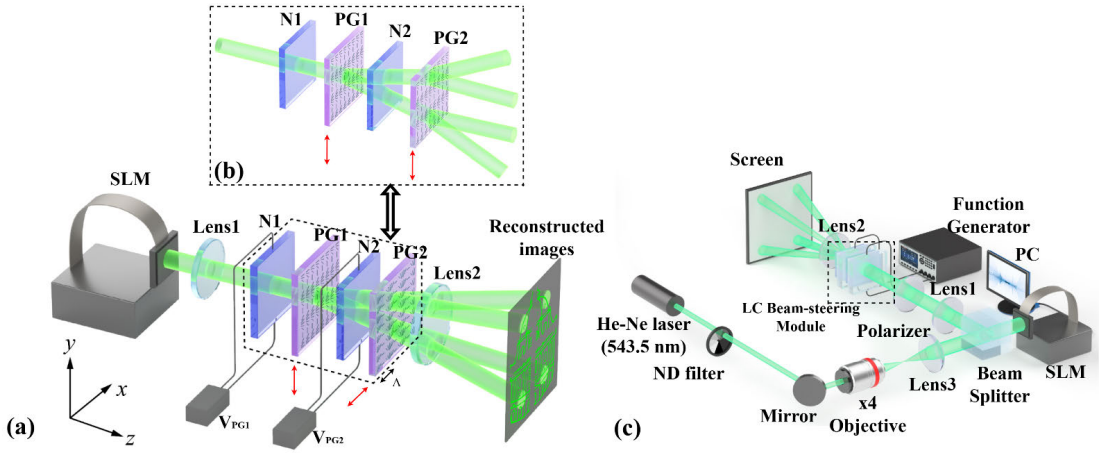


Figure 7.1: (a) Configuration for the fast-switching wide-area holographic projection display. Here two polarisation gratings (PGs) are arranged such that their axes are perpendicular to each other in order to generate a 2D holographic display. (b) Arrangement of the LC optical elements when the two PGs are placed such that their grating axes are aligned parallel in order to produce a one-dimensional holographic projection display. The double-headed arrows indicate the orientations of the diffraction gratings of each PG. The z-axis corresponds to the optical propagation direction of the incident beam, and the PG periodicity Λ lies along the x-axis. (c) Schematic of the experimental arrangement for the holographic projection display system. The dashed boxes indicate the LC beam-steering module. Reproduced from Ref. [20] under a CC BY 4.0 licence.

The second lens (Lens2, $f_2 = 25.4$ mm) served to magnify the reconstructed holographic image. To further demonstrate real-time control of the holographic display via an external electric field, a flexoelectric grating can alternatively be inserted in front of the first nematic LC pi-cell. Finally, the reconstructed CGH image was projected onto a screen for observation and analysis.

7.2.3 Synchronisation

To realise a large-scale holographic projection display, the first step was to dynamically steer the different CGH diffraction patterns into separate spatial locations so that when viewed together, they form a larger image. The nematic LC cells (N1 and N2) in the configuration serve as continuously tunable phase shifters,

allowing precise control over the polarisation state of the light incident on each PG. Thus, each PG is paired with a nematic LC pi-cell that modulates the polarisation, allowing precise steering of the CGH pattern towards the desired location.

For polarisation gratings (PG), when incident light was circularly polarised, diffraction occurred exclusively in a single order (+1 or −1) with a diffraction angle of approximately 10°. The number and orientation of the PGs, together with the number of nematic LC phase shifters, determine the total number of beam locations projected onto the screen. When the two PGs were arranged with their grating axes aligned orthogonally, a 2×2 array of four distinct beam-steering locations was produced, as shown in Figure 7.1(a). However, when the two PGs were arranged with their grating axes aligned parallel, a linear row of four distinct beam positions was generated, as shown in Figure 7.1(b).

Taking the four beam spots as an example, as shown in **Figure 7.2**, the first nematic LC phase shifter (N1) operated as either a quarter-wave plate or a three-quarter-wave plate, converting linearly polarised light into either left- or right-circularly polarised light depending on the applied AC voltage amplitude in each state ($V_{\mathrm{PG1,S1}}$, $V_{\mathrm{PG1,S2}}$, $V_{\mathrm{PG1,S3}}$, $V_{\mathrm{PG1,S4}}$). The second nematic LC phase shifter (N2), on the other hand, functioned as either a half-wave or full-wave plate, reversing or maintaining the handedness of the circularly polarised light under the applied voltages of each state ($V_{\mathrm{PG2,S1}}$, $V_{\mathrm{PG2,S2}}$, $V_{\mathrm{PG2,S3}}$, $V_{\mathrm{PG2,S4}}$). By controlling these voltages, the light can be dynamically steered to four discrete spatial locations.

An AC driving field was used instead of a DC field to avoid ionic screening effects, which would otherwise degrade the electro-optic performance of the LC devices. The original image can then be divided into four sub-images. Each sub-image is then converted into its corresponding hologram using the GS algorithm. In our work, the holograms employed are binary holograms, as this provides a high-

contrast intensity profile in which the bright regions represent strong amplitude values while the dark regions correspond to zero amplitude. This distinct separation improves the convergence of the iterative GS calculation and improves the accuracy of the reconstructed holographic pattern. The resulting holograms were sequentially combined to form a CGH video sequence, as shown in Figure 7.2(a), which was then loaded onto the SLM.

The CGH video sequence was played on a PC, while the SLM, mirroring the PC display, sequentially loaded each CGH frame. The PC and SLM were both synchronised at a refresh rate (f_{th}) of $f_{\mathrm{th}} = 60$ Hz via a DVI-D interface, ensuring that image transmission and display were synchronised. Lower frame-rate CGH sequences (e.g., $f_{\mathrm{vid}} = 1$, 5, 10, or 20 fps) that are integer divisors of the SLM refresh rate ($f_{\mathrm{th}} = 60$ Hz) were automatically synchronised by frame repetition, while higher frame-rate sequences (e.g., $f_{\mathrm{vid}} = 120$ fps) could not be displayed due to the 60 Hz refresh limit of the SLM interface. As demonstrated in Figure 7.2(b)–(c), to ensure the desired beam-steering state, the driving waveform of the nematic LC pi-cells was synchronised with the CGH sequence such that each voltage state corresponded precisely to the display duration of one hologram frame. The driving frequency of the nematic LC pi-cells, denoted as f_{LC}, was therefore set to satisfy the condition $f_{\mathrm{LC}} = f_{\mathrm{vid}}/N$, where N is an integer defining the number of sequential voltage states that constitute one hologram cycle. The duration of each of the four states (T) was set to $1/f_{\mathrm{LC}}$.

The temporal synchronisation guaranteed that the optical phase modulation of the nematic LC pi-cells and the SLM-displayed CGH were temporally aligned, producing the expected beam-steering direction, as illustrated in Figure 7.2(d) and Figure 7.2(e). We also synchronised the phase between the applied waveform and the CGH sequence. However, slight phase misalignments were occasionally

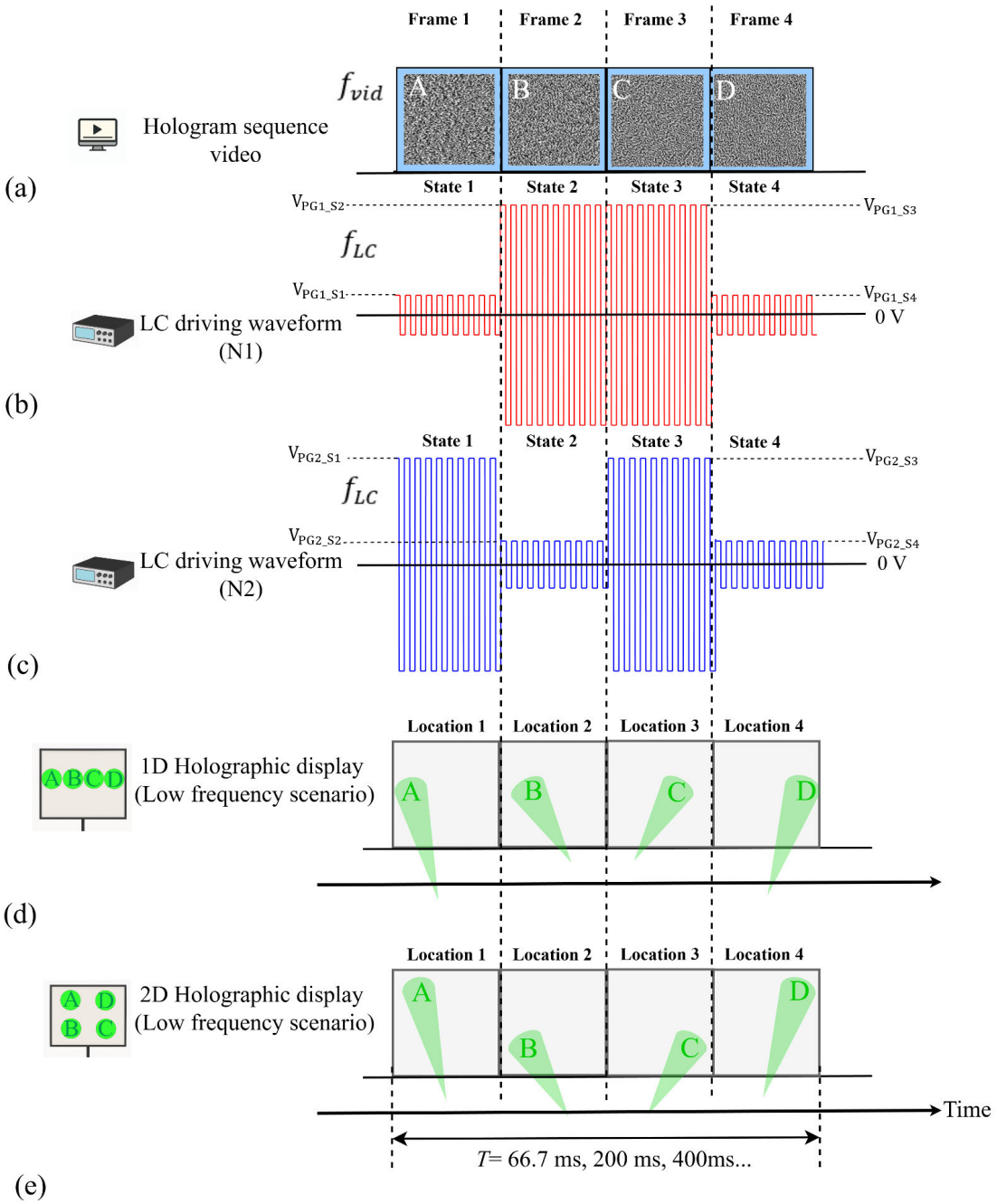


Figure 7.2: Example of the temporal synchronisation schematic of the holographic (CGH) display system. (a) The hologram sequence video run on the PC consists of four sub-hologram frames (A–D) at a frame rate of f_{vid}, which was mirrored on the SLM for dynamic display. (b–c) The two nematic LC pi-cells (N1 and N2) were driven by synchronised voltage waveforms that alternate between applied voltages of varying amplitudes. (d-e) Four distinct beam-steering spatial locations (A–D) of the replay field are produced through synchronised modulation between the CGH sequence and the LC driving signals, arranged in (d) a linear row (1D) and (e) a two-by-two configuration (2D). Reproduced from Ref. [20] under a CC BY 4.0 licence.

observed, mainly due to the asynchronous initialisation of the CGH sequence video. Because video playback on the PC commences at an arbitrary time relative to the output cycle of the function generator, the initial phase relationship between the displayed CGH and the applied voltage waveform can vary randomly. This issue was mitigated by manually adjusting the phase of the applied waveform on the function generator until the required beam-steering state was achieved.

Figure 7.2(d) and Figure 7.2(e) illustrate the concept of projected holographic display of the letters A, B, C, and D, which were displayed sequentially and repeatedly at four distinct spatial locations across a single linear axis (1D) and a two-by-two spatial configuration (2D) under low frequency operation. In this case, each CGH frame corresponds to one beam steering position, causing the letters to appear one after another. When the driving frequency of the LC pi-cells was increased and synchronised with a higher video frame rate, the rapid temporal switching leads to simultaneous visual perception of the four letters across different spatial locations, thereby effectively expanding the apparent size of the holographic display. The corresponding results are presented later in **Figure 7.5**(a). If a different number of beam-steering locations is desired, the number of AC voltage states must be adjusted accordingly. The replay fields were displayed on a white screen and captured using a CCD camera.

7.3 Switching Speed Characteristics and Transmittance Analysis

If the switching speed of the LC phase shifter is insufficient, temporal overlap between adjacent replay fields can introduce ghost images in temporally multiplexed holographic displays. The fast switching of the pi-cell used in this work is

expected to mitigate this effect by improving the temporal separation between sequential replay fields.

The nematic LC pi-cells were employed as the optical phase shifters in this experiment due to their superior switching speed compared to the anti-parallel rubbed Fréedericksz cells. As shown in **Figure 7.3**(a)(i), for the Fréedericksz cell, when no voltage or only a small voltage is applied, the LC director aligns with an almost zero tilt angle (θ), corresponding to the "off" state. However, when the applied voltage exceeds the threshold for director distortion but is not excessively high, the LC director undergoes a gradual elastic deformation across the LC layer, transitioning to the "on" state. The director reorientation during this process can be described in terms of the profile

$$\theta(z) = \theta_0 \sin\left(\frac{\pi z}{d}\right)$$

as illustrated in Figure 7.3(a)(ii), where $\theta(z)$ represents the director tilt angle at position z, θ_0 denotes the maximum tilt amplitude at the centre of the LC layer, and d is the cell gap.

In contrast, for the pi-cell, fast-switching behaviour occurs between the vertical (V) state and the transient "off" state, as shown in Figure 7.3(b)(i). When a sufficiently high voltage (greater than 5 V) is applied for 1–2 seconds, the pi-cell enters the V state. If the voltage is momentarily reduced or removed, the LC director relaxes into a transient "off" state. In this configuration, the LC director adopts a parallel surface alignment, and the switching between these two states can be expressed as

$$\theta(z) = \frac{\pi z}{d} - \theta_0 \sin\left(\frac{2\pi z}{d}\right) \tag{7.2}$$

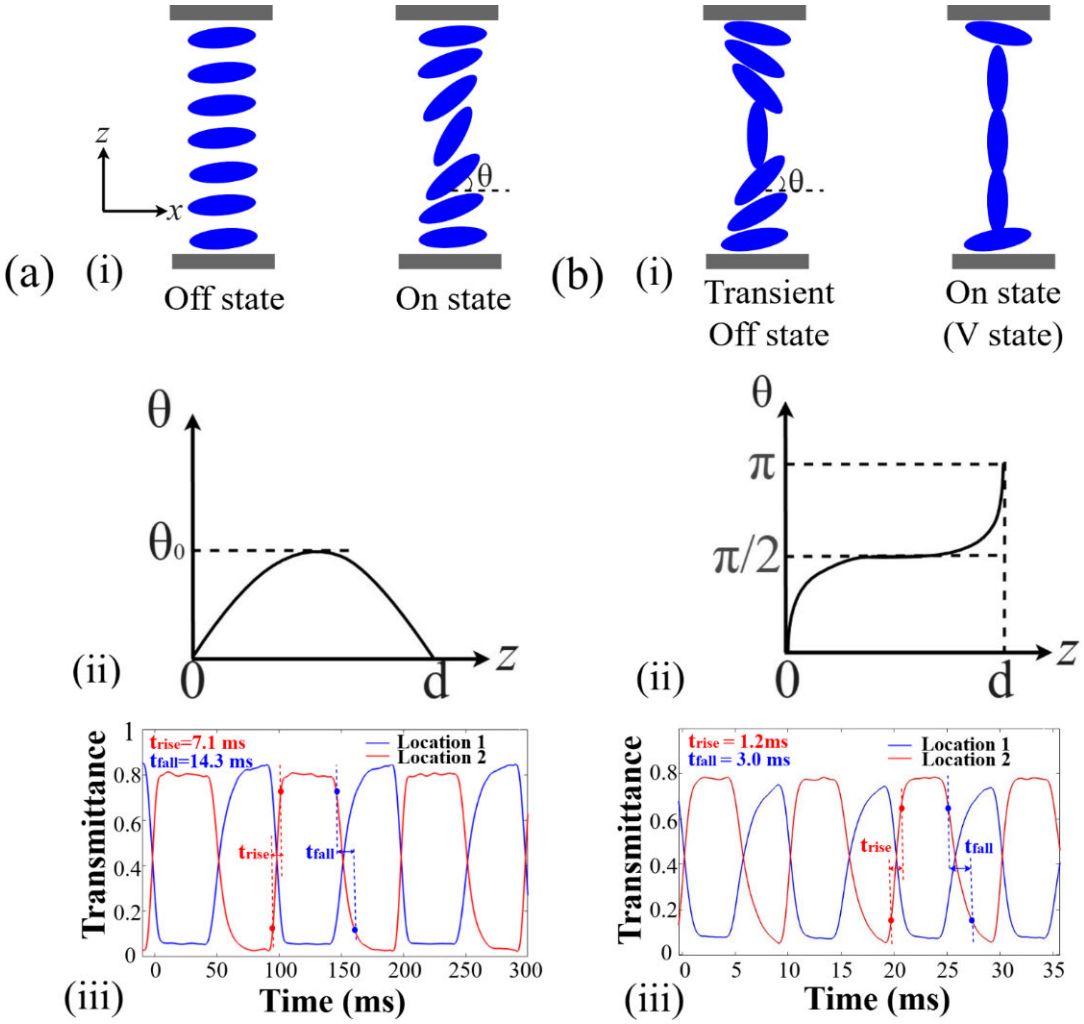


Figure 7.3: Schematic comparison of director reorientation in (a) a conventional nematic Fréedericksz cell and (b) a nematic pi-cell. (i) Illustrations of the director configurations in the "off" and "on" states under an applied voltage. (ii) Corresponding director tilt angle profiles. (iii) Measured transmittance variations at location 1 and location 2, illustrating the switching dynamics between two optical states. The pi-cell operated at $f_{\text{switching}} = 100$ Hz and the Fréedericksz cell operated at $f_{\text{switching}} = 10$ Hz. The measurements were performed by applying a modulated AC waveform with amplitudes alternating between 0.9 V and 5 V at the specified switching frequency. All experiments were conducted at a temperature of 25 °C. Reproduced from Ref. [20] under a CC BY 4.0 licence.

as illustrated in Figure 7.3(b)(ii). From these two expressions for the pi-cell and the Fréedericksz cell, we can establish that the characteristic length scale (D) of the Fréedericksz cell is twice that of the pi-cell. Since the LC switching time scales as $\tau \propto D^2$ [125], the pi-cell achieves a theoretically four-fold reduction in switching time compared to the Fréedericksz cell of equal thickness.

To evaluate the switching speed of the beam-steering system, two photodiodes were used in place of the projection screen to detect the light intensity at different steering locations. Location 1, corresponding to the beam-steering position where the holographic projection displays the letter 'A' in Figure 7.2(e), and Location 2, corresponding to the position displaying the letter 'B' in Figure 7.2(e), were selected as examples, and their corresponding photodiodes were connected to two channels of an oscilloscope. The waveform applied to N2 was disabled. Only the AC-modulated waveform corresponding to state 1 ($V_{\mathrm{PG1,S1}}$) and state 2 ($V_{\mathrm{PG1,S2}}$) of the waveform shown in Figure 7.2(b) was applied to the LC cell N1, allowing the vertical beam to be shifted between the two spatial positions. In this measurement, only these two stages of the full driving waveform in Figure 7.2(b) were selected to characterise the response speed. The applied voltage alternated between 0.9 V and 5 V with a switching frequency $f_{\mathrm{switching}}$.

When the voltage applied to N1 was set to $V_{\mathrm{PG1,S1}} = 0.9$ V, Location 1 appeared bright while Location 2 remained dark. When the voltage was increased to $V_{\mathrm{PG1,S2}} = 5$ V, the intensity distribution reversed, with Location 1 becoming dark and Location 2 bright. The transmittance (η) at each position was defined as

$$\eta = \frac{I_{\mathrm{out}}}{I_{\mathrm{in}}}, \tag{7.3}$$

where I_{out} is the intensity of the detected light at a given position and I_{in} is the intensity incident before entering the LC beam steer module (dashed box in

Figure 7.1). Using this arrangement, we compared our nematic pi-cell (parallel rubbed, thickness = 5 μm) with that of an anti-parallel rubbed Fréedericksz cell (assuming the same thickness). The results show that the pi-cell exhibited a rise time of $t_{\text{rise}} = 1.2$ ms and a fall time of $t_{\text{fall}} = 3$ ms, as presented in Figure 7.3(b)(iii). In contrast, the Fréedericksz cell showed slower switching characteristics, with a longer rise time of $t_{\text{rise}} = 7.1$ ms and a much longer fall time of $t_{\text{fall}} = 14.3$ ms under identical conditions, as shown in Figure 7.3(a)(iii).

These results indicate that pi-cell, when combined with a polarisation grating (PG), enables significantly faster optical switching between two spatial locations, approximately twenty times faster than previously reported patterned-electrode LC beam-steering devices [75]. However, the measured transmittance did not reach the theoretical extremes. The bright state achieved approximately 80% transmittance, while the dark state remained at approximately 5–10%. The two primary sources of loss are residual zero-order undiffracted light leakage due to imperfections in the PG structure and the wavelength mismatch between the $\lambda = 543.5\,\text{nm}$ of the He–Ne laser and the design wavelength of the commercially sourced PG, reported to be approximately 4% [132], and Fresnel reflection losses arising from reflections at the air–glass interfaces, estimated to be approximately 4% per interface. For a configuration consisting of one PG and one nematic phase shifter separated by air, there are four air–glass interfaces. Taking these reflections into account, together with the additional zero-order leakage 4%, the estimated total transmission is approximately 81.5%. This value is close to the experimentally measured transmittance of 80%, as discussed above. Light scattering, non-ideal retardance in the LC phase shifters, internal reflections within the LC layers, and absorption within the ITO electrodes and LC layers further contribute to transmittance loss. If the number of pairs of PG–phase shifters is denoted by M,

the total transmission can be estimated approximately as

$$\eta_{\text{total}} = 0.8^{M}. \tag{7.4}$$

Reflection losses at the air–glass interface can be further reduced in the future by employing index-matched stacking. In addition, two approaches could be used to suppress the zero-order leakage. First, polarisation gratings specifically designed for the operating wavelength could be employed. Second, careful control of the input polarisation state through precise adjustment of the pi-cell drive voltages can also help suppress unwanted zero-order light.

In summary, the 80% transmittance ($M = 1$) in each state helps to maintain a sufficient projection intensity and contributes to the overall quality of the holographic projection image. Meanwhile, fast-switching pi-cells provide a significant performance advantage for the wide-angle holographic projection display system. Rapid switching is essential for maintaining synchronisation with the SLM, enabling effective time-multiplexing, higher frame rates, and stable hologram reconstruction. For example, if the CGH sequence operates at $f_{\text{vid}} = 60$ fps, each frame lasts 16.7 ms. In our system the pi-cells switch the steering state in about 1.3 ms, which is roughly 13 times faster than the SLM frame duration. This rapid response ensures that each CGH frame is directed to a well-defined steering state without mixing. In comparison, systems using Fréedericksz cells typically switch only about twice as fast as the SLM frame period, making them more susceptible to ghost images, blurred reconstructions, and loss of temporal synchronisation.

A frame rate of approximately 30 fps is generally required to achieve a perceptually stable image reconstruction for human vision, corresponding to a frame period of approximately 33 ms. With the measured switching time of the nematic LC pi-cell used in this work (1.2–3 ms, as shown in Figure 7.3(iii)), a theoretical

maximum of approximately 11–27 replay fields could be sequentially addressed within this time window. However, in the present experiment, the system was limited by the available SLM refresh rate and the number of polarisation grating modules. Nevertheless, if higher refresh-rate SLM devices and an appropriate configuration with a sufficient number of polarisation gratings are employed, the proposed architecture has the potential to achieve a high level of spatiotemporal multiplexing without introducing perceptible flicker.

7.4 Holographic Projection Display Enlargement

When the PGs were arranged with their axes aligned parallel, a linear array of four beam spots (1D) was generated, as shown in **Figure 7.4**(a). The red arrows on each PG indicate the corresponding diffraction directions. The spacing between the gratings (L) determines the separation (H) between the two central diffracted orders, given by

$$H = 2L \tan 10^{\circ}. \tag{7.5}$$

As L decreases, the diffracted beams move closer together and eventually overlap. Therefore, in our experiment, three diffracted orders were selected for beam steering, resulting in a total of three steerable beam positions ($N = 3$).

The pi-cells were initially driven into the vertical (V) state by applying a 10 V AC field for 1–2 seconds. Once this stable state was established, different voltage levels were subsequently applied to the LC phase shifters, allowing them to function as various types of wave plates to steer the diffracted light into the desired spatial locations. As shown in **Table 7.1**, when the polarisation states after PG1 and PG2 are both right-circularly polarised (RCP) under applied voltages of 0.9 V

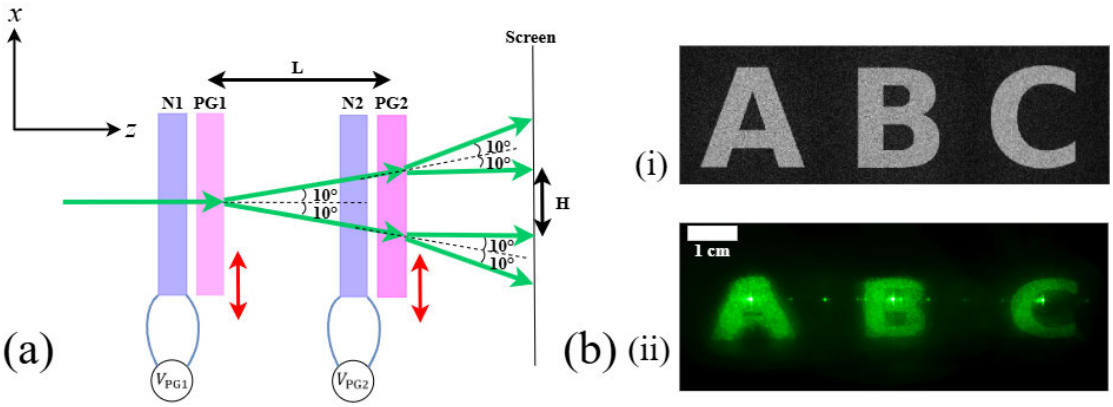


Figure 7.4: (a) Beam-steering demonstration (top view) using polarisation gratings, where two parallel PGs produce four distinct beam positions. Red arrows indicate the diffraction directions of each PG, with a diffraction angle of 10°. (b) Holographic reconstruction of the letters "A–C" under three beam-steering states: (i) the phase-only component of the Fourier spectrum, and (ii) the corresponding reconstructed holograms at different steering directions. The camera exposure time was set to 1 s, and the distance between the screen and the LC beam-steering module was 7.5 cm. Reproduced from Ref. [20] under a CC BY 4.0 licence.

and 9.0 V, respectively, the image in the replay field appears at the left position. However, when the polarisation states after PG1 and PG2 differ, the image shifts to the middle position. The third voltage state listed in Table 7.1 was not used, as it would cause the diffracted beam to overlap with that produced under the second voltage state. Finally, when the polarisation states after PG1 and PG2 are both left-circularly polarised (LCP) output under voltages of 5.0 V and 9.0 V, the image in the replay field moves to the right position.

In this configuration, three voltage states were applied per hologram cycle ($N = 3$). As shown in Figure 7.4(b)(ii), the holographic reconstruction of the letters "A–C" pattern was obtained. In this case, the CGH video sequence consisted of three frames, each generated from three sub-images using the Gerchberg–Saxton algorithm. The frame rate of the CGH video was set to $f_{\text{vid}} = 60$ fps, and the driving frequency of the waveform corresponding to the three voltage states applied to the nematic LC phase shifters was synchronised at $f_{\text{LC}} = 20$ Hz. These

results demonstrate the capability of the proposed device to generate holographic projection displays arranged in a linear horizontal array.

Table 7.1: Three different voltage states applied to the LC phase shifters (N1 and N2), corresponding to distinct beam-steering locations on the far-field screen. The 'Location' column refers to the four beam-steering positions shown in Figure 7.2(d), demonstrating the conceptual 1D holographic projection display.

Voltage State	V_{PG1} (V)	V_{PG2} (V)	Location
State 1	0.9	9.0	Location 1
State 2	0.9	2.1	Location 2
State 3 (not used)	5.0	2.1	Location 3
State 4	5.0	9.0	Location 4

As described previously, the holographic projection display can achieve beam steering to four distinct spatial locations (N = 4), forming a 2×2 array (2D) on the screen when the two PGs were orientated with their grating axes aligned perpendicular to one another. As shown in **Table 7.2**, by applying different voltage combinations to the LC phase shifters positioned before PG1 and PG2, the polarisation states of the incident light can be precisely controlled, allowing dynamic steering of the diffracted holographic image.

When the polarisation states after PG1 and PG2 are RCP light for applied voltages of 0.9 V and 9.0 V, respectively, the reconstructed holographic pattern appears at the top-left position (Location 1). When the output after PG1 becomes LCP while that after PG2 remains RCP (5.0 V and 2.1 V), the image shifts to the bottom-left (Location 2). When both PG1 and PG2 produce LCP light at voltages of 5.0 V and 9.0 V, respectively, the image moves to the bottom-right (Location 3). Finally, when PG1 outputs RCP light and PG2 outputs LCP (0.9 V and 2.1 V), the image in the replay field is directed to the top-right (Location 4).

As shown in Figure 7.5(a–c), replay-field images of letters A, B, C, and D, the University of Oxford buildings, and a panda are presented. In Figure 7.5(a–c)(i),

Table 7.2: Four different voltage states applied to the LC phase shifters (N1 and N2), corresponding to four distinct beam-steering spatial locations in the replay field. The 'Location' column refers to the four beam-steering positions shown in Figure 7.2(e), demonstrating the conceptual 2D holographic projection display.

Voltage State	V_{PG1} (V)	V_{PG2} (V)	Location
State 1	0.9	9.0	Location 1
State 2	5.0	2.1	Location 2
State 3	5.0	9.0	Location 3
State 4	0.9	2.1	Location 4

four reconstructed sub-images obtained using the phase-only component of the Fourier spectrum are presented. To achieve a flicker-free holographic projection display imperceptible to the human eye, the frame rate of the CGH video sequence was set to $f_{\mathrm{vid}} = 60$ fps, and the driving frequency of the LC phase shifters was synchronised at $f_{\mathrm{LC}} = 15$ Hz. By adjusting the distance between the LC beam-steering module (dashed box in Figure 7.1) and Lens 2, the sub-images can be brought closer together and seamlessly tiled, as demonstrated in Figure 7.5(a–c)(ii).

These results successfully demonstrate the realisation of holographic projection display enlargement. Previous reported approaches typically enlarge the field-of-view of the holographic display by employing electrically tunable LC gratings, in which the diffraction angle is controlled by electrically modifying the LC pitch to achieve angular-domain beam steering [136]. In contrast, the method proposed here operates on a fundamentally different principle. Rather than relying on continuous angular steering, our architecture achieves display enlargement through polarisation-controlled spatiotemporal replay-field tiling. Specifically, fast-response pi-cells are employed to dynamically modulate the polarisation state of the incident beam prior to a polarisation grating, enabling distinct diffraction states to be sequentially activated and temporally multiplexed. Furthermore, polarisation gratings are capable of theoretically achieving 100% % diffraction efficiency in a

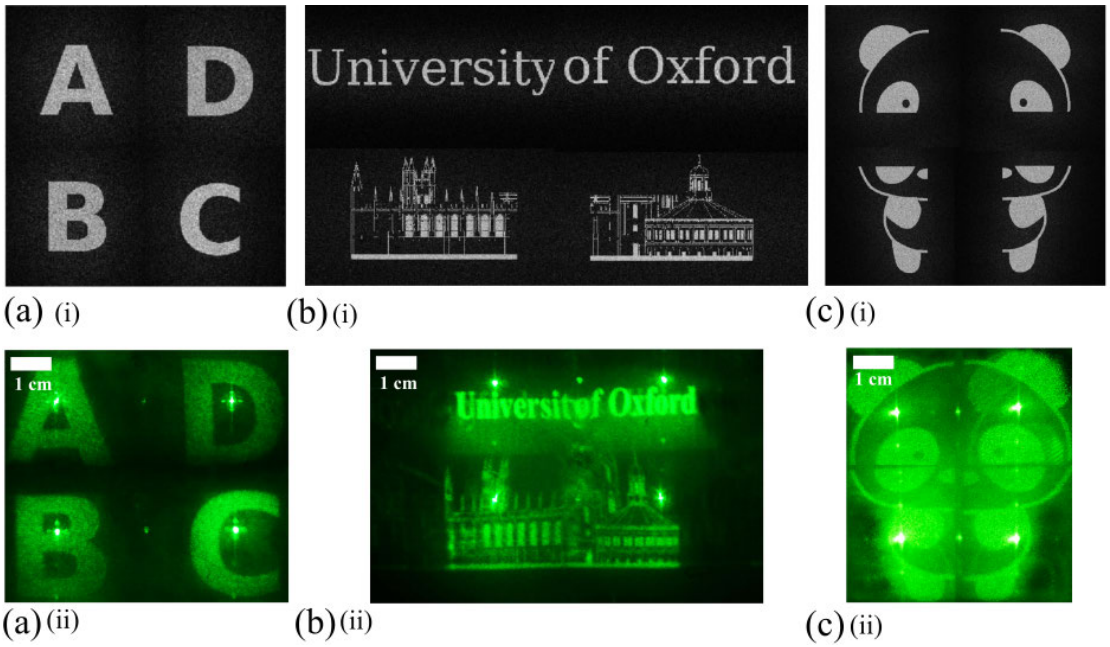


Figure 7.5: (a–c) Experimental demonstrations of holographic reconstruction of (a) letters "A–D," (b) the University of Oxford buildings, (c) a panda pattern, using the polarisation-grating-based beam-steering system. (i) Reconstructed images obtained using the phase-only component of the Fourier spectrum; (ii) corresponding tiled holographic reconstructions. The source image used for (b) was created with reference to the VectorStock "Oxford University Skyline" vector image [135], for which an Editorial License was obtained, with substantial modifications made to the final version. Permission to reuse the source image in this work was obtained through the VectorStock Editorial License. All images were recorded at an LC driving frequency of $f_{\mathrm{LC}} = 15$ Hz. The camera exposure time was set to 1 s, and the distance between the screen and the LC beam-steering module was 7.5 cm. Reproduced from Ref. [20] under a CC BY 4.0 licence.

selected diffraction order, thereby maximising light use and forming an enlarged effective display region.

As a result, the system achieves up to a three- or fourfold increase in display size compared with the original system without the PG-based LC beam-steering module. However, slight flickering remains due to the 60 fps refresh-rate limitation of the SLM (f_{th}), which prevents further increases in the driving frequency and video frame rate required to eliminate the perceptible flicker. Minor stitching artefacts may occur if the spatial separation between replay fields does not perfectly match the reconstructed tile size. However, these effects can be mitigated through appropriate

system design by selecting PGs with suitable diffraction angles and applying edge apodisation to smoothly blend adjacent replay fields. As the multiplexing number N increases, the illumination time allocated to each replay field within one period correspondingly decreases. As a result, the perceived brightness of each replay field scales approximately inversely with the number of tiles. The enlargement in the current demonstration originates from the spatial replication of the holographic image at fixed diffraction angles generated by the polarisation gratings. If PGs with different periodicities are introduced, the diffraction angles can be varied accordingly. Combining PGs with different diffraction angles would, therefore, provide greater flexibility for steering light to multiple spatial locations. The integration of additional PGs, together with a more advanced SLM featuring faster switching speeds and higher refresh rates, could potentially further expand the area of holographic projection display. As demonstrated in Section 7.5, the numerical framework and simulation results confirm the scalability of the PG-based beam-steering system, including the generation of sixteen steering locations using PGs with different periodicities.

7.5 Simulation of the Scalability of the System

The limited refresh rate of the SLM restricts the ability of the LC beam-steering module to further enlarge the size of the holographic display. To illustrate the potential scalability of the system in the future with more advanced SLM technology, simulations incorporating polarisation gratings and phase shifters were performed. Here, we reconstruct the far-field intensity distribution using the phase-only component of the Fourier spectrum of the hologram as the input field. The simulation was conducted following the theoretical framework described in Ref.

[132]. The beam emitted from the SLM is typically linearly polarised and is converted into circular polarisation by an LC phase shifter. However, for simplicity and convenience in the simulation model, the input beam was assumed to be either left- or right-circularly polarised, corresponding to the polarisation state after passing through the first LC phase shifter in the PG system, as illustrated in **Figure 7.6**(a). The assembly of the optical components was modelled using two parallel-PG combinations that steer the beam along the z and y directions, respectively. Each parallel-PG combination consists of two PGs aligned with their grating axes parallel to one another but with different periodicities, taking responsibility for beam deflection along one axis. As illustrated in Figure 7.6(a), the z-direction module includes one PG with a geometric-phase periodicity of $\Lambda = d$, producing a diffraction angle of approximately 20°, and another PG with twice the periodicity ($\Lambda = 2d$), resulting in a diffraction angle of about 10°. An identical parallel-PG combination was used for the y-direction module, also comprising PGs with periodicities of $\Lambda = d$ and $\Lambda = 2d$. This parallel-PG combination produces multiple diffraction orders whose distribution depends on the applied input phase and the retardance of an intermediate LC phase shifter.

For a single beam-steering direction, the output Jones vector was sampled over a set of uniformly divided segments and propagated through the optical elements according to the following sequence:

$$\mathbf{E}_{\text{out}} = M_2 M_{\text{sh}} M_1 \mathbf{E}_{\text{in}}, \tag{7.6}$$

where M_1 and M_2 are the Jones matrices of the two PGs, and M_{sh} represents the LC phase shifter. The output electric-field components were then Fourier-transformed to obtain the diffraction-order intensities along each direction. The diffracted intensities of the z- and y-direction modules were computed separately

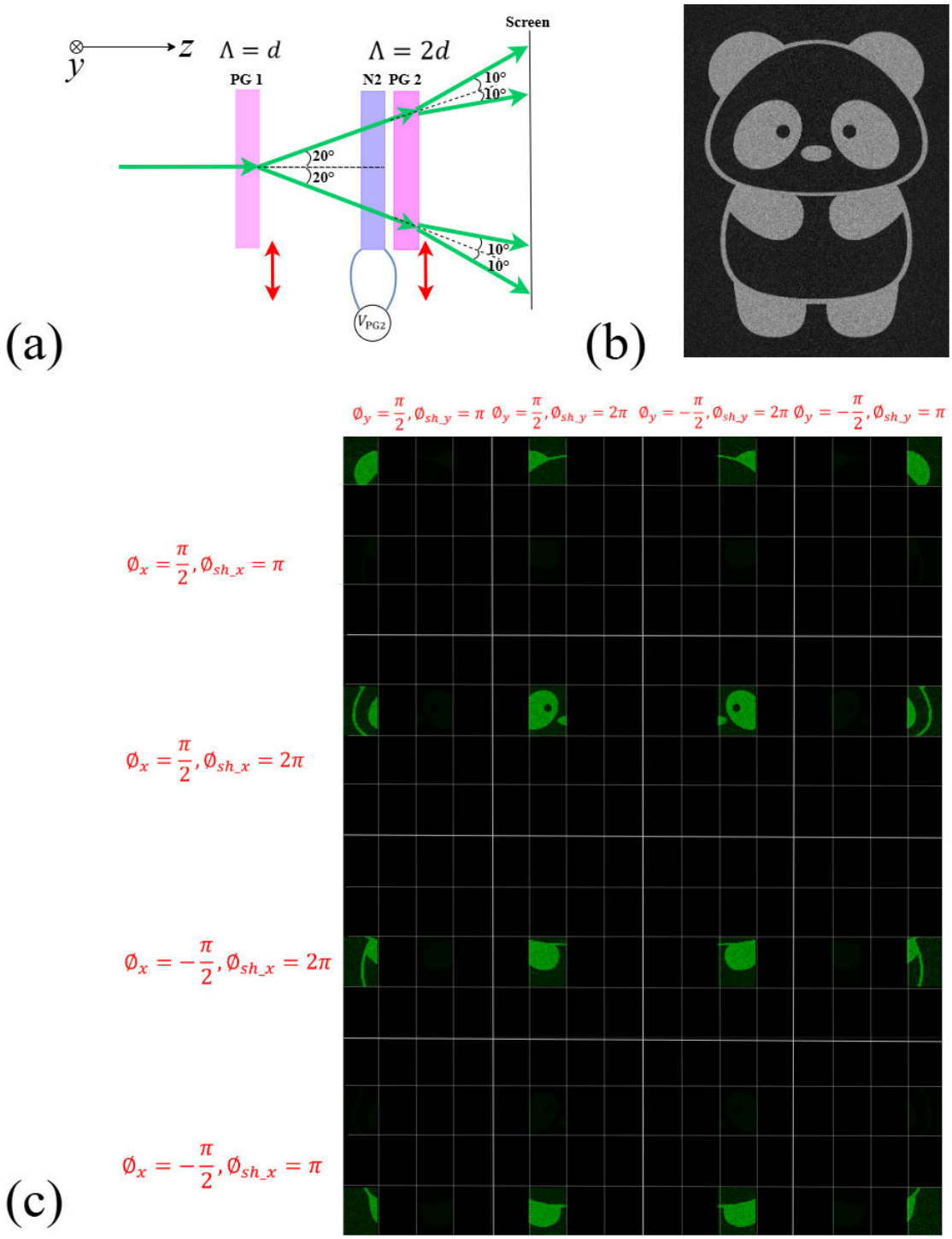


Figure 7.6: (a) Demonstration of generating sixteen beam-steering positions using polarisation gratings with different periodicities (Λ). (b) Reconstructed panda images obtained using only the phase component of the Fourier spectrum as the input for the simulation. (c) Simulated holographic projection display of the panda with sixteen separate beam steering positions. Reproduced from Ref. [20] under a CC BY 4.0 licence.

using Jones-matrix propagation and discrete Fourier transforms.

For each axis, four combinations of input circular polarisation ($\phi_z, \phi_y = \pm\pi/2$) and LC phase-shifter retardance ($\phi_{\mathrm{sh},z}, \phi_{\mathrm{sh},y} = \pi, 2\pi$) were applied. By combining the four states in the z-direction with the four states in the y-direction, a total of sixteen distinct diffraction outputs were generated, corresponding to sixteen spatially separated steering locations.

The simulation results are presented in Figure 7.6(c), where the input is the reconstructed image of the panda obtained using only the phase component of the hologram's Fourier spectrum, as shown in Figure 7.6(b). Because the holographic pattern is generated from a static phase-only input rather than time-sequential SLM frames, this approach demonstrates the intrinsic spatial scalability of the PG-based beam-steering system, unaffected by the refresh-rate limitation of the SLM.

7.6 Flexoelectric Grating for Electrically Controllable Wide Viewing Angles

To increase the diffraction angle of the holographic projection display and thereby expand the viewing angle of the reconstructed holographic image, a flexoelectric LC grating was introduced in front of the first nematic LC device. Unlike polarisation gratings, which provide fixed diffraction angles determined by their grating period, the flexoelectric grating enables electrically tunable beam diffraction through field-induced modulation of the grating structure.

The flexoelectric grating was selected because of its stable room-temperature operation and its ability to generate highly uniform diffraction patterns with minimal structural defects. These characteristics arise from the flexoelectrically induced pure splay–bend deformation and the negligible dielectric coupling of

the LC material, resulting in a more distinguishable diffraction pattern of the holographic image. Most importantly, it enables dynamic steering of the diffracted pattern over a relatively wide range of diffraction angles, providing an effective approach to dynamically controlling the position of the holographic image.

If the holographic pattern generated by the SLM is reflected and directly passes through the flexoelectric diffraction grating, without propagating through the LC beam-steering module (dashed boxes in Figure 7.1), incident light can be diffracted into multiple spatial locations under different applied DC voltages. **Figure 7.7**(a) shows the tunable viewing angles achieved with this configuration, while the measured diffraction angles for each diffraction order are summarised in **Table 7.3**.

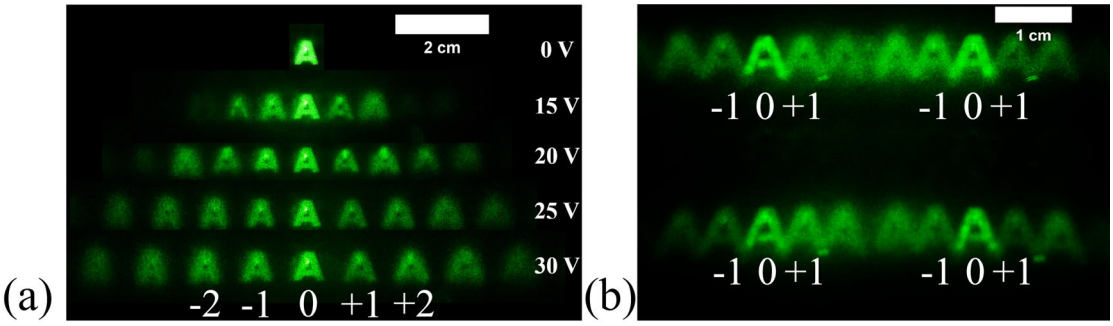


Figure 7.7: Diffraction behaviour of the holographic display incorporating a flexoelectric grating under different applied DC voltages. (a) Configuration where the flexoelectric grating replaces the LC beam-steering module. The experiment was performed at 25 °C, with the distance between the LC device and the screen set to 10 cm. (b) Configuration where the flexoelectric grating is added in front of the LC beam-steering module. The experiment was conducted at 25 °C, with the distance between the LC device and the screen set to 8 cm. The labelled diffraction orders range from −2 to +2 in (a), and from −1 to +1 at each steering position in (b). Reproduced from Ref. [20] under a CC BY 4.0 licence.

As discussed in Chapter 5, the formation and stability of the flexoelectric grating strongly depend on the applied DC voltage. Specifically, the minimum voltage required to activate the flexoelectric effect and generate a diffraction grating for beam steering was found to be 15 V. When the applied voltage exceeds 30 V, the flexoelectric grating becomes unstable, resulting in the suppression of diffraction.

Therefore, the experiments were conducted with applied DC voltages ranging from 15 V to 30 V. As shown in Figure 7.7(a), increasing the applied DC voltage results in a larger separation between each diffracted holographic image, corresponding to a reduction in the pitch of the grating induced by the enhanced flexoelectric deformation. The holographic image at the zero-order position exhibits the highest intensity in the absence of an external voltage because the incident light is not diffracted into higher orders. Once the voltage is applied, a portion of the light is redistributed into diffracted orders, reducing the zero-order intensity. At higher diffraction orders, the reconstructed holographic letters appear increasingly blurred because the higher-order beams carry significantly less optical power. Therefore, only the first three diffraction orders are considered for analysis. As summarised in Table 7.3, the diffraction angles increase with the applied voltage. When the applied voltage reaches 30 V, the second-order diffraction achieves an angle of 12.1°, which corresponds to a viewing range of 24.2°, while the third-order diffraction reaches 18.6°, which corresponds to a viewing range of 37.2°. These results demonstrate that real-time control of the viewing angle can be achieved by modulating the applied DC voltage across the flexoelectric grating.

Table 7.3: Diffraction angles of different diffraction orders under various applied DC voltages.

Voltage (V)	Diffraction angle (°)		
	1st order	2nd order	3rd order
15	4.0	8.1	N/A
20	5.1	9.8	14.4
25	5.7	11.2	16.8
30	6.0	12.1	18.6

Alternatively, the flexoelectric grating can be incorporated in front of the LC beam-steering module (dashed boxes in Figure 7.1), where each beam spot

in the 2×2 array was diffracted under an applied DC voltage of 15 V. As illustrated in Figure 7.7(b), this configuration allows the holographic display system to achieve a wider and more continuous field of view compared to the setup without the flexoelectric grating. However, the additional diffraction introduced by the flexoelectric grating also generates unwanted higher-order beams that degrade the image contrast.

The voltage-dependent diffraction angle allows the angular separation between the projected diffraction orders to be adjusted. This provides a way to control the positions of the replicated holographic images and the spacing between viewing zones. For a display designed with only a few predetermined viewing zones, fixed discrete steering angles may be sufficient. However, the present experiment demonstrates the flexibility of the flexoelectric grating to adjust the projection geometry after fabrication. Its continuous tunability may also be useful in future applications requiring adjustable beam direction, such as optical communications.

7.7 Summary

In this work, the enlargement of the replay field in holographic projection displays was demonstrated using a polarisation grating system combined with fast-response nematic LC pi-cells. This configuration enables rapidly switchable discrete beam-steering spatial locations that are visually perceived as simultaneous, thereby extending the effective projection coverage beyond the intrinsic limitations of a single spatial light modulator. The approach presented here fundamentally differs from tunable LC grating methods for holographic projection enlargement, which rely on patterned electrodes to form periodic structures that are typically limited by slow switching speeds.

The voltage-controlled pi-cells used as phase shifters exhibit rapid switching, with a rise time of 1.2 ms, which is approximately seven times faster than a Fréedericksz (anti-parallel rubbed planar-aligned) glass cell of identical thickness. Due to the characteristics of the LC diffraction grating, the optical transmittance in each state is approximately 80%, with only a small portion of the power leaking into undesired diffraction orders, thus supporting a high-quality holographic projection in the replay field. By synchronising the LC voltage driving waveforms with the computer-generated hologram sequence generated using the Gerchberg–Saxton algorithm, the reconstructed images can be dynamically directed to multiple spatial locations in real time.

Experiments confirm millisecond-scale beam steering among three discrete spatial positions arranged in a linear array (1D) and among four discrete spatial positions arranged in a two-by-two configuration (2D), depending on the relative orientation of the polarisation gratings and the polarisation state imparted by the nematic LC pi-cell phase shifters. This approach enables visual enlargement of the reconstructed holographic image by a factor of three to four through spatiotemporal tiling. Compared with angular tuning approaches, temporal multiplexing enables efficient replay field stitching while maintaining high diffraction efficiency for each replay field, since polarisation gratings can direct nearly all available optical power into a single diffraction order under the appropriate illumination polarisation condition. However, the limited refresh rate of the SLM used in this study currently constrains further expansion of the display area. Simulations further demonstrate the scalability of this method, showing that sixteen distinct beam-steering locations can be achieved by incorporating four polarisation gratings, two of which possess half-period structures. These results indicate that employing additional polarisation gratings and advanced high-refresh-rate SLMs can further extend the field of view

and the effective display area. In addition, the inclusion of a flexoelectric grating provides an extra mechanism for spatial control, enabling wide beam-steering angles under DC bias. For example, when a 30 V DC field is applied, a steering angle of 37.2° is obtained at the third diffraction order.

Overall, this holographic projection display system, assisted by LC diffraction gratings such as polarisation gratings and flexoelectric gratings, provides a practical and scalable solution for achieving holographic projection displays with visually enlarged display areas and wide viewing angles. The proposed approach lays the foundation for next-generation dynamic holographic imaging systems that combine optical efficiency, temporal multiplexing, and large-aperture performance.

8

Third Harmonic Generation Imaging of Liquid Crystals

8.1 Introduction

The study and optimisation of liquid crystal (LC)-based applications critically depend on a detailed understanding of their three-dimensional director profiles within the LC layer, which govern key optical properties such as phase modulation and beam-steering performance [18, 132, 137]. Polarised optical microscopy (POM) has been widely employed to visualise director profiles in a range of LC phases and geometries. Linear optical techniques are highly effective for obtaining two-dimensional, projection-based information and provide a convenient and non-invasive means of visualising birefringence [138, 139], in-plane director orientation, and large-scale domain structures. In addition, characterisation methods based

on electromagnetic radiation in the visible and X-ray spectral regions have also been extensively utilised [11, 12, 140]. However, these approaches have limited capability for resolving the full three-dimensional internal director configuration of liquid crystalline materials [138, 141].

To overcome the lack of depth resolution in linear birefringence-based techniques, confocal fluorescence microscopy and dye-based imaging methods have been explored for probing the 3D director field in LCs [142]. By incorporating fluorescent dyes that preferentially align with the LC director, confocal fluorescence techniques can provide depth-resolved images with optical sectioning capability, allowing visualisation of internal structures that are inaccessible to POM [143–145]. However, these approaches introduce a significant drawback. The addition of fluorescent dyes inevitably perturbs the LC system, potentially altering its elastic constants, dielectric properties, and electro-optic response, which may compromise the accuracy of quantitative measurements and device characterisation [146–150].

Harmonic generation microscopy (HGM) is a powerful, label-free imaging technique that enables three-dimensional visualisation of internal structures and has been widely applied in various cells and tissue structures [151–153]. HGM has also been used to study human and fossil vertebrate teeth [154], 3D engineered human adipose tissue [155, 156], and small organisms [152, 157]. It typically employs laser wavelengths in the near-infrared region (1200–1500 nm), which reduces the absorption and scattering of incident photons [158–160]. This technology has rarely been applied to LCs. Due to its intrinsic nonlinear contrast, HGM provides an effective route to investigate internal LC structures in 3D [161, 162], thus potentially overcoming the limitations of conventional linear optical characterisation methods discussed above.

HGM encompasses second-harmonic generation (SHG) and third-harmonic gen-

eration (THG). In the nonlinear regime, the relationship between the polarisation of the material $\vec{P}$ arising from the interaction between light and materials and the electric field strength $\vec{E}$ of incident light can be described as follows [163]:

$$\vec{P} = \varepsilon_0 \left(\chi^{(1)} \vec{E} + \chi^{(2)} \vec{E}^{\,2} + \chi^{(3)} \vec{E}^{\,3} + \cdots \right) \tag{8.1}$$

where ε_0 is the vacuum permittivity, $\chi^{(1)}$ is the first-order (linear) electric susceptibility of a material, and $\chi^{(2)}$ and $\chi^{(3)}$ are the respective second and third-order susceptibility tensors. The second-order nonlinear polarisation term $\varepsilon_0 \chi^{(2)} \vec{E}^{\,2}$ gives rise to SHG. In contrast, the third-order nonlinear polarisation term $\varepsilon_0 \chi^{(3)} \vec{E}^{\,3}$ leads to THG [164]. SHG and THG result in the generation of photons at half and one-third the illumination wavelength, respectively, and are produced at the focus of a short-pulse laser beam [158, 159], revealing the internal structure of LCs.

SHG has been widely used for microscopy of certain crystalline samples [165, 166] and for specialised biological imaging [167]. However, SHG requires non-centrosymmetric media and is thus forbidden in the bulk of centrosymmetric materials, making the technique extremely well suited for the analysis of interfaces [168].

THG microscopy is a powerful technique for producing 3D images of transparent materials, including LCs [169, 170]. Unlike SHG, THG can be present in both centrosymmetric and non-centrosymmetric media, as it does not rely on symmetry breaking [163]. Instead, the dominant contrast mechanism in THG microscopy originates from third-order susceptibility [171, 172]. In typical nematic and chiral nematic LC glass cells, the molecules are generally centrosymmetric, resulting in weak or negligible SHG signals away from the alignment layers. This characteristic makes THG particularly advantageous for internal LC imaging. Meanwhile, the THG signal originates from third-order nonlinear polarisation and scales cubically with the electric field amplitude through the third-order nonlinear term $\vec{P}^{(3)} \propto \vec{E}^{\,3}$.

Consequently, THG is generated predominantly within the central region of the focal volume, where the optical field intensity is highest. Therefore, the use of high-numerical-aperture (NA) objectives is necessary to maximise nonlinear conversion efficiency and enable high-resolution imaging. These features generate strong THG contrast, enabling direct, label-free, three-dimensional visualisation of internal LC structures [151].

However, THG is highly susceptible to optical aberrations introduced by imperfections in the imaging system. This sensitivity is particularly pronounced when operating at excitation wavelengths that fall outside the design specifications of most microscope objectives, where aberrations are more readily introduced. To mitigate these effects and improve signal efficiency, adaptive optics (AO) can be used to dynamically correct wavefront distortions and restore optimal focusing conditions [159, 173].

Over the past several decades, extensive research has demonstrated that THG microscopy is a powerful modality for biological imaging, owing to its strong sensitivity to refractive index variations, particularly at interfaces [174–176]. However, comparatively few studies have explored the application of THG imaging in LCs, with most early work dating back more than 20 years. For example, D. Yelin and J. S. Patel demonstrated that THG signals could be used to probe the internal structures of nematic and twisted nematic LCs and examined how temperature-induced distortions influence THG intensity [140, 177]. However, their studies were restricted to nematic and twisted nematic LCs, and chiral nematic LCs were not considered. In addition, the physical mechanisms responsible for the observed THG intensity variations were not fully investigated and the resulting image quality was relatively limited. Subsequently, Rajesh S. Pillai et al. reported a three-dimensional visualisation of LC defects using THG microscopy, revealing a

polarisation-dependent contrast associated with the relative orientation between the incident optical field and the local LC director [178]. Although this work clearly demonstrated the capability of THG imaging for defect visualisation, the analysis remained largely qualitative and was confined to static defect configurations. A systematic investigation of the THG contrast mechanisms across different LC device geometries and under practical operating conditions was not undertaken.

In this chapter, we investigate THG microscopy in chiral nematic and flexoelectric nematic LC structures. We successfully demonstrate the THG signal generation and show how it can be used to analyse the internal three-dimensional architecture of chiral nematic LCs across varying chiral dopant concentrations. Imaging performance is further enhanced by implementing adaptive optics. In addition, THG imaging is used to investigate the behaviour of flexoelectric nematic LC devices under different applied voltage states. The experimentally observed THG features are compared with simulation results, which show qualitative agreement in several key aspects. In addition, the introduction of adaptive optics is shown to significantly improve THG image quality. The manuscript describing this work is currently in submission.

8.2 Experimental Methods

In this section, we present the methodology for employing THG to investigate the properties of the chiral nematic LC developed in this work.

8.2.1 Materials

In this study, nematic and chiral nematic LCs are the primary materials investigated. The nematic LC mixture employed is E7 (Merck KGaA). Chiral nematic LCs were

prepared by doping E7 with the chiral dopant R811 (Merck KGaA), which has a helical twisting power (HTP) of approximately $10\,\mu m^{-1}$ [106]. To investigate THG behaviour in chiral nematic LCs across a range of pitches, various R811 mixtures of differing concentrations were prepared and tested. The helical pitches were estimated using Eq. 2.2, as introduced in Section 2.3. As detailed in **Table 8.1**, a mixture containing 1 wt.% R811 and 99 wt.% E7 produces a helical pitch of approximately $10\,\mu m$ at room temperature. Increasing the R811 concentration to 2 wt.% results in a pitch of approximately $5\,\mu m$, while 5 wt.% R811 (95 wt.% E7) produces a pitch of approximately $2\,\mu m$ at room temperature.

Table 8.1: Composition of the mixtures considered in this study with varying concentrations of R811.

Mixture ID	**R811 (wt.%)**	**E7 (wt.%)**	**Pitch (p)**
Mixture 1	1	99	$10\,\mu m$
Mixture 2	2	98	$5\,\mu m$
Mixture 3	5	95	$2\,\mu m$

The LC mixture used to fabricate the flexoelectric diffractive LC device, which will be discussed in Section 8.5.4, was the same as that presented in Chapter 5, comprising 9 wt.% BL006, 81 wt.% MLC-6882, and 10 wt.% CB7CB. Characterised by low dielectric anisotropy, this mixture exhibits the formation of a flexoelectric nematic LC diffraction grating at room temperature [18].

8.2.2 Cell Preparation

In this experiment, THG imaging requires high NA objectives to achieve efficient nonlinear signal generation and high spatial resolution. However, high-NA objectives typically have a short working distance, making it difficult to image through standard commercial glass substrates that are too thick. As a result, the LC layer located between the substrates cannot be brought into focus. To

overcome this limitation, conductive coverslips from Diamond Coatings were used as substrates. The coverslips had a thickness of 0.13–0.16 mm, a sheet resistance of 70–100 Ω per square, and dimensions of 20 mm × 20 mm. The LC glass cells were then fabricated using two coverslips with patterned transparent electrodes using the method mentioned in Section 3.2.

8.2.3 THG Imaging System

THG imaging was performed using a custom-built laser scanning microscope system, as schematically illustrated in **Figure 8.1**. An Insight DeepSee femtosecond laser (Spectra-Physics, Newport Corporation) was used as the excitation light source, delivering pulses of $\sim$ 120 fs duration at a repetition rate of 80 MHz. A central wavelength of 1205 nm was used for all THG images. The power of the laser beam was controlled by a rotating half-wave plate (HWP) followed by a polarisation beam splitter (PBS), enabling continuous adjustment of the incident power. A beam block (B) was placed on the S-side of a polarisation-sensitive beam splitter. The beam was expanded and collimated using a beam-expanding telescope formed by lenses L1 ($f = 50$ mm) and L2 ($f = 150$ mm). A diode laser at 633 nm was introduced into the optical path through a flip mirror for beam alignment and system calibration. Beam power was monitored using a power meter positioned at a designated pick-off point along the beam path. The beam was then further expanded by lenses L3 ($f = 100$ mm) and L4 ($f = 150$ mm) to match the clear aperture of the downstream optics, including a deformable mirror and an objective lens.

A deformable mirror (Boston Micromachine Corporation Multi3.5) was used for sensorless adaptive optic aberration correction, compensating for wavefront distortions introduced by the optical system and the samples. Beam scanning was achieved using a pair of galvanometric mirrors (Galvo X, Galvo Y) that provided

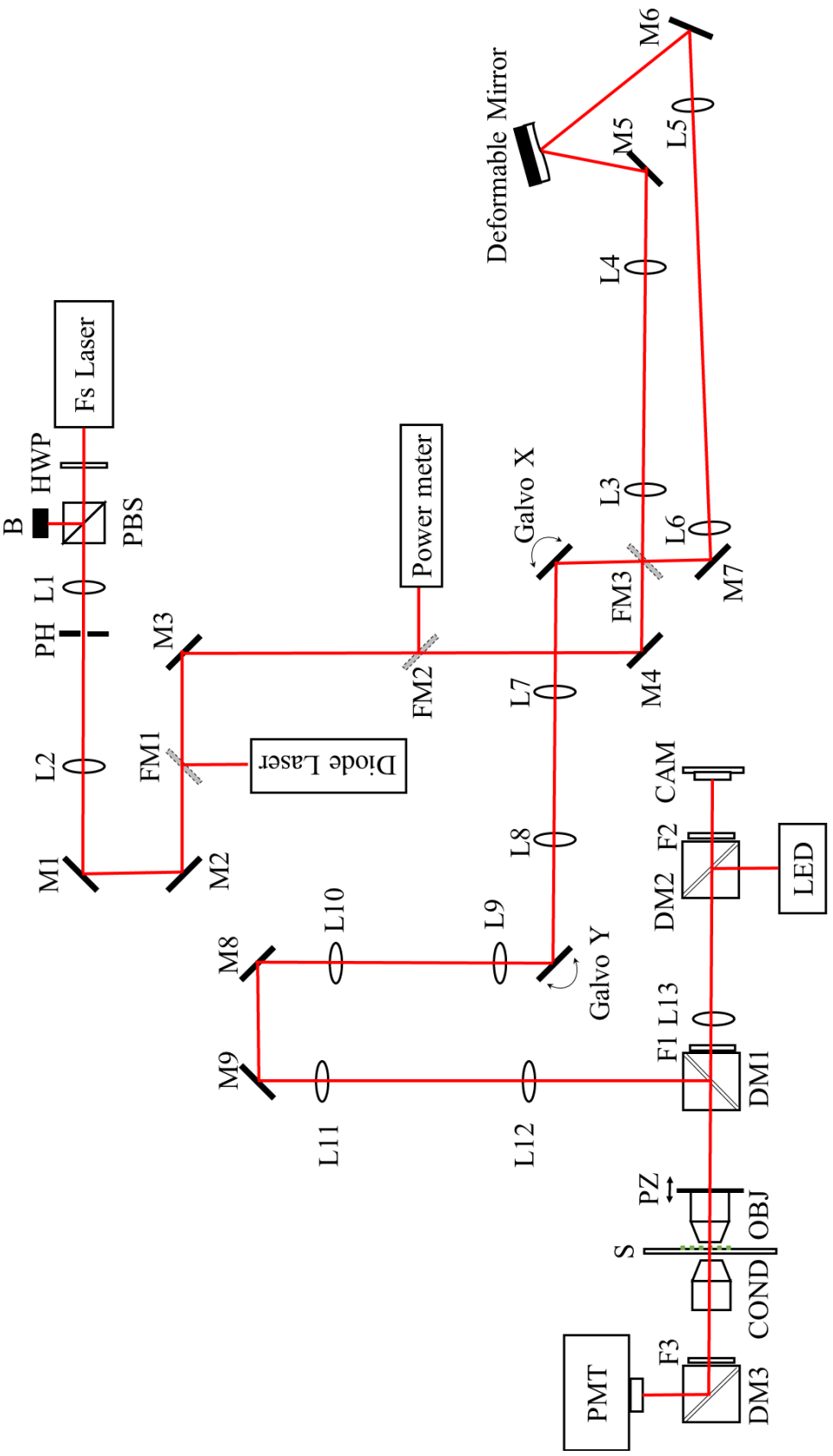


Figure 8.1: Schematic of the THG microscopy setup used to characterise LC samples. The red lines are included for visual clarity to indicate the optical paths, and the excitation wavelength lies in the infrared and is not visible. AS: aperture stop; B: block; CAM: camera; COND: condenser; DM1–DM3: dichroic mirrors; F1–F3: filters; FM1–FM3: flip mirrors; Galvo X/Y: galvanometric scanners; HWP: half-wave plate; L1–L13: achromatic doublet lenses; LED: illumination source; M1–M9: mirrors; OBJ: objective lens; PBS: polarising beam splitter; PH: pinhole; PMT: photomultiplier tube; PZ: piezo stage; S: sample. The THG microscopy setup was developed in collaboration with Dr. Jingyu Wang.

independent deflection in the X and Y directions, and thus enabled lateral spatial mapping during laser scanning. For an XY raster scan, the total time required to acquire a single frame, denoted T_{frame}, is given by

$$T_{\text{frame}} = T_{\text{retrace}} + N_x N_y t_{\text{dwell}} \tag{8.2}$$

where N_x and N_y represent the number of pixels along the X and Y directions, respectively, T_{retrace} is the retrace time required for the scanning beam to return to the starting position for the next scan line or frame, and t_{dwell} is defined as the duration for which the laser beam remains at each pixel to collect the signal. Setting $t_{\text{dwell}} = 10\,\mu\text{s}$, scan sizes of 88×128 and 216×256 pixels produce frame acquisition times of 0.164 s and 0.655 s, corresponding to retrace times of 51.36 ms and 102.04 ms, respectively.

A series of relay lens pairs was used to relay the deformable mirror and the Galvo scanners to the conjugation plane of the objective back pupil throughout the optical system. Specifically, lenses L5 ($f = 200$ mm) and L6 ($f = 150$ mm) established pupil conjugation between the deformable mirror and the Galvo X. Lenses L7 ($f = 75$ mm) and L8 ($f = 75$ mm) relayed the rotation axes of the Galvo X and Galvo Y. Lenses L9 ($f = 75$ mm) and L10 ($f = 120$ mm) transferred the conjugate plane of the Galvo Y to the downstream optical path. Finally, lenses L11 ($f = 75$ mm) and L12 ($f = 150$ mm) relayed the upstream conjugation plane to the focal plane of the microscope objective, allowing telecentric scanning of the sample.

The sample (S) was mounted on the XY translation stage. The excitation beam was focused onto the sample using an Olympus UAPO N340 40× water-immersion microscope objective (OBJ, NA = 1.15) mounted on a piezo stage (PZ) that enables precise axial positioning for three-dimensional imaging. The forward-propagating nonlinear signal transmitted through the sample was collected by an Aplanat

Achromat condenser (CND, NA up to 1.4) and subsequently spectrally filtered by filter F3 and DM3 to suppress residual excitation light. The filtered signal was reflected by a dichroic mirror (DM3) and directed onto a photomultiplier tube (PMT), where the weak THG signal was converted into an electrical signal and amplified for detection. In parallel, an auxiliary LED-based transmission imaging path incorporating filters F1, F2 and F3, together with dichroic mirrors DM1, DM2 and DM3, was implemented for sample observation and locating. The average power at the sample is around 30 mW.

The optical configuration used in this work therefore enabled depth-resolved THG imaging with high spatial resolution, allowing direct visualisation of internal structural variations within the nematic and chiral nematic LC phases.

8.3 Third Harmonic Generation

The relationship between the LC director profile and the THG signal is very complex, and the majority key coefficients ($\chi^{(3)}$) have not been measured for most LC materials. However, it is well established in THG imaging that the gradient of the effective refractive index along the direction of the optical field is the primary mechanism responsible for the generation of the THG signal [140]. As illustrated in the following, **Figure 8.2**(a) depicts a chiral nematic LC in which the helix axis (HA) is aligned along the z-axis for the Grandjean state (or the x-axis for the ULH state) over one pitch, p. In this configuration, the effective refractive index experienced by the optical field varies periodically between the extraordinary refractive index (n_{e}) and the ordinary refractive index (n_{o}), as shown in Figure 8.2(b). Figure 8.2(c) further presents the corresponding refractive index gradient along the z-axis (or the x-axis for the ULH state). Four gradient peaks

(two positive and two negative) occur within one pitch, leading to four potential THG signal stripes. Figure 8.2(d) illustrates the convolution of the refractive index gradient along the z-axis (or the x-axis for the ULH state). The resulting convolved profile is subsequently used in Section 8.4.2 to simulate the THG signal, incorporating the finite spatial resolution of the optical system.

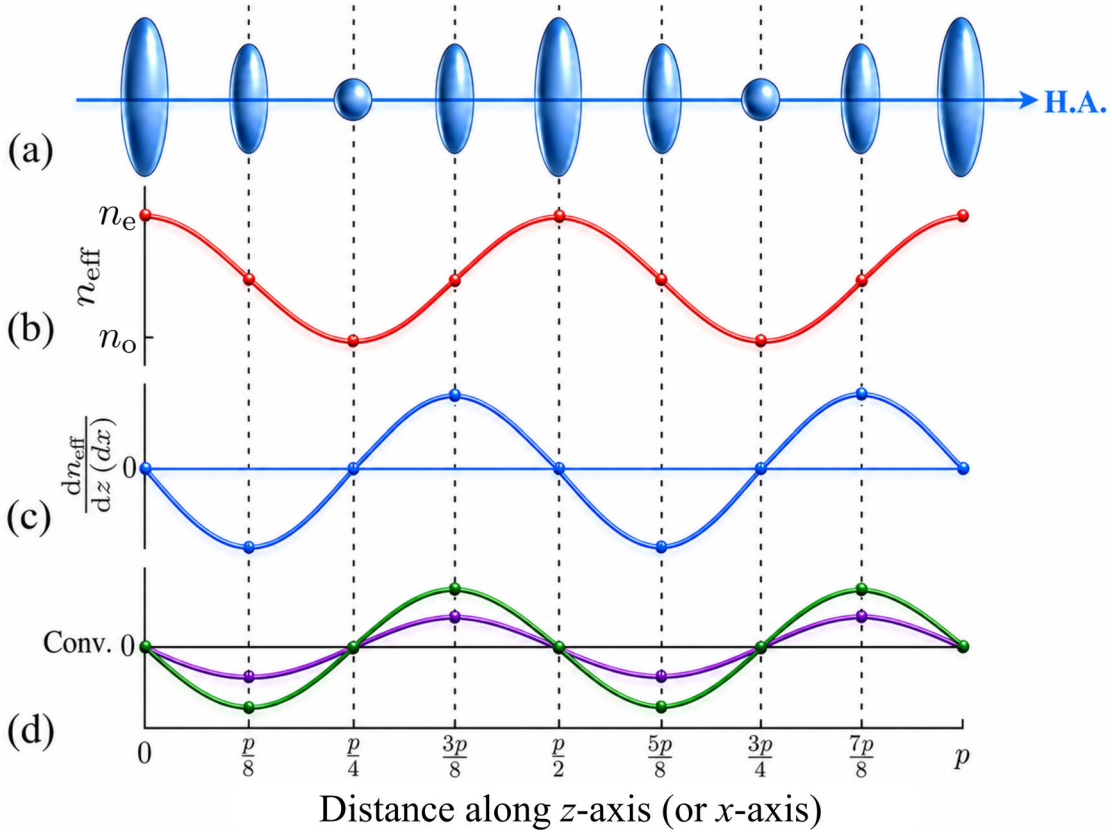


Figure 8.2: Schematic illustration of third-harmonic generation in a chiral nematic LC over one pitch p along the z-axis for the Grandjean state (or the x-axis for the ULH state). (a) The spatial variation of the chiral nematic LC director along the helix axis (H.A.). (b) The corresponding effective refractive index experienced by the optical field (n_{eff}) oscillates between the extraordinary (n_{e}) and ordinary (n_{o}) refractive indices. (c) The gradient has alternating positive and negative regions. (d) The convolution (Conv.) of the refractive index gradient. The green and purple lines represent the convolution curves for different focal spot sizes.

The spatial variation of the effective refractive index can be estimated from the local orientation of the LC director with respect to the optical electric field.

For a chiral nematic LC in the Grandjean state, the effective refractive index experienced by a linearly polarised optical field is given by

$$\frac{1}{n_{\text{eff}}^2(z)} = \frac{\cos^2\theta(z)}{n_{\text{e}}^2} + \frac{\sin^2\theta(z)}{n_{\text{o}}^2} \tag{8.3}$$

Here, $\theta(z)$ denotes the local angle between the LC director $\vec{n}(z)$ and the direction of the optical field [179].

For a Grandjean state whose axis is along the z-direction, the director can be written as

$$\vec{n}(z) = (\cos kz, \sin kz, 0), \tag{8.4}$$

where $k = \frac{2\pi}{p}$, and p is the helical pitch. If the optical field is linearly polarised along the x-direction, $\vec{E} = (1, 0, 0)$, the angle $\theta(z)$ is determined by the projection of the director onto the optical field direction,

$$\cos\theta(z) = \vec{n}(z) \cdot \vec{E} = \cos kz \tag{8.5}$$

Consequently, inserting Eq. (8.5) into the effective refractive index relation Eq. (8.3) gives

$$\frac{1}{n_{\text{eff}}^2(z)} = \frac{\cos^2(kz)}{n_{\text{e}}^2} + \frac{1-\cos^2(kz)}{n_{\text{o}}^2} \tag{8.6}$$

This can be rearranged as

$$\frac{1}{n_{\text{eff}}^2(z)} = A + B\cos^2(kz) \tag{8.7}$$

where $A = \frac{1}{n_o^2}$, $B = \frac{1}{n_e^2} - \frac{1}{n_o^2}$. Thus, the effective refractive index is

$$n_{\text{eff}}(z) = \left[A + B\cos^2(kz)\right]^{-\frac{1}{2}} \tag{8.8}$$

The spatial gradient of the effective refractive index along the z-axis is, therefore, given by

$$\frac{dn_{\text{eff}}}{dz} = -\frac{1}{2}\left[A + B\cos^2(kz)\right]^{-\frac{3}{2}} B\frac{d}{dz}\cos^2(kz) \tag{8.9}$$

the gradient becomes

$$\frac{dn_{\text{eff}}}{dz} = \left[A + B\cos^2(kz)\right]^{-\frac{3}{2}} Bk\sin(kz)\cos(kz) \tag{8.10}$$

Then, this can be written as

$$\frac{dn_{\text{eff}}}{dz} = \frac{Bk}{2}\sin(2kz)\left[A + B\cos^2(kz)\right]^{-\frac{3}{2}} \tag{8.11}$$

This expression shows that, in the Grandjean state with the optical field polarised along the x-axis, the effective-index gradient exhibits a dominant $\sin(2kz)$ dependence. Since $k = \frac{2\pi}{p}$, the spatial period of this gradient is $\frac{p}{2}$, corresponding to half of the helical pitch. A similar result is obtained for the ULH state when the director is described as $\vec{n}(x) = (0, \cos kx, \sin kx)$, with the helix axis aligned along the x-direction. When the optical field is polarised along the y-axis, $\vec{E} = (0, 1, 0)$, the effective refractive-index gradient also follows $\frac{dn_{\text{eff}}}{dx} \propto \sin(2kx)$. This result is consistent with the illustration shown in Figure 8.2(c).

In investigating the Grandjean state of chiral nematic LC using THG, an important consideration must be addressed. When the LC material is spatially uniform within the focal spot, the third harmonic waves generated on either side of

the focus interfere destructively, resulting in zero net THG signal [151]. Therefore, a sufficient gradient in the refractive index across the focal volume is required. Consequently, when imaging chiral nematic LCs, the pitch must fall within an appropriate range. If the pitch is excessively long, the LC director remains uniform within the focal spot, and the absence of a refractive index gradient leads to destructive interference and zero net THG signal, as shown in **Figure 8.3**(a). Conversely, if the pitch is too short, the effective refractive index undergoes rapid periodic changes across the focal volume. In this case, the averaging effect of many oscillations within the focal spot again results in destructive interference and no detectable signal, as shown in Figure 8.3(b).

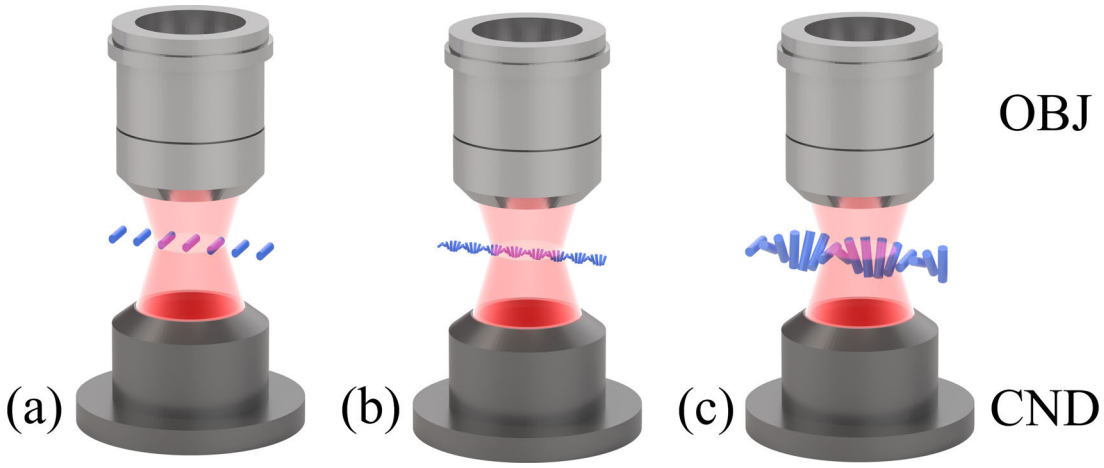


Figure 8.3: Schematic illustration of the interaction between a focused beam and chiral nematic LC structures with different pitches for third-harmonic generation. (a) long-pitch helix, (b) short-pitch helix, and (c) optimal-pitch helix. OBJ is used to focus the excitation beam, while CND collects the forward-generated THG signal. The lighter region denotes the effective focal volume, within which the fundamental intensity is sufficiently high to generate a detectable THG signal.

The optimal condition is achieved when the length scale of the refractive index gradient is comparable to the focal spot size of the laser beam. Under these circumstances, a gradient of effective refractive index exists within the focal volume, giving rise to a measurable THG signal, as shown in Figure 8.3(c). Under this

condition, with a fixed pitch, variations in focal spot size influence the convolution profile. As illustrated in Figure 8.2(d), the purple curve corresponds to a larger focal spot size, whereas the green curve represents a smaller one. The increased spot size improves spatial averaging, producing a smoother profile.

8.4 Simulations

In this section, we simulate the LC director profiles and the corresponding THG signals in both the ULH and Grandjean states.

8.4.1 Simulations of LC Director Profile

In our work, we used a computational model based on the theoretical framework previously mentioned in Section 6.2. The model uses finite-difference spatial derivatives to simulate the director configuration of chiral nematic LCs under strong surface anchoring conditions. The total free energy used in the model is given by Eq. 6.2, and the corresponding schematic illustration of the homogeneous alignment is presented in **Figure 8.4**.

When no electric field is applied, the chiral nematic LC is in the Grandjean state, where the helix axis is aligned along the z-axis with a constant pitch p_G, as shown in Figure 8.4(a). As illustrated in Figure 8.4(b), upon application of an electric field, an ULH configuration is formed in which the helical axis becomes parallel to the substrate surfaces. This configuration is inherently incompatible with the pre-existing uniform planar alignment imposed by surface treatment, leading to structural distortions within the transition regions [180].

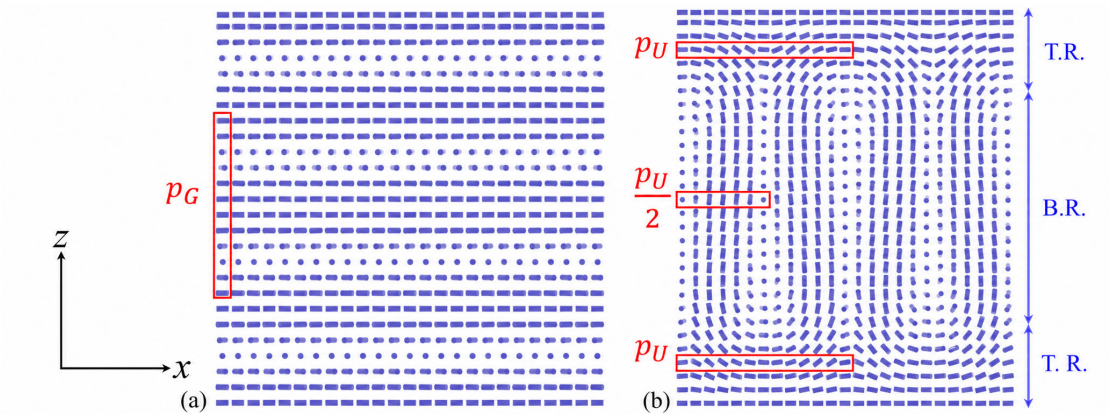


Figure 8.4: Simulated long-pitch chiral nematic LC director profiles of the (a) Grandjean state and (b) ULH state with continuous unwinding under an applied voltage of 5 V_{rms}. The elastic constants were chosen to closely match the reported values of the nematic LC mixture, E7, at room temperature, with $K_{11} = 13.4$ pN, $K_{22} = 6.7$ pN, and $K_{33} = 16.7$ pN. The dielectric anisotropy was set to $\Delta\varepsilon = 14$. The red boxes indicate the pitch p_G of the Grandjean state, the pitch p_U of the transition region (T.R.) in the ULH state, and the half-pitch $\frac{p_U}{2}$ of the bulk region (B.R.) in the ULH state.

8.4.2 Simulations of THG Signal

To represent and interpret the THG images, we determine the local gradients in refractive index for the LC and then convolve these with the laser field of the focal spot from the THG imaging system to produce a qualitative prediction of the THG image.

The THG signal was numerically simulated based on the LC director distribution obtained from the director-profile simulation. This dataset provides the three spatial components of the local LC orientation vector at each spatial position and was used as the input for calculating the gradient of the effective refractive index. To model the optical response, the effective refractive index experienced by the optical field n_{eff} was calculated using Eq. (8.3). Therefore, the gradients of n_{eff} in specific directions were calculated using finite differences. To account for the finite resolution of the optical system, the gradient field was convolved with a three-dimensional Gaussian point spread function (PSF). This convolution

simulates the spatial averaging imposed by the focused excitation beam.

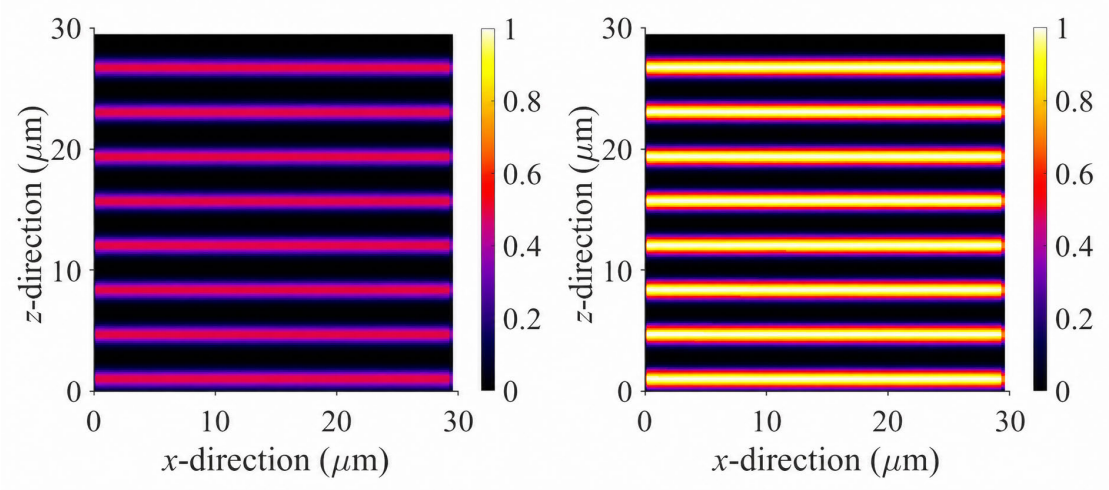


Figure 8.5: Simulated THG intensity maps of a chiral nematic LC in the Grandjean state. (a) A smaller gradient of n_{eff} results in a weaker THG signal. (b) A larger gradient of n_{eff} leads to a significantly enhanced THG response with higher intensity. The colour bar represents the normalised THG intensity, with values scaled from 0 to 1 using a common global maximum for direct comparison between the two cases. The optical field is along the x-axis. In this simulation, the refractive indices are set to $n_o = 1.5$ and $n_e = 1.75$ and 1.9, respectively, with a pitch of $p = 15\,\mu\text{m}$. The thickness of the LC layer was set to $30\,\mu\text{m}$.

To investigate the effect of the gradient of the effective refractive index $\frac{dn_{\text{eff}}}{dz}$, simulations were performed for different gradient magnitudes. As shown in **Figure 8.5**, the corresponding THG intensity maps for a chiral nematic LC in the Grandjean state were calculated and normalised. The case with a larger gradient produces a stronger THG signal, indicating that the THG process is predominantly driven by spatial variations in the effective refractive index experienced by the optical field. This approach establishes a direct link between the LC director distribution and the resulting nonlinear optical response.

8.5 THG Results

This section presents THG signals detected by the PMT from chiral nematic LCs with varying pitches, investigated in both the Grandjean and ULH states of chiral

nematic LC devices, as well as from conventional nematic and flexoelectric nematic LC devices. Adaptive optics were employed to enhance signal quality.

There is an issue that in THG imaging, particularly when investigating the x–z or y–z planes, due to the refractive index mismatch at the interface between LC and the glass, the mechanical displacement of the piezo stage does not correspond directly to the actual focal shift within the sample. Therefore, the THG-measured thickness d_{THG} will be larger than the real physical device thickness d_{real}. The relationship is

$$d_{\mathrm{THG}} = \frac{n_{\mathrm{LC}}}{n_{\mathrm{glass}}} d_{\mathrm{real}} \tag{8.12}$$

Assuming that the thickness measured by THG scanning is $d_{\mathrm{THG}} = 35\,\mu\mathrm{m}$, $n_{\mathrm{LC}} = 1.7$, and $n_{\mathrm{glass}} = 1.5$, the actual thickness of this LC device can be estimated as

$$d_{\mathrm{real}} = \frac{n_{\mathrm{glass}}}{n_{\mathrm{LC}}} d_{\mathrm{THG}} = 30.9\,\mu\mathrm{m} \tag{8.13}$$

This issue occurs only when investigating the x–z or y–z planes and does not arise when examining the x–y plane. In all subsequent normalised intensity profiles along the z-axis, the axis scale has been calibrated using the corrected physical distance. Although Eq. 8.12 is generally valid under the small-NA approximation, it remains applicable in our high-NA configuration because of the use of aberration correction.

Vignetting is another issue that can affect the THG images by causing non-uniform brightness across the field of view. This effect is associated with the galvo-mirror scanning system, since the excitation beam may not pass through the optical system with the same efficiency at different scan positions. As a

result, some regions may appear brighter, while other regions appear weaker, even if the LC structure is uniform across the sample. This effect may come from non-uniform illumination, imperfect optical alignment or different collection efficiency across the image [181].

8.5.1 Nematic LC

To establish a reference for the generation of THG signal in LCs, a conventional nematic LC mixture, E7, was first investigated. In this case, the director orientation is primarily governed by surface anchoring and any externally applied electric field, as mentioned in Chapter 2. When different electric field magnitudes are applied, the LC in the bulk area will tilt at a different angle. However, almost the whole bulk area has the same tilt angle across the LC layer, resulting in a relatively uniform refractive index distribution in the bulk. Therefore, as shown in **Figure 8.6**, the THG signal remains zero in the bulk area.

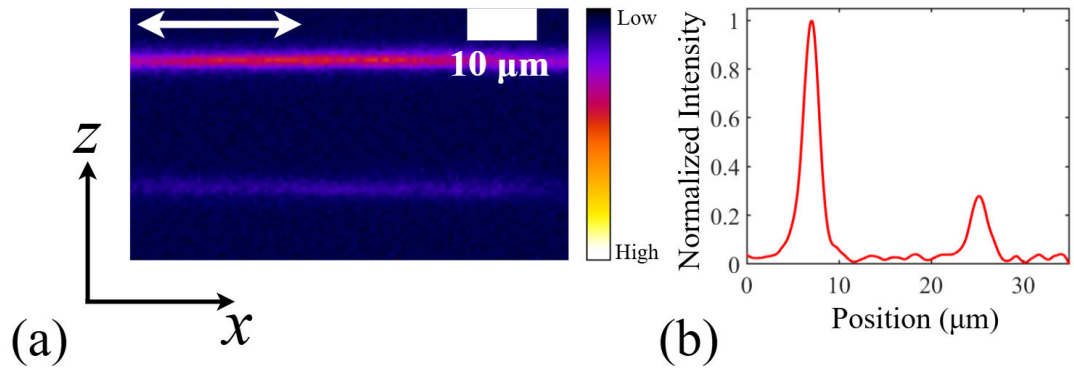


Figure 8.6: (a) x–z plane THG signal of neat E7 under an applied voltage of 5 V_{rms}. (b) Corresponding normalised intensity profile along the z-axis, where the intensity was normalised by setting the maximum pixel intensity in the THG image to 1. The colour bar in (a) represents the relative THG signal intensity, with brighter colours corresponding to stronger THG signals. The white double-headed arrow indicates both the rubbing direction and the optical field, aligned parallel to the x-axis. The LC cell has a thickness of approximately 18 µm, and the experiment was conducted at a temperature of approximately 20 °C. This experimental work was carried out in collaboration with Dr. Jingyu Wang.

However, as seen in Figure 8.6, enhanced THG signals are observed near the substrate interfaces. In this configuration, with the rubbing direction aligned parallel to the x-axis, LC molecules near both the top and bottom substrates have their long axes aligned parallel to the rubbing direction. The glass–LC interface introduces a refractive index mismatch. Along the x-axis, the effective refractive index corresponds to the extraordinary refractive index, n_{e}, which is approximately 1.75 [182], and is higher than that of the glass substrate ($n_{\mathrm{glass}} = 1.5$). This significant refractive index mismatch leads to a strong THG response at the interfaces. The THG signal at the bottom substrate is comparatively weaker than that at the top, which is due to a combination of depth-dependent optical aberrations and polarisation-related effects during beam propagation through the LC layer.

This behaviour is consistent with the known sensitivity of THG imaging to refractive index discontinuities and gradients, and serves as a useful baseline for comparison with more complex structures such as chiral nematic and flexoelectric nematic LC devices.

8.5.2 Chiral Nematic LC (Grandjean state)

In the Grandjean state of a chiral nematic LC, where the helix axis is perpendicular to the substrates with no electric field applied, we set the rubbing direction and incident optical field parallel to the x-axis, as shown in **Figure 8.7**(a). The corresponding intensity variation along the z-axis is shown in Figure 8.7(b). In this investigation, a mixture of 1 wt.% R811 and 99 wt.% E7 (Mixture 1) is used, which is expected to produce a pitch of $p = 10\,\mu\mathrm{m}$. In this case, the length scale of the refractive index gradient is comparable to the focal spot size, which is approximately $2.5\,\mu\mathrm{m}$ in our setup.

Similar to the case of a neat nematic LC, the significant refractive index mismatch between the LC molecular long axis and the glass substrate leads to strong THG signals near the surfaces, as shown in Figure 8.7(a). The THG signal is also weaker at the bottom substrate as a result of aberrations and polarisation-related effects, as mentioned above.

The bulk region of the experimental THG signal obtained from the Grandjean state of the chiral nematic LC, shown in Figure 8.7(a), exhibits strong similarity to the simulated result presented in Figure 8.5(a). The simulation was performed using the same look-up table and the same values of n_o and n_e. This close agreement demonstrates the consistency between the experimental results and the simulated THG response.

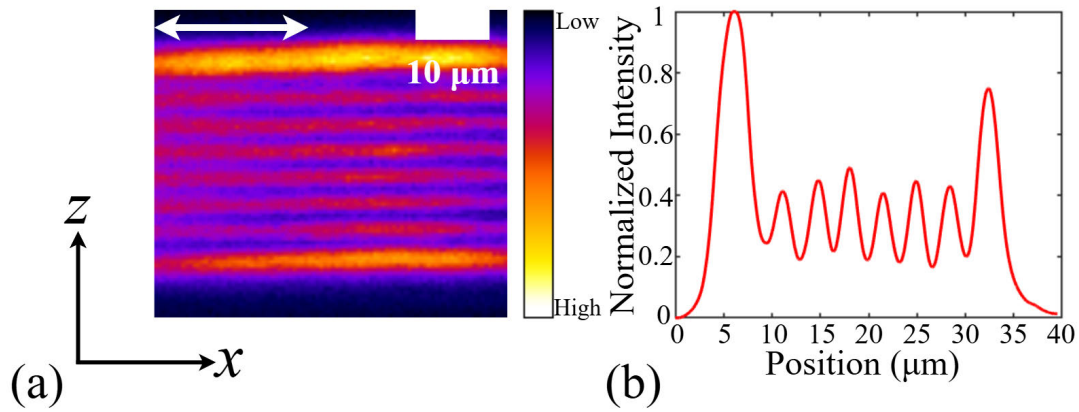


Figure 8.7: (a) The x–z plane THG signal of a chiral nematic LC (Mixture 1) in the Grandjean state. (b) The corresponding normalised intensity profile along the z-axis, where the intensity was normalised by setting the maximum pixel intensity in the THG image to 1. The colour bar in (a) represents the relative THG signal intensity, with brighter colours corresponding to stronger THG signals. The white double-headed arrow represents both the rubbing direction and the optical field, aligned parallel to the x-axis. The thickness of the LC layer is around 30 µm. The working temperature of this experiment is around 20 °C. This experimental work was conducted in collaboration with Dr. Jingyu Wang.

8.5.3 Chiral Nematic LC (ULH state)

In the ULH state, the generation of the THG signal is not expected to be limited by the focal spot size of the laser beam, as the helix axis lies horizontally along the x-axis. Consequently, refractive-index modulation occurs primarily in the lateral direction, allowing the THG signal to avoid complete destructive interference along the z-axis. Therefore, Mixtures 1–3 can all be used for THG characterisation in the ULH state. To generate a THG signal in the ULH state, it is essential that the helix axis be perpendicular to the optical field. If the helix axis is parallel to the optical field, the effective refractive index in the bulk corresponds solely to the ordinary refractive index, n_{o}, resulting in no gradient of the effective refractive index along the optical field direction ($\frac{dn_{\mathrm{eff}}}{dz\,(dx)} = 0$). Consequently, no THG signal is generated.

The simulation results presented in Section 8.4.1 demonstrate that the pitch differs between the bulk and transition regions when a chiral nematic LC in the ULH state is subjected to a 5 V_{rms} applied electric field. This phenomenon has been well documented in the literature, which highlights that long-pitch chiral nematic LCs more readily undergo continuous unwinding, leading to variations in the periodicity across the cell thickness. Therefore, to investigate this effect, Mixture 1 with a pitch of 10 µm was employed in this study [180]. The top glass substrate was then gently rubbed in one direction under the applied electric field, thereby facilitating the formation of a more uniform ULH structure.

Conventional POM lacks the capability to visualise the surface transitional regions effectively. Researchers have previously employed fluorescence confocal polarising microscopy to capture three-dimensional images of these distorted domains [180]. Therefore, it is worthwhile exploring the potential of label-free THG imaging as an alternative imaging modality for investigating this phenomenon.

The THG response observed in **Figure 8.8** can be interpreted in conjunction

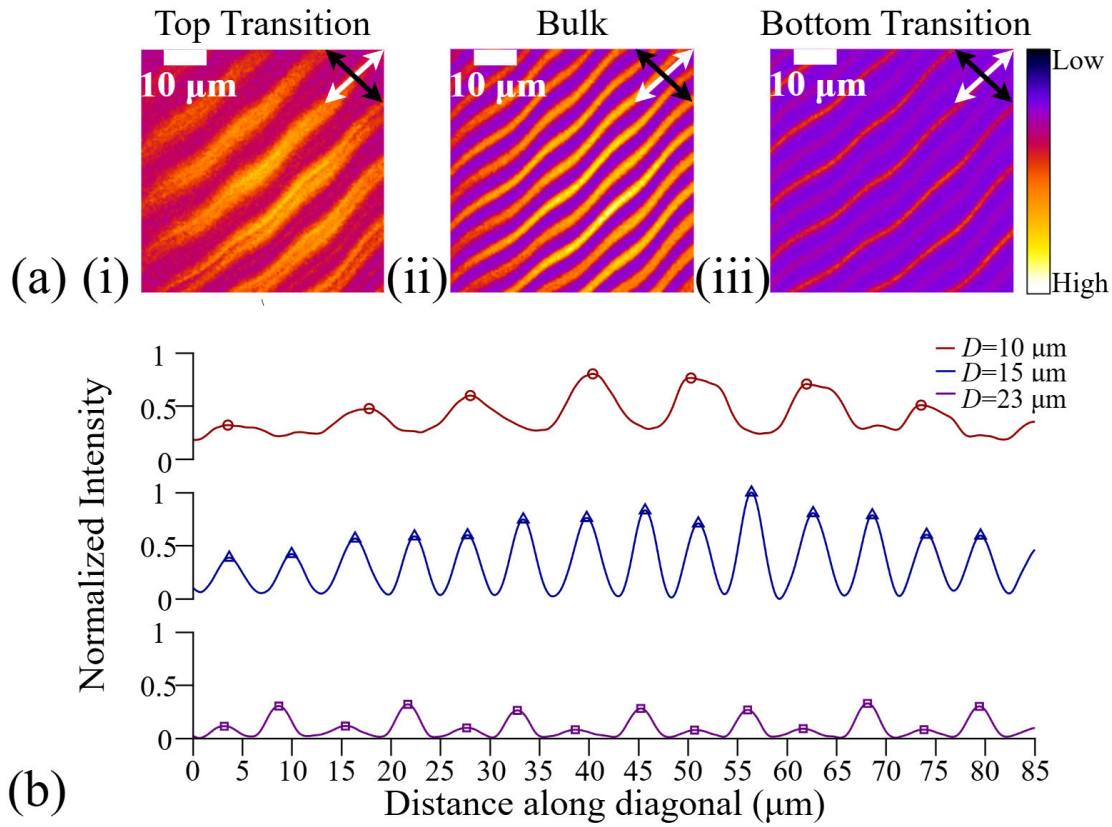


Figure 8.8: (a) THG signals of the chiral nematic LC (Mixture 1) in the ULH state at different depths within the LC layer: (i) $D = 10\,\mu m$ (top transition region), (ii) $D = 15\,\mu m$ (bulk region), and (iii) $D = 23\,\mu m$ (bottom transition region) under an applied voltage of 5 V_{rms}. (b) Corresponding normalised intensity profiles along the diagonal, which is parallel to the helix axis of the ULH structure from the top-left to the bottom-right. The colour bar in (a) represents the relative THG signal intensity, with brighter colours corresponding to stronger THG signals. Results in (b) were normalised using the same intensity scale, with the global maximum intensity set to 1. The white double-headed arrow represents both the rubbing direction and the optical field, aligned parallel to the x-axis. The black double-headed arrow represents the orientation of the helix axis of the chiral nematic LC. The LC layer has a thickness of approximately 30 µm, and the experiment was conducted at a temperature of around 20 °C. This experimental work was carried out in collaboration with Dr. Jingyu Wang.

with the director profile of the ULH state (shown in Figure 8.4(b)). Different x–y planes were investigated at varying depths along the z-axis from the upper surface (D). Figure 8.8(a)(i) and Figure 8.8(a)(iii) show the x–y plane of the THG signal for Mixture 1 ($p = 10\,\mu\text{m}$) in the top and bottom transition regions, respectively, where one stripe is observed per pitch. Figure 8.8(a)(ii) presents the x–y plane in the bulk region, where two stripes appear per pitch.

Meanwhile, as shown in Figure 8.8(b), a notable feature of the depth-resolved THG images is the lateral shift of the bright stripes along the helix axis. Near the top substrate, THG signal stripes appear in alternating lateral positions with a periodicity of one full pitch (10 µm). In the bulk region, bright stripes are observed at every half pitch (5 µm). Near the bottom substrate, the THG signal also appears with a full-pitch periodicity (10 µm), but is shifted to complementary lateral positions, corresponding to an approximate half-pitch (5 µm) offset relative to the top surface case. This behaviour is consistent with the simulated director profile shown in Figure 8.4(b), in which two transition regions form near the top and bottom substrates due to surface anchoring, while the bulk retains a simple ULH structure. Because the transition regions are approximately symmetric about the mid-plane, the director deformation near the bottom substrate can be regarded as the mirror counterpart of that near the top substrate.

This successfully demonstrates the capability of THG imaging to resolve pitch variations across different regions through the thickness of the LC cell, and investigate the LC structure in 3D, providing richer structural information than conventional techniques such as polarisation microscopy.

As shown in **Figure 8.9**, Mixture 2 (2 wt.% R811, $p = 5\,\mu\text{m}$) and Mixture 3 (5 wt.% R811, $p = 2\,\mu\text{m}$) were also investigated to examine the THG imaging response in shorter-pitch samples. In both mixtures, two stripes per pitch were

consistently observed throughout the entire LC device, indicating a uniform pitch structure throughout the sample thickness, unlike the depth-dependent pitch variation observed in Mixture 1. This phenomenon is expected. In a short-pitch device, defect structures, such as disclination lines, are more likely to form near the boundaries. In this case, the LC tends to release the elastic distortion by forming defects rather than maintaining a continuous director deformation, resulting in the absence of a smooth pitch variation between the surface and the bulk. Conversely, in a long-pitch device, as shown in Figure 8.4(b), continuous unwinding is more likely to occur without the formation of defects, which can directly lead to a pronounced pitch difference between the surface region and the bulk area [180]. Compared with the THG images of Mixture 1 shown in Figure 8.8, these results clearly demonstrate that different R811 concentrations produce distinct pitch differences, highlighting the capability of THG imaging to differentiate LC devices with different compositions through their pitch characteristics.

In THG imaging of LCs, refractive index variations between the transition regions and the bulk across the LC cell introduce sample-induced spherical aberration due to the refractive index of the LC being higher than that of the immersion medium. Therefore, aberration correction is required to reduce specimen-induced optical aberrations and improve image quality. The standard 5N sensorless AO correction was applied to the sample imaging plane prior to imaging acquisition [183].

To evaluate the effect of aberration correction on the THG signal, sensorless AO was performed at a selected depth along the z-axis from the upper surface of $D = 13\,\mu\text{m}$ within the bulk region of the LC device, where the THG signal is dominated by refractive-index inhomogeneities inside the LC layer rather than by strong interface contributions. After optimisation, the AO correction phase pattern

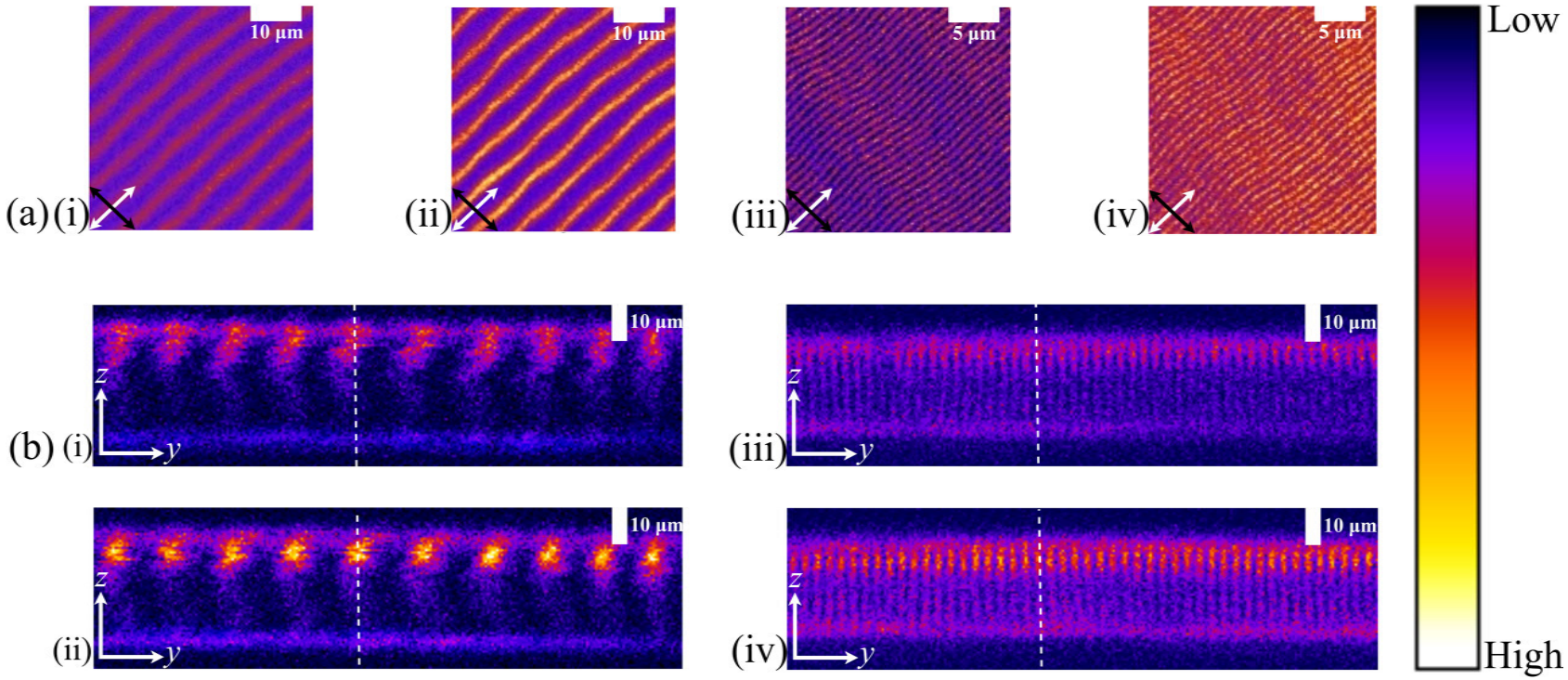


Figure 8.9: THG signals of chiral nematic LCs in the ULH state (bulk region, $D = 13\,\mu\text{m}$). (a) x–y plane images and (b) corresponding y–z cross-sections for Mixture 2 (i, ii) and Mixture 3 (iii, iv). Images (i) and (iii) are obtained before adaptive-optics correction, while (ii) and (iv) are after correction. The black double-headed arrow denotes the helix axis of the chiral nematic LC. The white double-headed arrows indicate both the rubbing direction and the optical field direction, aligned parallel to the x-axis. The white scale bars in (a) correspond to distances in the x–y plane, while the scale bars in (b) represent z-axis distance only. The colour bar represents the relative THG signal intensity, with brighter colours corresponding to stronger THG signals. The LC glass cells containing Mixture 2 and Mixture 3 had air gaps of 28 µm and 23 µm, respectively, and all measurements were conducted at 20 °C. This experimental work was carried out in collaboration with Dr. Jingyu Wang.

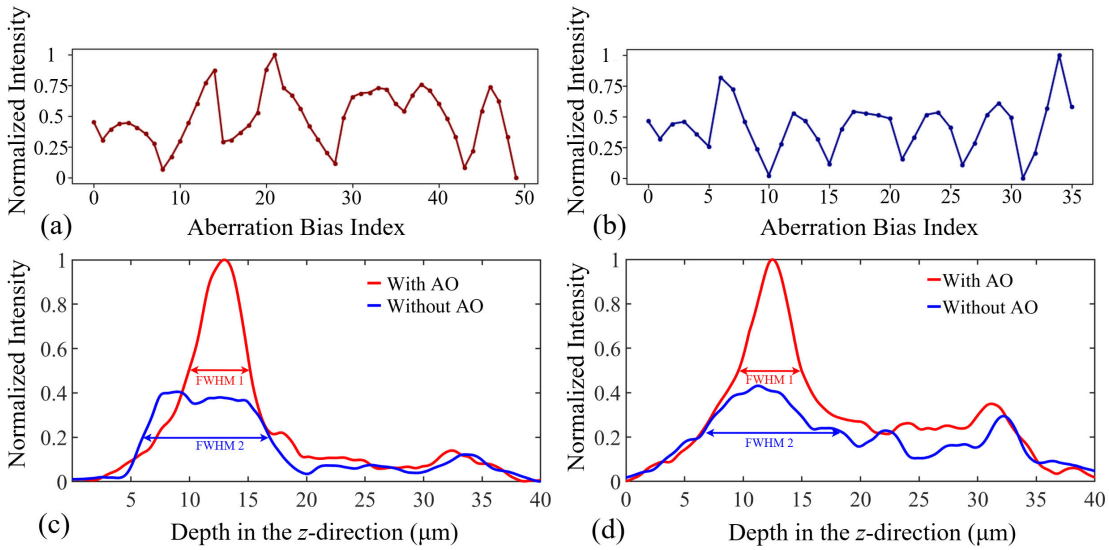


Figure 8.10: Convergence of the sensorless adaptive optics image metric for THG image enhancement in (a) Mixture 2 and (b) Mixture 3. THG intensity profiles along the z-axis for (c) Mixture 2 and (d) Mixture 3, extracted from the dashed white line across a bright stripe in the y–z plane of Figure 8.9(b). Profiles obtained with and without adaptive optics correction are compared. The profiles with and without AO correction were normalised using the same intensity scale, with the global maximum intensity set to 1.

obtained at this depth was fixed and subsequently applied during volumetric imaging of the entire LC device. Figure 8.9 compares the x–y and y–z planes acquired with and without AO correction. Compared with images acquired without AO correction (Figure 8.9(i, iii)), AO-corrected images (Figure 8.9(ii, iv)) exhibit a clear enhancement of the THG signal and improved axial resolution. This improvement is mainly attributed to the compensation of spherical aberration caused by the refractive-index mismatch between the LC device and the immersion water medium. Such aberration predominantly broadens the axial point spread function and reduces the peak intensity.

The convergence behaviour of the AO optimisation process for mixtures 2 and 3 is shown in **Figure 8.10**(a) and Figure 8.10(b), respectively. The total image intensity was used as the AO optimisation metric. Adaptive optics correction was

performed using a modal sensorless optimisation strategy based on the sequential 5N algorithm described by Facomprez et al. [184]. Using this approach, the metric was optimised sequentially over groups of five bias images corresponding to different selected Zernike modes. Approximately two iterations of correction were sufficient for convergence. After optimisation, the total-intensity metric increased relative to the initial uncorrected value, indicating effective enhancement of the THG signal through AO correction.

To further quantify the improvement in axial signal confinement, intensity profiles were extracted along the dashed white line in the y–z plane shown in Figure 8.9(b). The corresponding normalised THG intensity profiles for mixture 2 and mixture 3 are shown in Figure 8.10(c) and Figure 8.10(d), respectively. In both cases, compensation of the wavefront distortion results in a more confined axial intensity profile. Compared with the profiles obtained without AO correction, the corrected profiles exhibit more than a 150% increase in peak intensity and an approximately 50% reduction in the axial full width at half maximum (FWHM), where FWHM 1 and FWHM 2 denote the axial full widths at half maximum of the intensity profiles obtained with and without AO correction, respectively.

It should also be noted that the AO correction was optimised at a single axial layer near the upper region of the LC device. For simplicity, the same correction obtained at this optimisation plane was subsequently applied to the acquisition of the entire imaging volume. Therefore, the improvement is expected to be most pronounced at depths close to the optimisation plane, while the correction efficiency may gradually decrease farther away from this layer. Overall, these results confirm that aberration correction effectively enhances image quality.

Notably, in the experimental results for both the ULH and Grandjean states, we observe that within each pitch there are only two pronounced stripes. This

observation is not consistent with our initial understanding of the THG generation mechanism, which would predict four strong bright stripes per pitch. We suggest that the primary reason for this discrepancy lies in the intrinsic complexity of LCs, particularly their anisotropic permittivity tensor with off-diagonal components. These off-diagonal terms can have opposite signs, so that one contributes constructively to the THG signal while the other suppresses it. In addition, some studies have reported that only positive refractive index gradients contribute to THG generation, whereas negative gradients do not produce a detectable THG response [175]. This will require further study in the future to allow for a more complete understanding of THG images in LC.

8.5.4 Flexoelectric Nematic LC

As discussed in Chapter 5, the internal structure of the flexoelectric nematic LC device is inherently complex. The flexoelectric mixture used in Chapter 5 forms a periodic splay-bend structure under an applied electric field, as demonstrated in Chapter 4 and Chapter 5. Previous studies suggest that when an applied voltage exceeds the threshold value, the splay–bend configuration responds differently depending on the magnitude of the electric field. As illustrated in **Figure 8.11**, numerical simulations of the internal structure of the LC director under the flexoelectric effect are presented in different planes. The elastic constant was set at $K = 13$ pN, the dielectric anisotropy ($\Delta\varepsilon$) was set at $\Delta\varepsilon = 0.01$ to ensure that the flexoelectric effect is dominant, and the effective flexoelectric coefficient was defined as $e^* = 5.5$ pC/m. All parameters used in the simulation were based on the experimental mixture, comprising 9 wt.% BL006, 81 wt.% MLC-6882, and 10 wt.% CB7CB.

The director reorientation behaviour considered in this simulation follows the

flexoelectric and dielectric mechanisms discussed in Chapter 4. Assuming the rubbing direction is along the x-axis, a moderate electric field exceeding the threshold (low-voltage state) induces a gradual reorientation of the LC director across the x–y, x–z, and y–z planes. This behaviour arises from the combined influence of flexoelectric and dielectric effects. In contrast, under a sufficiently strong electric field (high-voltage state), the LC director exhibits a dominant tilt in the y–z plane, while the tilting components in the x–y and x–z planes become negligible, as demonstrated in Figure 8.11.

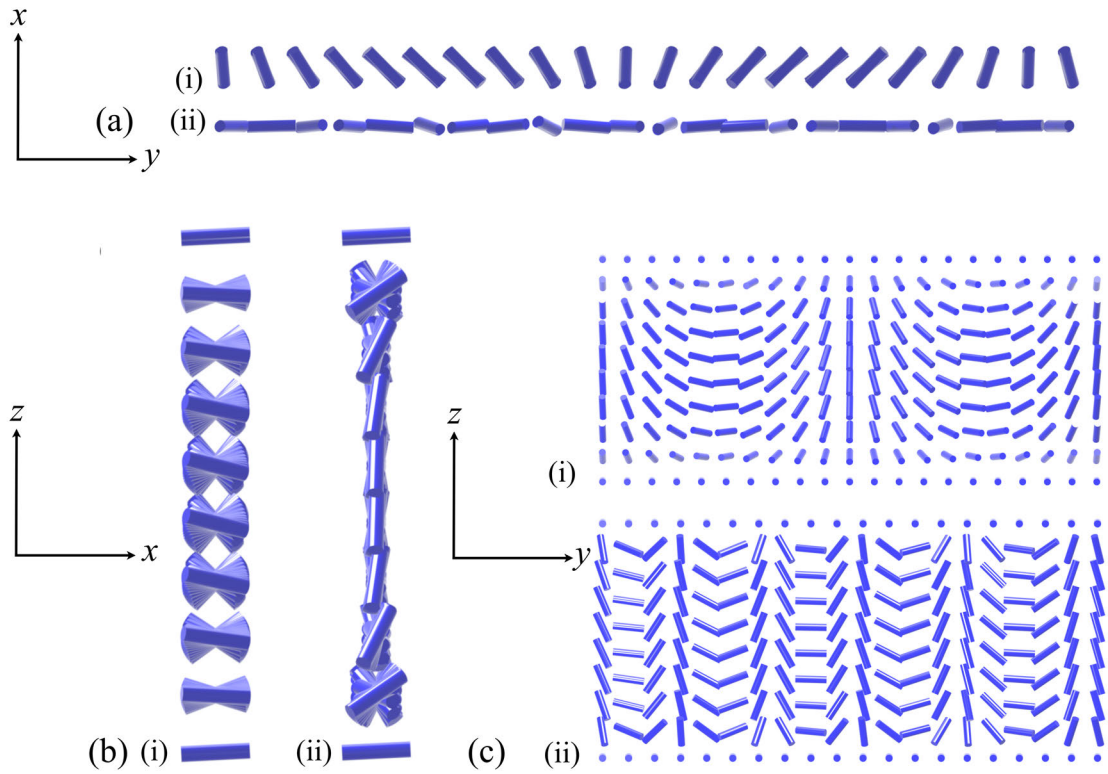


Figure 8.11: LC director configurations under flexoelectric coupling in the (a) x–y plane (without surface anchoring), (b) x–z plane (with surface anchoring), and (c) y–z plane (with surface anchoring) for (i) the low-voltage state and (ii) the high-voltage state. The rubbing direction is along the x-axis. The simulations were conducted with parameters: $K = 13$ pN and $e^* = 5.5$ pC/m.

The flexoelectric nematic LC devices investigated in this experiment were

fabricated using coverslips and had a thickness of approximately 10 µm. The low-voltage state, in which the LC director exhibits behaviour similar to that shown in Figure 8.11(i), was obtained at approximately 12–25 V. In contrast, the high-voltage state, corresponding to the director behaviour shown in Figure 8.11(ii), was observed at approximately 40–60 V.

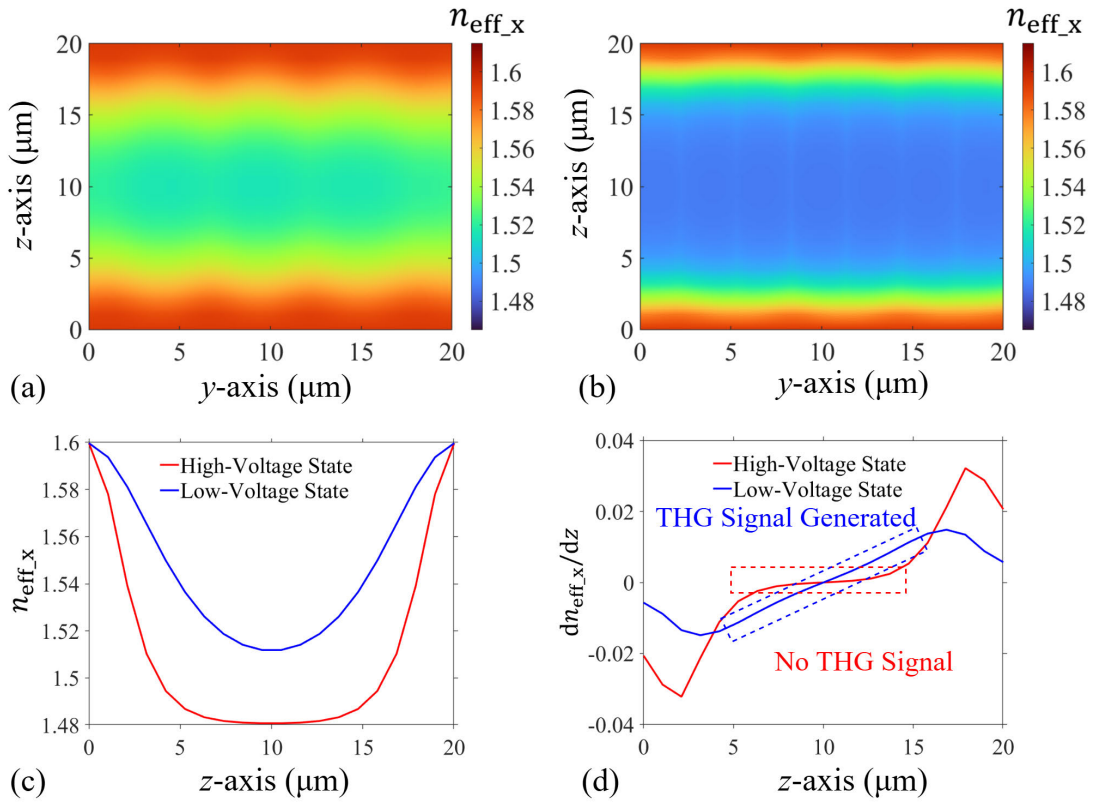


Figure 8.12: Spatial distributions of the x-polarised effective refractive index, $n_{\text{eff_x}}$, in the y–z plane for the (a) low-voltage state (15 V) and (b) high-voltage state (60 V). (c) Variation of $n_{\text{eff_x}}$ along the z-axis at a fixed position of $y = 15$ µm for both voltage states. (d) Corresponding spatial gradient, $\frac{dn_{\text{eff_x}}}{dz}$, along the z-axis at $y = 15$ µm for the two voltage states. The simulations were conducted with parameters: $K = 13$ pN, $e^* = 5.5$ pC/m, $n_{e_\text{flexo}} = 1.6$, $n_{o_\text{flexo}} = 1.48$, and $d = 20$ µm.

Figure 8.12 presents the simulated spatial distributions of the x-polarised effective refractive index, $n_{\text{eff_x}}$, in the y–z plane for two different operating states of the device, where the rubbing direction is aligned along the x-axis. In the simulations of the flexoelectric nematic LC mixture used in this work, the

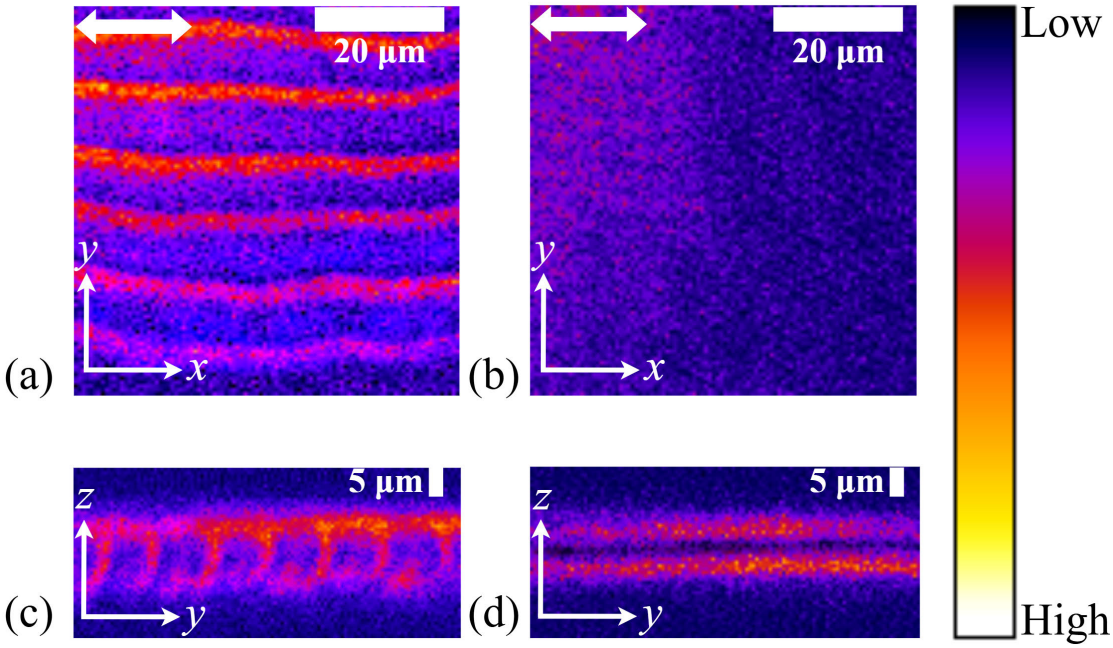


Figure 8.13: THG signals from the flexoelectric nematic LC device in the x–y plane within the bulk region ($D = 8\,\mu m$) under (a) 15 V DC and (b) 60 V DC, and in the y–z plane across the device thickness under (c) 15 V DC and (d) 60 V DC. The white scale bars in (a) and (b) correspond to distances in the x–y plane, while the scale bars in (c) and (d) represent distances along the z-axis only. The colour bar represents the relative THG signal intensity, with brighter colours corresponding to stronger THG signals. The white double-headed arrow represents both the rubbing direction and the optical field, aligned parallel to the x-axis. The LC layer has a thickness of approximately 10 µm, and the experiment was conducted at a temperature of around 20 °C. This experimental work was carried out in collaboration with Dr. Jingyu Wang.

extraordinary refractive index, $n_{e,\text{flexo}}$, and the ordinary refractive index, $n_{o,\text{flexo}}$, were set to 1.60 and 1.48, respectively. **Figure 8.13** presents the experimentally measured THG intensity distributions of the flexoelectric nematic LC device under both low- and high-voltage operating conditions, characterised in the x–y and y–z planes.

Figure 8.12(a) shows the simulated low-voltage state under an applied DC voltage of 15 V. Near the substrates, strong surface anchoring constrains the LC molecules, maintaining the effective refractive index along the x-axis, $n_{\text{eff_x}}$, close to the extraordinary refractive index, $n_{e,\text{flexo}}$. The simulation results in

Figure 8.11(c)(i) and Figure 8.12(a,c) indicate that the refractive-index variation reaches its maximum within the bulk region, particularly around the mid-plane of the cell at $z = 10\,\mu\text{m}$. In this region, $n_{\text{eff_x}}$ gradually varies through the bulk of LC, producing a significant refractive-index gradient ($\frac{dn_{\text{eff_x}}}{dz}$) and consequently a strong THG response, as illustrated in Figure 8.12(d). As a result, THG signals are generated not only near the interfaces but also throughout the bulk region of the device. This behaviour is consistent with the experimental THG images obtained for $D = 8\,\mu\text{m}$ under an applied DC voltage of 15 V, as shown in Figure 8.13(a,c).

In contrast, in the simulated high-voltage state at 60 V Figure 8.12(b,c), the bulk region of the device becomes optically more homogeneous, exhibiting a nearly uniform and lower x-polarised effective refractive index. As shown in Figure 8.12(d), $n_{\text{eff_x}}$ within the bulk region approaches $n_{o,\text{flexo}}$ and no longer exhibits significant spatial variation. Consequently, the gradient $\frac{dn_{\text{eff_x}}}{dz}$ becomes largely confined to the top and bottom boundary regions, while remaining close to zero throughout the bulk. As a result, in the high-voltage state, the THG signal is strongly suppressed within the LC bulk and remains primarily localised near the interfaces. This behaviour is in excellent agreement with the experimental results shown in Figure 8.13(b,d).

The experimental results are consistent with the refractive-index-gradient analysis obtained from the corresponding simulations presented above, supporting the proposed theoretical model. These findings confirm that the spatial evolution of the THG intensity within the flexoelectric nematic LC device is predominantly governed by the voltage-dependent redistribution of the effective refractive-index gradient across the LC layer. This agreement further supports our understanding of the THG generation mechanism and provides deeper insight into the optical behaviour of the flexoelectric nematic LC device.

8.6 Summary

This chapter presented a comprehensive investigation of THG imaging applied to nematic and chiral nematic LCs, combining experimental characterisation and numerical simulations. The underlying mechanism of THG in LCs is discussed, highlighting the critical role of gradients in the effective refractive index along the optical field direction and the size of the focal spot of the laser beam. It was demonstrated that THG signals are strongly associated with regions exhibiting significant gradients of the effective refractive index, particularly near interfaces and within periodically modulated structures.

Numerical simulations were performed to model both the LC director profiles and the corresponding THG response. The experimentally observed THG signal is consistent with the simulated results, supporting the validity of the simulation and indicating that the THG signal arises from spatial variations in the LC director field. This agreement further validates the use of a gradient-based convolutional model to predict the THG response.

Experimentally, THG imaging was applied to different LC configurations. In nematic LCs, strong signals were observed near substrate interfaces due to refractive index mismatch. In chiral nematic LCs, distinct THG patterns were identified in both the Grandjean and ULH states. The depth-resolved measurements revealed variations in pitch and structural distortions near the surfaces and the bulk region. Furthermore, the implementation of adaptive optics significantly improved signal intensity and axial resolution by correcting aberrations induced by the LC medium, demonstrating its effectiveness for high-quality THG imaging. THG imaging was also used to investigate flexoelectric nematic LC devices under different applied electric fields. The results revealed clear differences in director deformation between low-voltage and high-voltage states, consistent with the behaviours investigated in

Chapters 4 and 5, highlighting the capability of THG imaging as a powerful tool for visualising electrically driven structural changes in complex LC systems.

Overall, this chapter demonstrates that THG imaging is a powerful, non-invasive technique for resolving three-dimensional LC structures and provides valuable insight into the relationship between LC director configuration, refractive index modulation, and nonlinear optical response.

9

Conclusions and Future Work

9.1 Thesis Conclusions

This thesis investigates several distinct types of LC diffractive structures, encompassing theoretical modelling, numerical simulation, experimental fabrication, electro-optic characterisation, and application to holographic display systems and advanced imaging techniques.

Chapter 2 established the theoretical and conceptual foundations underpinning the subsequent work presented in this thesis. The fundamental properties of LC phases were reviewed, including birefringence, light propagation in anisotropic media, and the elastic continuum theory governing director deformations. The dielectric and flexoelectric effects, which are central to the operation of the devices studied in Chapters 4 and 5, were also introduced to provide the necessary theoretical background for later discussion. In addition, the structural characteristics of

the uniform lying helix configuration were described, as this represents the key LC structure used in the chiral-dopant-based diffractive devices discussed in Chapter 6. The chapter then introduced the basic principles of diffraction theory and related them to LC-based diffractive structures. Finally, the role of beam steering elements in SLM-based holographic display systems was outlined, thereby providing the broader application context for the experimental contributions of this thesis.

Chapter 3 summarised the experimental methods and characterisation techniques used throughout this thesis. Standard but essential techniques in LC research were presented, including LC cell preparation, the formulation of nematic and chiral nematic LC mixtures, and polarisation optical microscopy for the direct visualisation of director textures. Two additional characterisation methods were introduced with specific relevance to later chapters. The flexoelectro-optic tilt angle measurement technique was described as a means of quantifying the flexoelectric response of chiral nematic LC cells, laying the groundwork for the tilt angle analysis presented in Chapter 6. Capacitance measurement was outlined as a tool for extracting key material parameters, including the elastic constants and dielectric permittivity of the LC systems, which are essential for supporting the modelling, mixture optimisation, and interpretation of the experimental results presented in the later chapters.

Chapters 4–6 trace the development of flexoelectric and chiral nematic LC diffractive devices, examining how these devices can be harnessed to achieve controllable beam steering. Chapter 4 established the theoretical foundations for understanding and predicting the diffraction behaviour arising from the flexoelectric effect in nematic LCs. Several analytical frameworks were reviewed and critically assessed, culminating in the development of a nonlinear numerical model that most accurately describes the LC director configuration under the flexoelectric effect.

The model further predicted the far-field diffraction behaviour and simulated the appearance of the LC grating texture under polarising optical microscopy. These results provide useful guidance for LC mixture design and device optimisation, as they allow the expected electro-optic behaviour to be evaluated before cell fabrication, thereby reducing experimental time and effort. The predictions obtained in Chapter 4 are subsequently compared with the experimental results presented in Chapter 5, providing a means of validating the nonlinear model.

Chapter 5 reported the experimental realisation of flexoelectric diffraction gratings, demonstrating that both AC and DC electric fields could be employed to induce flexoelectric nematic LC grating structures at room temperature. In addition, it was demonstrated that the pitch of the grating could be systematically tuned through the applied field conditions, ranging from approximately 3 µm to 8 µm, which in turn controlled the diffraction angle. The limitations of this grating platform were also identified and discussed, including crystal formation, which can affect the long-term stability of the mixture, and imperfect grating uniformity, which degrades diffraction quality. The flexoelectric nematic LC structures examined in Chapters 4 and 5 were therefore thoroughly characterised through modelling, simulation, and experiment, establishing them as well-understood reference systems for the holographic projection display studies discussed in Chapter 7 and the THG imaging investigations presented in Chapter 8.

Chapter 6 demonstrated the fabrication and characterisation of diffraction gratings based on chiral nematic LCs, exploiting both the intrinsic structural periodicity of the cholesteric helix and its susceptibility to electric field driven unwinding transitions. By applying a customised waveform and carefully controlling the cell thickness to pitch ratio, a switchable and rotatable grating was achieved. This behaviour arises from the asymmetric flexoelectric tilt of the LC director

induced under the applied electric field. The resulting rotatable grating allowed continuous azimuthal rotation of the diffraction pattern throughout the 360° range by controlling the duration of specific segments within a tailored driving waveform, eliminating the need for mechanically moving components. This represents a significant advance over conventional grating technologies that rely on the physical rotation of optical elements. The demonstrated capability extends the functionality of LC based beam steering devices and broadens their potential applications, including adaptive optics, optical communications, and holographic display systems.

Chapter 7 builds directly on this foundation by demonstrating one of the most compelling practical applications of beam steering, namely, the enlargement of both the viewing angle and the projected image size in a holographic display system. A polarisation grating based beam steering module was designed and experimentally validated to enlarge the holographic projection field of view through spatiotemporal tiling, achieving a fourfold enlargement of the holographic image experimentally. The simulation results further indicated that a sixteenfold enlargement is achievable with the adoption of advanced spatial light modulators, suggesting considerable potential for further scaling of the system. In addition, the flexoelectric nematic LC gratings developed in Chapter 5 were incorporated into the system to diffract the holographic image into higher diffraction orders. This increased the viewing angle of the holographic display and demonstrated the broader potential of flexoelectric nematic LC devices as active components in holographic display architectures.

Chapter 8 complements the preceding device-oriented work by presenting a characterisation technique capable of resolving the three-dimensional internal director structures of LC devices. Flexoelectric nematic LCs and chiral nematic LCs with different pitches were investigated to examine how refractive index gradients within LC structures influence the generation of THG images, as further supported

by simulated THG results obtained after convolution. This study provided three-dimensional evidence of the internal structure of flexoelectric nematic LC structures, supporting the simulation and experimental results presented in Chapters 4 and 5. It also demonstrated that adaptive optics can improve image quality by compensating for optical aberrations during THG imaging. In addition, this work provides a new observational pathway for studying the behaviour of LCs under external stimuli. Compared with conventional approaches based primarily on numerical simulations and macroscopic electro-optic measurements, THG imaging enables the internal structural response of LC materials to be visualised more directly and intuitively in three dimensions. This provides a valuable complementary approach to verifying simulated director configurations, interpreting experimentally observed optical behaviour, and investigating the structural properties of LCs and other anisotropic materials.

As shown in **Table 9.1**, compared with polarisation-grating-based beam steering, the two LC approaches developed in this thesis offer distinct advantages for electrically controllable diffraction. Polarisation gratings, sourced from Edmund Optics, provide high diffraction efficiency and well-defined diffraction orders, making them highly suitable for efficient beam deflection and holographic display architectures. However, their steering direction is usually fixed to a single diffraction angle by the fabricated grating geometry, which corresponds to 10° in this work, and cascaded optical components are required to achieve multidirectional beam steering. In contrast, the flexoelectric nematic LC grating enables electrical tuning of the first-order diffraction angle over a range from 4° to 7.8°, while maintaining a first-order diffraction efficiency of approximately 40% to 60%. In addition, the corresponding second-order diffraction angle ranges from 8° to 15.6°, with a second-order diffraction efficiency of approximately 18% to 25%. However, this

approach requires a relatively high driving voltage, typically 16–35 V_{DC}. The chiral nematic LC grating operates at a much lower applied voltage of approximately 2–3 V_{rms}. The first-order diffraction angle is relatively large, spanning a range from 15° to 20°, while producing a first-order diffraction efficiency of around 20% to 25%. Furthermore, the second-order diffraction angle ranges from 28° to 35°, with a second-order diffraction efficiency of approximately 10% to 15%. Although this efficiency is lower and the uniformity of the grating is more moderate, this approach offers the unique advantage of achieving electrically controlled, continuously rotatable in-plane beam steering using only a low-voltage AC field.

Therefore, polarisation gratings are most advantageous for high-efficiency fixed or discretely switched beam steering, flexoelectric nematic LC gratings are suitable for efficient electrically tunable beam steering, and chiral nematic LC gratings provide the strongest capability for low-voltage, continuously rotatable in-plane beam steering.

Table 9.1: Comparison of beam-steering performance among tunable flexoelectric nematic LC gratings, rotatable chiral nematic LC gratings, and commercially available polarisation gratings obtained from Edmund Optics. D.A. denotes diffraction angle, and D.E. denotes diffraction efficiency.

Beam Steering Methods	**1st-order D.A.**	**1st-order D.E.**	**2nd-order D.A.**	**2nd-order D.E.**
Tunable Flexoelectric LCs ($V_{th} < V_{DC} < 35$ V)	$4° - 7.8°$	40%-60%	$8° - 15.6°$	18%-25%
Rotatable Chiral Nematic LCs (2 V $< V_{rms} <$ 3 V)	$15° - 20°$	20%-25%	$28° - 35°$	10%-15%
Polarisation Gratings	Fixed at 10°	80%	N/A	N/A

To conclude, the work presented in this thesis addresses several outstanding challenges in the field, including the precise theoretical description of LC director behaviour under the flexoelectric effect, the controlled formation of diffraction grat-

ings in both flexoelectric nematic and chiral nematic LC systems, the development of electrically switchable and continuously rotatable diffractive grating architectures, the exploitation of polarisation-sensitive gratings and flexoelectric nematic LC devices for holographic projection display enlargement, and the introduction of THG imaging as a label-free three-dimensional imaging modality to help understand the relationship between the internal director configuration and the observed optical and diffractive behaviour. Together, these advances contribute to a more complete understanding of how the LC director can be modelled, controlled, implemented, and visualised, and they provide a foundation for the development of next-generation reconfigurable photonic devices.

9.2 Future Work

This section outlines potential directions for future work that could further advance, refine, and extend the research presented in this thesis.

9.2.1 UV Photo-polymerisation

The orientation order of LC can be stabilised (locked) by generating a polymer network through photopolymerization with mesogenic molecules containing functional groups of acrylate [185, 186]. These LC monomers are referred to as reactive mesogens. A typical example of a diacrylate reactive mesogen is RM257, which consists of LC molecules with built-in reactive groups (as shown in **Figure 9.1**) that can form covalent bonds when exposed to specific stimuli such as ultraviolet illumination (e.g., using a ThorLabs CS2010 UV 365 nm curing LED system). When UV light is applied to a mixture containing the diacrylate reactive mesogen RM257 and the photoinitiator IR819, both commonly used in our laboratory

and dispersed in a non-reactive LC host, the exposure initiates a free-radical polymerisation process [26]. This polymerisation results in the construction of a polymer network that locks in the alignment of the LC directors [187–189].

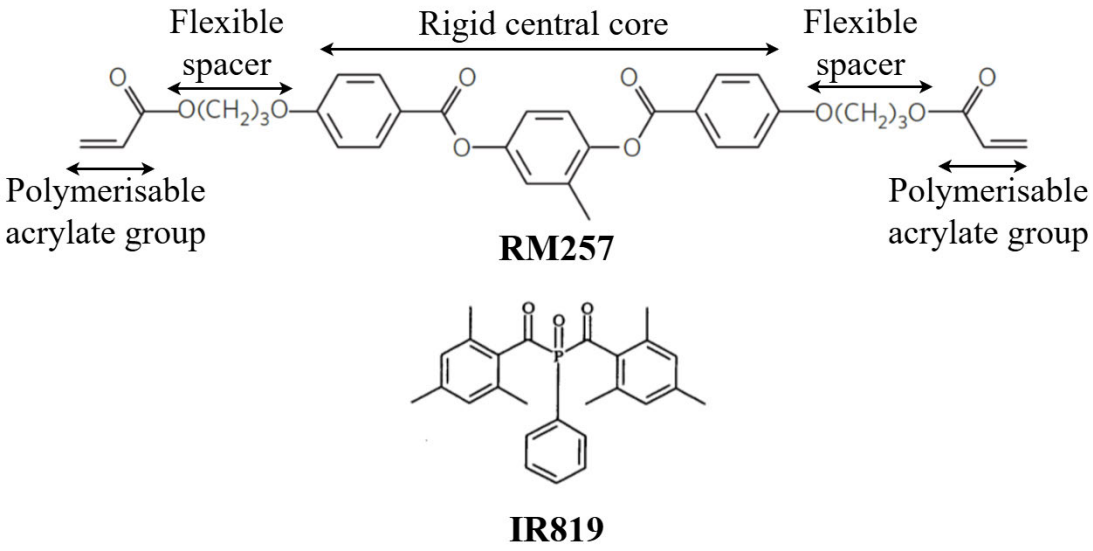


Figure 9.1: The chemical structure of RM257 and the typical photoinitiator IR819.

The photopolymerisation technique can be employed to lock the alignment of LC molecules, serving several important purposes. For the nematic flexoelectric LC system, it can help suppress the crystal formation discussed in Section 5.7.2, potentially improving both the stability and lifetime of the optimised LC mixture proposed for the flexoelectric diffraction grating. Furthermore, the formation of a solid polymer network enhances the overall structural stability by minimising or even eliminating the electrohydrodynamic instability arising from ionic motion, as described in Section 5.7.1. In the context of the chiral nematic LCs discussed in Chapter 6, locking the molecular alignment may also influence the tilt angle. It would therefore be of interest to investigate how photopolymerisation affects the measured tilt angle and, in turn, the rotational capability of the chiral LC diffraction grating.

9.2.2 Pixelation in LC Devices

In the devices developed in this thesis, the electric field is applied across the entire LC cell, producing a uniform periodic splay–bend structure in flexoelectric nematic LC devices and a uniform pitch in chiral LC devices. Although this global addressing approach enables controllable diffraction and beam steering, it does not provide local control over different regions of the LC layer. This limits the ability of the device to generate more complex and spatially varying beam-steering functions. A promising direction for future work would therefore be to introduce pixelated electrode structures, as illustrated in **Figure 9.2**. In flexoelectric nematic LC devices, for example, applying different voltages to different pixel regions could produce spatially varying splay–bend periodicities across the device. As a result, different regions of the LC cell could steer light in different directions, significantly increasing the spatial programmability of the device and providing a route towards more flexible and multifunctional beam steering.

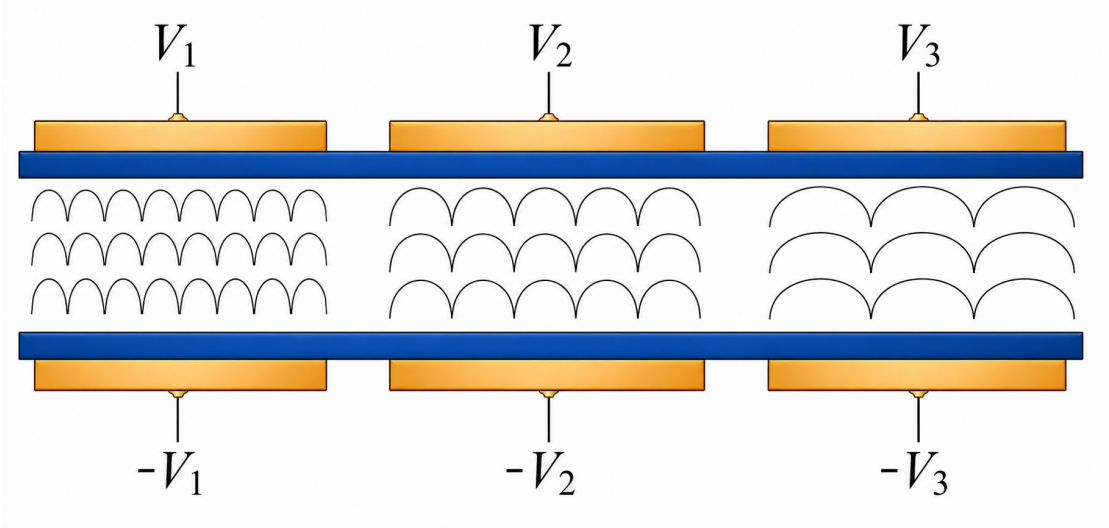


Figure 9.2: Pixelated flexoelectric splay-bend structures with variable voltage application, where $V_1 > V_2 > V_3$.

Such a system could also be considered as a new type of LC-based spatial light

modulator. Its performance could be evaluated in terms of key parameters such as modulation speed, phase modulation range, diffraction efficiency, and optical uniformity. This future research would help to further refine and optimise the proposed technology, while expanding its potential applications in adaptive optics, holographic displays, and programmable beam-steering systems.

9.2.3 Suppression of Unwanted Diffraction Orders

By using the flexoelectric nematic LC diffraction grating and the chiral nematic LC grating, light can be successfully steered to different positions through different diffraction orders. However, if diffracted light could be selectively directed into a single desired order, the power distributed into unwanted diffraction orders could be suppressed, thereby improving the overall optical efficiency. As discussed in

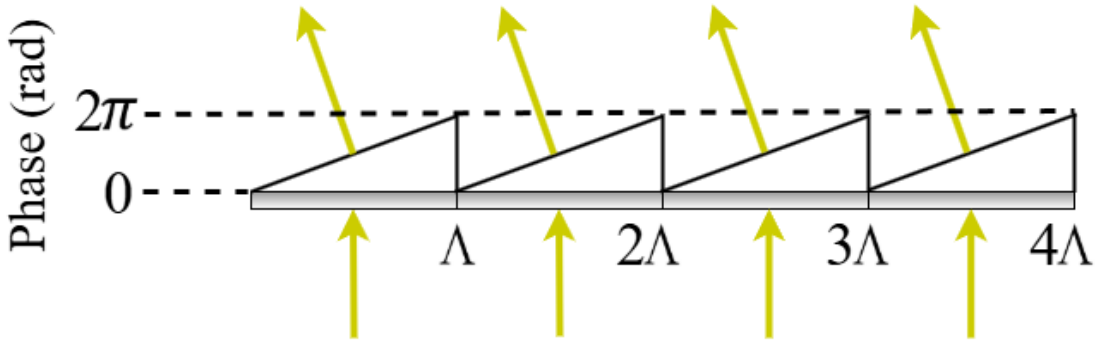


Figure 9.3: Schematic of beam steering using an ideal blazed grating with a 2π phase ramp across each grating pitch.

Chapter 7, the main advantage of using a polarisation grating is that it can steer light into a single diffraction order with high efficiency. However, its steering direction and diffraction angle are fixed, which limits its tunability. This restricted diffraction angle can, in some cases, lead to overlap between adjacent replay fields. Therefore, developing an electrically controllable grating capable of efficiently directing light into a selected single diffraction order would increase the flexibility of

the holographic projection system, reduce unwanted diffraction artefacts, suppress ghost images, and enhance the overall image quality. A potential method for

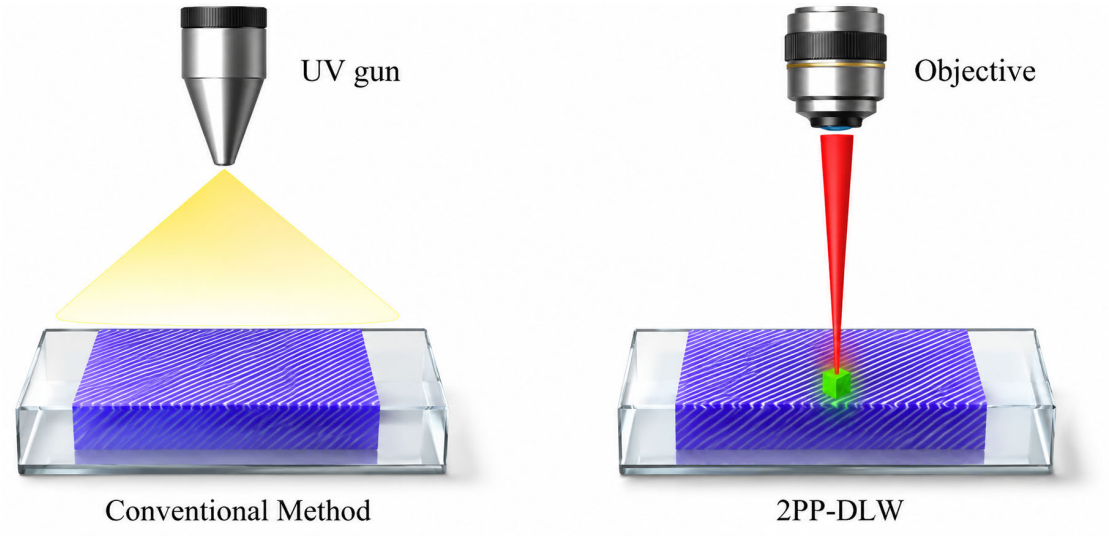


Figure 9.4: Photopolymerisation methods in LC devices. Left: conventional UV photopolymerisation, which exposes a broad region of the LC mixture. Right: two-photon polymerisation direct laser writing (TPP-DLW), which polymerises a small, localised volume inside the LC cell. The blue region represents the LC mixture containing reactive mesogen, and the green region indicates the precisely polymerised region. This author-created illustration was enhanced using AI tools for visual clarity.

mitigating unwanted diffraction orders is to modify the phase profile of the LC diffraction grating. If a blazed grating with a 2π phase ramp across each grating pitch (Λ) can be produced, as shown in **Figure 9.3**, a sawtooth-like phase profile can be formed, allowing light to be steered predominantly into a single selected diffraction order. One possible route to achieve this is through photopolymerisation, as discussed above. In this approach, a tightly focused laser beam could be scanned through the LC cell using two-photon polymerisation direct laser writing (TPP-DLW) to polymerise selected regions and define the desired polymer structure. As depicted in **Figure 9.4**, compared to the conventional photopolymerisation method, rather than curing polymer everywhere, we can fabricate the polymer in a particular location by using the two-photon direct laser writing technique.

By appropriately designing the laser-written structure, the effective phase ramp can be controlled under different applied voltages, enabling the device to direct light selectively into different diffraction orders. A second possible approach is to use pixelated LC devices, in which a stepped phase profile can be generated to approximate an ideal blazed grating.

9.2.4 High-Speed LC Devices

The LC devices demonstrated in this thesis provide effective electrical control of diffraction and beam steering. However, their switching speeds predominantly remain in the millisecond range, which constitutes a key limitation of LC-based photonic devices. For example, even the pi-cell configuration filled with E7 LC, discussed in Chapter 7, achieves a switching speed of only 1 ms to 3 ms. Although this represents a competitive figure for nematic LC devices, it remains a significant constraint for high-refresh-rate holographic projection systems. As demonstrated in the holographic projection work described in Chapter 7, when multiple replay fields or diffraction states must be displayed within a single frame period, the switching speed of the LC devices directly determines the extent to which flicker and ghosting artefacts can be suppressed. Surface alignment treatment could be explored as a practical route to improving the switching performance of LC devices. For example, photoalignment represents an attractive approach to improving the switching speed. When combined with subsequently polymerised reactive mesogens, the surface anchoring energy can be enhanced, providing a larger restoring torque for the LC director after removal of the electric field. This can accelerate the relaxation process and reduce response time [190, 191]. However, to achieve effective switching performance, this approach should also be combined with properly engineered pre-tilt angle control [10, 192].

Blue-phase LCs offer another promising route to overcome this limitation. Unlike conventional nematic phases, blue phases possess a pre-existing three-dimensional cubic defect lattice. Upon application of an electric field, the optical response arises from localised director reorientation and field-induced electrostriction of this lattice, rather than from bulk director reorientation across the full cell thickness. This fundamentally reduces the effective switching length scale and consequently the response time [193]. Polymer-stabilised blue-phase LCs have been reported to exhibit sub-millisecond switching, with response times in the microsecond regime [194–196], representing a substantial improvement over conventional nematic LC devices and addressing one of the most significant constraints on the practical development of LC-based photonic systems.

Therefore, future optimisation through surface alignment engineering and blue-phase LC materials could potentially enable faster LC-based photonic devices, thereby supporting a wider range of applications that require rapid optical modulation, including high-refresh-rate holographic projection and other adaptive photonic systems.

9.2.5 THG Imaging in Other LC Phases and Devices

In Chapter 8, THG imaging was used mainly to investigate the internal three-dimensional structures of flexoelectric nematic LC devices and the Grandjean and ULH states of chiral nematic LCs with homogeneous alignment. However, the switchable and rotatable chiral nematic LC diffraction gratings demonstrated in Chapter 6 were based on commercial Instec cells with homeotropic alignment. In that chapter, the grating was shown to switch and rotate under applied electric fields, and the observed behaviour was attributed to the additional torque generated by an asymmetric tilt angle. More experimental evidence is required to confirm

this mechanism. A valuable direction for future work would therefore be to apply THG imaging to homeotropically aligned chiral nematic LC cells. Due to the lack of suitable homeotropic polyimide for self-fabricated coverslip cells, this experiment could not be carried out in the present work. If such cells could be fabricated using coverslips, THG microscopy would allow the internal director evolution to be investigated during grating switching and rotation. This would be particularly useful for understanding the director behaviour during the transitional Grandjean state that appears after removal of the electric field, as discussed in Chapter 6. It would also allow the director configurations at different rotation angles to be compared directly.

With regard to the polymer-network LC gratings widely employed in LC research, THG imaging presents a compelling avenue for further structural characterisation. Specifically, it could help distinguish the LC-rich and polymer-rich regions, examine how the polymer network constrains the motion of the director, and reveal how the internal structure changes under applied fields. In addition, as discussed above, blue-phase LCs are particularly interesting because they contain a three-dimensional cubic defect lattice. THG imaging could potentially allow for visualisation of the internal periodic structure, the defect network, and field-induced lattice distortions. Such characterisations are highly valuable for elucidating the mechanisms underpinning the high-speed switching behaviour of blue-phase devices, as well as for understanding the influence of polymer stabilisation on their internal structural organisation.

These studies would further establish THG microscopy as a powerful tool for linking the internal three-dimensional organisation of LC materials to their macroscopic electro-optic and diffractive behaviour.

References

1. Jovicic, A., Li, J. & Richardson, T. Visible light communication: opportunities, challenges and the path to market. *IEEE Communications Magazine* **51**, 26–32 (2013).

2. Matheus, L. E. M., Vieira, A. B., Vieira, L. F. M., Vieira, M. A. M. & Gnawali, O. Visible Light Communication: Concepts, Applications and Challenges. *IEEE Communications Surveys & Tutorials* **21**, 3204–3237 (2019).

3. Ji, R., Wang, S., Liu, Q. & Lu, W. High-Speed Visible Light Communications: Enabling Technologies and State of the Art. *Applied Sciences* **8**, 589 (2018).

4. Zohrabi, M. et al. Lidar system with nonmechanical electrowetting-based wide-angle beam steering. *Optics Express* **27**, 4404–4415 (2019).

5. Andrienko, D. Introduction to liquid crystals. *Journal of Molecular Liquids* **267**, 520–541 (2018).

6. Slinger, C., Cameron, C. & Stanley, M. Computer-generated holography as a generic display technology. *Computer* **38**, 46–53 (2005).

7. Chen, H., Weng, Y., Xu, D., Tabiryan, N. V. & Wu, S. T. Beam steering for virtual/augmented reality displays with a cycloidal diffractive waveplate. *Optics Express* **24**, 7287–7298 (2016).

8. Heck, M. J. R. Highly integrated optical phased arrays: photonic integrated circuits for optical beam shaping and beam steering. *Nanophotonics* **6**, 93–107 (2017).

9. Mai, V. V. & Kim, H. Non-mechanical beam steering and adaptive beam control using variable focus lenses for free-space optical communications. *Journal of Lightwave Technology* **39**, 7600–7608 (2021).

10. Xi, X., Yan, C., Shen, L. Z., Wang, Y. & Cheng, P. Liquid crystal photoalignment technique: Basics, developments, and flexible/stretchable device applications. *Materials Today Electronics* **6**, 100069 (2023).

11. Davidson, P., Petermann, D. & Levelut, A. M. The measurement of the nematic order parameter by X-ray scattering reconsidered. *Journal de Physique II France* **5**, 113–131 (1995).

12. Sims, M. T., Abbott, L. C., Richardson, R. M., Goodby, J. W. & Moore, J. N. Considerations in the determination of orientational order parameters from X-ray scattering experiments. *Liquid Crystals* **46**, 11–24 (2019).

13. Ricci, P. et al. Acousto-optic deflectors in experimental neuroscience: overview of theory and applications. *Journal of Physics: Photonics* **6**, 022001 (2024).

14. Lin, Q. et al. Optical multi-beam steering and communication using integrated acousto-optic devices. *Nature Communications* **16**, 4714 (2025).

15. Liao, Z., Sun, Q., Hu, Y. & Jiang, N. Free-space optical multiplexing scheme based on acousto-optic deflector (AOD) with orbital angular momentum. *Optics Express* **33**, 23605–23615 (2025).

16. Ting, K.-T., Philbrick, C. P., Feldkhun, D. & Wagner, K. H. Fourier-basis active structured illumination sensing lidar imaging using crossed acousto-optic devices. *Applied Optics* **65**, 454–465 (2026).

17. He, Z. et al. Liquid crystal beam steering devices: principles, recent advances, and future developments. *Crystals* **9**, 292 (2019).

18. Han, Q., Elston, S. J., Kamal, W., Xue, L. & Morris, S. M. A nonlinear model of flexoelectric liquid crystal diffraction gratings. *Optics & Laser Technology* **180**, 111502 (2025).

19. Han, Q., Elston, S. J., Kamal, W., Xue, L. & Morris, S. M. A switchable and rotatable chiral nematic liquid crystal diffraction grating for beam-steering technology. *Advanced Optical Materials* **13**, 2500794 (2025).

20. Han, Q. et al. Holographic projection display enlargement via polarization-grating beam steering with fast-response liquid crystal pi-cells. *ACS Photonics* **13**, 2943–2953 (2026). Available at: `https://pubs.acs.org/doi/full/10.1021/acsphotonics.6c00353`.

21. Kuczyński, W., Żywucki, B. & Małecki, J. Determination of orientational order parameter in various liquid-crystalline phases. *Molecular Crystals and Liquid Crystals* **381**, 1–19 (2002).

22. Palffy-Muhoray, P. The diverse world of liquid crystals. *Physics Today* **60**, 54–60 (2007).

23. Collings, P. J. & Hird, M. *Introduction to Liquid Crystals: Chemistry and Physics* first edition. (CRC Press, London, UK, 1997).

24. Yang, D.-K. & Wu, S.-T. *Fundamentals of liquid crystal devices* second edition. (John Wiley & Sons, Chichester, UK, 2014).

25. Tartan, C. *Flexoelectricity and multi-dimensional structures for liquid crystal photonics* PhD thesis (University of Oxford, Oxford, 2017).

26. Sandford O'Neill, J. J. *Two-photon polymerisation direct laser writing for liquid crystal photonics* PhD thesis (University of Oxford, Oxford, 2021).

27. Jones, R. C. A new calculus for the treatment of optical systems. IV. *Journal of the Optical Society of America* **32**, 486–493 (1942).

28. Gu, C. & Yeh, P. Extended Jones matrix method and its application in the analysis of compensators for liquid crystal displays. *Displays* **20**, 237–257 (1999).

29. Yu, F. H., Chen, J. & Kwok, H. S. Comparison of extended Jones matrices for twisted nematic liquid-crystal displays at oblique angles of incidence. *Journal of the Optical Society of America A* **16**, 2772–2780 (1999).

30. Frank, F. C. I. Liquid crystals. On the theory of liquid crystals. *Discussions of The Faraday Society* **25**, 19–28 (1958).

31. Zocher, H. The effect of a magnetic field on the nematic state. *Transactions of the Faraday Society* **29**, 945–957 (1933).

32. Adler, J. H., Atherton, T. J., Benson, T. R., Emerson, D. B. & MacLachlan, S. P. Energy minimization for liquid crystal equilibrium with electric and flexoelectric effects. *SIAM Journal on Scientific Computing* **37**, S157–S176 (2015).

33. Dierking, I. Flexoelectricity in liquid crystals. *Liquid Crystals Today* **22**, 48 (2013).

34. Coles, H. J. & Morris, S. M. Flexoelectro-Optic Liquid Crystal Displays. *Handbook of Visual Display Technology* 1681–1694 (Springer, Berlin, Heidelberg, 2012).

35. Lee, S. D., Patel, J. S. & Meyer, R. B. Effect of flexoelectric coupling on helix distortions in cholesteric liquid crystals. *Journal of Applied Physics* **67**, 1293–1297 (1990).

36. Rudquist, P., Buivydas, M., Komitov, L. & Lagerwall, S. T. Linear electro-optic effect based on flexoelectricity in a cholesteric with sign change of dielectric anisotropy. *Journal of Applied Physics* **76**, 7778–7783 (1994).

37. Varanytsia, A. & Chien, L. C. Giant flexoelectro-optic effect with liquid crystal dimer CB7CB. *Scientific Reports* **7**, 41333 (2017).

38. Outram, B. *Flexoelectric and dielectric phenomena in helicoidal liquid crystals* PhD thesis (University of Oxford, Oxford, 2013).

39. Ghatak, A. K. & Thyagarajan, K. *Optical Electronics* first edition. (Cambridge University Press, Cambridge, UK, 1989).

40. Bonod, N. & Neauport, J. Diffraction gratings: from principles to applications in high-intensity lasers. *Advances in Optics and Photonics* **8**, 156–199 (2016).

41. Shin, Y., Zhou, Z., Halder, S., Zhang, X. & Yang, D. K. Reconfigurable liquid crystal diffraction grating based on flexoelectric effect. *Journal of Molecular Liquids* **357**, 119150 (2022).

42. Crawford, G. P., Eakin, J. N., Radcliffe, M. D., Callan-Jones, A. & Pelcovits, R. A. Liquid-crystal diffraction gratings using polarization holography alignment techniques. *Journal of Applied Physics* **98**, 123102 (2005).

43. Zola, R. S. et al. Dynamic control of light direction enabled by stimuli-responsive liquid crystal gratings. *Advanced Materials* **31**, 1806172 (2019).

44. Wang, X., Wilson, D., Muller, R., Maker, P. & Psaltis, D. Liquid-crystal blazed-grating beam deflector. *Applied Optics* **39**, 6545–6555 (2000).

45. Chen, J., Bos, P. J., Vithana, H. & Johnson, D. L. An electro-optically controlled liquid crystal diffraction grating. *Applied Physics Letters* **67**, 2588–2590 (1995).

46. Sutherland, R. L., Natarajan, L. V., Tondiglia, V. P. & Bunning, T. J. Bragg gratings in an acrylate polymer consisting of periodic polymer-dispersed liquid-crystal planes. *Chemistry of Materials* **5**, 1533–1538 (1993).

47. Jang, E., Kim, H. R., Na, Y. J. & Lee, S. D. Multistage optical memory of a liquid crystal diffraction grating in a single beam rewriting scheme. *Applied Physics Letters* **91**, 071109 (2007).

48. Morris, R., Jones, J. C. & Nagaraj, M. Inducing variable pitch gratings in nematic liquid crystals using chirped surface acoustic wave transducers. *Journal of Physics D: Applied Physics* **55**, 335301 (2022).

49. Zhou, J., Collard, D. M. & Srinivasarao, M. Switchable gratings by spatially periodic alignment of liquid crystals via patterned photopolymerization. *Optics Letters* **31**, 652–654 (2006).

50. Gupta, V. K. & Abbott, N. L. Design of surfaces for patterned alignment of liquid crystals on planar and curved substrates. *Science* **276**, 1533–1536 (1997).

51. Gibbons, W. M., Shannon, P. J., Sun, S. T. & Swetlin, B. J. Surface-mediated alignment of nematic liquid crystals with polarized laser light. *Nature* **351**, 49–50 (1991).

52. Wen, B., Petschek, R. G. & Rosenblatt, C. Nematic liquid-crystal polarization gratings by modification of surface alignment. *Applied Optics* **41**, 1246–1250 (2002).

53. Presnyakov, V., Asatryan, K., Galstian, T. & Chigrinov, V. Optical polarization grating induced liquid crystal micro-structure using azo-dye command layer. *Optics Express* **14**, 10558–10564 (2006).

54. Xiang, Y. et al. Tunable optical grating based on the flexoelectric effect in a bent-core nematic liquid crystal. *Physical Review Applied* **7**, 064032 (2017).

55. Palto, S. P. Dynamic and photonic properties of field-induced gratings in flexoelectric LC layers. *Crystals* **11**, 894 (2021).

56. Park, S. G., Lee, Y. L., Kim, W. S. & Oh, S. W. A simulation of liquid crystal grating with field-induced twist deformation for beam-steering applications. *Advanced Photonics Research* **4**, 2200135 (2023).

57. Kriezis, E. E. & Elston, S. J. Wide-angle beam propagation method for liquid-crystal device calculations. *Applied Optics* **39**, 5707–5714 (2000).

58. Yang, Y., Forbes, A. & Cao, L. A review of liquid crystal spatial light modulators: devices and applications. *Opto-Electronic Science* **2**, 230026-1–230026-29 (2023).

59. Peng, Y., Choi, S., Padmanaban, N. & Wetzstein, G. Neural holography with camera-in-the-loop training. *ACM Transactions on Graphics* **39**, 185 (2020).

60. Kozacki, T., Kujawinska, M., Finke, G., Zaperty, W. & Hennelly, B. Holographic display with tilted spatial light modulator. *Applied Optics* **50**, 3579–3588 (2011).

61. Jin, Y. *Liquid crystal technologies for enhanced optical system functionality* PhD thesis (University of Oxford, Oxford, 2023).

62. Chae, B. G. Viewing-angle expansion in holographic displays implemented with a modulator having finite space-bandwidth. *Optics Express* **31**, 37900–37910 (2023).

63. Wang, D. et al. Large viewing angle holographic 3D display system based on maximum diffraction modulation. *Light: Advanced Manufacturing* **4**, 195–205 (2023).

64. Sando, Y. et al. Super-wide viewing-zone holographic 3D display using a convex parabolic mirror. *Scientific Reports* **8**, 11333 (2018).

65. Éber, N., Xiang, Y. & Buka, Á. Bent core nematics as optical gratings. *Journal of Molecular Liquids* **267**, 436–444 (2018).

66. Xu, M. Y. et al. Domain structures as optical gratings controlled by electric field in a bent-core nematic. *Optics Express* **23**, 15224–15234 (2015).

67. Bobylev, Y. P. & Pikin, S. A. Threshold piezoelectric instability in a liquid crystal. *Soviet Journal of Experimental and Theoretical Physics* **45**, 195 (1977).

68. Parry-Jones, L. A., Meyer, R. B. & Elston, S. J. Mechanisms of flexoelectric switching in a zenithally bistable nematic device. *Journal of Applied Physics* **106**, 014510 (2009).

69. Lorenz, A. et al. Electrical addressing of polymer stabilized hyper-twisted chiral nematic liquid crystals with interdigitated electrodes: Experiment and model. *Applied Physics Letters* **104**, 071102 (2014).

70. Babakhanova, G. et al. Elastic and viscous properties of the nematic dimer CB7CB. *Physical Review E* **96**, 062704 (2017).

71. Li, J., Baird, G., Lin, Y. H., Ren, H. & Wu, S.-T. Refractive-index matching between liquid crystals and photopolymers. *Journal of the Society for Information Display* **13**, 1017–1026 (2005).

72. Chen, Y., Peng, F., Yamaguchi, T., Song, X. & Wu, S.-T. High performance negative dielectric anisotropy liquid crystals for display applications. *Crystals* **3**, 483–503 (2013).

73. Billmeyer Jr., F. W. & Fairman, H. S. CIE method for calculating tristimulus values. *Color Research & Application* **12**, 27–36 (1987).

74. Kim, J., Suh, J. H., Lee, B. Y., Kim, S. U. & Lee, S. D. Optically switchable grating based on dye-doped ferroelectric liquid crystal with high efficiency. *Optics Express* **23**, 12619–12627 (2015).

75. Li, Y. L. et al. Tunable liquid crystal grating based holographic 3D display system with wide viewing angle and large size. *Light: Science & Applications* **11**, 188 (2022).

76. Tien, C. L., Lin, R. J., Su, S. H. & Horng, C. T. Electrically tunable diffraction grating based on liquid crystals. *Advances in Condensed Matter Physics* **2018**, 7849529 (2018).

77. Huang, S. Y., Huang, B. Y., Kang, C. C. & Kuo, C. T. Diffraction and polarization properties of electrically–tunable nematic liquid crystal grating. *Polymers* **12**, 1929 (2020).

78. Gao, K., Cheng, H. H., Bhowmik, A. K. & Bos, P. J. Thin-film Pancharatnam lens with low f-number and high quality. *Optics Express* **23**, 26086–26094 (2015).

79. Kamiak, K., Kabanova, O., Rushnova, I., Melnikova, E. & Tolstik, A. Switchable diffraction gratings based on the periodic binary alignment of a nematic liquid crystal. *Bulletin of the Russian Academy of Sciences: Physics* **85**, 1496–1500 (2021).

80. Subacius, D., Shiyanovskii, S. V., Bos, P. & Lavrentovich, O. D. Cholesteric gratings with field-controlled period. *Applied Physics Letters* **71**, 3323–3325 (1997).

81. Hamdi, R., Petriashvili, G., De Santo, M. P., Lombardo, G. & Barberi, R. Electrically controlled 1D and 2D cholesteric liquid crystal gratings. *Molecular Crystals and Liquid Crystals* **553**, 97–102 (2012).

82. Li, Y. et al. Low voltage dual-period liquid crystal grating with tunable diffraction efficiency. *Displays* **80**, 102562 (2023).

83. Blinov, L. M. Electrohydrodynamic effects in liquid crystals. *Science Progress (1933-)* **70**, 263–286 (1986).

84. Gruler, H. Williams domains and dielectric alignment in a nematic liquid crystal. *Molecular Crystals and Liquid Crystals* **27**, 31–41 (1974).

85. Blinov, L. Domain instabilities in liquid crystals. *Le Journal de Physique Colloques* **40**, C3–247 (1979).

86. Tadapatri, P., Krishnamurthy, K. S. & Weissflog, W. Patterned flexoelectric instability in a bent-core nematic liquid crystal. *Soft Matter* **8**, 1202–1214 (2012).

87. Jau, H. C. et al. Direction switching and beam steering of cholesteric liquid crystal gratings. *Applied Physics Letters* **100**, 131909 (2012).

88. Fuh, A. Y. G., Lin, C. H. & Huang, C. Y. Dynamic pattern formation and beam-steering characteristics of cholesteric gratings. *Japanese Journal of Applied Physics* **41**, 211 (2002).

89. Sohn, H. J., Oh, S. W., Choi, Y., Ji, S. M. & Yoon, T. H. A switchable cholesteric phase grating with a low operating voltage. *Crystals* **11**, 100 (2021).

90. Gvozdovskyy, I., Yaroshchuk, O., Serbina, M. & Yamaguchi, R. Photoinduced helical inversion in cholesteric liquid crystal cells with homeotropic anchoring. *Optics Express* **20**, 3499–3508 (2012).

91. Nose, T., Miyanishi, T., Aizawa, Y., Ito, R. & Honma, M. Rotational behavior of stripe domains appearing in hybrid aligned chiral nematic liquid crystal cells. *Japanese Journal of Applied Physics* **49**, 051701 (2010).

92. Wu, J. J., Chen, F. C., Wu, Y. S. & Chen, S. H. Phase gratings in pretilted homeotropic cholesteric liquid crystal films. *Japanese Journal of Applied Physics* **41**, 6108 (2002).

93. Zel'dovich, B. Y. & Tabiryan, N. V. Equilibrium structure of a cholesteric with homeotropic orientation on the walls. *Zhurnal Éksperimental'noi i Teoreticheskoi Fiziki* **83**, 990–1004 (1982).

94. Yip, W. C., Welch, C., Mehl, G. H. & Wilkinson, T. D. A cholesteric liquid crystal device having stable uniform lying helix structure. *Journal of Molecular Liquids* **299**, 112141 (2020).

95. Jia, Z. et al. Engineering the uniform lying helical structure in chiral nematic liquid crystals: from morphology transition to dimension control. *Crystals* **11**, 414 (2021).

96. Hegde, G. & Komitov, L. Periodic anchoring condition for alignment of a short pitch cholesteric liquid crystal in uniform lying helix texture. *Applied Physics Letters* **96**, 113503 (2010).

97. Xiang, J. et al. Electrically tunable laser based on oblique heliconical cholesteric liquid crystal. *Proceedings of the National Academy of Sciences* **113**, 12925–12928 (2016).

98. Kudoh, Y., Uchida, Y. & Takahashi, T. Control of the pretilt angle for liquid crystal alignment using novel electrospray deposition methods with two capillaries. *Journal of the Society for Information Display* **22**, 357–363 (2014).

99. Wu, J. J., Wu, Y. S., Chen, F. C. & Chen, S. H. Formation of phase grating in planar aligned cholesteric liquid crystal film. *Japanese Journal of Applied Physics* **41**, L1318 (2002).

100. Zhang, L. et al. Dynamic orthogonal switching of a thermoresponsive self-organized helical superstructure. *Advanced Materials* **29**, 1700676 (2017).

101. Blanc, C. et al. Helfrich-Hurault elastic instabilities driven by geometrical frustration. *Reviews of Modern Physics* **95**, 015004 (2023).

102. Ma, L. L. et al. Programmable self-propelling actuators enabled by a dynamic helical medium. *Science Advances* **7**, eabh3505 (2021).

103. Ma, L. L. et al. Rationally designed dynamic superstructures enabled by photoaligning cholesteric liquid crystals. *Advanced Optical Materials* **3**, 1691–1696 (2015).

104. Elston, S. J. Flexoelectricity in nematic domain walls. *Physical Review E—Statistical, Nonlinear, and Soft Matter Physics* **78**, 011701 (2008).

105. Yu, C. H., Wu, P. C. & Lee, W. Electro-thermal formation of uniform lying helix alignment in a cholesteric liquid crystal cell. *Crystals* **9**, 183 (2019).

106. Dierking, I. *Polymer-Modified Liquid Crystals* first edition. (Royal Society of Chemistry, Cambridge, UK, 2019).

107. Hirayama, R., Martinez Plasencia, D., Masuda, N. & Subramanian, S. A volumetric display for visual, tactile and audio presentation using acoustic trapping. *Nature* **575**, 320–323 (2019).

108. Smalley, D. et al. A photophoretic-trap volumetric display. *Nature* **553**, 486–490 (2018).

109. Song, W. et al. Large-scale Huygens' metasurfaces for holographic 3D near-eye displays. *Laser & Photonics Reviews* **15**, 2000538 (2021).

110. Lin, H. C. & Wu, Y. H. Augmented reality using holographic display. *Optical Data Processing and Storage* **3**, 101–106 (2017).

111. Gopakumar, M. et al. Full-colour 3D holographic augmented-reality displays with metasurface waveguides. *Nature* **629**, 791–797 (2024).

112. Park, J. H. & Lee, B. Holographic techniques for augmented reality and virtual reality near-eye displays. *Light: Advanced Manufacturing* **3**, 137–150 (2022).

113. Chang, C., Bang, K., Wetzstein, G., Lee, B. & Gao, L. Toward the next-generation VR/AR optics: a review of holographic near-eye displays from a human-centric perspective. *Optica* **7**, 1563–1578 (2020).

114. Boffi, P., Ubaldi, M. C., Piccinin, D., Frascolla, C. & Martinelli, M. 1550-nm volume holography for optical communication devices. *IEEE Photonics Technology Letters* **12**, 1355–1357 (2002).

115. Hsu, W. F. & Weng, M. H. Compact holographic projection display using liquid-crystal-on-silicon spatial light modulator. *Materials* **9**, 768 (2016).

116. Jesacher, A., Bernet, S. & Ritsch-Marte, M. Colour hologram projection with an SLM by exploiting its full phase modulation range. *Optics Express* **22**, 20530–20541 (2014).

117. Márquez, A. & Lizana, Á. *Liquid Crystal on Silicon Devices: Modeling and Advanced Spatial Light Modulation Applications* (MDPI, Basel, Switzerland, 2019).

118. Li, N. N., Wang, D., Liu, C., Lin, S. F. & Wang, Q. H. Large-size holographic display method based on effective utilization of two spatial light modulators. *Optics Communications* **453**, 124311 (2019).

119. Zhang, X. et al. Holographic display system with enhanced viewing angle using boundary folding mirrors. *Optics Communications* **482**, 126580 (2021).

120. Li, J., Smithwick, Q. & Chu, D. Holobricks: modular coarse integral holographic displays. *Light: Science & Applications* **11**, 57 (2022).

121. Kozacki, T., Kujawińska, M., Finke, G., Hennelly, B. & Pandey, N. Extended viewing angle holographic display system with tilted SLMs in a circular configuration. *Applied Optics* **51**, 1771–1780 (2012).

122. Yaraş, F., Kang, H. & Onural, L. Circular holographic video display system. *Optics Express* **19**, 9147–9156 (2011).

123. Wang, D., Liu, C., Shen, C., Xing, Y. & Wang, Q. H. Holographic capture and projection system of real object based on tunable zoom lens. *PhotoniX* **1**, 6 (2020).

124. Wakunami, K. et al. Projection-type see-through holographic three-dimensional display. *Nature Communications* **7**, 12954 (2016).

125. Zou, J. et al. Fast-response liquid crystal for spatial light modulator and LiDAR applications. *Crystals* **11**, 93 (2021).

126. Chen, H. W., Lee, J. H., Lin, B. Y., Chen, S. & Wu, S.-T. Liquid crystal display and organic light-emitting diode display: present status and future perspectives. *Light: Science & Applications* **7**, 17168–17168 (2018).

127. Zou, J., Zhan, T., Xiong, J. & Wu, S.-T. Broadband wide-view Pancharatnam–Berry phase deflector. *Optics Express* **28**, 4921–4927 (2020).

128. Cincotti, G. Polarization gratings: design and applications. *IEEE Journal of Quantum Electronics* **39**, 1645–1652 (2003).

129. Zhan, T. et al. Pancharatnam–Berry optical elements for head-up and near-eye displays. *Journal of the Optical Society of America B* **36**, D52–D65 (2019).

130. Escuti, M. J. & Jones, W. M. Polarization-independent switching with high contrast from a liquid crystal polarization grating. *SID Symposium Digest of Technical Papers* **37**, 1443–1446 (2006).

131. Kim, J., Oh, C., Serati, S. & Escuti, M. J. Wide-angle, nonmechanical beam steering with high throughput utilizing polarization gratings. *Applied Optics* **50**, 2636–2639 (2011).

132. Zhang, G. et al. Non-mechanical optical beam-steering of a liquid crystal laser. *Optics & Laser Technology* **157**, 108623 (2023).

133. Xiong, J., Wang, Z., Shan, Y., Cheng, D. & Wang, Y. Eliminating chromatic aberrations of diffractive lenses in varifocal virtual reality displays. *Photonics Research* **13**, 3466–3475 (2025).

134. Xiong, J., Li, Y., Li, K. & Wu, S.-T. Aberration-free pupil steerable Maxwellian display for augmented reality with cholesteric liquid crystal holographic lenses. *Optics Letters* **46**, 1760–1763 (2021).

135. *Oxford University Skyline Vector Image* `https://www.vectorstock.com/royalty-free-vectors/oxford-skyline-vectors`. Accessed: 2026-5-23.

136. Wang, D. et al. Color liquid crystal grating based color holographic 3D display system with large viewing angle. *Light: Science & Applications* **13**, 16 (2024).

137. Jin, Y. et al. Backflow-assisted time-resolved phase modulation in nematic liquid crystal Pi-Cells. *Optics & Laser Technology* **156**, 108596 (2022).

138. Lionheart, W. R. B. & Newton, C. J. P. Analysis of the inverse problem for determining nematic liquid crystal director profiles from optical measurements using singular value decomposition. *New Journal of Physics* **9**, 63 (2007).

139. Rajabi, M., Lavrentovich, O. D. & Shribak, M. Instantaneous mapping of liquid crystal orientation using a polychromatic polarizing microscope. *Liquid Crystals* **50**, 181–190 (2023).

140. Yelin, D., Silberberg, Y., Barad, Y. & Patel, J. S. Depth-resolved imaging of nematic liquid crystals by third-harmonic microscopy. *Applied Physics Letters* **74**, 3107–3109 (1999).

141. Fergason, J. L. Liquid crystals in nondestructive testing. *Applied Optics* **7**, 1729–1737 (1968).

142. Smalyukh, I. I., Shiyanovskii, S. V. & Lavrentovich, O. D. Three-dimensional imaging of orientational order by fluorescence confocal polarizing microscopy. *Chemical Physics Letters* **336**, 88–96 (2001).

143. Dierking, I. Fluorescence confocal polarizing microscopy: imaging liquid crystal director fields in three dimensions. *ChemPhysChem* **2**, 663–664 (2001).

144. Nowicka, K., Bielejewska, N., Kuczyński, W., Knapkiewicz, M. & Hoffmann, J. Exploration of liquid crystal structures using fluorescent confocal polarizing microscopy. *Phase Transitions* **87**, 1073–1079 (2014).

145. Lavrentovich, O. D. Fluorescence confocal polarizing microscopy: three-dimensional imaging of the director. *Pramana* **61**, 373–384 (2003).

146. Pathak, G. et al. Dispersion of fluorescent dye in the nematic liquid crystal: Enhanced photoluminescence and high birefringence. *Opto-Electronics Review* **26**, 317–324 (2018).

147. Pathak, G. et al. Tuning of birefringence, response time, and dielectric anisotropy by the dispersion of fluorescent dye into the nematic liquid crystal. *Applied Physics A* **124**, 463 (2018).

148. Misra, A. K., Tripathi, P. K. & Manohar, R. Reduction of optical response time for fluorescent dye doped ferroelectric liquid crystal. *Journal of Molecular Liquids* **175**, 67–71 (2012).

149. Misra, A. K., Tripathi, P. K. & Manohar, R. Fluorescent dye doped ferroelectric liquid crystal: An anchoring energy, electro-optical and fluorescence study. *Journal of Molecular Liquids* **214**, 418–421 (2016).

150. Misra, A. K., Tripathi, P. K. & Manohar, R. Electro-optical study of fluorescent dye-doped ferroelectric liquid crystal. *Molecular Crystals and Liquid Crystals* **574**, 82–90 (2013).

151. Yelin, D. & Silberberg, Y. Laser scanning third-harmonic-generation microscopy in biology. *Optics Express* **5**, 169–175 (1999).

152. Sun, C. K. et al. Higher harmonic generation microscopy for developmental biology. *Journal of Structural Biology* **147**, 19–30 (2004).

153. Débarre, D. et al. Imaging lipid bodies in cells and tissues using third-harmonic generation microscopy. *Nature Methods* **3**, 47–53 (2006).

154. Chen, Y. C. et al. Third-harmonic generation microscopy reveals dental anatomy in ancient fossils. *Optics Letters* **40**, 1354–1357 (2015).

155. Chang, T. et al. Non-invasive monitoring of cell metabolism and lipid production in 3D engineered human adipose tissues using label-free multiphoton microscopy. *Biomaterials* **34**, 8607–8616 (2013).

156. Tsai, C.-K. et al. Virtual optical biopsy of human adipocytes with third harmonic generation microscopy. *Biomedical Optics Express* **4**, 178–186 (2013).

157. Débarre, D. et al. Velocimetric third-harmonic generation microscopy: micrometer-scale quantification of morphogenetic movements in unstained embryos. *Optics Letters* **29**, 2881–2883 (2004).

158. Jesacher, A. et al. Adaptive harmonic generation microscopy of mammalian embryos. *Optics Letters* **34**, 3154–3156 (2009).

159. Watanabe, T. et al. Characterisation of the dynamic behaviour of lipid droplets in the early mouse embryo using adaptive harmonic generation microscopy. *BMC Cell Biology* **11**, 38 (2010).

160. Vogel, A. & Venugopalan, V. Mechanisms of pulsed laser ablation of biological tissues. *Chemical Reviews* **103**, 577–644 (2003).

161. Campagnola, P. Second harmonic generation imaging microscopy: applications to diseases diagnostics. *Analytical Chemistry* **83**, 3224–3231 (2011).

162. Deniset-Besseau, A., De Sa Peixoto, P., Mosser, G. & Schanne-Klein, M.-C. Nonlinear optical imaging of lyotropic cholesteric liquid crystals. *Optics Express* **18**, 1113–1121 (2010).

163. Zhou, L. et al. Nonlinear optical characterization of 2D materials. *Nanomaterials* **10**, 2263 (2020).

164. Kodikara, M. S., Stranger, R. & Humphrey, M. G. Computational studies of the nonlinear optical properties of organometallic complexes. *Coordination Chemistry Reviews* **375**, 389–409 (2018).

165. Hellwarth, R. & Christensen, P. Nonlinear optical microscopic examination of structure in polycrystalline ZnSe. *Optics Communications* **12**, 318–322 (1974).

166. Gauderon, R., Lukins, P. B. & Sheppard, C. J. R. Three-dimensional second-harmonic generation imaging with femtosecond laser pulses. *Optics Letters* **23**, 1209–1211 (1998).

167. Peleg, G. et al. Gigantic optical non-linearities from nanoparticle-enhanced molecular probes with potential for selectively imaging the structure and physiology of nanometric regions in cellular systems. *Bioimaging* **4**, 215–224 (1996).

168. Kriech, M. A. & Conboy, J. C. Imaging chirality with surface second harmonic generation microscopy. *Journal of the American Chemical Society* **127**, 2835–2840 (2005).

169. Barad, Y., Eisenberg, H., Horowitz, M. & Silberberg, Y. Nonlinear scanning laser microscopy by third harmonic generation. *Applied Physics Letters* **70**, 922–924 (1997).

170. Squier, J. A., Müller, M., Brakenhoff, G. J. & Wilson, K. R. Third harmonic generation microscopy. *Optics Express* **3**, 315–324 (1998).

171. Rodríguez, C. et al. Adaptive optical third-harmonic generation microscopy for in vivo imaging of tissues. *Biomedical Optics Express* **15**, 4513–4524 (2024).

172. Pajić, I. et al. Label-free third harmonic generation imaging and quantification of lipid droplets in live filamentous fungi. *Scientific Reports* **12**, 18760 (2022).

173. Booth, M. J. Adaptive optics in microscopy. *Philosophical Transactions of the Royal Society A: Mathematical, Physical and Engineering Sciences* **365**, 2829–2843 (2007).

174. Weigelin, B., Bakker, G. J. & Friedl, P. Third harmonic generation microscopy of cells and tissue organization. *Journal of Cell Science* **129**, 245–255 (2016).

175. Oron, D. et al. Depth-resolved structural imaging by third-harmonic generation microscopy. *Journal of Structural Biology* **147**, 3–11 (2004).

176. Débarre, D. & Beaurepaire, E. Quantitative characterization of biological liquids for third-harmonic generation microscopy. *Biophysical Journal* **92**, 603–612 (2007).

177. Yelin, D., Silberberg, Y., Barad, Y. & Patel, J. S. Phase-matched third-harmonic generation in a nematic liquid crystal cell. *Physical Review Letters* **82**, 3046–3049 (1999).

178. Pillai, R. S., Oh-e, M., Yokoyama, H., Brakenhoff, G. J. & Müller, M. Imaging colloidal particle induced topological defects in a nematic liquid crystal using third harmonic generation microscopy. *Optics Express* **14**, 12976–12983 (2006).

179. Castles, F., Morris, S. M. & Coles, H. J. Flexoelectro-optic properties of chiral nematic liquid crystals in the uniform standing helix configuration. *Physical Review E* **80**, 031709 (2009).

180. Salter, P. S., Carbone, G., Jewell, S. A., Elston, S. J. & Raynes, P. Unwinding of the uniform lying helix structure in cholesteric liquid crystals next to a spatially uniform aligning surface. *Physical Review E* **80**, 041707 (2009).

181. Wang, J. et al. Correction of uneven illumination in color microscopic image based on fully convolutional network. *Optics Express* **29**, 28503–28520 (2021).

182. Li, J., Wu, S.-T., Brugioni, S., Meucci, R. & Faetti, S. Infrared refractive indices of liquid crystals. *Journal of Applied Physics* **97**, 073501 (2005).

183. Débarre, D. et al. Image-based adaptive optics for two-photon microscopy. *Optics Letters* **34**, 2495–2497 (2009).

184. Facomprez, A., Beaurepaire, E. & Débarre, D. Accuracy of correction in modal sensorless adaptive optics. *Optics Express* **20**, 2598–2612 (2012).

185. Broer, D., Finkelmann, H. & Kondo, K. In-situ photopolymerization of an oriented liquid-crystalline acrylate. *Die Makromolekulare Chemie* **189**, 185–194 (1988).

186. Broer, D., Crawford, G. P. & Zumer, S. *Cross-linked liquid crystalline systems: from rigid polymer networks to elastomers* first edition. (CRC Press, Boca Raton, FL, USA, 2011).

187. Dierking, I. Polymer network-stabilized liquid crystals. *Advanced Materials* **12**, 167–181 (2000).

188. Liu, D. & Broer, D. J. Liquid crystal polymer networks: preparation, properties, and applications of films with patterned molecular alignment. *Langmuir* **30**, 13499–13509 (2014).

189. Fung, Y. K. et al. Polymer networks formed in liquid crystals. *Liquid Crystals* **19**, 797–801 (1995).

190. Mun, B. J. et al. High-speed in-plane switching liquid crystal cell by using photo alignment method. *Molecular Crystals and Liquid Crystals* **613**, 167–173 (2015).

191. Lee, Y. J. et al. Enhanced surface anchoring energy for the photo-alignment layer with reactive mesogens for fast response time of liquid crystal displays. *Journal of Physics D: Applied Physics* **46**, 145305 (2013).

192. McGinty, C. P., Kolacz, J. & Spillmann, C. M. Large rewritable liquid crystal pretilt angle by in situ photoalignment of brilliant yellow films. *Applied Physics Letters* **119**, 141111 (2021).

193. Coles, H. J. & Pivnenko, M. N. Liquid crystal 'blue phases' with a wide temperature range. *Nature* **436**, 997–1000 (2005).

194. Jo, S. Y. et al. Polymer stabilization of liquid-crystal blue phase II toward photonic crystals. *ACS Applied Materials & Interfaces* **9**, 8941–8947 (2017).

195. Yan, J. & Wu, S.-T. Polymer-stabilized blue phase liquid crystals: a tutorial. *Optical Materials Express* **1**, 1527–1535 (2011).

196. Kikuchi, H., Yokota, M., Hisakado, Y., Yang, H. & Kajiyama, T. Polymer-stabilized liquid crystal blue phases. *Nature Materials* **1**, 64–68 (2002).